

Lecture Notes in Mechanical Engineering

Zitouni Azari · Khalid El Had ·
Mohamed ElAmine Ait Ali ·
Aberrahim El Mahi · Fakher Chaari ·
Mohamed Haddar *Editors*

Advances in Applied Mechanics


Proceedings of The Eleventh
International Congress for Applied
Mechanics (JET'2022), November
16–18, 2022, Marrakech, Morocco

 Springer

Lecture Notes in Mechanical Engineering

Series Editors


Fakher Chaari, *National School of Engineers, University of Sfax, Sfax, Tunisia*

Francesco Gherardini , *Dipartimento di Ingegneria “Enzo Ferrari”, Università di Modena e Reggio Emilia, Modena, Italy*

Vitalii Ivanov, *Department of Manufacturing Engineering, Machines and Tools, Sumy State University, Sumy, Ukraine*

Mohamed Haddar, *National School of Engineers of Sfax (ENIS), Sfax, Tunisia*

Editorial Board Members

Francisco Cavas-Martínez , *Departamento de Estructuras, Construcción y Expresión Gráfica Universidad Politécnica de Cartagena, Cartagena, Murcia, Spain*

Francesca di Mare, *Institute of Energy Technology, Ruhr-Universität Bochum, Bochum, Nordrhein-Westfalen, Germany*

Young W. Kwon, *Department of Manufacturing Engineering and Aerospace Engineering, Graduate School of Engineering and Applied Science, Monterey, CA, USA*

Justyna Trojanowska, *Poznan University of Technology, Poznan, Poland*

Jinyang Xu, *School of Mechanical Engineering, Shanghai Jiao Tong University, Shanghai, China*

Lecture Notes in Mechanical Engineering (LNME) publishes the latest developments in Mechanical Engineering—quickly, informally and with high quality. Original research reported in proceedings and post-proceedings represents the core of LNME. Volumes published in LNME embrace all aspects, subfields and new challenges of mechanical engineering.

To submit a proposal or request further information, please contact the Springer Editor of your location:

Europe, USA, Africa: Leontina Di Cecco at Leontina.dicecco@springer.com

China: Ella Zhang at ella.zhang@springer.com

India: Priya Vyas at priya.vyas@springer.com

Rest of Asia, Australia, New Zealand: Swati Meherishi at swati.meherishi@springer.com

Topics in the series include:

- Engineering Design
- Machinery and Machine Elements
- Mechanical Structures and Stress Analysis
- Automotive Engineering
- Engine Technology
- Aerospace Technology and Astronautics
- Nanotechnology and Microengineering
- Control, Robotics, Mechatronics
- MEMS
- Theoretical and Applied Mechanics
- Dynamical Systems, Control
- Fluid Mechanics
- Engineering Thermodynamics, Heat and Mass Transfer
- Manufacturing Engineering and Smart Manufacturing
- Precision Engineering, Instrumentation, Measurement
- Materials Engineering
- Tribology and Surface Technology

Indexed by SCOPUS, EI Compendex, and INSPEC.

All books published in the series are evaluated by Web of Science for the Conference Proceedings Citation Index (CPCI).

To submit a proposal for a monograph, please check our Springer Tracts in Mechanical Engineering at <https://link.springer.com/bookseries/11693>.


Zitouni Azari · Khalid El Had ·
Mohamed ElAmine Ait Ali ·
Aberrahim El Mahi · Fakher Chaari ·
Mohamed Haddar
Editors

Advances in Applied Mechanics

Proceedings of The Eleventh International
Congress for Applied Mechanics (JET'2022),
November 16–18, 2022, Marrakech, Morocco

Editors

Zitouni Azari
Ecole Nationale d'Ingénieurs de Metz, LEM3
University of Lorraine
Metz, France

Mohamed ElAmine Ait Ali 
Mohammadia School of Engineers
Mohammed V University in Rabat
Rabat, Morocco

Fakher Chaari 
Sfax, Tunisia

Khalid El Had
Higher Institute for Maritime Studies
Casablanca, Morocco

Aberrahim El Mahi
Acoustics Laboratory (LAUM)
Université du Maine
Le Mans, France

Mohamed Haddar
Sfax, Tunisia

ISSN 2195-4356 ISSN 2195-4364 (electronic)
Lecture Notes in Mechanical Engineering
ISBN 978-3-031-49726-1 ISBN 978-3-031-49727-8 (eBook)
<https://doi.org/10.1007/978-3-031-49727-8>

© The Editor(s) (if applicable) and The Author(s), under exclusive license
to Springer Nature Switzerland AG 2024

This work is subject to copyright. All rights are solely and exclusively licensed by the Publisher, whether the whole or part of the material is concerned, specifically the rights of translation, reprinting, reuse of illustrations, recitation, broadcasting, reproduction on microfilms or in any other physical way, and transmission or information storage and retrieval, electronic adaptation, computer software, or by similar or dissimilar methodology now known or hereafter developed.

The use of general descriptive names, registered names, trademarks, service marks, etc. in this publication does not imply, even in the absence of a specific statement, that such names are exempt from the relevant protective laws and regulations and therefore free for general use.

The publisher, the authors, and the editors are safe to assume that the advice and information in this book are believed to be true and accurate at the date of publication. Neither the publisher nor the authors or the editors give a warranty, expressed or implied, with respect to the material contained herein or for any errors or omissions that may have been made. The publisher remains neutral with regard to jurisdictional claims in published maps and institutional affiliations.

This Springer imprint is published by the registered company Springer Nature Switzerland AG
The registered company address is: Gewerbestrasse 11, 6330 Cham, Switzerland

Paper in this product is recyclable.

Preface

This book contains selected contributions from the 11th edition of the International Congress for Applied Mechanics (known as Technical Study Days, JET2022), which was held in Marrakesh, from November 16 to 18th, 2022. Initiated in 2000 by the Franco-Maghreb Association of Mechanics and Materials (AF3M, af3m-assoc.org), this congress has been held periodically every two years. The 11th edition was organized in collaboration with the Moroccan Society of Mechanical Sciences (SMSM, smsm.org.ma). The goal of these events is to review research and practical advances in mechanical sciences and materials that are contributing to sustainable development and environmental protection.

Mechanical sciences and materials are fundamental elements of a major technological change necessary to meet the challenges of sustainable development. The emergence of renewable energies, the importance of energy transition, and the extension of the operating life of equipment and industrial installations. It is therefore necessary to put more and more knowledge into the design, production, and operation of equipment by massively using artificial intelligence. At the same time, the evolution of materials based on biomimetics or bio-based materials will influence many industrial sectors by their mechanical, electrical, phonic, and thermal properties. Currently, bio-composites are increasingly used in several industrial sectors (mechanical, building, aeronautic) for their biodegradability, their lightness, and their exceptional resistance, very important assets in order to reduce the impact of industrial products on the environment. The main idea is to take advantage of local materials in order to reduce production and operation costs. In coherence with these arguments, the themes of these events and the 11th edition are: **1) Design/Optimization/Lightening/Lifetime and integrity check; 2) Materials/Production processes/Recycling and Life Cycle; 3) Renewable Energies/Energy saving/monitoring of equipment, Artificial Intelligence; 4) Bio-sourced materials/Eco-materials/Eco-Design; 5) Hydrogen in production, storage, transport and conversion.**

After the congress, the editors of this book selected sixteen papers from the presented forty-four contributions and asked the authors to submit an extended version of their work for reviewing. Each submission was evaluated, using a single-blind review process, by at least two reviewers from the scientific committee of the congress edition. As a result, this book contains sixteen original contributions, and they cover the five themes listed above and are relating to the major industrial sectors of energy, transport, and mechanical industries. Thus, this book is expected to be of interest for both researchers and industrial actors.

The editors acknowledge the big efforts of the authors of the scientific committee and Springer editorial team of the book series “Lecture Notes in Mechanical Engineering.”

We thank them for their contribution to the accomplishment of this book. We would like to thank also the organizing committee together with all the participants for contributing to the success of the 11th edition. We hope that this event stays and continues to grow as a platform for scholars from around the world to meet and discuss their innovations.

Organization

Organization Committee

Azari Z. (Chair)	Univ. Lorraine, France
Hariri S.	IMT-Lille Douai, France
Khalij L.	INSA de Rouen, France
Lachat J. C.	Engineer, France
Laksimi A.	UTC, France
El Mahi A.	Univ. du Maine-Le Mans, France
Elmoumen A.	Univ. Du Havre, France
Elhad K. (Chair)	ISEM-Casablanca, Morocco
Ait Ali M. E.	Univ. Mohammed V in Rabat-EMI, Morocco
Bouchgl J.	ISPM-Agadir, Morocco
Boukendil M.	Univ. Cadi Ayyad-FSSM, Morocco
Hachim A.	ISEM-Casablanca, Morocco
Mabchour H.	ISEM-Casablanca, Morocco
Mouhib N.	ISEM-Casablanca, Morocco
Sandabad S.	ISEM-Casablanca, Morocco

Scientific Committee

Aberkane M.	UMM Algérie, Algeria
Abouchadi H.	ENSAM-Rabat, Morocco
Agouzoul M.	Univ. Mohammed V in Rabat-EMI, Morocco
Ait Ali M. E.	Univ. Mohammed V in Rabat-EMI, Morocco
Amrouche A.	Univ-Artois, France
Aniss S.	Univ. HASSAN II-FSAC, Morocco
Assarar A.	IUT de Troyes, France
Assih J.	Univ. Reims, France
Atcholi K. E.	UTBM, France
Ayad R.	Univ. Reims, France
Azari Z.	Univ. Lorraine, France
Azrar L.	ENSAM-Rabat, Morocco
Benamara A.	Enim, Tunisia
Benguediab M.	USBA, Algeria
Benmedakhene S.	Pyromera, France
Benyahia A.	USTHB, Algeria

Bezazi A.	Univ. Guelma, Algeria
Bonfoh N.	Univ. Lorraine, France
Bou-Ali M. M.	Univ. Mondragon, Spain
Bouchouicha B.	Univ. Sidi Bel Abbés, Algeria
Boukamel A.	Centrale Casablanca, Morocco
Bouraoui C.	ENISo, Tunisia
Bouvier S.	UTC, France
Bradai C.	ENIS, Tunisia
Casavola K.	Politecnico di Bari, Italy
Chaari F.	ENI-Sfax, Tunisia
Charif D'ouazzane S.	ENSMR, Morocco
Chergui M.	ENSEM, Morocco
Damil N.	Univ. HASSAN II-FSB, Morocco
Dantec C.	Univ. Artois, France
El Bikri A.	ENSAM-Rabat, Morocco
El Gharad A.	ENSAM-Rabat, Morocco
El Ghorba M.	ENSEM, Morocco
El Had K.	ISEM-Casablanca, Morocco
El Hami A.	INSA-Rouen, France
El Mahi A.	LAUM-Le Mans, France
El Mahmoudi H.	UMP6P, Morocco
El Minor H.	ENSA-Agadir, Morocco
Erchiqui F.	UQUAT, Canada
Ghorbel E.	Univ. Cergy-Pontoise, France
Gong Xiao-Lu	UTT, France
Haddar M.	ENI-Sfax, Tunisia
Hadj Meliani M.	UHBC, Algeria
Hamdi M. A.	UTC-ESI, France
Hamza S.	INSAT, Tunisia
Hamzaoui N.	INSA-Lyon, France
Hariri S.	IMT-Lille Douai, France
Harizi W.	UTC, France
Imad A.	Polytech-Lille, France
Jalid A.	ENSAM-Rabat, Rabat
Kanit T.	Univ. Lille, France
Laghzale N.	ENSAM-Rabat, Morocco
Laksimi A.	UTC, France
Maslouhi A.	Univ. Sherbrooke, Canada
Maslouhi A.	Univ. Ibn Tofail, Morocco
Matadi R.	Univ. Lorraine, France
Mordane S.	Univ. HASSAN II-FSB, Morocco
Nait M. A.	Polytech-Lille, France

Nawab Y.	NTI-Faisalabad, Pakistan
Ouazzani Touhami M.	Univ. HASSAN II-FSAC, Morocco
Panier S.	Univ. Amiens, France
Pappa-Lettere C.	Politecnico di Bari, Italy
Pizette P.	IMT-Lille Douai, France
Rahmoune M.	Univ. Moulay Ismail-ESTM, Morocco
Roger F.	IMT-Lille Douai, France
Rusinek A.	Univ. Lorraine, France
Saouab A.	Univ. Le Havre, France
Taha Janane M.	ENSAM-Rabat, Morocco
Tarfaoui M.	ENSTA, France
Toubal L.	UQTR. Québec, Canada
Tri J.	ISEM-Casablanca, Morocco
Vassinkov D.	IMT-Lille Douai, France

Contents

Effect of the Nanostrength® M53 on Elastic Properties of Glass Fiber Reinforced Acrylic Thermoplastic Resin	1
<i>A. Y. E. Kouassi, R. Matadi Boumbimba, and M. K. Sangaré</i>	
Assessment of Filament Deposition Aero-Modelling for UAV Design Development	16
<i>Mohamed Hakim, Saad Choukri, and Mohamed Oubrek</i>	
Modeling the Propagation of Ultrasonic Guided Waves in Four-Layer Laminated Composites	25
<i>Ismaïne Zitouni, Hassan Rhimini, and Abdelkerim Chouaf</i>	
Numerical Investigation of Combined Natural Convection, Conduction and Radiation Through Concrete Hollow Bricks	34
<i>Jamal Bouchaib, Lahcen El Moutaouakil, Mohammed Boukendil, Abdelbaki Abdelhalim, and Zaki Zrikem</i>	
Time Domain Analysis of Skin Effect in Nonuniform Interconnection Using the FDTD Technique	43
<i>Nadir Youssef, Belahrach Hassan, Ghammaz Abdelilah, Naamane Aze-eddine, and Mohammed Radouani</i>	
Effect of the Temperature on the Mechanical Properties of Jute Fabric Reinforced Epoxy Composite	54
<i>Youssef Ben smail, Ahmed El moumen, Fatima Lmai, and Abdellatif Imad</i>	
Two and Three-Dimensional Computation of Dispersion Curves of Ultrasonic Guided Waves in Isotropic Plates by the Spectral Collocation Method	63
<i>Moussa Mekkaoui, Salah Nissabouri, and Hassan Rhimini</i>	
Numerical Analysis of Mixed Convection Coupled with Thermal Radiation in a Ventilated Channel Containing Various Heat-Generating Blocks	73
<i>Rachid Hidki, Lahcen El Moutaouakil, Mohammed Boukendil, Zouhair Charqui, Zaki Zrikem, and Abdelhalim Abdelbaki</i>	

Experimental and Numerical Analysis of the Vibration Behavior
of a Bio-Based Sandwich with an Auxetic Core in a Humid Environment 85
*Zeineb Kesentini, Abderrahim El Mahi, Jean Luc Rebiere,
Rachid El Guerjouma, Moez Beyaoui, and Mohamed Haddar*

A Microstructurally Motivated Hyperelastic Model for Elastomer Materials 92
Ayoub Ouardi, Adnane Boukamel, and Nouredine Damil

Meshless Approach for the Simulation of Compressible Isothermal Fluid
Flows 99
Rajaa Fadil, Mohammed Rammane, Abdeljalil Tri, and Bouazza Braikat

Effect of Thermal Parametric Excitation on the Destabilization
of a Linearly Stable System 109
*Mohamed Sakine, Mohamed Hayani Choujaa, Mehdi Riahi,
Abdelmajid Daya, and Saïd Aniss*

A High-Order Implicit Algorithm Using an RBF-Type Meshless Method
for the Simulation of Cardiac Electrical Activity 120
*Sita Kaba, Loubna Salhi, Nouredine Damil, Nabyl El Moçayd,
and Adnane Boukamel*

Effect of Vertical Periodic Oscillation with Two Commensurate
Frequencies on the Rayleigh-Taylor Instability 130
Chaimaa Taouzer, Mouh Assoul, and Saïd Aniss

On a Novel Micromechanical Modeling of the Elastic Behavior
of Nanocomposites 139
El Hassane Barhdadi

Effect of Number of Engines and Payload Weight on Static Stability
of an Unmanned Aerial Vehicle 148
Amina Kottat and Mohamed ElAmine Ait Ali

Author Index 159



Effect of the Nanostrength® M53 on Elastic Properties of Glass Fiber Reinforced Acrylic Thermoplastic Resin

A. Y. E. Kouassi^{1,2}, R. Matadi Boumbimba¹✉, and M. K. Sangaré²

¹ Université de Lorraine, CNRS, Arts et Métiers ParisTech, LEM3, F-57000 Metz, France
{alexis.kouassi, rodrigue.matadi-boumbimba}@univ-lorraine.fr,
alexis.kouasssi@inphb.ci

² Unité Mixte de Recherche et d'Innovation en Mécanique et Science des Matériaux (UMRI 18), Ecole Doctorale Polytechnique, Institut National Polytechnique Félix Houphouët-Boigny de Yamoussoukro, BP 1093 Yamoussoukro, Côte d'Ivoire
moustapha.sangare@inphb.ci

Abstract. This paper aims to study the elastic properties of glass fibers reinforced acrylic thermoplastic resin-based Nanostrength® M53. The acrylic resin was filled with three weight fractions (5, 10 and 15 wt %) of the Nanostrength® M53. The effect of Nanostrength® M53 on the elastic properties was studied using tensile tests and finite element method-based RVEs by means of Digimat-FE. For this purpose, platelet inclusions and three aspect ratios (AR) were considered for microstructures reconstruction. A multi-scales homogenization scheme was used for the determination of the effective elastic properties using Digimat-FE solver. From the experimental and numerical results, the elastic properties decreased slightly while the weight fraction (wt %) of the Nanostrength® M53 increased in the composites. The loss in Young modulus was estimated at about 9.5 to 10% according to the Nanostrength weight fractions of 10 wt % and the comparison of the elastic properties was consistent. The use of the Nanostrength® M53 would then be a source of a slight loss of elastic properties, however, the Nanostrengths® M53 were suitable for many applications that needed an increase in resistance to crack propagation, and in the literature, the laminate composites filled with 10 wt % of Nanostrength® M53 depicted better low-velocity impact resistance.

Keywords: Elastic properties · Elium Acrylic resin · Nanostrength® M53 · Copolymers · Laminate composites · Digimat-FE · RVEs · Multi-scales homogenization

1 Introduction

In recent decades, composite materials have played an important role in the development of new technologies, thanks to their numerous advantages in various fields such as automobile, aeronautics, naval, etc. Composite materials stand out for their ease of implementation and light weight. They have good mechanical and physicochemical

properties that offer them a wide range of possibilities in terms of design and use in any kind of environment [1–5]. One of the disadvantages of polymer-based laminate composites is the fragile appearance of their amorphous matrix facing mechanical stresses. The fact that the matrix is rigid would lead to the initiation of damage phenomena such as matrix cracking, fiber-matrix decohesion, delamination and fiber breakage [6]. To overcome these early damage phenomena, additives like block copolymers and shock modifiers, consisting of various nanostructures (A-B-S, M-A-M, S-B-M, etc.), were added to the matrix during the process with the objective of improving the toughness of the matrix [7, 8]. The Nanostrengths® M53, a tri-block copolymer (M-A-M) developed by Arkema company, which consists of a centered PABu block surrounded by two blocks of PMMA, can be miscible with polymer resins like epoxy and thermoplastic matrices and offers good improvement in low-velocity impact resistance [9]. The environmental issues that favour recyclable materials lead researchers to use more and more thermoplastics instead of thermosetting materials (epoxy, polyester, etc.). For this purpose, Arkema implemented a thermoplastic resin called Elium acrylic. This resin, which has the ability to polymerize at room temperature, depicts good adhesion with glass fibers. Moreover, the laminated composite with a glass fiber-reinforced Elium acrylic matrix showed better low-velocity impact resistance compared to epoxy and polyester matrices composites [10]. It has also been shown in the literature that the laminated composites with an acrylic Elium matrix filled with Nanostrength® M53 offer better impact resistance for a weight concentration of 10 wt % [11]. However, the prediction of the elastic properties of these composites had not yet been studied, and therefore their overall mechanical behaviour remained unknown.

The mechanical behavior of a laminated composite can be quantified not only by experimental tests on conventional machines but also by numerical simulation using advanced software such as Abaqus, Ansys, etc. [12–14]. Digimat-FE is part of the software used for creating complex microstructures (REVs) and computing the effective elastic properties by the homogenization of the constituent model [15–17]. Digimat-FE is one of Digimat's tools which is a multi-scale modeling platform for materials and structures developed by the HEXAGON group [18]. To better analyze the microstructure of materials and determine the sizes of nanoparticles, the ImageJ software is often used, and it can be combined with Digimat to predict accurate elastic properties [19–21].

The objective of our work is to analyze the effect of nanostrength® M53 on the microstructure of glass fiber-reinforced Elium acrylic resin and to quantify the mechanical behavior of the constituent composite. The Elium acrylic resin was filled with three Nanostrength weight fractions (5, 10 and 15 wt %). The glass fabric (taffetas) has been used as the main reinforcement for laminate composites. The estimation of the elastic properties was carried out initially by tensile tests on the samples. The microstructures were analyzed using scanning electron microscopy (SEM), and the results allowed the reconstruction of the microstructures using ImageJ and Digimat-FE softwares. The effective properties were subsequently determined by multi-scale homogenization of the obtained numerical models.

2 Experiments

2.1 Materials

The Elium (E150) resin used is a thermoplastic liquid resin developed by ARKEMA company. The kinematic viscosity of this resin was 150 cPs. The Elium resin is a mixture of acrylic-based polymer diluted in a reactive monomer and additives. This formulation gives a very fluid behaviour to the resin with a translucent appearance and the characteristic of curing at room temperature (~ 20 °C). The bi-directional glass fabrics (taffetas) used were supplied by CHOROMAT company. The surface density of the fabric was 600 g/m^2 and it had an identical pattern of 7.8 mm frequency in both warp and weft directions. The Nanostrength® M53 used is part of the family of self-assembled block copolymers, and it was supplied by ARKEMA (GRL, France). The Nanostrength® M53 is the acrylic tri-block copolymer M53 and also a symmetric M-A-M copolymer. M-A-M copolymers are composed of poly (butylacrylate) central blocks and two poly (methyl methacrylate) side blocks. These copolymers are designed for epoxy formulations such as Diglycidyl Ether of Bisphenol A (DGEBA). The properties of the materials used are presented in Table 1.

2.2 Processing

A vacuum resin infusion process at a pressure of 100 mbars was used for the laminate processing and its can be described in three steps. Firstly, the infusion table was cleaned with a release treatment which facilitated the release of the composite after infusion. The glass fabrics of $600 \text{ mm} \times 600 \text{ mm}$ dimensions and $0/90^\circ$ orientation were adjusted and arranged in sets of four plies. The fabrics were covered successively with a release film and a draining grid. A batch covered the entire work surface creating a closed enclosure that was sealed by a mastic glue. Secondly, the resin was degassed with a vacuum bell at rate of 450 rpm and a pressure of 250 mbars for 15 min. For the Nanostrength®M53 loaded matrix laminated composites, the nanoparticles were added to the resin and mixed for approximately 2h to ensure good dispersion of them. Three weight fractions of the Nanostrength® M53 (5, 10 and 15 wt %) were used. The resulting resin was also degassed in the same conditions as mentioned above. Thirdly, the peroxide catalyst was added and mixed with the resin, and the infusion was started at room temperature. The designation of the samples is presented in Table 2.

2.3 Microstructure Characterization

The microstructures of the Nanostrength® M53 reinforced laminate composites were analyzed by scanning electron microscopy (SEM FEI QUANTA FEG 250). For this analysis, the samples of $10 \text{ mm} \times 10 \text{ mm}$ dimensions were cut using a water jet to ensure good surface condition after cutting. The samples were then cold-coated in moulds using the acrylic resin ClaroCit Kit UN1866 provided by STRUERS company. After the mechanical polishing, the ionic polishing was carried out for 1h at the energy of 5.5 keV using the PECS II model 695 device. Ionic polishing was used to obtain a good polish surface, which allows easy identification of the reinforced Nanostrength® M53 in the

matrix reach regions. The two polishing methods were carried out on the thickness of the samples and in the same plane.

2.4 Tensile Test

The uniaxial tensile tests were performed at room temperature using a MTS 20/M machine with capacity of 100 kN. This device was equipped with a control console and workstation, which were used for the test piloting. The samples used were rectangular in the shape of 250 mm \times 25 mm dimensions and thickness of around 2 mm. A biaxial extensometer measured the deformation in the longitudinal and transverse directions. The tensile tests were achieved at a stain rate of 10^{-4}s^{-1} , which corresponds to a travelling rate of 1 mm/min. Five samples of each laminate composite were tested for the repeatability of the tensile test and to ensure better results.

Table 1. Material properties

Material	Acrylic resin E150	Glass fiber	Nanostrength® M53
Density (g/cm^3)	1.18	2.56	1.1
Young modulus (GPa)	3.3	73	0.1
Poisson ratio (-)	0.4	0.22	0.43

Table 2. Designation of the laminate composites

Matrix	Nanostrength® M53	Laminate composites
Acrylic resin E150	–	E150/GF
	5 wt %	E150_NS5/GF
	10 wt %	E150_NS10/GF
	15 wt %	E150_NS15/GF

3 Numerical Simulation

3.1 Homogenization Concept

The effective elastic properties computation of the laminates composites was based on multi-scale homogenization illustrated by the Fig. 1. The first scale was the homogenization of the acrylic resin filled with Nanostrength® M53 according to their weight fractions (wt %). Then, the resulting blended resin and the glass fabrics were used for the second homogenization. The multi-scale homogenizations were based on finite element homogenization (FEH) [22] using Digimat-FE [18].

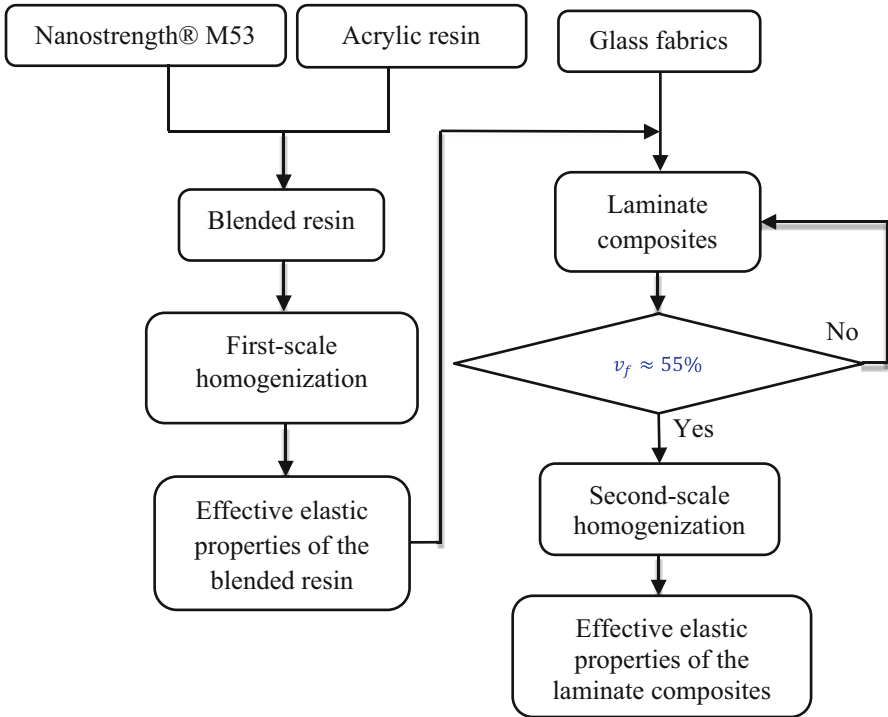


Fig. 1. Flowchart of the computing of the effective elastic properties of laminate composites

3.2 Finite Elements Modeling

The REV of laminate composites were designed by Digimat-FE 2021.3 based on the characterization of the microstructures. From Digimat-FE 2021.3, the mechanical analysis type was selected, and the reconstruction of the microstructures was performed in two steps, illustrated by the Fig. 1. The first step concerned the acrylic resin and the Nanostrength® M53 which were assumed as matrix and inclusions phases, respectively. ImageJ software was used previously to determine the size and morphology of the nanoparticles based on the SEM images, as reported in [17]. Thus from the nanoparticles dispersion state, platelet inclusions types and random 3D orientation were considered in the inclusion phase creation. Three aspect ratios (AR) were calculated based on SEM images using ImageJ software. The aspect ratio was defined by the ratio of the thickness of the nanoparticles (10–100 nm) by their mean diameters obtained by ImageJ software analysis. The RVEs of the blended resin were obtained according to the set of parameters such as materials properties (Table 1), the diameters (minimum, maximum) of platelet inclusions and the nanoparticles weight fractions (wt %). The second step concerned the blended matrix and the glass fabrics. The effective elastic properties of the blended resin were considered as the parameters of a new matrix, and 2D woven was designed by using the data sheet parameters of the glass fabrics (taffetas). A condition has been fixed on the volume fraction (v_f) of fiber into the laminate, which should be about 55% in reference to the infusion process [10, 23, 24]. Another condition was applied on yarn

parameters because of the glass fabrics manipulation during the infusion process. Indeed, glass fabrics are very flexible and this characteristic often leads yarn deformation during the placement of the layers. Two numerical parameters can be explained the deformation of yarn as shown on the Fig. 2. The yarn spacing ratio is the ratio between the height of a resin zone introduced between the yarn and the yarn height. As illustrated on the Fig. 2a, the higher the yarn spacing ratio, the higher the yarn height. The default value of yarn spacing ratio is 0. The Fig. 2b shows yarn crimp which describes the yarn tortuosity. The higher the yarn crimp, the higher the warp yarn tortuosity and the lower the weft yarn tortuosity. The same tortuosity is applied to the warp and weft yarn for the default value of 0.5. According to the vacuum infusion process of which the pressure was normal to the glass fabrics layers, the yarn spacing ratio was used as default value. However, the yarn tortuosity was considered for the yarn crimp value of 0.75. The laminate composites was obtained by creating four similar layers oriented at $0/90^\circ$.

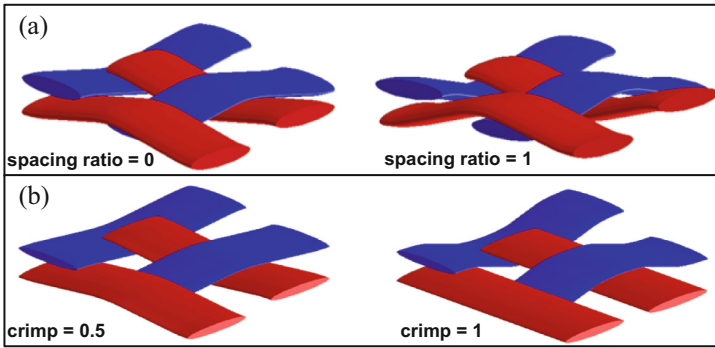


Fig. 2. 2D woven morphologies [18], (a) Yarn spacing ratio and (b) Yarn crimp

3.3 Conditions of Computing

The computing of the effective elastic properties was carried out by mechanical conditions, which were displacements. For the blended resin RVEs, the periodic boundary conditions (PBC) were fixed on the numerical models. These conditions ensure that the displacement is periodic concerning the faces of the RVE, and the RVEs should be as small as possible to obtain better effective elastic properties [22, 25, 26]. The REV's of $1,5 \mu\text{m}$ were meshed by the integrated Abaqus/CAE module, and conforming meshing with tetrahedral elements was used. The automatic meshing type was selected, and the main parameters were the sizes of the elements (minimum and indicative). The number of elements required for convergence of the RVE was about 250 000 elements. In the case of the laminate composites, only the PBC in plane (x, y) was used because the RVEs were periodic in plane (x, y) and therefore they represented an orthotropic symmetry in the global basis (x, y, z). The RVEs size was $8 \text{ mm} \times 8 \text{ mm} \times 2 \text{ mm}$ and the voxel meshing type was used. The number of meshing elements was about 500 000 elements. The loading types imposed on RVEs was uniaxial- x loading and biaxial- x, y loading for blended

resin and laminate composite, respectively. The automatic properties evaluation and the Digimat solver were selected as the loading source and computing solver, respectively. The required elastic engineering constants were computed in quasi-static mode.

4 Results and Discussions

4.1 Microstructures

The SEM images of the laminate composites are shown in Fig. 3. The Fig. 3a shows the microstructure of the composite without Nanostrength® M53 of which the texture of neat Elium resin was observed. As shown in Fig. 3b, the microstructure of E150_NS5/GF presented different sizes of glass fibers and at the scale of 50 μm a continuous matrix phase can be observed. The diameters of the fibers varied from 14.8 μm to 20 μm . The cross sections of the yarns were elliptical, and their small and large diameters varied from 0.37 mm to 0.57 mm and from 2.73 mm to 3.5 mm, respectively. For nanostrength reinforced acrylic resin shown in Fig. 3c, d, two phases can be observed, in particular, a continuous phase and clustered phase. Figure 3c shows the microstructure of E150_NS5/GF in which some isolated clustered areas were observed. However, the continuous phase texture was denser compared to the pure acrylic matrix. The microstructure of E150_NS15/GF shown in Fig. 3d presents a two phases morphology, and the nanoparticle sizes were larger than those for the other composites. The higher the weight fraction of nanoparticles was, the higher the saturation of the matrix was. The inclusions sizes were in the range of 1 to 2 μm , 3 to 10 μm and 3 to 30 μm for the composites E150_NS5/GF, E150_NS10/GF and E150_NS15/GF, respectively. The higher the weight fraction of nanoparticles was, the higher the inclusions were visible and close together. These clustered microstructures could explain the slow diffusion of the blended resin during the infusion process. We observed that the viscosity increased with the weight fraction of the Nanostrength, which did not allow the composite E150_NS15/GF to be fully infused. The infused composite plates were square in size of 600 mm \times 600 mm and their thickness was around 2 mm. The glass fabrics were weighed before and after the infusion process which allowed the average fibers volume ratio (v_f) of about 55.11%. This fiber volume ratio is in agreement of the literature concerning the infusion process [10, 23, 24].

4.2 Elastic Constants (E_{11} and ν_{12})

The elastic constants were determined during the post-treatment of the tensile tests carried out on the samples oriented at 0/90°. The initial tensile length was about 150 mm. The 0/90° oriented samples allowed the determination of the Young moduli E_{11} and the Poisson ratio ν_{12} according to the longitudinal strain range ($0,005 \leq \epsilon \leq 0,0025$) given by the standard NF EN 527-1. The Young modulus was the guiding coefficient of the linear part of the curve of the nominal stress according to the nominal strain in the longitudinal direction of the samples. The Poisson ratio was determined by the ratio of transverse deformation to longitudinal deformation.

The elastic constants are mentioned in Table 3. The Young modulus decreased while the weight fraction (wt %) of the Nanostrength increased in the composite. However, the

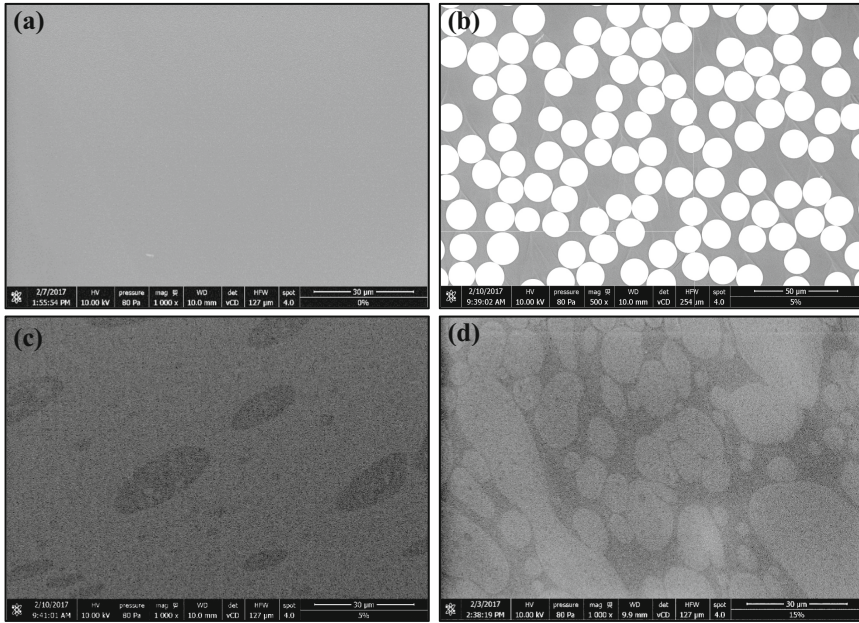


Fig. 3. SEM images of laminate composites, (a, b) Microstructures of E150/GF, (c) Microstructure of E150_NS5/GF and (d) Microstructure of E150_NS15/GF

deviations were not high according to their standard deviations. The Poisson ratios presented the same trends. Considering the results of the tensile test, the use of nanostrength leads to a slight decrease in the elastic properties of the laminate composites. According to Arkema, the nanostrength would reinforce the mechanical properties of the matrices at the molecular scale [9]. The nanostrengths are suitable for every application that need an increase in resistance to crack propagation while maintaining the T_g and modulus of the systems. Indeed in the literature, the Nanostrength were often used to improve impact resistance [7, 11, 27–29]. It has been proved that the impact resistance increases more for 10 wt % of nanostrength reinforced acrylic resin compared to other composites [11]. At the same weight fraction, the Young modulus decreased by about 9.5%.

Table 3. Elastic constants (E_{11} and ν_{12})

Laminate composites	E150/GF	E150_NS5/GF	E150_NS10/GF	E150_NS15/GF
Young modulus E_{11} (GPa)	23.59 ± 0.46	22.13 ± 0.85	21.36 ± 0.69	–
Poisson ratio ν_{12} (–)	0.20 ± 0.05	0.15 ± 0.03	0.13 ± 0.09	–

4.3 Effective Elastic Properties

4.3.1 First-Scale Homogenization

Microstructures of the Blended Resin

The Fig. 4 shows the microstructures of the blended resin with platelet inclusion types. The choice of the platelet inclusion types was made according to the SEM images (Fig. 3) which show globally circular morphology of nanoparticles. Considering the particle size of 10 nm and following the same procedure in [17], the aspect ratios were 0.02, 0.05 and 0.08 according to the weight fractions 5, 10 and 15 wt %, respectively. The more the weight fraction of nanoparticles increases in RVEs, the more the nanoparticle thickness increases, and the more the aspect ratio also increases. Indeed, the increase in thickness would increasingly show a clustered microstructure. This is what could explain the bi-phasic morphology observed for the high weight fraction (Fig. 3). As shown in Fig. 5, the numerical models were obtained based on RVEs. Figure 5a shows the random orientation of the nanoparticles. Figure 5b shows the numerical model contained the matrix phase and the random 3D oriented nanoparticles. The tetrahedral meshing elements is shown in Fig. 5c.

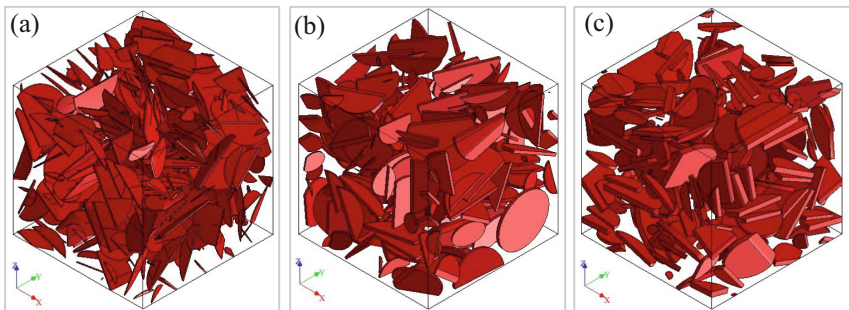


Fig. 4. RVEs of acrylic filled Nanostrength®M53, assuming as platelet inclusions, (a) E150_NS5/GF, (b) E150_NS10/GF and (c) E150_NS15/GF.

Effective Elastic Properties of the Blended Resin

The blended resin presented an isotropic symmetric material. Considering this observation, the Young modulus (E) and the Poisson ratio (ν) were considered for illustrations shown in the Fig. 6. The Young modulus shown in the Fig. 6a decreased with the volume fraction (v_p %) of the Nanostrength®M53. This observation was also made for the Poisson ratio (Fig. 6b). According to the characteristic data provided by Arkema company, the elongation at the break of the nanostrength was about 90%. The elongation at break is a characteristic value describing the maximum percentage elongation that a tensile specimen experiences at the break. It, therefore, describes the deformability of a material under tensile load. Using nanostrength in the acrylic resin has improved the deformability of the blended matrix. This is what could explain the slight loss in the elastic module.

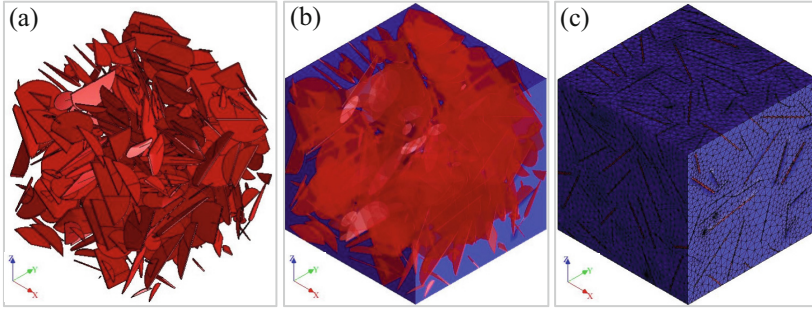


Fig. 5. Random orientation of Nanostrength®M53 at 5 wt % reinforced RVE, (a) platelet inclusions, (b) numerical model, and (c) Meshing with tetrahedral elements C3D4

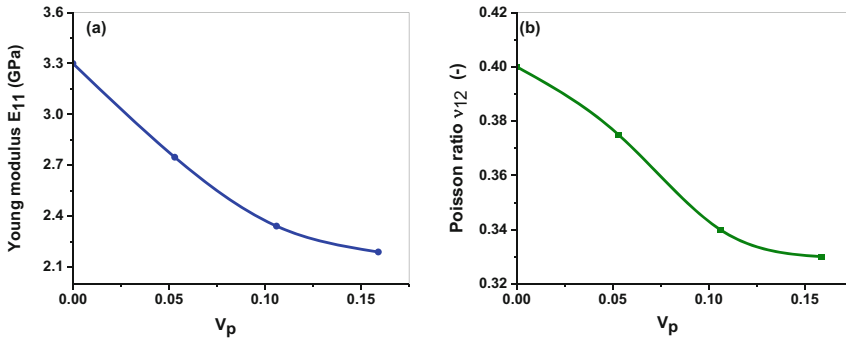


Fig. 6. Effective elastic properties of the blended resin, (a) Young modulus and (b) Poisson ratio

4.4 Second-Scale Homogenization

Microstructures of the Laminate Composites

Figure 7 shows the reconstruction steps of the laminate composites. As shown in Fig. 7a, the acrylic resin and fibers properties were used to create the yarn. The yarn cross section dimensions were 3.12 mm and 0.21 mm and the fiber's diameter was 0.017 mm. A mesoscopic glass fabric was obtained by considering two yarns in the both warp and weft directions as shown in the Fig. 7b. The resulting pattern was similar to the actual glass fabric (taffetas) in terms of periodicity in warp and weft directions. The laminate composite shown in Fig. 7c was obtained by filling four plies of glass fabric. For all studied laminate composites, the same modeling characteristics were considered except for the weight fraction of Nanostrength. According to these RVEs parameters, the fibers volume ratio was about 55.08%. From the obtained RVEs, the numerical models were meshed as shown in Fig. 7d in order to compute the effective elastic properties.

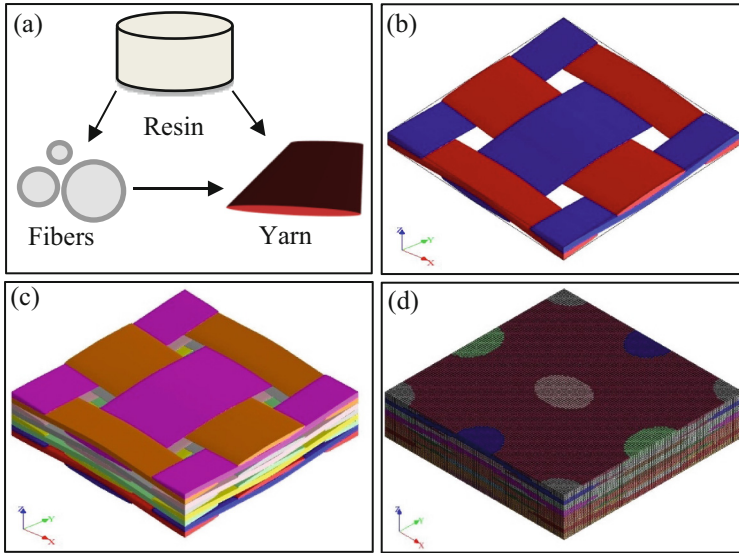


Fig. 7. Reconstruction steps of laminate composites, (a) Section of fiber and yarn, (b) RVE of two yarns in one ply, (c) RVE of laminate in four plies and (d) voxel meshing

Effective Elastic Properties of the Laminate Composites

Figure 8 shows the effective elastic properties of the laminate composites. The general observation is that the curves were similar to those in Fig. 6 except for the values of the properties, which were higher. The increase in values was due to the high strength of the glass fibers compared to that of the blended resin. However, the values of the properties decreased while the volume fraction (v_p %) of Nanostrength increased in the composite. As shown in Fig. 8a, the variation of the Young modulus is approximately linear in the range of 0 to 0.05 v_p %. The same trends can be observed in the case of the Poisson ratio shown in Fig. 8b. This observation was probably due to the good dispersion of the Nanostrength below 0.05 v_p % in the acrylic resin. From 0.05 to 0.16 v_p %, the curves of Young modulus and Poisson ratio presented a less sharp slope with a small difference in values. This could be due to a non-homogeneous dispersion of nanoparticles in the acrylic resin. Indeed, as shown in Fig. 4, the thickness of the nanoparticles increased with the volume fraction in RVE and this observation reflecting clustered inclusions illustrated by Fig. 3d. A clustered microstructures could be a source of loss of mechanical properties

due to the poor interfacial adhesion between the acrylic resin matrix and the clustered inclusions.

Comparison of Effective Elastic Properties and Experimental Data

Figure 8 also shows the experimental elastic constants graphs which presented the same trends compared to the effective elastic properties. As shown in Fig. 8a, the curve of the effective Young modulus coincided approximatively with experimental data. The effective Young modulus decreased by about 10% at 10 wt % of Nanostrength, and compared to that of the experimental, the results were consistent. Moreover, the decrease in effective properties was also observed for 15 wt %. In the case of the Poisson ratio, the results presented in Fig. 8b, revealed a slight deviation for pure composite, when compared to the experimental value. For the other composites, the curve of effective Poisson ratio was in agreement with experimental data.

The general observation was that the elastic properties decreased slightly by adding Nanostrength to the laminate composites. As mentioned above [9, 11], this nanoparticle type was used to improve the impact and cracking resistance and could also maintain elastic properties for low weight fractions.

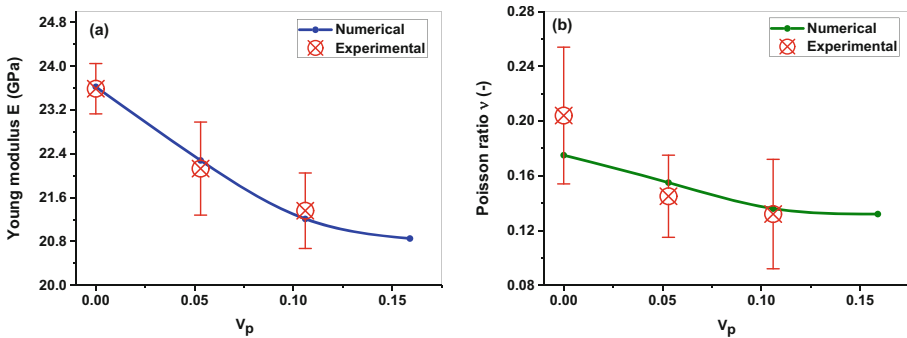


Fig. 8. Comparison of effective elastic properties and experimental data according to the volume fraction (v_p %) of Nanostrength

5 Conclusion

This work is about the experiments and numerical determination of the elastic properties of glass fibers reinforced acrylic thermoplastic resin-based Nanostrength® M53 at weight fractions of 5, 10 and 15 wt %. The microstructures were characterized by SEM analysis, and ImageJ software was used to access the nanoparticles distribution. The microstructures were then reconstructed based on the Nanostrength® M53 distribution and their aspect ratios (AR) using platelet inclusion by means of Digimat-FE. Multi-scales homogenization-based RVEs was used and the effective elastic properties were computed by Digimat-FE solver. The experimental elastic properties decreased while the weight fraction (wt %) of the Nanostrength® M53 increased, as well as the effective

elastic properties of the blended matrices and the constituent laminate composites. At the Nanostrength weight fraction of 10 wt %, the loss in Young modulus was estimated at about 9.5% and 10% for the experimental and numerical results, respectively. The slight decrease of the young modulus may be permissible because in the literature, the laminate composite would show a better low-velocity impact resistance at the weight fraction of 10 wt %. In addition, the Nanostrength® M53 can be used as a better reinforcement for the laminate composite-based acrylic resin thanks to their advantages like tensile and low-velocity impact resistances.

Declarations.

Conflict of Interest: None.

References

1. Gelineau, P., Stepień, M., Weigand, S., Cauvin, L., Bédoui, F.: Elastic properties prediction of nano-clay reinforced polymer using multi-scale modeling based on a multi-scale characterization. *Mech. Mater.* **89**, 12–22 (2015). <https://doi.org/10.1016/j.mechmat.2015.03.013>
2. Boumbimba, R.M., et al.: Dispersion and morphology of polypropylene nanocomposites: characterization based on a compact and flexible optical sensor. *Polym. Test.* **31**, 800–809 (2012)
3. Sharma, B., Mahajan, S., Chhibber, R., Mehta, R.: Glass fiber reinforced polymer-clay nanocomposites: processing, structure and hygrothermal effects on mechanical properties. *Procedia Chem.* **4**, 39–46 (2012). <https://doi.org/10.1016/j.proche.2012.06.006>
4. Fu, C., Wang, X.: Prediction of the cohesive strength for simulating composite delamination by a micro-mechanical model based on random RVE. *Compos. Struct.* **262**, 113343 (2021). <https://doi.org/10.1016/j.compstruct.2020.113343>
5. Brassart, L., Doghri, I., Delannay, L.: Homogenization of elasto-plastic composites coupled with a nonlinear finite element analysis of the equivalent inclusion problem. *Int. J. Solids Struct.* **47**, 716–729 (2010). <https://doi.org/10.1016/j.ijsolstr.2009.11.013>
6. Matadi Boumbimba, R., Froustey, C., Viot, P., Gerard, P.: Low velocity impact response and damage of laminate composite glass fibre/epoxy based tri-block copolymer. *Compos. Part B Eng.* **76**, 332–342 (2015). <https://doi.org/10.1016/j.compositesb.2015.02.007>
7. Matadi Boumbimba, R., et al.: Preparation and mechanical characterisation of laminate composites made of glass fibre/epoxy resin filled with tri bloc copolymers. *Compos. Struct.* **116**, 414–422 (2014). <https://doi.org/10.1016/j.compstruct.2014.05.028>
8. Bashar, M., Sundararaj, U.: Nanostructured Acrylic Triblock-Copolymer as Toughening Agents for Epoxy (2013). <https://doi.org/10.2417/spepro.004990>
9. Arkema launches Nanostrength for advanced composite materials. *Addit. Polym.* **2005**, 3 (2005). [https://doi.org/10.1016/S0306-3747\(05\)70387-0](https://doi.org/10.1016/S0306-3747(05)70387-0)
10. Kinvi-Dossou, G., et al.: Innovative acrylic thermoplastic composites versus conventional composites: Improving the impact performances. *Compos. Struct.* **217**, 1–13 (2019). <https://doi.org/10.1016/j.compstruct.2019.02.090>
11. Matadi Boumbimba, R., Coulibaly, M., Khabouchi, A., Kinvi-Dossou, G., Bonfoh, N., Gerard, P.: Glass fibres reinforced acrylic thermoplastic resin-based tri-block copolymers composites: low velocity impact response at various temperatures. *Compos. Struct.* **160**, 939–951 (2017). <https://doi.org/10.1016/j.compstruct.2016.10.127>

12. Azoti, W.L., Elmarakbi, A.: Multiscale modelling of graphene platelets-based nanocomposite materials. *Compos. Struct.* **168**, 313–321 (2017). <https://doi.org/10.1016/j.compstruct.2017.02.022>
13. Elmarakbi, A., Azoti, W., Serry, M.: Multiscale modelling of hybrid glass fibres reinforced graphene platelets polyamide PA6 matrix composites for crashworthiness applications. *Appl. Mater. Today* **6**, 1–8 (2017). <https://doi.org/10.1016/j.apmt.2016.11.003>
14. Elmasry, A., Azoti, W., Elmarakbi, M., Elmarakbi, A.: Interaction modelling of the thermomechanical behaviour of spatially-oriented graphene platelets (GPLs) reinforced polymer matrix. *Int. J. Solids Struct.* **232**, 111183 (2021). <https://doi.org/10.1016/j.ijsolstr.2021.111183>
15. Isaincu, A., Dan, M., Ungureanu, V., Marşavina, L.: Numerical investigation on the influence of fiber orientation mapping procedure to the mechanical response of short-fiber reinforced composites using Moldflow, Digimat and Ansys software. *Mater. Today Proc.* **45**, 4304–4309 (2021). <https://doi.org/10.1016/j.matpr.2020.12.792>
16. Trzepieciński, T., Rzyzińska, G., Biglar, M., Gromada, M.: Modelling of multilayer actuator layers by homogenisation technique using Digimat software. *Ceram. Int.* **43**, 3259–3266 (2017). <https://doi.org/10.1016/j.ceramint.2016.11.157>
17. Kouassi, A.Y.E., Matadi Boumbimba, R., Sangaré, M.K., Koutsawa, Y., Benelfellah, A., Demais, V.: Dispersion and morphology analysis of PMMA/organoclay nanocomposites using the Ripley functions and determination of effective elastic properties. *Compos. Struct.* **116881** (2023). <https://doi.org/10.1016/j.compstruct.2023.116881>
18. Digimat FE User's Guide-2021.3. 227 (2021)
19. Agra, A.A., et al.: Automated procedure for coke microstructural characterization in imageJ software aiming industrial application. *Fuel* **304**, 121374 (2021). <https://doi.org/10.1016/j.fuel.2021.121374>
20. Ash, N.F., Massengill, M.T., Harmer, L., Jafri, A., Lewin, A.S.: Automated segmentation and analysis of retinal microglia within ImageJ. *Exp. Eye Res.* **203**, 108416 (2021). <https://doi.org/10.1016/j.exer.2020.108416>
21. Trzepieciński, T., Rzyzińska, G., Gromada, M., Biglar, M.: 3D microstructure-based modelling of the deformation behaviour of ceramic matrix composites. *J. Eur. Ceram. Soc.* **38**, 2911–2919 (2018). <https://doi.org/10.1016/j.jeurceramsoc.2017.11.038>
22. Jagath Narayana, K., Burela, R.G.: Multi-scale modeling and simulation of natural fiber reinforced composites (Bio-composites). *J. Phys. Conf. Ser.* **1240**, 012103 (2019). <https://doi.org/10.1088/1742-6596/1240/1/012103>
23. Rigas, E., Mulkern, T., Walsh, S., Nguyen, S.: Effects of Processing Conditions on Vacuum Assisted Resin Transfer Molding Process (VARTM), vol. 54 (2001)
24. Sunilpete, M.A., Cadambi, R.M.: Development of cost effective out-of-autoclave technology – vacuum infusion process with tailored fibre volume fraction. *Mater. Today Proc.* **21**, 1293–1297 (2020). <https://doi.org/10.1016/j.matpr.2020.01.165>
25. Hollister, S.J., Kikuchi, N.: A comparison of homogenization and standard mechanics analyses for periodic porous composites. *Comput. Mech.* **10**, 73–95 (1992). <https://doi.org/10.1007/BF00369853>
26. Choi, S., Sankar, B.V.: Micromechanical analysis of composite laminates at cryogenic temperatures. *J. Compos. Mater.* **40**, 1077–1091 (2006). <https://doi.org/10.1177/0021998305057365>
27. Matadi Boumbimba, R., Viot, P., Froustey, C., Léonardi, F., Gerard, P., Inoubli, R.: Comportement à l'impact des composites fibres de verre/Epoxy modifiée copolymères à blocs. In: *de Mécanique, A.F. (éd.) CFM 2013 - 21ème Congrès Français de Mécanique. AFM, Maison de la Mécanique, Bordeaux* (2013)

28. Ramakrishnan, K.R., Guérard, S., Viot, P., Shankar, K.: Effect of block copolymer nano-reinforcements on the low velocity impact response of sandwich structures. *Compos. Struct.* **110**, 174–182 (2014). <https://doi.org/10.1016/j.compstruct.2013.12.001>
29. Rubin, A., Rébutin, N., Gérard, P., Gauthier, C.: Mechanical properties of a rubber-reinforced block copolymer PMMA: effect of the nanostructuration on tribological performances. *Mater. Lett.* **135**, 184–187 (2014). <https://doi.org/10.1016/j.matlet.2014.07.121>



Assessment of Filament Deposition Aero-Modelling for UAV Design Development

Mohamed Hakim^{1(✉)}, Saad Choukri¹, and Mohamed Oubrek²

¹ Mohammadia School of Engineers, Mechanical Engineering and Energetics
Research Team: Modeling and Experimentation, Mohammed V University, Agdal,
Rabat 10090, Morocco

`mohamed.hakim@um5.ac.ma`

² National Higher School of Arts and Crafts, PCMT, Mohammed V University,
Rabat, Morocco

Abstract. Due to the large applications field of Unmanned Aerial Vehicles (UAV) in civil, military, and scientific activities, with the associated missions' specific operating points requirements, there is a need for a large amount of experimental and numerical testing for new concepts development. In aerodynamic studies, aeromodelling or more specifically; small scale models, are often used in wind tunnel testing or numerical simulations thanks to Reynolds number similarity. On another hand, the possible uses of additive manufacturing (AM) have significantly increased in recent years, due to the freedom it offers for the manufacture of complex parts and the reduced cycle time to manufacturing, in contrast to conventional processes. For rapid aero-models manufacturing, we focus in this work on the filament deposition modelling (FDM), which is the most affordable, compared to other AM technics. But, before going from CAD to physical model, some preliminary assessments of the process fidelity have to be introduced. In this context, the aim of our present paper is the manufacture of a small scale UAV Blended Wing Body (BWB) using FDM for subsonic wind tunnel testing. The results of the models in the wind tunnel are compared to numerical results obtained from XFLR5, and then the process fidelity is discussed.

Keywords: fused deposition modeling · process fidelity · unmanned aerial vehicles · wind tunnel · numerical testing

1 Introduction

It is well known that wind tunnel testing is a useful experimental method for flow characterization, visualization, and aerodynamic performances measuring, which also serves to numerical models and CAD validations. Regarding this last point, a recent study [1], elaborates an integrated and cost effective approach to deal with UAV preliminary analysis where many missions and flight requirements have to be fulfilled by a trial-and-error iterations. It is shown in conceptual and

preliminary design stage, that integration of a proven medium fidelity numerical tool; such as XFLR5; based on potential and 3D panel methods, is a viable and appropriate solution for selecting candidate configuration for detailed analysis. This is in contrast to high fidelity simulations, based on advanced Navier Stocks resolution methods, which are very skilled topics requiring large time and computational resources.

For new UAV development, it is essential to use wind tunnel testing in conjunction with numerical simulations to reduce the development cycle time and prevent errors in the early design stages. However, one of the main challenges associated with wind tunnel testing is the fabrication of complex models with intricate shapes and planforms. To overcome this difficulty, Additive Manufacturing (AM) processes have made significant progress in recent years by enabling the rapid and cost-effective fabrication of complex shapes using automated manufacturing [2]. AM has bridged the gap between the physical and digital worlds by allowing individuals to easily create tangible objects from digital files, making it possible to design, scan, distribute, and transmit digital versions of physical items.

In UAV manufacturing, several additive methods are frequently used, including fused deposition modelling (FDM), selective laser sintering (SLS), stereolithography (SLA), selective laser melting (SLM), and electron-beam melting (EBM). For example, Michelson et al. [3] used FDM and SLA to construct a robust and intricate wing rib structure for an entomopter in 1998. Easter et al. [4] conducted a comparative study on ABS and UltemTM materials for manufacturing wing structures using an FDM printer, and they also used the same technology to design and build a blended-wing-body UAV. Zhang et al. [5] used an FDM printer to print the frame, tail, and gears for a UAV with flapping wings.

Due to its technical and economic advantages in the rapid prototyping process of complex aerodynamic designs (such as twist and sweep), our focus is on evaluating the fidelity of the Fused Deposition Modeling (FDM) process in terms of shape and dimensional accuracy. The subsequent sections describe the tools and methodology employed in this study.

2 Manufacturing Models

2.1 Fused Deposition Machine

From the several existing additive manufacturing technologies, we have chosen fused deposition modeling (FDM) due to the following reasons. First, it is an affordable rapid prototyping solution compared to other technologies. Second, it provides rigid and lightweight plastic parts that can withstand the applied forces. The machine used for FDM is the Prusa i3 MK3S with a working volume of 210 mm × 210 mm × 250 mm, as shown in Fig. 1. The material chosen for printing is Polylactic Acid (PLA) because it is simpler and more practical than other materials. It also shrinks far less, lays flat on the print bed, is less ductile, has a higher tensile strength, and is less expensive [6].

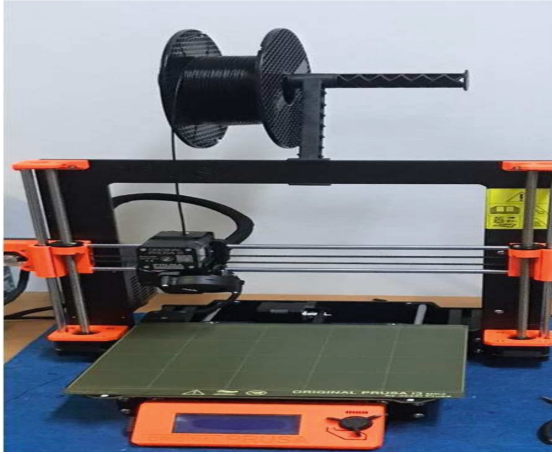


Fig. 1. Prusa i3 MK3S

2.2 Model Design

The primary goal of the design was discussed in [1], and its geometric parameters are listed in Table 1. The solid model of the design was created using Catia V5 software, and it was divided into two symmetrical models: the right and left models, as shown in Fig. 2(a). Due to the machine length restrictions, each part was split into two parts, labeled as Part 1 and Part 2, and assembled after printing using adhesive and steel bar rods as inserts, as illustrated in Fig. 2(b). An hexagonal orifice was implemented in the models to serve as a fixture point and ensure the link to the wind tunnel by a steel bar. The choice of the hexagonal shape was justified to prevent model rotation during the tests. The solid model was then converted to an STL file with a carefully surface mesh, which was exported to the printer.

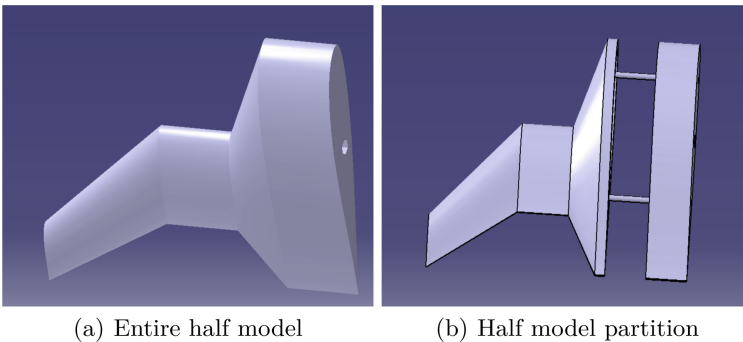


Fig. 2. Design in CATIA V5

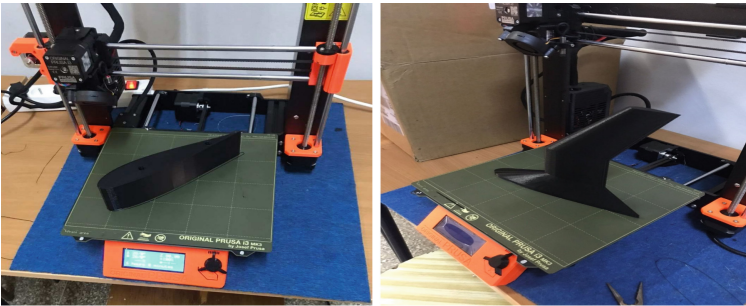
Table 1. Geometric parameters

Model (right or left)					
Section	Chord	y position	x position	Twist	Aspect ratio
S_0	208 mm	0	0	4°	4.29
S_1	208 mm	56 mm	0	4°	
S_2	80 mm	88 mm	80 mm	0°	
S_3	80 mm	144 mm	80 mm	0°	
S_4	48 mm	240 mm	167 mm	0°	

In order to set the printing parameters, we used the PrusaSlicer software to generate the G code that is used as input to the printing machine. The PrusaSlicer software provides a simulation for the settings of different features, such as filling, the amount of filament used, and printing time. These features are listed in Table 2. The printing process is illustrated in Fig. 3.

Table 2. Printing parameters

Model/Parameter	Time printing	Used filament	Infill	Temperature	Layer height	Nozzle diameter
Part a	7h35	30.10 m	15%	215°C	0.2 m	0.4 m
Part b	8h44	30.64 m	15%	215°C	0.2 m	0.4 m



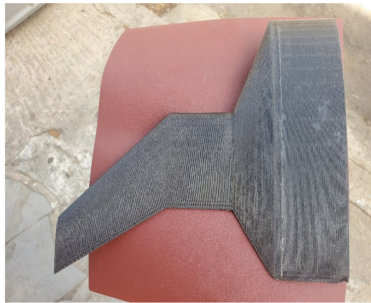
(a) Part 1

(b) Part 2

Fig. 3. Part printing

2.3 Post Printing Process

One of the most well-known limitations of 3D printing is the poor surface quality of the parts obtained from the process. In our case, the models had noticeable ridges on their surfaces due to the layers of filaments deposited during the manufacturing process. Since surface cleanliness is an important criterion, a series of surface treatment steps was planned for each model. Both models were smoothed using sandpaper, as shown in Fig. 4(a). The left model was then treated with a polyester mastic, primer, and paint, while the right model was treated with plastoflex primer and paint, as shown in Fig. 4(b) and 4(c).



(a) Completely left model (part1+part2) before smoothing



(b) Left model after smoothing



(c) Right model after smoothing

Fig. 4. Models before and after surface treatment

3 Wind Tunnel Testing

In the field of aerodynamic studies, access to full-scale flight test results is limited for most researchers and engineers. Therefore, they heavily rely on wind tunnels as a common tool for aerodynamic studies. Wind tunnels provide highly

accurate results, as long as the scaling effect and reduced Reynolds numbers are considered. For our study, we used the AF100 subsonic wind tunnel (shown in Fig. 5). This wind tunnel is an open return suction type with a variable speed axial fan ($V_{max} = 36 \text{ m/s}$) that pulls air through an aerodynamic diffuser with a conical geometry and consists of a closed test section with dimensions of $305 \text{ mm} \times 305 \text{ mm} \times 600 \text{ mm}$. The objective of the diffuser is to accelerate the air in a linear way. The velocity of the air is calculated by measuring the pressure with a pitot tube that is integrated into the test section through slots. The aerodynamic characteristics are measured by an aerodynamic balance of the three components (lift, drag, and pitching moment).



Fig. 5. AF100 subsonic wind tunnel

4 Simulation Tool

XFLR5 [7] is an open-source software that is capable of simulating the performance of an aircraft configuration at any point in the design process. It does so by coupling 2D airfoil analysis from XFOIL [8] with a 3D solver. For the purpose of wing design and related analysis, XFLR5 provides three numerical methods: the nonlinear Lifting Line Theory (LLT), the Vortex Lattice Method (VLM), and a 3D Panel Method (as shown in Fig. 6). In our study, we made use of the 3D Panel Method for our wing analysis.

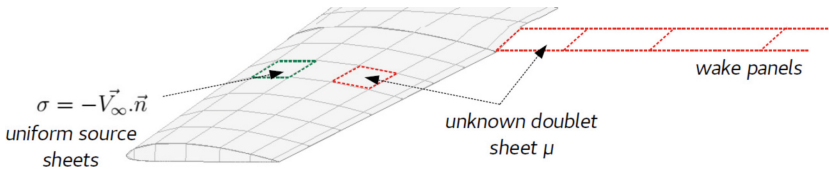
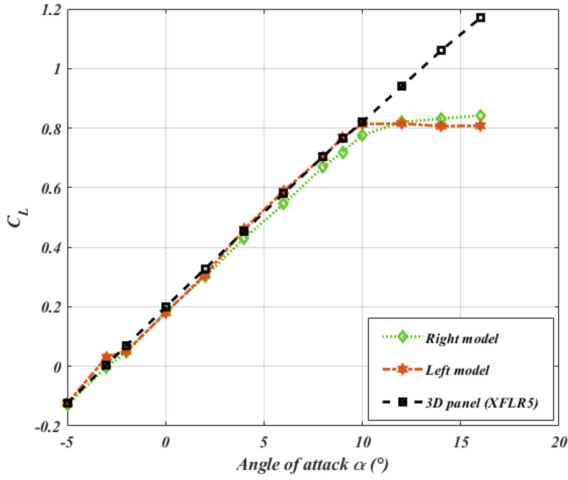


Fig. 6. 3D panel method

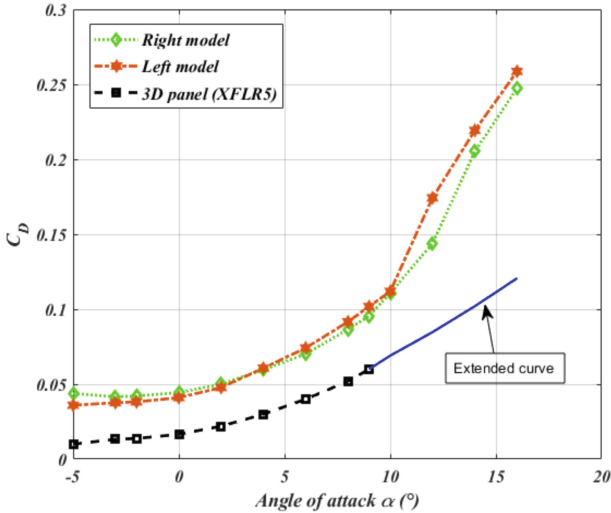
Given that the wing is the most critical component in a flying wing design, the XFLR5 software's ability to provide trends and analyze the sensitivity to design parameters makes it well-suited for our intended use. Additionally, since the software is widely used and has been verified and validated within the potential methods validity, we can rely on it for our analysis.

5 Results and Discussion

The accuracy and calibration of the *AF100* subsonic wind tunnel have been discussed in [9]. In our study, we compared the wind tunnel results of the two printed models with their respective XFLR5 numerical values on the nominal model (*Catia V5* model). Figure 7 shows the lift, drag, and pitch moment coefficients versus different angles of attack for a wind speed of $V = 33$ m/s, corresponding

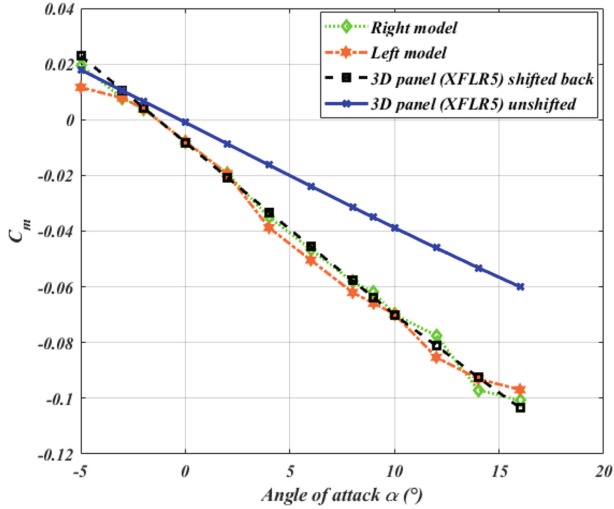


(a) Lift coefficient versus angle of attack



(b) Drag coefficient versus angle of attack

Fig. 7. (continued)



(c) Pitch moment coefficient versus angle of attack

Fig. 7. Polars of the models

to a mean chord Reynolds number of 3.02×10^5 (The choice of this value is based on the highest Reynolds achieved on the sub-scaled model, when working 10% below maximum wind tunnel speed). We observe a clear agreement between the experimental and numerical results for the lift coefficient in the small angle of attack (linear) region before reaching the stall region. However, at high angles of attack, the 3D panel method cannot predict the stall behavior, leading to differences between the numerical and experimental drag coefficients. Nevertheless, we obtained the same trend in the curve before the stall region. Regarding the pitch moment coefficient, we noticed a deviation between the experimental and numerical values, which we corrected by shifting the fixture point 5 mm towards the leading edge in the nominal model. Additionally, the experimental curves show a relative retarding effect of the stall for the right model, which had less surface treatment and more roughness, leading to possible turbulent reattachment.

The results presented here, in addition to the drag polar discussed earlier, lead us to conclude that the effects of aspect ratio, sweep, and twist are well represented by the printed models within the linear region of $-5 < \alpha < 10$, where the numerical model is valid. However, the pitch moment polar showed a discrepancy in the fixture point on the printed model, which could be attributed to shrinkage during the printing process.

6 Conclusion

The study presented here demonstrates the successful agreement between wind tunnel experimental results and numerical results for aero models produced by

3D fused deposition. This assessment confirms the fidelity of the FDM process in replicating aspect ratio, sweep, and twist and suggests that other configurations can be tested with confidence using this method. Future work should focus on quantitative analysis of shrinkage reduction and metrological aspects such as form and dimensional inspections. Additionally, extending the numerical modeling to the boundary layer development would allow for a better understanding of the nonlinear behavior of the models.




Acknowledgements. The authors express their gratitude to the Centre National de la Recherche Scientifique of Morocco for providing funding for this study, and to Mohammed V University in Rabat for project management.

References

1. Hakim, M., Choukri, S.: An integrated preliminary approach elaboration for the analysis of a blended wing body aerostructure concept. In: 12th International Conference on Integrated Design and Production, Rabat (2022)
2. Wohlers Associates, et al.: 3D Printing and Additive Manufacturing Global State of the Industry. Wohlers Report 2022, Wohlers Associates (2022). <https://wohlersassociates.com/product/wohlers-report-2022/>
3. Michelson, R.C., Reece, S.: Update on flapping wing micro air vehicle research—ongoing work to develop a flapping wing, crawling “Entomopter”. In: 13th Bristol International RPV/UAV Systems Conference Proceedings, Bristol, pp. 30–31 (1998)
4. Easter, S., et al.: Using advanced manufacturing to produce unmanned aerial vehicles: a feasibility study. In: Ground/Air Multisensor Interoperability, Integration, and Networking for Persistent ISR IV, vol. 8742, pp. 20–35. SPIE, Baltimore (2013)
5. Zhang, T., Zhou, C., Su, S.: Design and development of bio-inspired flapping wing aerial vehicles. In: 2015 International Conference on Advanced Robotics and Intelligent Systems, pp. 1–6. IEEE, Taipei (2015)
6. Cakir, M.T., Hancer, M., Abay, M.: Experimental investigation of 3d printer specimen PLA filament on primary structures of small UAV. In: 10th Ankara International Aerospace Conference. AIAC, Ankara (2019)
7. Deperrois, A.: Guide Pour XFLR5. <http://www.xflr5.tech/xflr5.htm>. Accessed 11 Feb 2023
8. Drela, M.: Xfoil: an analysis and design system for low Reynolds number airfoils. In: Low Reynolds Number Aerodynamics, pp. 1–12 (1989)
9. Hakim, M., Choukri, S.: Etude expdruit d’aile fuselage int. In: 10e Rencontre Nationale des Jeunes Chercheurs en Physique, Casablanca (2021)
10. Hart, R.T.: Biomedical engineering accredited undergraduate programs: 4 decades of growth. *Ann. Biomed. Eng.* **43**(8), 1713–1715 (2015). <https://doi.org/10.1007/s10439-015-1319-2>
11. Johnsen, E.B., Hähnle, R., Schäfer, J., Schlatte, R., Steffen, M.: ABS: a core language for abstract behavioral specification. In: Aichernig, B.K., de Boer, F.S., Bonsangue, M.M. (eds.) FMCO 2010. LNCS, vol. 6957, pp. 142–164. Springer, Heidelberg (2011). https://doi.org/10.1007/978-3-642-25271-6_8



Modeling the Propagation of Ultrasonic Guided Waves in Four-Layer Laminated Composites

Ismaine Zitouni^(✉) , Hassan Rhimini , and Abdelkerim Chouaf 

Laboratory of Mechanics, Engineering and Innovation, National High School of Electricity and Mechanics, Hassan II University, Casablanca, Morocco
Ismaine.zitouni.doc20@ensem.ac.ma

Abstract. Graphite-epoxy composites are widely used in the space industry. They have the advantage of being resistant to thermal distortion with high structural rigidity and minimal weight. However, the non-complete adhesion between fiber and matrix and the defects resulting from the manufacturing processes can affect these structures. It seems therefore necessary to control these materials. The non-destructive testing by ultrasonic guided waves presents an interesting alternative for the detection of these imperfections. For a proper ultrasonic non-destructive testing by guided waves, the knowledge of dispersion curves is an essential step to determine the modes susceptible to propagate in our material during the control.

In this paper, we present analytical matrix methods for plotting the dispersion curves of a graphite-epoxy laminate composite material. The formulations and limitations of these methods have been presented. We have modeled the propagation of ultrasonic guided waves in two- and four-layer anisotropic laminates for different fiber orientations. The accuracy of the obtained results has been checked with the help of the software DISPERSION CALCULATOR.

Keywords: Guided waves · dispersion curves · layered composite · matrix method

1 Introduction

Ultrasonic Guided Waves (UGW) are widely used in the field of Non-Destructive Testing (NDT) of diverse structures, especially laminated composite structures. They are widely used in very sensitive areas where the safety of these structures is capital. A reliable and precise calculation of the dispersion curves of UGW allows to well define the conditions of generation and detection of the waves susceptible to propagate in these structures. Traditionally the dispersion curves are determined by Roots-Finding Methods (RFM) which are based on numerical algorithms to find the roots of the characteristic equations as a function of frequency and wave number. Analytical methods dedicated in general to the calculation of dispersion curves for simple cases such as free or fluid loaded elastic plates are known since Lord Rayleigh [1–4]. Some exact solutions for isotropic media of standard geometry are available in books or articles such as Mindlin [5] or Pao [6]. These methods remain relatively simple for simple standard cases. However, the introduction

of curvature, inhomogeneity, damping, anisotropy or when the studied structures are multi-layered, the calculations become expensive and fastidious. A challenge is then presented to the researchers and the industrialists to overcome the deficiencies of the classical methods. Several solutions have been proposed to improve the performance and the quality of plotting these dispersion curves. Among these methods, we cite the Transfer Matrix Method (TMM). It was initially introduced by Thomson [6] and Haskell [7] to calculate the dispersion curves in a layered structure made of anisotropic materials. Later Nayfeh [8] extended it for the treatment of horizontal shear waves SH (Shear Horizontal). Despite the fact that it is easy to formulate, the TMM remains limited in these results [9]. Indeed, this method presents instabilities especially in the case of thick layers and high frequencies. Rokhlin [9] has stated that under these conditions, this method presents singular values because of its dependence on the exponential. The SMM (Stiffness Matrix Method) [9, 10] was subsequently introduced to overcome these singularities. A reformulation of the problem, which consists in regrouping the stresses of a layer into a single vector, has been implemented. The resulting matrix of this manipulation is a stiffness matrix. This last one does not include the instabilities presented by the TMM. However, when the number of layers becomes more important, both methods remain inadequate. The Global Matrix Method (GMM) has also been introduced for the plotting of the dispersion curves. By exploiting the potential of the technique, LOWE has developed the industrial software DISPERSE [1] which is the leader in the field of ultrasonic NDT and which has been appreciated by many authors, but remains inadequate when the laminate exceeds a few hundred of layers. Monnier [10, 11] proposed the equivalent matrix method, which consists in the calculation of an equivalent behavior matrix for the whole laminate. However, the accuracy of the results is only valid for the low frequencies of the first S_0 and A_0 modes for periodical piles (0° and 90°). Several other methods were introduced later, such as the semi-analytical SAFE (Semi Analytical Finite Elements) method [10, 12], the spectral method [13] and the method based on the Legendre polynomial [14]. These numerical methods present a great gain in computational time with a simplicity of coding. In addition to the DISPERSE software, recently we have noticed the appearance of free software and applications allowing the calculation of dispersion properties of UGW in different types of waveguides. For example, the interactive interface GUIGUW [15] using the semi-analytical SAFE method, the DC (Dispersion Calculator) software, developed by Huber [16], based on the SMM, capable of modeling the propagation of UGW in layered composites composed of a few hundred layers.

In this paper, we introduce a new formulation based on the work of Nayfeh [8, 17] concerning the decoupling of ultrasonic guided waves for certain configurations of multilayer composite waveguides. For this purpose, we have used the analytical matrix methods SMM and TMM with some modifications. These modifications concern the separation of the Lamb wave and horizontal transverse wave formulations. This separation allowed us to obtain more accuracy and less instability. The proposed approach has been applied for four-layer structures for symmetric and asymmetric piles. The results obtained are compared with those of the DISPERSION CALCULATOR (DC) software based on the SMM formulation [16]. A perfect agreement of the results of the two techniques was observed.

2 Theoretical Formulation

We consider the propagation of UGW in a laminated composite with N layers that is free from stresses, the thickness of each layer is h along the x_3 direction. The structure is considered unlimited along the two directions x_1 and x_2 (Fig. 1).

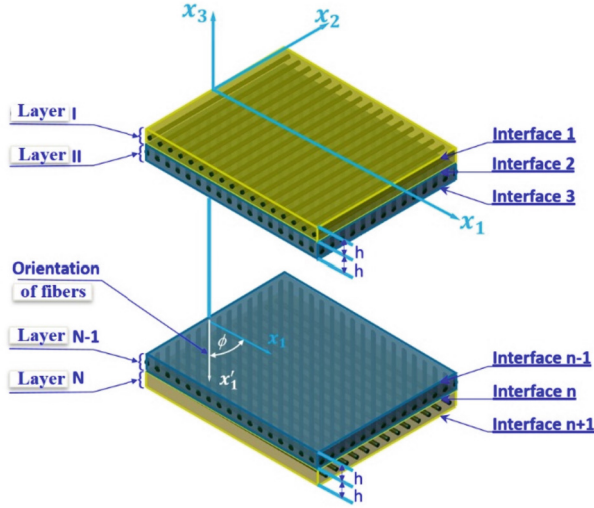


Fig. 1. Laminated composite with N layers.

The displacement components are written:

$$\left(u_1^{(l)}, u_2^{(l)}, u_3^{(l)} \right) = \sum_{q=1}^6 \left(1, V_q^{(l)}, W_q^{(l)} \right) U_{1q}^{(l)} e^{ik(x_1 + \alpha_q^{(l)} x_3 - ct)} \quad (1)$$

where $u_j^{(l)}$ ($j = 1, 2, 3$) are the displacement components of the layer l along the x_j directions, $V_q^{(l)}$ and $W_q^{(l)}$ are the amplitude ratios developed in [17], $U_{1q}^{(l)}$ are the amplitudes of the displacements, k is the wave number along the direction of propagation x_1 , c is the phase velocity and the index l represents the number of the layer, it varies from 1 to N .

Using Hooke's law and the strain-displacement relations, the expression of the stresses related to these displacements are written [17]:

$$\left(\sigma_{33}^{(l)}, \sigma_{23}^{(l)}, \sigma_{13}^{(l)} \right) = \sum_{q=1}^6 \left(D_{1q}^{(l)}, D_{2q}^{(l)}, D_{3q}^{(l)} \right) U_{1q}^{(l)} e^{ik(x_1 + \alpha_q^{(l)} x_3 - ct)} \quad (2)$$

3 Transfer Matrix Method TMM

The TMM consists of expressing the displacements and stresses of the upper interface of the laminate as a function of those of the lower interface while respecting the continuity of displacements and stresses between the layers. For this purpose, the displacements (1)

and the stresses (2) are combined into a single vector, called the state vector $P^{(l)}$. This vector depends on the displacement magnitudes $U_{1q}^{(l)}$. By expressing it on the two sides of the same layer, we obtain a relation that joins the components of the displacements and the stresses of the two sides of the same layer. The resulting matrix is called the transfer matrix $A^{(l)}$, to calculate it, we just have to multiply the transfer matrices of each layer $A = A^{(l)}A^{(l)} \dots A^{(N)}$.

$$\begin{cases} \{P\}_{(6,1)}^{(l)} = [X]_{(6,6)}^{(l)} \{U_{jq}\}_{(6,1)}^{(l)} \\ \{P\}_{(6,1)}^1 = [A]_{6,6} \{P\}_{(6,1)}^{n+1} \end{cases} \quad (3)$$

The matrix $A(4 : 6, 1 : 3)$ expresses the boundary conditions of the free laminate which results in the cancellation of the stresses on the top and bottom faces.

4 Stiffness Matrix Method SMM

Instead of having a transfer matrix between layers, the SMM method consists in grouping the stresses at the upper and lower interfaces of a layer into a single vector and expressing them in accordance with their associated displacements. This gives a stiffness matrix of the layer:

$$\begin{Bmatrix} \sigma_1 \\ \sigma_2 \end{Bmatrix}_{(6,1)} = [S]_{(6,6)} \begin{Bmatrix} u_1 \\ u_2 \end{Bmatrix}_{(6,1)} \quad (4)$$

where $[S]_{(6,6)}$ is the layer stiffness matrix expressed in [9], it depends on $D_{jq}^{(l)}, V_q^{(l)}, W_q^{(l)}$ and $\alpha_q^{(l)}$.

Thereafter, the global stiffness matrix of the laminate is obtained by using a recursive algorithm between layers (based on the equality of the stresses between layers). In this way we obtain a system that links the stresses on the top and bottom faces of the laminate. Assuming that the stresses are zero at faces 1 and $n + 1$ (see Fig. 1), the characteristic dispersion equation of the laminate is obtained by considering the cancellation of the determinant of the global stiffness matrix.

5 Numerical Results and Discussion

Consider the case of a unidirectional fiber graphite-epoxy laminate composite of thickness h and density $\rho = 1.61 \text{ g/cm}^3$. The values of the elastic constants of this material are given in Table 1 and are expressed in GPa.

Table 1. Elastic constants of the graphite-epoxy composite plate [9].

C_{11}	C_{22}	C_{33}	C_{12}	C_{13}	C_{23}	C_{44}	C_{55}	C_{66}
162	17	17	11.8	11.8	8.2	4.4	8	8

To plot the dispersion of this material, we developed a Matlab program that plots these curves in the (frequency, wavenumber) plane. The frequency range used is $f = 10 : 50 : 610^6$ (Hz) and the wave number $k = 10^{-5} : 100 : 12000$ (m^{-1}). We compare our results with the Dispersion Calculation (DC) software [16]. Figure 2 shows the variation of the elastic constants of the graphite-epoxy material as a function of the ϕ angle. For angles of 0° , 90° , 180° and 270° the constants C_{16} , C_{26} , C_{36} and C_{45} are zero and the transversely isotropic material is described by these nine constants (C_{11} , C_{12} , C_{13} , C_{22} , C_{23} , C_{33} , C_{44} , C_{55} and C_{66}). On the other hand, for angles different from those mentioned before, the material has a monoclinic behavior and is therefore described by 13 elastic constants (C_{16} , C_{26} , C_{36} and $C_{45} \neq 0$).

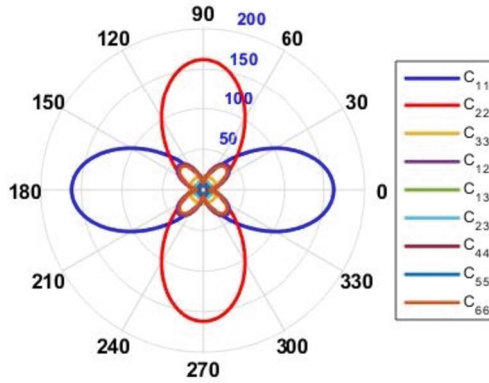


Fig. 2. Polar diagram of the elastic constants of the epoxy graphite plate.

5.1 Laminated Composites

In this subsection, we will study the dispersion of UGW in layered composite structures. These structures are assumed to consist of a repetition of the $[0^\circ/90^\circ]$ motif in a symmetric or asymmetric arrangement. The $[0^\circ/90^\circ]$ motif is an assembly of two graphite-epoxy layers (Table 1) with fiber orientations of 0° and 90° respectively. For these orientations, the Lamb modes are decoupled from the SH modes. For a 0° orientation, the material has a transverse isotropic behavior and the matrix of elastic constants contains five independent constants. For a 90° orientation, the material behavior remains the same (transverse isotropic) and we have a 90° permutation of the elastic constants. For example, the value of the constant C_{11} at 0° becomes that of the constant C_{22} at 90° (Fig. 2). In addition, the symmetrical or asymmetrical arrangement of the $[0^\circ/90^\circ]$ motif will influence the nature of the modes generated in the laminate.

The considered structures have all a total thickness of 4 mm equally distributed on the number of constituting layers. First, we will study a structure composed of a single motif $[0^\circ/90^\circ]$. Next, we will study a four-layer structure consisting of a symmetrical arrangement of the $[0^\circ/90^\circ]$ motif that is, $[0^\circ/90^\circ/90^\circ/0^\circ]$ and finally, we consider a four-layer structure consisting of an asymmetrical repetition of the $[0^\circ/90^\circ]$ motif

that is $[0^\circ/90^\circ/0^\circ/90^\circ]$. We apply TMM and SMM to plot the dispersion curves of the considered structures. The results obtained will then be compared to those of the DC (Dispersion Calculator) software for validation.

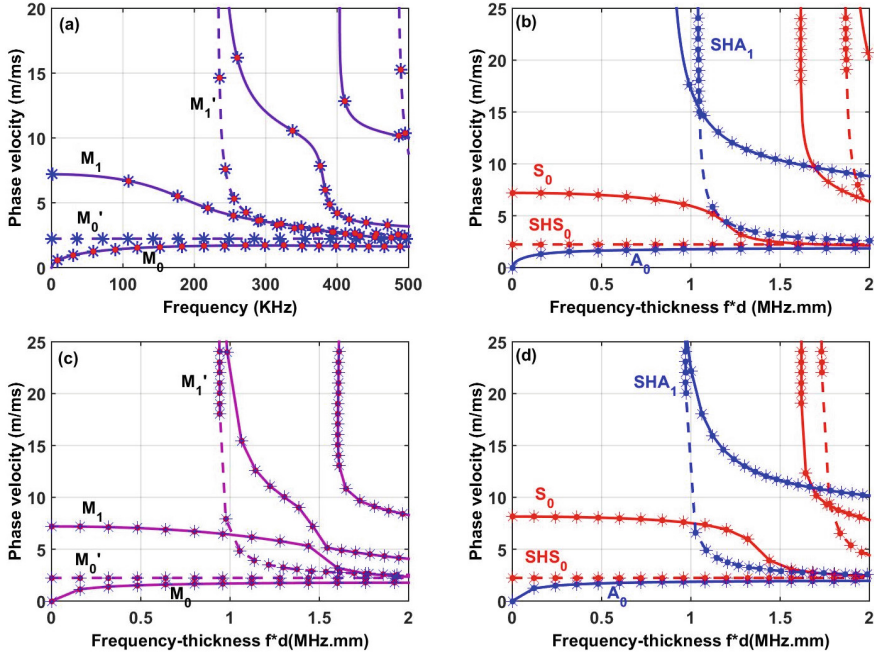


Fig. 3. Dispersion curves of a 4 mm bilayer plate $[0^\circ/90^\circ]$ (a), a 4 mm tetra-layer plate for $[0^\circ/90^\circ/90^\circ/0^\circ]$ (b), $[0^\circ/90^\circ/0^\circ/90^\circ]$ (c) and a 3 mm tetra-layer plate for $[0^\circ/90^\circ/90^\circ/0^\circ]$ (d) of the epoxy graphite composite. Solid lines: DC software; Points: TMM; Stars: SMM.

Figure 3 shows the dispersion curves of the four laminated composites. Figure 3a and 3c show asymmetric arrangements of the layers with respect to the median axis, the modes present in these structures do not resemble the ones mentioned before. Here we find modes (M_n) that we call pseudo-Lamb modes, and modes (M_n') that we call pseudo horizontal shear modes. Concerning Fig. 3b and 3d, they represent symmetrical arrangements of the layers, the modes that propagate there are Lamb modes (S_n and A_n) and horizontal shear modes (SH). We have developed an efficient procedure [18] to classify the obtained results by exploiting the symmetry and antisymmetry properties of Lamb and SH modes. As results, the red solid line curves represent symmetric Lamb modes and the blue solid line curves represent antisymmetric Lamb modes. For the SH modes, represented by dashed curves, we have symmetric SHS_n (red color) and antisymmetric SHA_n (blue color) modes.

Both matrix methods were able to model the UGW dispersion of a four-layer composite laminate. Since the laminates consist of layers with angles ϕ of 0° and 90° , Lamb waves and horizontal shear waves are then uncoupled and so their formulations are separated [8, 17]. Effectively, in this case the displacements that define the propagation of

the pseudo-Lamb modes will depend on four constants and those of the pseudo transverse modes on two constants. This dependence influences the size of the matrix and consequently the dispersion relations. We then find more simplified formulations in both methods (SMM and TMM). For the TMM, the instabilities are almost no longer present in the M_n' modes (solution obtained in the whole frequency range), but remain in the case of the M_n modes (solution valid for $0 < fd \leq 2$ MHz.mm). Note that this simplification cannot be implemented in the case where Lamb modes are coupled to SH modes (fiber directions different from 0° and 90°) [10, 19]. For a three-layer laminated composite, of 3 mm thickness and with a motif $[0^\circ/90^\circ/0^\circ]$, the DC software does not allow to treat this type of structure. DC considers this structure as symmetrical and requires to consider only the half. To overcome this problem, we then considered a four-layer structure $[0^\circ/90^\circ/90^\circ/0^\circ]$ while considering the two central layers $[90^\circ/90^\circ]$ as a single layer of each thickness are equal to 0.5 mm. The example in Fig. 3d shows a pile of 4 layers, the first and the fourth layer have thicknesses of 1 mm and the central layers of 0.5 mm. In contrast to the DC software, our program plots the dispersion curves of the laminate with the $[0^\circ/90^\circ/0^\circ]$ motif. The results presented in Fig. 3d show a very good agreement. This reflects the ability of our program to plot dispersion curves for motifs that are not supported by the DC software. We note that our formulation allows us to plot the dispersion curves of a laminate with layer thickness variation, which is not the case for some methods [11]. This advantage can be very useful for some industrial applications where the layer thickness is variable, for example, the coating of a structure.

Table 2. Comparison of the calculation time between the used methods.

Methods	DC software	TMM	SMM
Calculation time (s)	750	2540	1983

Table 2 shows the calculation times of the methods used to plot the dispersion curves of the four-layer laminate with a representation of $[0^\circ/90^\circ/90^\circ/0^\circ]$. We note that the DC software allows us to have the dispersion curves in a lower time than the other methods (TMM and SMM). This large computation time of the matrix methods is mainly caused by the roots finding algorithm used. We use here the bisection method. Despite its certitude of convergence, the dichotomy method remains expensive in computation time. Indeed, the scanning in some domains where the solution does not exist and the very large number of iterations remain limits of the method.

As perspectives, we consider the use of hybrid analytical methods combining two to three roots finding algorithms to decrease the computation time. As an example, the hybrid method used in reference [20] combining the dichotomy method and the Newton-Raphson method. This combination allowed a gain in computation time of almost 50% of the time used by the bisection method alone.

6 Conclusion

Matrix methods offer a very competitive way to plot the dispersion curves of graphite-epoxy multilayer composites. In this work, we have focused on the TMM transfer matrix method, which has shown some instabilities for large values of the frequency and the wavenumber. We proposed a simplified formulation for the case where the modes are uncoupled, which allowed a significant decrease in the size of the matrix and thus the appearance of less singular values in the matrix. We have also been interested in the stiffness matrix method SMM. This method does not include the weaknesses specific to the TMM, but remains nevertheless dependent on the number of layers chosen and the thickness of the structure to be controlled. In the same way, a simplified formulation was implemented in the case of mode uncoupling which allowed the reinforcement of the stiffness matrix and the reduction of these variables. The reliability of the results obtained was demonstrated during the comparison with the DC software. The encouraging results obtained for the case of a four-layer structure with symmetrical and asymmetrical piling and with variable layer thickness motivate us in future work to study the influence of the orientation of the plies, especially in materials with deficient pilings on the dispersion curves.

References

1. Pavlakovic, B., Lowe, M., Alleyne, D., Cawley, P.: DISPERSE: a general purpose program for creating dispersion curves. *Rev. Prog. Quant. Non-destruct. Eval.* **16**, 185–192 (1987)
2. Graff, K.F.: *Rayleigh and Lamb Waves*, pp. 1–649. Dover, New York (1991)
3. Auld, B.A.: *Acoustic Fields and Waves in Solids*, 2nd edn., pp. 1–878. Krieger Publishing Company, FL (1990)
4. Rose, J.L.: *Ultrasonic Waves in Solid Media*, pp. 1–476. Cambridge University Press, Cambridge (1999)
5. Achenbach, J.D.: *Wave Propagation in Elastic Solids*, pp. 1–440. North-Holland, Amsterdam (1973)
6. Thomson, W.: Transmission of elastic waves through a stratified solid medium. *J. Appl. Phys.* **21**, 89–93 (1950)
7. Haskell, N.: Dispersion of surface waves on multilayered media. *Bull. Seism. Soc. Am.* **43**, 17–34 (1953)
8. Nayfeh, A.H.: The propagation of horizontally polarized shear waves in multilayered anisotropic media. *J. Acoust. Soc. Am.* **86**(5), 2007–2012 (1989)
9. Rokhlin, S., Chimenti, D., Nagy, P.: *Physical Ultrasonics of Composites*. Oxford University Press (2011)
10. Kamal, A.M., Gresil, M., Giurgiutiu, V.: Comparative study of several methods for the calculation of ultrasonic guided waves in composites. In: 54th AIAA/ASME/ASCE/AHS/ASC Structures, Structural Dynamics, and Materials Conference, p. 1901 (2013)
11. Monnier, T.: Lamb waves-based impact damage monitoring of a stiffened aircraft panel using piezoelectric transducers. *J. Intell. Mater. Syst. Struct.* **17**(5), 411–421 (2006)
12. Barazanchy, D., Giurgiutiu, V.: A comparative convergence and accuracy study of composite guided-ultrasonic wave solution methods: comparing the unified analytic method, SAFE method and DISPERSE. *Proc. Inst. Mech. Eng. C J. Mech. Eng. Sci.* **231**(16), 2961–2973 (2017)

13. Ismaïne, Z., Hassan, R., Abdelkerim, C.: New spectral displacement post-processing approach for modeling ultrasonic guided waves. In: 2023 3rd International Conference on Innovative Research in Applied Science, Engineering and Technology (IRASET), pp. 1–8. IEEE (May 2023)
14. Zheng, M., He, C., Lu, Y., Wu, B.: State-vector formalism and the Legendre polynomial solution for modelling guided waves in anisotropic plates. *J. Sound Vib.* **412**, 372–388 (2018)
15. Bocchini, P., Marzani, A., Viola, E.: Graphical user interface for guided acoustic waves. *J. Comput. Civ. Eng.* **25**(3), 202–210 (2011)
16. Huber, A.: Dispersion Calculator (DC) (2021). <https://www.dlr.de/zlp/en/desktopdefault.aspx/tabid-14332/24874read-61142/#/gallery/33485>
17. Nayfeh, A.H.: The general problem of elastic wave propagation in multilayered anisotropic media. *J. Acoust. Soc. Am.* **89**(4), 1521–1531 (1991)
18. Zitouni, I., Rhimini, H., Chouaf, A.: Modeling the propagation of ultrasonic guided waves in a composite plate by a spectral approximation method. *Eng. Trans.* **71**(2), 213–227 (2023)
19. Barski, M., Pajak, P.: Determination of dispersion curves for composite materials with the use of stiffness matrix method. *Acta Mech. Automat.* **11**(2) (2017)
20. Zitouni, I., Rhimini, H., Chouaf, A.: Comparative study of the spectral method, DISPERSE and other classical methods for plotting the dispersion curves in anisotropic plates. *J. Appl. Comput. Mech.* **9**(4), 955–973 (2023). <https://doi.org/10.22055/jacm.2023.42530.3941>



Numerical Investigation of Combined Natural Convection, Conduction and Radiation Through Concrete Hollow Bricks

Jamal Bouchaib^(✉), Lahcen El Moutaouakil, Mohammed Boukendil, Abdelbaki Abdelhalim, and Zaki Zrikem

Faculty of Sciences Semlalia, Department of Physics, Cadi Ayyad University, LMFE, Marrakesh, Morocco

bouchaib.jamal@ced.uca.ma

Abstract. This work aims to examine combined heat transfers through concrete hollow bricks. The thermal behavior of hollow bricks is simulated using a mathematical model based on the conservation of mass, momentum and energy. The effect of internal surfaces emissivity, aspect ratio of inner holes and solid wall thermal conductivity on global heat transfer is investigated using practical values of the thermal excitations. The results show that the contribution of radiation to the overall heat transfer through hollow bricks increases progressively with higher values of the thermal emissivity. The results reveal also that the overall heat flux through the concrete bricks is greatly influenced by the solid walls' thermal conductivity. Since thermal conductivity cannot be adjusted after construction, this finding emphasizes the importance of careful material selection in designing energy-efficient structures, especially in regions characterized by hot and arid climates. Based on these results, we propose a practical recommendation to opt for concrete with low thermal conductivity in such climates. By adopting this approach, construction practices can be tailored to enhance the overall energy efficiency and thermal performance of buildings, providing sustainable solutions for the challenges posed by extreme environmental conditions.

Keywords: Concrete hollow brick · Coupled heat transfer · 3D numerical simulation

1 Introduction

The enormous amount of energy consumed to heat or cool buildings has led researchers to explore the best ways to improve building wall thermal efficiency. In fact, the residential sector represents 40% of the world's energy consumption [1]. The building envelope can act as a barrier between the cold or unpleasant heat from the outside and indoor climate, decreasing the demand for mechanical heating or cooling. Hence, the best strategy for reducing building energy use is to properly design the building envelope [2].

Because of their high compression and long life, hollow bricks have been an essential building material for over a century. Bricks are mainly used in building construction because they offer a number of advantages including quick construction, excellent mechanical resistivity and resistance to moisture variations.

In recent years, several numerical and experimental studies have been performed to evaluate the thermal performances of hollow bricks. Dos Santos [3] carried out a numerical investigation on the heat conductivity of hollow concrete blocks. The findings demonstrate that through concrete hollow blocks, thermal radiation may be a significant factor in the overall heat flux and that bigger holes offer greater transmittance values owing to convection. Fioretti and Principi [4] evaluated the thermal efficiency of hollow bricks. They demonstrate that the coating method reduces radiation in the cells, thus increasing the thermal resistance offered by the block. The equivalent conductivity can be reduced by 55% to 70% using the low emissivity coating.

The research presented above actually uses a two-dimensional (2D) model. The three-dimensional (3D) model has only been used in a very small number of researches to examine the coupled heat exchange through hollow bricks. In a three-dimensional partitioned enclosure, the coupled heat transfers were examined by Gossard and Lartigue [5]. They found that thermal conductivity and emissivity significantly impacted the thermal resistance of the enclosure. Shi et al. [6] analyzed combined heat transfer in hollow blocks. They discovered that the equivalent conductivity of hollow blocks can be effectively reduced from 13.65% to 40.42% by installing partitions vertical to the heat flux.

The literature review reveals that there is limited three-dimensional research on the combined heat transfer through concrete hollow bricks. Due to the arrangement of the bricks in the walls, the heat exchange through the hollow brick walls is really three-dimensional. Therefore, 3D numerical simulation can be used to more accurately describe the heat transfer and fluid flow process.

The present work aims to investigate the effect of the aspect ratio of the inner holes and the thermal emissivity and conductivity on the heat transfer for different realistic values of thermal excitations.

2 Mathematical Formulation

The considered configuration is illustrated in Fig. 1 using the coordinate system. It represents a concrete hollow brick composed of three cells surrounded by solid walls. In Morocco, the construction of building walls frequently uses this prefabricated element which has the geometrical parameters indicated in Table 1. The outer and inner surfaces of the blocks are assumed to be isothermal, while the other surfaces are supposed to be adiabatic. Air in the holes is assumed Newtonian and laminar [7]. For radiative heat exchange, the fluid is supposed perfectly transparent and cavity surfaces are supposed gray with diffuse emission and reflection [8].

The following are the key equations for the studied problem:

$$\frac{\partial U}{\partial X} + \frac{\partial V}{\partial Y} + \frac{\partial W}{\partial Z} = 0 \quad (1)$$

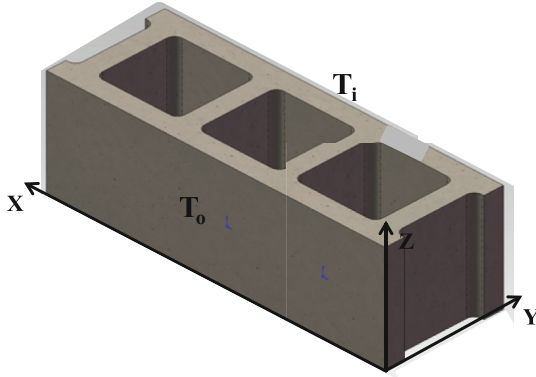


Fig. 1. Studied concrete hollow brick.

Table 1. Dimensions of each aspect ratio of the considered hollow bricks.

Aspect ratio	L (cm)	H (cm)	W (cm)	$A_h = H/W$
A_{h1}	50	20	10	2
A_{h2}	50	20	15	1.34
A_{h3}	50	20	20	1

$$\frac{\partial U}{\partial \tau} + U \frac{\partial U}{\partial X} + V \frac{\partial U}{\partial Y} + W \frac{\partial U}{\partial Z} = -\frac{\partial P}{\partial X} + \text{Pr} \left(\frac{\partial^2 U}{\partial X^2} + \frac{\partial^2 U}{\partial Y^2} + \frac{\partial^2 U}{\partial Z^2} \right) \quad (2)$$

$$\frac{\partial V}{\partial \tau} + U \frac{\partial V}{\partial X} + V \frac{\partial V}{\partial Y} + W \frac{\partial V}{\partial Z} = -\frac{\partial P}{\partial Y} + \text{Pr} \left(\frac{\partial^2 V}{\partial X^2} + \frac{\partial^2 V}{\partial Y^2} + \frac{\partial^2 V}{\partial Z^2} \right) \quad (3)$$

$$\frac{\partial W}{\partial \tau} + U \frac{\partial W}{\partial X} + V \frac{\partial W}{\partial Y} + W \frac{\partial W}{\partial Z} = -\frac{\partial P}{\partial Z} + \text{Pr} \left(\frac{\partial^2 W}{\partial X^2} + \frac{\partial^2 W}{\partial Y^2} + \frac{\partial^2 W}{\partial Z^2} \right) + \text{Ra} \cdot \text{Pr} \cdot \theta_f \quad (4)$$

$$\frac{\partial \theta_a}{\partial \tau} + U \frac{\partial \theta_a}{\partial X} + V \frac{\partial \theta_a}{\partial Y} + W \frac{\partial \theta_a}{\partial Z} = \frac{\partial^2 \theta_a}{\partial X^2} + \frac{\partial^2 \theta_a}{\partial Y^2} + \frac{\partial^2 \theta_a}{\partial Z^2} - \frac{\tau^*}{\text{Pl}} \left[4 \left(\frac{\theta_a}{T_R} + 1 \right)^4 - \int_0^{4\pi} I_R d\Omega \right] \quad (5)$$

Prandtl number is Pr, Planck number is P and Rayleigh number is Ra given as follows:

$$\text{Ra} = \frac{g\beta(T_o - T_i)H^3}{(\nu\alpha)_f} \quad (6)$$

$$\text{Pl} = \frac{k_a(T_e - T_i)}{\sigma T_i^4 L} \quad (7)$$

The dimensionless conduction equation is expressed as follows:

$$\frac{\partial \theta_s}{\partial \tau} = \frac{\alpha_s}{\alpha_f} \left(\frac{\partial^2 \theta_s}{\partial X^2} + \frac{\partial^2 \theta_s}{\partial Y^2} + \frac{\partial^2 \theta_s}{\partial Z^2} \right) \quad (8)$$

The analyzed problem's boundary conditions are as follows:

$$\theta_s = 1 \text{ at } Y = 0 \quad (9)$$

$$\theta_s = 0 \text{ at } Y = 1 \quad (10)$$

- Condition of adiabaticity:

$$\frac{\partial \theta_s}{\partial \eta} = 0 \quad (11)$$

On the interior surfaces of the cavities, the no-slip velocity conditions are applied:

$$U = V = 0 \quad (12)$$

The conditions below are imposed on the solid-fluid boundary:

$$\theta_s(X, Y) = \theta_f(X, Y) \quad (13)$$

$$-\frac{\partial \theta_s}{\partial n} = -N_k \frac{\partial \theta_f}{\partial n} + N_r Q_R \quad (14)$$

The following expression provides the dimensionless average heat flux through the concrete hollow brick:

$$q_a = - \int_0^L \int_0^H \frac{\partial \theta_s(X, Z)}{\partial Y} \Big|_{Y=0} dXdZ = - \int_0^L \int_0^H \frac{\partial \theta_s(X, Z)}{\partial Y} \Big|_{Y=1} dXdZ \quad (15)$$

3 Numerical Procedure and Validation

The control volume approach is adopted to discretize the governing equations. A self-developed Fortran program is used to perform the numerical computations.

The developed numerical code was validated by confronting our results with those of the literature in the presence of convection in a cubic cavity. Table 2 presents the obtained results. The comparison results show strong agreement, with a maximum difference of 1.16%.

The resulting code was additionally verified for conjugate natural convection and radiation based on credible works in the literature. Hu et al. [11] carried out a benchmark work on combined convective and radiative in a cubic cavity. Table 3 shows that the results of the computational code and those of Hu et al. [11] are in good agreement.

Table 2. Nusselt numbers are compared to those in the literature.

Ra	Frederick and Moraga [9]	Tric et al. [10]	Present study
10^3	1.071	1.070	1.069
10^4	2.057	2.054	2.049
10^5	4.353	4.337	4.322
10^6	8.740	8.640	8.638

Table 3. Validation of our model with the benchmark (Hu et al. [11]): H (hot wall); C (cold wall); R (radiative).

	Ra	Nu _{CH}	Nu _{CC}	Nu _{RH}	Nu _{RC}
Hu et al. [11]	10^4	2.0906	2.0966	0.22746	0.22153
	10^5	4.2726	4.2848	0.51514	0.50295
	10^6	8.3237	8.3499	1.1171	1.0903
Present work	10^4	2.0901	2.0957	0.2301	0.2232
	10^5	4.2867	4.2961	0.5194	0.5063
	10^6	8.3458	8.3702	1.1265	1.0971

4 Results and Discussion

4.1 Heat Transfer by Radiation

To investigate the impact of radiation on total heat flux through the concrete hollow brick, Fig. 2 illustrates the evolution of the heat flux q . The results illustrate that the thermal emissivity ϵ has an considerable impact on the total flux through the brick. In fact, the global heat flux for emissive walls is greater in comparison with the case where $\epsilon = 0.1$. The improvement in heat flux is approximately 26% when the emissivity increases from 0.1 to 0.9. Interestingly, the role of radiation in global heat transfer is significant for hollow concrete brick surfaces with high emissivity values. Therefore, the heat transfer is drastically decreased by lowering the thermal emissivity, which can improve the walls thermal resistance.

4.2 Effect of the Aspect Ratio of the Hole A_h

Figures 3(a)–(c) illustrate the isotherms obtained for hollow bricks with various aspect ratios A_{h1} , A_{h2} and A_{h3} . As shown, the temperature fields are strongly affected by the aspect ratio A_h . In the proximity of the top and bottom inner faces of the right and left sidewalls, the isotherms become tighter when rising the A_h from A_{h1} to A_{h3} , while the fluid is in a condition of thermal stratification as the isotherms become parallel to

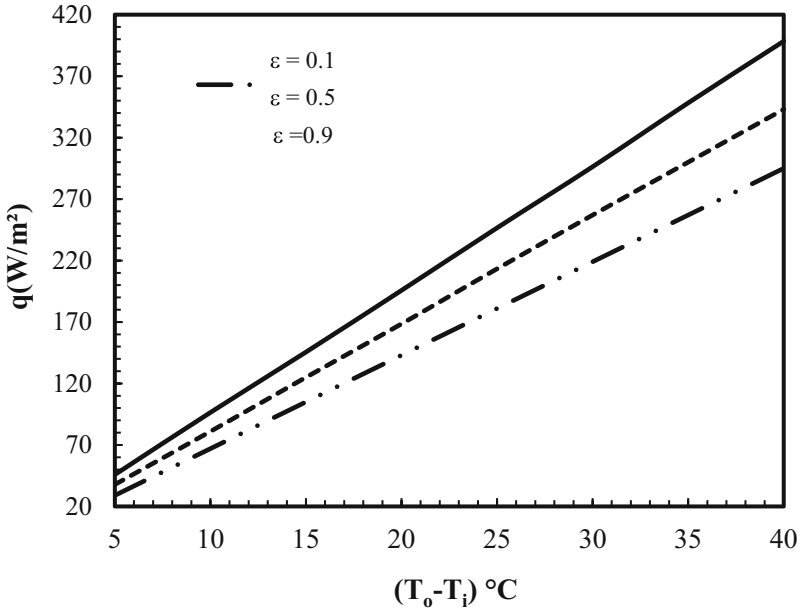


Fig. 2. Variation of the global heat flux for different thermal emissivity values.

the horizontal sides in the middle of the holes. Furthermore, the intensity of convection increases, as shown by the distortion of the isotherms. It is worth noting that the temperature profiles in the solid walls are almost linear.

4.3 Contribution of Various Heat Exchange Modes

Using the simulation results, it is very advantageous to estimate the contribution of each heat exchange mode to the total heat flux through the studied bricks. The percentages of the three modes are given in Table 4. The results show that conduction is predominant, which accounts for more than 50% of total flux. The heat transfer by radiation accounts for about 30%. As for convection, it has a lower percentage (about 15%) but undergoes an augmentation according to ΔT . We also note that when ΔT increases, the fraction of heat transfer by conduction reduces while the proportion of radiative and convective exchanges increases.

4.4 Effect of Solid Walls' Heat Conductivity

The variations of heat flux with different values of thermal conductivity are shown in Fig. 4. The results reveal that the overall heat flux is strongly affected by the increase of the thermal conductivity, especially for high ΔT . In fact, when the conductivity k_s varies from 1 W/mK to 2 W/mK, the heat flux increases by 80% for $\Delta T = 40$ °C. This is due to the interaction between convective and radiative transfers and mainly to the increase of the conduction rate at the expense of the other modes when the thermal conductivity k_s

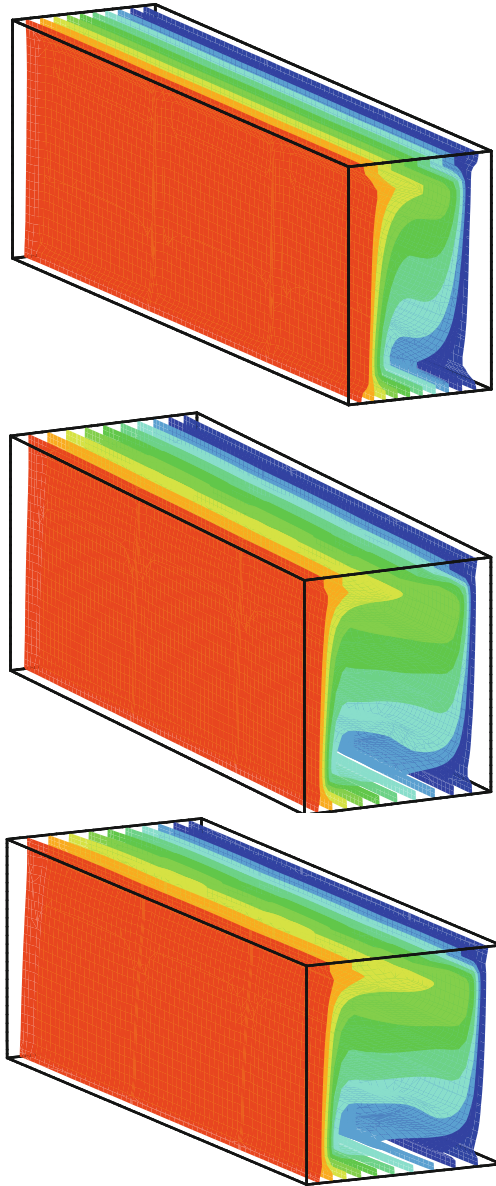
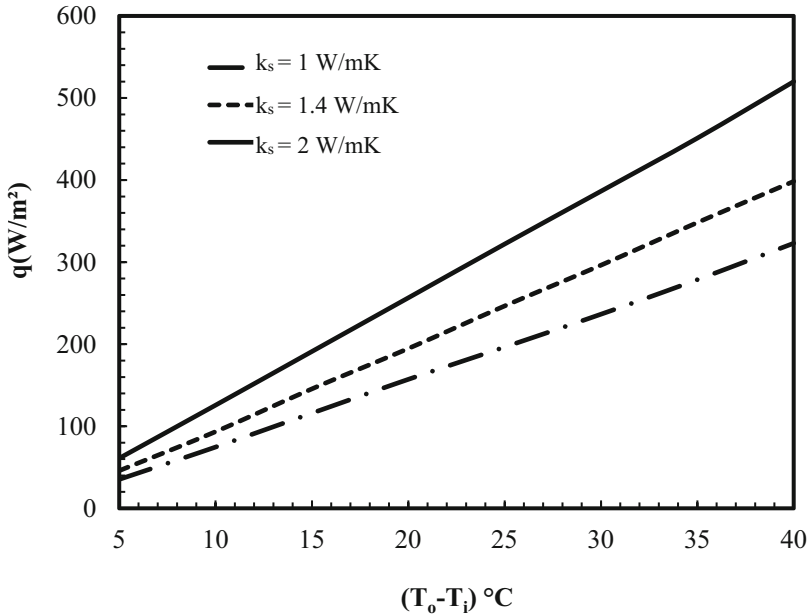


Fig. 3. Isotherms obtained for $\Delta T = 30\text{ }^{\circ}\text{C}$ and various aspect ratios: (a) $A_h = A_{h1}$, (b) $A_h = A_{h2}$ and (c) $A_h = A_{h3}$.

increases. These findings demonstrate that the global heat flux is considerably influenced by the solid material's conductivity greater than 1 W/mK .

Table 4. Heat transfer modes contribution to the global heat flux.

ΔT	q_{cond} (%)	q_{rad} (%)	q_{conv} (%)
10	64.43	25.21	10.36
20	60.11	27.79	12.10
30	57.84	28.24	13.92
40	55.72	29.65	14.63

**Fig. 4.** Evolution of the heat flux with various values of thermal conductivity.

5 Conclusion

This study involved a numerical simulation of combined heat transfer through hollow concrete bricks. A computational model has been developed to simulate the heat exchange properties of hollow concrete bricks. The effect of the inner surfaces' thermal emissivity, the thermal conductivity and the aspect ratio of inner cells on the heat exchange and fluid flow is investigated for various practical values of the thermal excitations. The results reveal that the contribution of radiation to the global heat transfer through the hollow bricks is increasingly significant for high interior surface emissivity values. Therefore, coating the interior surfaces of concrete bricks with a low-emissivity substance limits heat transfer, which can increase the thermal resistance of the building walls.

References

1. Pylsy, P., Lylykangas, K., Kurnitski, J.: Buildings' energy efficiency measures effect on CO₂ emissions in combined heating, cooling and electricity production. *Renew. Sustain. Energy Rev.* **134** (2020)
2. Meng, X., Luo, T., Gao, Y.N., Zhang, L.L., Shen, Q., Long, E.S.: A new simple method to measure wall thermal transmittance in situ and its adaptability analysis. *Appl. Therm. Eng.* **122**, 747–757 (2017)
3. Dos Santos, H.G., Fogiatto, M.A., Endes, N.: Numerical analysis of thermal transmittance of hollow concrete blocks. *J. Building Phys.* **41**, 1–18 (2017)
4. Fioretti, R., Principi, P.: Thermal performance of hollow clay brick with low emissivity treatment in surface enclosures. *Coatings* **4**, 715–731 (2014)
5. Gossard, D., Lartigue, B.: Three-dimensional conjugate heat transfer in partitioned enclosures: determination of geometrical and thermal properties by an inverse method. *Appl. Therm. Eng.* **54**, 549–558 (2013)
6. Shi, G.Z., Li, L.P., Song, C.F., Cheng, S.M., Tao, W.Q., He, Y.L.: 3D numerical thermal optimization of the roofs constructed with cast-in-situ hollow concrete floor system by finite volume method. *Energy and Building* **131**, 142–152 (2016)
7. Abdelbaki, A., Zrikem, Z.: Simulation numérique des transferts thermiques couplés à travers les parois alvéolaires des bâtiments. *Int. J. Therm. Sci.* **38**, 719–730 (1999)
8. Kim, D., Viskanta, R.: Effect of wall conduction and radiation on natural convection in a rectangular cavity. *Numer. Heat Transf.* **7**, 449–470 (1984)
9. Frederick, R.L., Moraga, S.G.: Three-dimensional natural convection in finned cubical enclosures. *Int. J. Heat Fluid Flow* **28**, 289–298 (2007)
10. Tric, E., Labrosse, G., Betrouni, M.: A first incursion into the 3D structure of natural convection of air in a differentially heated cubic cavity, from accurate numerical solutions. *Int. J. Heat Mass Transf.* **43**, 4043–4056 (2000)
11. Hu, L., Xin, S., Chena, Y.C., Chergui, J., Le Quéré, P.: Benchmark solution of 3D natural convection flows with surface radiation in air-filled cavity. In: *Second International Conference on Computational Methods for Thermal Problems, Dalian* (2011)



Time Domain Analysis of Skin Effect in Nonuniform Interconnection Using the FDTD Technique

Nadir Youssef^{1,2}(✉), Belahrach Hassan^{2,3}, Ghammaz Abdelilah³,
Naamane Aze-eddine^{1,2}, and Mohammed Radouani¹

¹ L2MC Laboratory, Moulay Ismail University, Meknes, Morocco
josse.nadir@gmail.com

² Electrical Laboratory, Royal School of Aeronautics, Marrakech, Morocco

³ Laboratory LSEEET, University Cadi Ayyad, Marrakech, Morocco

Abstract. During the last decades, manufacturers have opted for the miniaturization of electronic devices as an answer to high-performance equipment demand. However, Downscaling the Integrated Circuit (IC) technology has several side effects on the device's performance. Considered one of the IC problems in the design, the skin effect impacts the IC design. In addition, high clock frequency can lead to severe Electromagnetic Compatibility (EMC) issues. The present work has used an efficient numerical method for transient analysis based on the Finite Difference Time Domain (FDTD) Method to investigate the previous phenomenon. It is used to examine the skin and incident electromagnetic field effect on the signals applied in non-uniform submicron CMOS interconnects. We have selected two research situations of non-uniform interconnects loaded by linear terminals, either in the absence or presence of an incident field. The MATLAB tool is used to implement the proposed algorithms. The outcomes are contrasted with PSPICE's results. A close match was obtained between the two results.

Keywords: Skin effect · Nonuniform Interconnections · Electromagnetic Coupling · FDTD · CMOS Driver

1 Introduction

A variety of high-speed interconnect phenomena, including distortion, reflections, signal delay, and crosstalk, must be taken into account when designing high-frequency integrated circuits (ICs). Skin effect is also one of the previous design side effects. It is manifested in interconnections by the resistance increase of those conductors due to a current crowding electromagnetic effect in the metal conductor under high frequency [1, 2]. In addition, the nonuniform interconnections structures are frequently utilized in microwave systems and high-speed electronics. For instance, they are employed in RF and microwave circuits as filters, resonators, impedance matching, delay equalizers, analog signal processing, wave shaping, VLSI interconnects, etc. [3]. The use of high-frequency devices can cause electromagnetic compatibility (EMC) problems. EMC is a

device or system's ability to run in its electromagnetic environment without compromising its functions and without faults and vice versa. The effects of EMC are increasing in several domains, such as microelectronics, automotive, and aeronautics [4]. Several approaches have thus far been suggested to study the uniform transmission lines [5–7] and the nonuniform ones [8] in the absence and presence of a radiated EM wave coupling such as the finite difference quadrature [9].

The goal of this manuscript is to propose and develop a model that represents the skin effect in coupled nonuniform interconnect. The novelty of this work is due to the study of skin effect influence in presence of incident electromagnetic field and the nonuniform interconnect behavior in such an environment. Indeed, this work is dispatched as follows: Sect. 2 is reserved to the formulation of the electromagnetic coupling in nonuniform interconnections with the existence of a parasitic electromagnetic field means of the FDTD method. Section 3 of the paper provides examples of electromagnetic coupling with skin effect. The examples are presented both in the absence and presence of incident field excitation. Section 4 concludes the paper.

2 Electromagnetic Coupling of Nonuniform Interconnect Lines

On the one hand, transmission lines full-wave analysis can give greater accuracy. On the other hand, it is computationally more expensive than solving the multiconductor transmission line equations (MTL). Therefore, the MTL model is often used as a good approximation. It assumes that the parasitic field is a transverse electromagnetic (TEM) field, composed of an electric and magnetic field lying in a line axis transverse plane [10]. This section explains the modeling of the electromagnetic coupling of nonuniform interconnects suffered from skin effects and radiated by an incident field.

2.1 The FDTD Formulation for Electromagnetic Coupling

The quasi-transverse electromagnetic model is assumed to investigate and evaluate the skin effect of coupled nonuniform interconnections [10]. Thus, by applying the Kirchhoff law on the circuit shown in Fig. 1, we obtain the linked partial differential equations system shown below. (Telegrapher's equations) [11, 12]:

$$\begin{cases} \frac{\partial}{\partial x} V(x, t) + Z(x, t)I(x, t) + L(x) \frac{\partial}{\partial t} I(x, t) = \mathbf{V}_s(x, t) \\ \frac{\partial}{\partial x} I(x, t) + G(x)I(x, t) + C(x) \frac{\partial}{\partial t} V(x, t) = \mathbf{I}_s(x, t) \end{cases} \quad (1)$$

where the currents \mathbf{I} and voltages \mathbf{V} are written in $M \times 1$ column vector form. The interconnect per unit parameters \mathbf{R} , \mathbf{L} , \mathbf{C} and \mathbf{G} are given by $M \times M$ matrices. \mathbf{V}_s and \mathbf{I}_s are representing respectively per unit length electromagnetic induced field, and are written as follows [12]:

$$\mathbf{V}_s(x, t) = -\frac{\partial}{\partial x} \mathbf{E}_T(x, t) + \mathbf{E}_L(x, t) \quad (2)$$

$$\mathbf{I}_s(x, t) = -\mathbf{G}(x)\mathbf{E}_T(x, t) - \mathbf{C}(x) \frac{\partial}{\partial x} \mathbf{E}_T(x, t) \quad (3)$$

where \mathbf{I}_S and \mathbf{V}_S are expressed in $M \times 1$ column vector. \mathbf{E}_T and \mathbf{E}_L are respectively the transverse and longitudinal components of the incident electric field.

The skin effect can be approximated as internal impedance that includes a resistance and an internal inductance, and we may write [10]:

$$\mathbf{Z}(x, t)\mathbf{I}(x, t) = \mathbf{R}(x)\mathbf{I}(x, t) + \frac{\mathbf{B}(x)}{\sqrt{\pi}} \int_0^t \frac{1}{\sqrt{u}} \frac{\partial \mathbf{I}(x, t-u)}{\partial (t-u)} du \quad (4)$$

where: $\mathbf{R}(x) = \frac{100}{1+K(x)}$; $\mathbf{B}(x) = \frac{\sqrt{\frac{\mu}{\epsilon}}}{2 \cdot 10^{-6}(5+50K(x))}$; $K(x) = 0.25[1 + \sin(6.25\pi x + \frac{\pi}{4})]$.

To solve Eq. (1), we used finite difference time domain (FDTD) method. This algorithm divides the time and space domains into N_t intervals and N_x cells, each with a duration of Δt and a length of Δx , respectively. This discretization uses Yee's grid where the currents are determined at $(t + \Delta t/2)$ steps and $(x + \Delta x)$ positions, while the voltages are computed at $(t + \Delta t)$ steps and $(x + \Delta x/2)$ positions. To ensure the model's stability, the spatial increment step Δx must be smaller than the wavelength propagated on the line and Δt must be minor to satisfy Courant-Friedrichs-Lewy condition [13].

The equations describing the recurrent voltage and current along an interconnect line are expressed:

For $k = 2, 3, \dots, N_x$

$$\mathbf{V}_k^{n+1} = A_4^{-1} \left(A_5 \mathbf{V}_k^n + \Delta x \mathbf{I}_{sk}^n + \mathbf{I}_k^{n+\frac{1}{2}} + \mathbf{I}_{k+1}^{n+\frac{1}{2}} \right) \quad (5)$$

with:

$$\mathbf{I}_{sk}^n = \left[G(k) \mathbf{E}_{gk}^n + \frac{C(k)}{\Delta t} (\mathbf{E}_{gk}^n - \mathbf{E}_{gk}^{n-1}) \right] \{A_i\} \quad (6)$$

For $k = 1, 2, 3, \dots, N_x$

$$\mathbf{I}_k^{n+\frac{3}{2}} = A_1^{-1} \left(A_2 \mathbf{I}_k^{n+\frac{1}{2}} + \Delta x \mathbf{V}_{sk}^n + \mathbf{V}_k^{n+1} - \mathbf{V}_{k+1}^{n+1} - A_3 \mathbf{J}_k^n \right) \quad (7)$$

with:

$$\mathbf{V}_{sk}^n = \frac{(\mathbf{E}_{gk}^{n+1} - \mathbf{E}_{gk}^n)}{\Delta t} \cdot \{D_i\} \quad (8)$$

In (8), the term \mathbf{J}_k^n represents the skin effect and it is written as:

$$\mathbf{J}_k^n = \sum_{m=1}^n \mathbf{P}_0(m) \left(\mathbf{I}_k^{n+\frac{3}{2}+m} - \mathbf{I}_k^{n+\frac{1}{2}-m} \right) \quad (9)$$

with A_1, A_2, A_3, A_4 , and A_5 are square matrices $M \times M$, line parameters dependent. The $M \times 1$ column vectors A_i and D_i based on the the interconnections i^{th} position, the modal velocities propagated in the structure and the characteristics of the incident field.

Therefore, $A_1 = \mathbf{L}(\mathbf{k}) \frac{\Delta x}{\Delta t} + \mathbf{R}(\mathbf{k}) \frac{\Delta x}{2} + \mathbf{B}(\mathbf{k}) \frac{\Delta x}{\sqrt{\pi \Delta t}} \mathbf{P}_0(0)$;

$$A_2 = \mathbf{L}(\mathbf{k}) \frac{\Delta x}{\Delta t} - \mathbf{R}(\mathbf{k}) \frac{\Delta x}{2} + \mathbf{B}(\mathbf{k}) \frac{\Delta x}{\sqrt{\pi \Delta t}} \mathbf{P}_0(0); A_3 = \mathbf{B}(\mathbf{k}) \frac{\Delta x}{\sqrt{\pi \Delta t}};$$

$A_4 = \frac{\Delta x}{\Delta t} \mathbf{C}(\mathbf{k}) + \frac{\Delta x}{2} \mathbf{G}(\mathbf{k})$, and $A_5 = \frac{\Delta x}{\Delta t} \mathbf{C}(\mathbf{k}) - \frac{\Delta x}{2} \mathbf{G}(\mathbf{k})$ with E_k^n is the incident field at position k and time n .

The load circuits must be detailed to calculate the currents and voltages at the ends of the line structure. The following subsection describes in detail the CMOS nonlinear loads.

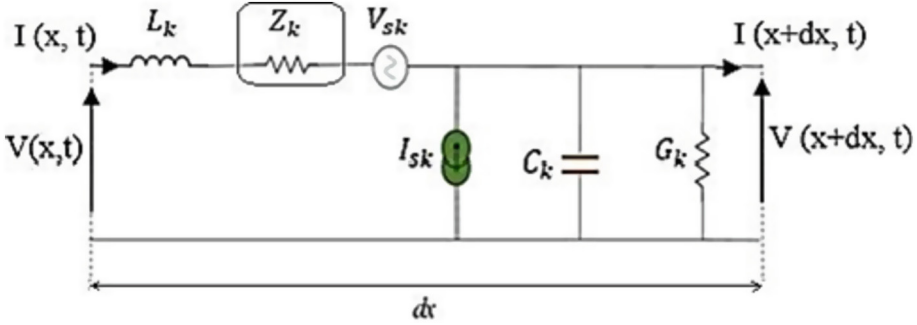


Fig. 1. Equivalent circuit model of single interconnect illuminated by an incident field \vec{E} .

2.2 The Boundary Condition

By considering Fig. 2, we obtain the following equations:

$$V_g = R_s I_{in} + V_{in} \quad (10)$$

$$I_{in} + \frac{\Delta x}{2} I_{s1} = I_1 + G_1 \frac{\Delta x}{2} \left(V_{in} + \frac{\Delta x}{2} V_{s1} \right) + C_1 \frac{\Delta x}{2} \frac{\partial}{\partial t} \left(V_{in} + \frac{\Delta x}{2} V_{s1} \right) \quad (11)$$

By combining the previous equations, we get:

$$G_s (V_g - V_{in}) + \frac{\Delta x}{2} I_{s1} = I_1 + G_1 \frac{\Delta x}{2} \left(V_{in} + \frac{\Delta x}{2} V_{s1} \right) + C_1 \frac{\Delta x}{2} \frac{\partial V_{in}}{\partial t} + C_1 \left(\frac{\Delta x}{2} \right)^2 \frac{\partial V_{s1}}{\partial t} \quad (12)$$

After simplification, (12) is written as:

$$V_{in}^n = B_1^{-1} \frac{\Delta x}{2 \Delta t} \left(C_1 V_{in}^{n-1} + G_s V_g^n - I_1^n + B_2 E_{g1}^n - B_3 E_{g1}^{n-1} + B_4 E_{g1}^{n+1} \right) \quad (13)$$

where: $B_1 = G_s + \frac{\Delta x}{2} C_1 + \frac{\Delta x}{2 \Delta t} C_1$; $B_2 = \frac{\Delta x}{2} \left(G_1 + \frac{C_1}{\Delta t} \right) A_1 - \left(\frac{\Delta x}{2} \right)^2 \frac{G_1}{\Delta t} D_1 + 2 \left(\frac{\Delta x}{2 \Delta t} \right)^2 C_1 D_1$;
 $B_3 = \frac{\Delta x}{2} \left(\frac{C_1}{\Delta t} \right) A_1 - \left(\frac{\Delta x}{2} \right)^2 \frac{G_1}{\Delta t} D_1 + \left(\frac{\Delta x}{2 \Delta t} \right)^2 C_1 D_1$; $B_4 = \left(\frac{\Delta x}{2 \Delta t} \right)^2 C_1 D_1$.

By considering Fig. 3, we obtain the following equations:

$$G_L V_{out}^n = I_{Ndx}^n + \frac{\Delta x}{2} I_{sNdx}^n - \frac{\Delta x}{2} G_{Ndx}^n \left(V_{out}^n + \frac{\Delta x}{2} V_{sNdx}^n \right) - \frac{\Delta x}{2} C_{Ndx}^n \left(V_{out}^n + \frac{\Delta x}{2} V_{sNdx}^n \right) \quad (14)$$

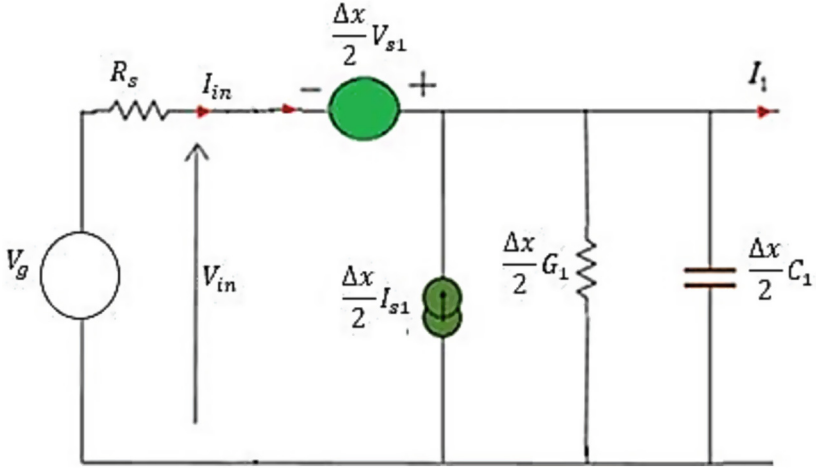


Fig. 2. Equivalent circuit model of single interconnect illuminated by an incident field \vec{E} .

Thus, (14) can be simplified as:

$$V_{\text{out}}^n = F_1^{-1} \left(I_{\text{Ndx}}^n + \frac{\Delta x}{2} \frac{C_{\text{Ndx}}^n}{\Delta t} V_{\text{out}}^{n-1} + F_2 E_{\text{gNdx}}^n - F_3 E_{\text{gNdx}}^{n-1} + F_4 E_{\text{gNdx}}^{n+1} \right) \quad (15)$$

where: $F_1 = G_L + \frac{\Delta x}{2} C_{\text{Ndx}} + \frac{\Delta x}{2\Delta t} C_{\text{Ndx}}$; $F_2 \frac{\Delta x}{2} \left(G_{\text{Ndx}} + \frac{C_{\text{Ndx}}}{\Delta t} \right) A_{\text{Ndx}} - \left(\frac{\Delta x}{2} \right)^2 \frac{G_{\text{Ndx}}}{\Delta t} D_{\text{Ndx}} + 2 \left(\frac{\Delta x}{2\Delta t} \right)^2 C_{\text{Ndx}} D_{\text{Ndx}}$; $F_3 = \frac{\Delta x}{2} \left(\frac{C_{\text{Ndx}}}{\Delta t} \right) A_{\text{Ndx}} - \left(\frac{\Delta x}{2} \right)^2 \frac{G_1}{\Delta t} D_{\text{Ndx}} + \left(\frac{\Delta x}{2\Delta t} \right)^2 C_{\text{Ndx}} D_{\text{Ndx}}$; $F_4 = \left(\frac{\Delta x}{2\Delta t} \right)^2 C_{\text{Ndx}} D_{\text{Ndx}}$.

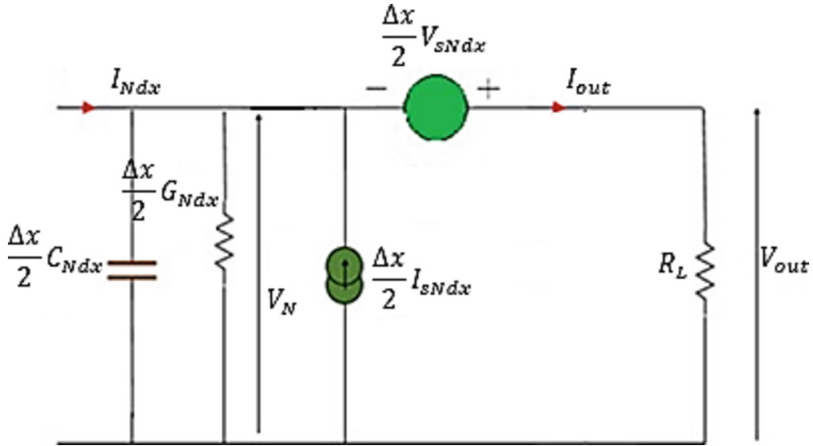


Fig. 3. Single interconnect's equivalent circuit model illuminated by an incident field \vec{E} .

The following section will study some cases of voltage and current implementation in MATLAB.

3 Study Cases and Discussions

3.1 Nonuniform Interconnects Loaded with Linear Circuits and the Absence of Incident Field Excitation

A trapezoidal pulse with an amplitude of 1 kV/m, rise and fall time of 100 ps, and pulse width of 0.3 ns is applied to the first line.



Fig. 4. Two interconnects test circuit with linear loads.

We used MATLAB to implement near and far-end voltage recurrence relations. The results at the far end voltage of the first line are shown in Fig. 5-a. PSPICE tool simulation of Fig. 4 is shown in Fig. 5-b.

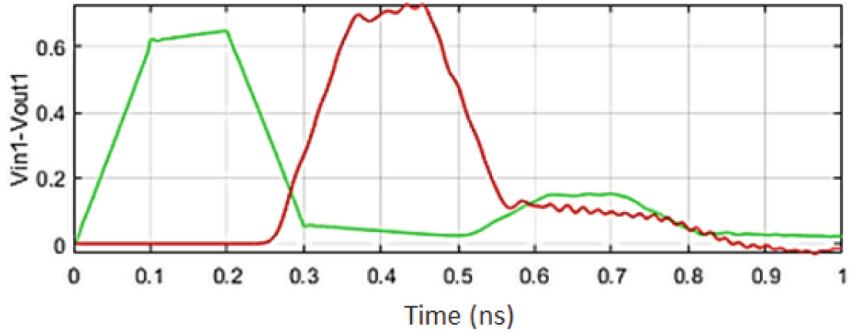
Similarly, we have simulated the structure and plotted second line output voltage using MATLAB (Fig. 6-a), and PSPICE (Fig. 6-b).

In the previous figures, it has been observed that the skin effect has impacted generally the amplitude of the different voltages. For instance, the input and the output of the first line are going respectively more than 600 mV and up to 1 V (Fig. 5). The apparent fluctuations in Matlab results (Fig. 5-a) and (Fig. 6-a) and their absence in PSPICE results (Fig. 5-b) and (Fig. 6-b) are due in part to discretization in the FDTD method.

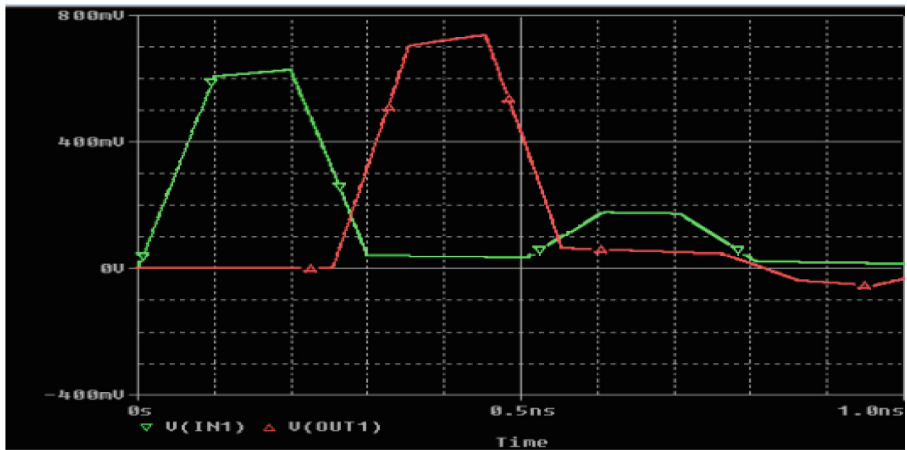
In a conclusion, we found that MATLAB outcomes match closely the industrial-level PSPICE. Thus, the accuracy of our model is proven.

3.2 Excitation by an Incident Field of Nonuniform Interconnects with Linear Loads

The following discussed study case is commonly found in reality. The growing demand for faster data transmission and processing in telecommunication systems has led to an increased interest in modeling the non-ideal effects of conductors that connect different subsystems. The second study case schematic in Fig. 7 shows two nonuniform interconnect lines, where the whole circuit is excited by an incident field of 3ns delay, with an application of a trapezoidal voltage source of 1ns delay on the first line.



(a)



(b)

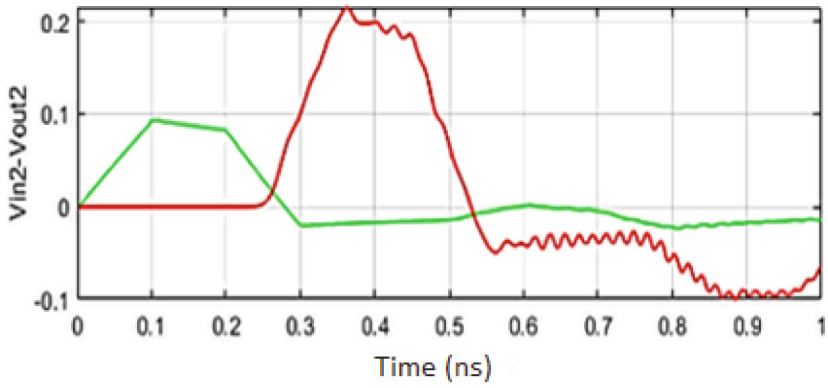
Fig. 5. First line simulation, (a) MATLAB (b) PSPICE.

For the example given, and considering the previous parameters, we have done some MATLAB (Fig. 8.a) and PSPICE tool (Fig. 8.b) simulations.

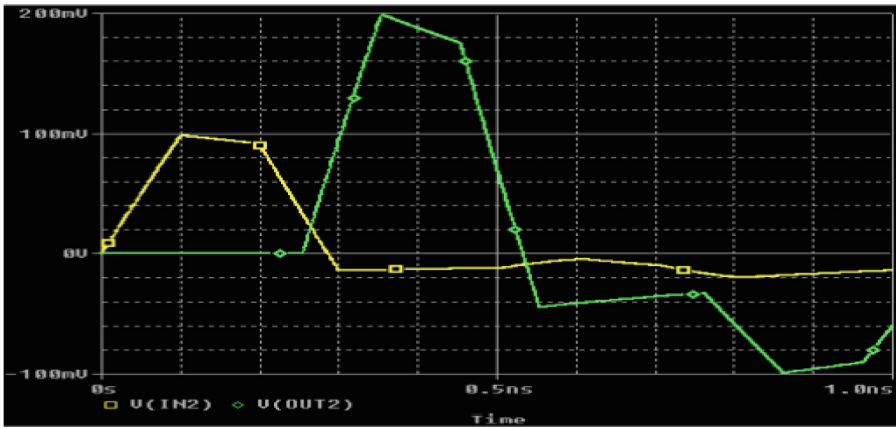
The induced voltage at the second line input is considered as a victim and it is shown in Fig. 9.

On the one hand, Figs. 8 and 9 have confirmed the skin effect influence on the amplitude of the various signals, for example, the input voltage of the first line is going up to 600 mV to reach 800 mV. On the other hand, sharp peaks have appeared at the output voltage which can be explained by the incident field impact.

The comparison of the results from MATLAB and PSPICE, it was observed a good agreement between them. Thus, came the conclusion of the validity of the proposed model.



(a)



(b)

Fig. 6. Second line simulation, (a) MATLAB (b) PSPICE.

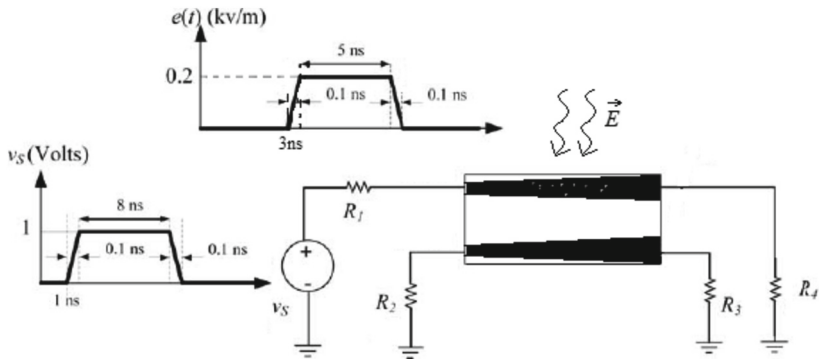
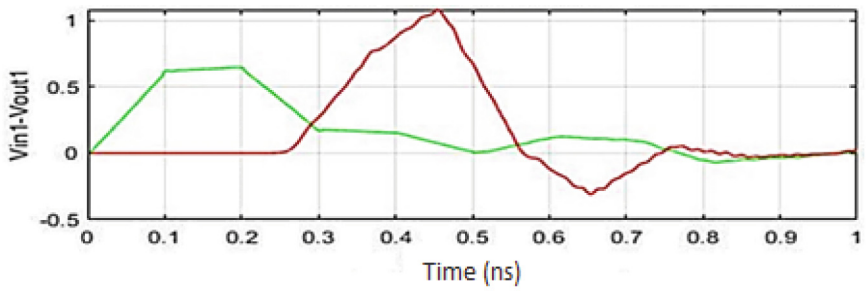
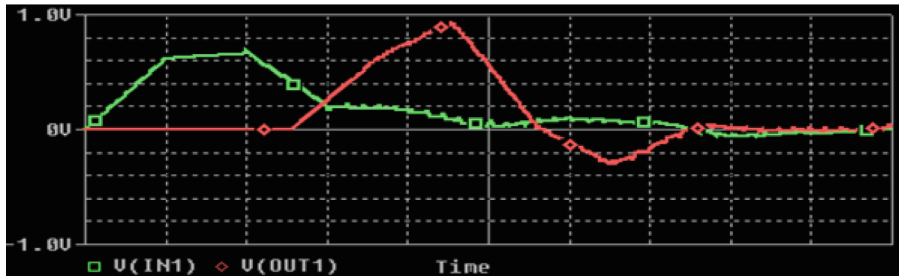


Fig. 7. Two interconnects test circuit excited by an external field \vec{E} .

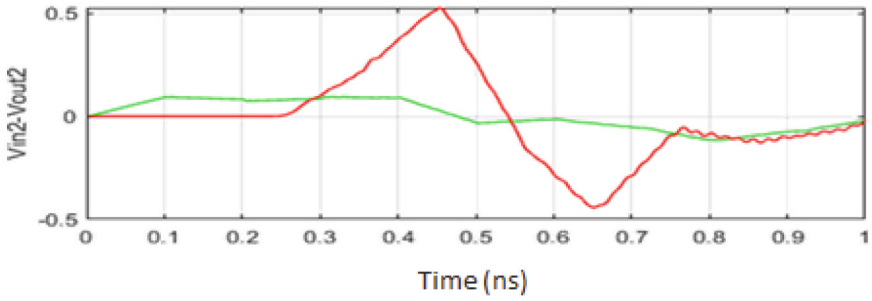


(a)

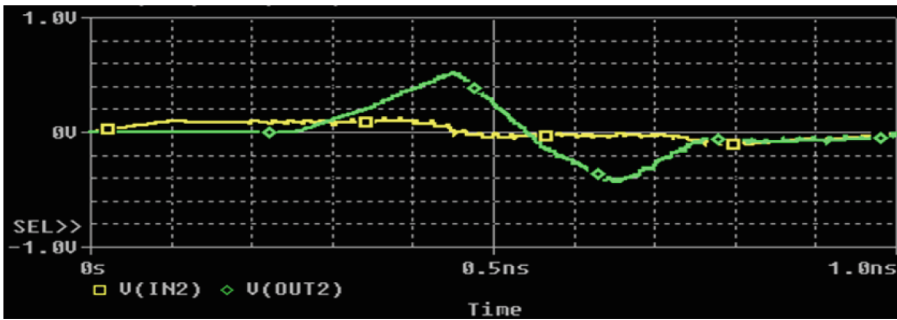


(b)

Fig. 8. First line simulation, (a) MATLAB (b) PSPICE.



(a)



(b)

Fig. 9. Second line simulation, (a) MATLAB (b) PSPICE.

4 Conclusion

The paper presents a model and simulation of nonuniform interconnect lines electromagnetic coupling affected by skin effect. The telegrapher equations and the FDTD method were employed to model the coupling. The signal propagation mode is assumed to be quasi-TEM. The validity of the algorithm is analyzed using MATLAB and PSPICE, in the absence and presence of external incident disturbances. The outcomes demonstrate a close match between MATLAB and PSPICE simulations.

References

1. Wu, W., Yuan, J.S.: Skin effect of on-chip copper interconnects on electromigration. *Solid-State Electron.* **46**(12), 2269–2272 (2002). [https://doi.org/10.1016/S0038-1101\(02\)00232-0](https://doi.org/10.1016/S0038-1101(02)00232-0)
2. Orlandi, A., Paul, C.R.: FDTD analysis of lossy multiconductor transmission lines terminated in arbitrary loads. *IEEE Trans. Electromag. Compat.* **38**(3), 388–399 (1996)

3. Dhaene, T., De Zutter, D.: Extended Thevenin models for transient analysis of non-uniform dispersive lossy multiconductor transmission lines. In: *Proceeding of the 1992 IEEE International Symposium on Circuits and Systems*, vol. 4, pp. 1772–1775 (1992). <https://doi.org/10.1109/ISCAS.1992.230411>
4. Lee, M., Pak, J.S., Kim, J.: *Electrical Design of Through Silicon Via*. Springer, Heidelberg (2014). <https://doi.org/10.1007/978-94-017-9038-3>
5. Kumar, A., Kaushik, B.K.: Transient analysis of hybrid Cu–CNT on-chip interconnects using MRA technique. *IEEE Open J. Nanotechnol.* **3**, 24–35 (2021). <https://doi.org/10.1109/OJNANO.2021.3138344>
6. Nadir, Y., Hassan, B., Abdelilah, G., Naamane, A.-E., Mohammed, R.: Modeling crosstalk effects of hybrid copper carbon nanotube interconnects using a novel accurate FDTD based method. *Microelectron. J.* **129**, 105589 (2022). <https://doi.org/10.1016/j.mejo.2022.105589>
7. Kumar, R., Kaushik, B.K., Patnaik, A.: An accurate model for dynamic crosstalk analysis of CMOS gate driven on-chip interconnects using FDTD method. *Microelectron. J.* **45**, 441–448 (2014). <https://doi.org/10.1016/j.mejo.2014.02.004>
8. Wang, W., Liu, P.-G., Qin, Y.-J.: An unconditional stable 1D-FDTD method for modeling transmission lines based on precise split-step scheme. *Prog. Electromagnet. Res.* **135**, 245–260 (2013). <https://doi.org/10.2528/PIER12103007>
9. Xu, Q., Mazumder, P.: Efficient modeling of transmission lines with electromagnetic wave coupling by using the finite difference quadrature method. *IEEE Trans. VLSI Syst.* **15**(125), 1289–1302 (2007). <https://doi.org/10.1109/TVLSI.2007.904105>
10. Afrooz, K., Abdipour, A., Tavakoli, A., Movahhedi, M.: Time domain analysis of lossy nonuniform transmission line using FDTD technique. In: *2007 Asia-Pacific Conference on Applied Electromagnetics*, pp. 1–5 (2007). <https://doi.org/10.1109/APACE.2007.4603880>
11. Qinwei, X.U.: A efficient modeling of transmission lines with electromagnetic wave coupling by using the finite quadrature method. *Trans. Very Large Integrat. Syst.* **15**, 1289–1302 (2007)
12. Rachidi, F., Tkachenko, S.V.: Electromagnetic field interaction with transmission lines from classical theory to HF radiation effects. In: *Advances in Electrical Engineering and Electromagnetics*, vol. 29 (2008)
13. Rebelli, S., Nistala, B.: An efficient MRTD model for the analysis of crosstalk in CMOS-driven coupled Cu interconnects. *Radioengineering.* **27**, 532–540 (2018). <https://doi.org/10.13164/re.2018.0532>



Effect of the Temperature on the Mechanical Properties of Jute Fabric Reinforced Epoxy Composite

Youssef Ben smail¹(✉), Ahmed El moumen², Fatima Lmai³, and Abdellatif Imad⁴

¹ Industrial and Surface Engineering Laboratory, Faculty of Science and Technology, Béni-Mellal, Morocco

y.bensmail@gmail.com

² Normandy University, UNIHAVRE, CNRS, LOMC UMR 6294, Le Havre, France

³ Faculty of sciences–Ain Chock, Physics of Advanced Materials and Thermal Laboratory, Casablanca, Morocco

⁴ Lille University, Mechanical Unit of Lille - J. Boussinesq - UML - EA 7512, F-59000 Lille, France

Abstract. This work presents an experimental evaluation into the effect of the temperature upon the thermal properties and the mechanical properties of jute fabric/epoxy composite heated at different temperatures. The jute fabric/epoxy was prepared at the ambient temperature and fixed volume fraction of jute (four fabric layers) using infusion method. To examine the effect of the temperature, the composite was heated at different temperatures. The mechanical properties of the jute fabric/epoxy heated at different temperatures were carefully investigated. The results shows that the composites exposed to the high temperature are prone to the lower mechanical properties. At the temperature (80 °C), the composite shows a high ability to deformation due to the matrix softening which reduces the cohesion between the epoxy and the jute fabric, which is the reason for the decrease of the tensile stress. Moreover, the matrix softening increase with an increase of heating temperature. The lowest tensile stress (reduce by more than 58%) was determined in the case of the composite heated at the temperature 80 °C. The results in this research confirm the limitation of the composite use in different applications, especially at high temperature.

Keywords: Jute fabric · epoxy · composite · thermal properties · mechanical properties

1 Introduction

Because of increasing environmental alertness, vegetal fibers have become the most requested materials by researchers and in the industry as reinforcement for polymer resin. The vegetal fibers have many advantages such as environmentally friendly, low cost, availability in all world region, renewability and good mechanical properties [1]. The composite reinforced by vegetal fibers are used in many applications such as automobile,

aerospace and construction [2, 3]. However, the composites reinforced by the natural fibers are exposed to the environmental conditions such as temperature and humidity [4, 5]. These conditions influence the mechanical properties of composites [6, 7]. This changes in the properties due to the changes on their mechanical properties of the components of the composite [8]. Bensmail et al [6] investigate the effects of the heat treatment on the mechanical properties of the jute yarns. The results found shows that the tensile stress and modulus of elasticity are influenced by water evaporation and reduce at the heated temperature 100 °C. As reported by Debarati et al. [9] the performance of ozone treated jute fabric / epoxy composites was evaluated at different temperatures after incorporation of ozonized and pulverized corn husk particles. The results of this investigation show that the filler was found successful in removal of non-cellulosic contents. Moreover, the treatment of the particles and their incorporation in the composite reduce the creep deformation of jute fabric/epoxy composite. This behavior was due to increased mechanical bonding between the jute fabric and the matrix epoxy. Sagar et al. [10] studied the effect of Nano-SiO₂ powder on the mechanical properties of a jute fabric/epoxy composite and showed that the composite is significantly improved by incorporation of the filler especially the improvement of the tensile stress. Parabina et al. [11] indicate that the incorporation of the groundnut shell particulate filler in the jute fabric/epoxy composite reveal that the tensile stress is increased and reach a maximum up to 15 wt% filler. In this investigation, the effect of the heat treatment on the mechanical properties of the composite jute fabric/epoxy is evaluated and the specimens are exposed to the temperature less than 100 °C [6]. The tensile tests are carried out to determine tensile strength, modulus of elasticity and elongation at break for each specimen based on the temperatures. The thermal stability of the jute fabric, epoxy and composite are also evaluated.

2 Materials and Methods

2.1 Materials

The jute fabric is extracted from fabric used for the manufacturing of agricultural products bags in the southeast of Asia. The epoxy is Resoltech 1800 ECO/1804 ECO it is 34% biobased on the mix from resoltech: advanced technology resin, French. The manufacturing process of the specimens is summarized in the figure (Fig. 1).

2.2 Thermal Analysis

The thermal stability of the samples was determined by thermogravimetric analysis (Shimadzu TGA device). The samples weight loss is between 3 and 8 mg of epoxy, jute fabric and composite. Each specimen was examined under air atmospheric with the heating speed at 10 °C/min from the ambient temperature to 600 °C.

2.3 Mechanical Testing Method

The mechanical properties of the jute fabric and the composite at different temperatures was carried to studies the mechanical performance of the samples. The jute fabric dimension estimated are 1 mm × 20 mm × 50 mm (Fig. 2) and the composite dimension are

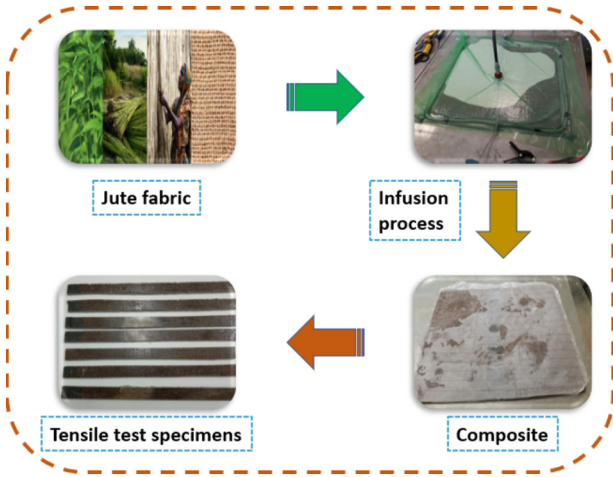


Fig. 1. Fabrication process of the composite Jute fabric/epoxy.

4 mm × 20 mm × 50 mm (Fig. 3). The tensile test speed of the specimens is 2 mm/min. Before each test the samples are heated at different temperatures for 24 h.



Fig. 2. Fixation system of Jute fabric specimen.

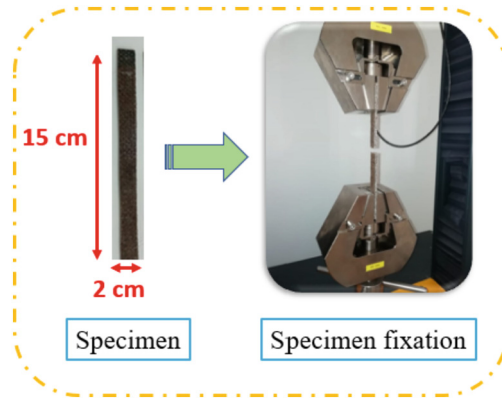


Fig. 3. Dimensions and fixation system of the composite Jute fabric specimen.

3 Results and Discussion

3.1 Thermal Analysis

The thermal stability curves of the jute fabric, epoxy resin and the composite jute fabric/epoxy are shown in Fig. 4 (a). The first weight loss below 100 °C is due to water evaporation. The second decomposition occurred at the temperature range of 240–350 °C due to degradation of the hemicellulose and α -cellulose [12]. The third decomposition occurred at the temperature range of 350–450 which is due to the degradation of the cellulose and non-cellulosic substances [1, 6]. The matrix decomposition occurs on the main steps: the first one occurs at the temperature range of 200–350 °C due to volatilization of epoxy by random chain scission and intermolecular transfer demanding tertiary hydrogen extractions from the polymer [13]. The second decomposition is the degradation of the residue formed after degradation takes place at higher temperatures. The composite is less stable than the matrix epoxy and their decomposition occur on three steps: the first decomposition is due to water release, the second decomposition in due to decomposition of the jute fibers and the volatilization of the matrix epoxy [14, 7]. The last decomposition is due to the degradation non-cellulosic substances and the residue of the polymer degradation. The DTA curves confirm the degradation occurred during the decomposition of the materials used in this study (Fig. 4 (b)).

3.2 Tensile Properties of Jute Fabric

The tensile stress-strain curves of the jute fabric are presented in the figure (Fig. 5 (a)). The results show a dispersion of the mechanical properties due to the natural composition of the jute fibres, the jute yarns which are constituted of continuous and discontinuous fibres and number of the fibres in each jute fabric. The figure (Fig. 5 (b)) show the typical tensile stress-strain curve. The curve can be divided into four zones: the first zone (Z1) is due to the alignment of the jute yarns and the fibres lose their twisted. The second zone (Z2) is the elastic zone used on the determination of the Yong modulus. This aligned zone is followed by a third zone (Z3) which is characterised by non-alignment of the

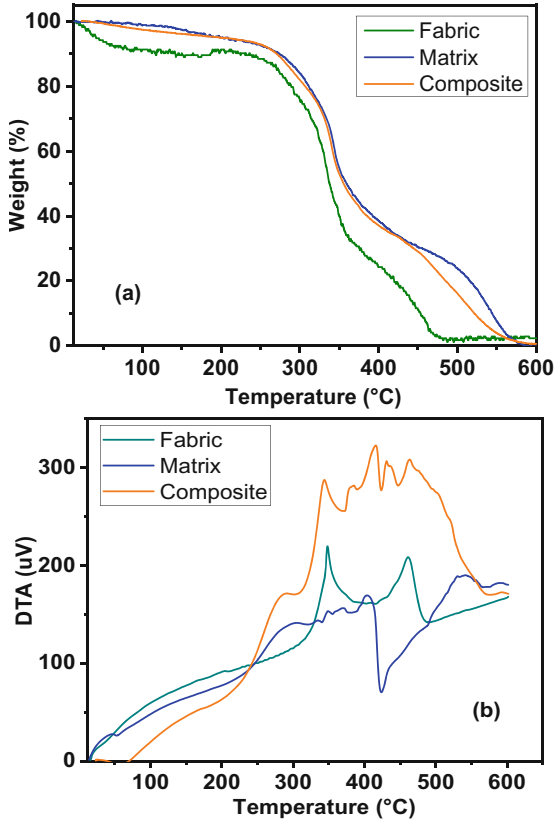


Fig. 4. TGA (a) and DTA (b) curves of jute fabric, epoxy matrix and composite jute/epoxy.

curve and damage of the fibres. The last zone (Z4) where occur a gradual drop of tensile stress until the total rupture of the jute fabric specimens [15]. The table (Table 1) plot the mechanical properties average of ten specimens of the jute fabric [7].

3.3 Tensile Properties of Composite

The heat treatment effect on the mechanical properties of the composite jute fabric/epoxy is evaluated in this study. The stress-strain curves of the composite jute fabric/epoxy at ambient temperature which are used to determine the mechanical properties are presented in figure (Fig. 6 (a)). The figure (Fig. 6 (b)) plots the effect of heat treatment on the tensile strength of the composite. The results show that the tensile strength of the composite is less than that of the pure matrix due to several factors: the tensile strength of the fabric is less compared of that of the matrix, the adhesion between the matrix and the jute fabric and the cavity content on the composite. The tensile strength of the composite reduces with the increase of the heated temperature due to the softening of the matrix. The module of elasticity decreases with the increase of temperature due to the composite deformation caused by the softening of the matrix and the loads are transferred by jute

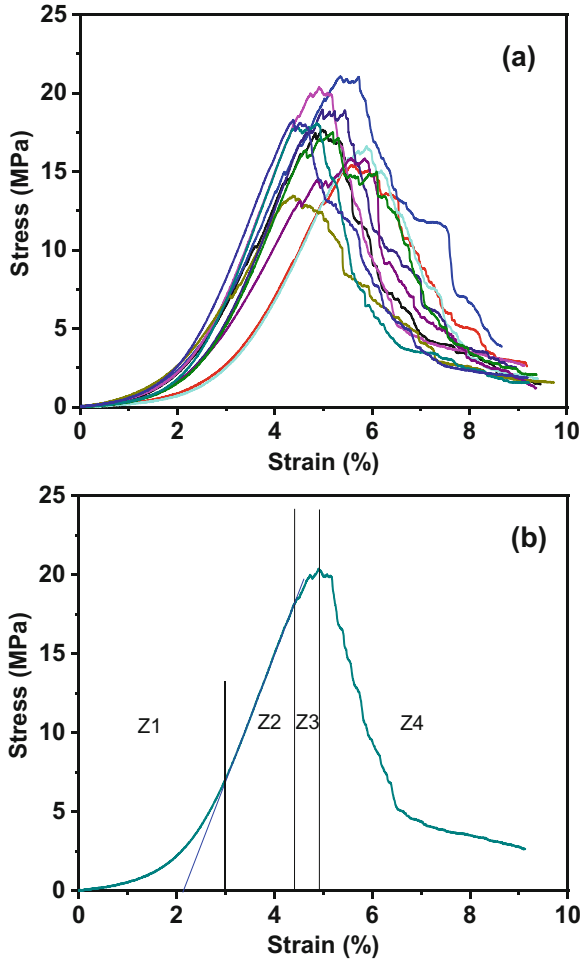


Fig. 5. (a) Stress-strain curves of ten specimens and (b) typical experimental curve stress-strain of jute fabric.

Table 1. The average mechanical properties of ten jute fabric specimens.

Tensile Stress (MPa)	Modulus of elasticity (GPa)	Tensile Strain (%)
17.98 ± 1.8	0.72 ± 0.089	5.16 ± 0.439

fabric which have a module of elasticity less than that of the pure matrix (Fig. 6 (c)). The tensile strain increases with the increases of the temperature due to the ability of deformation of the composite caused by softening of the matrix (Fig. 6 (d)).

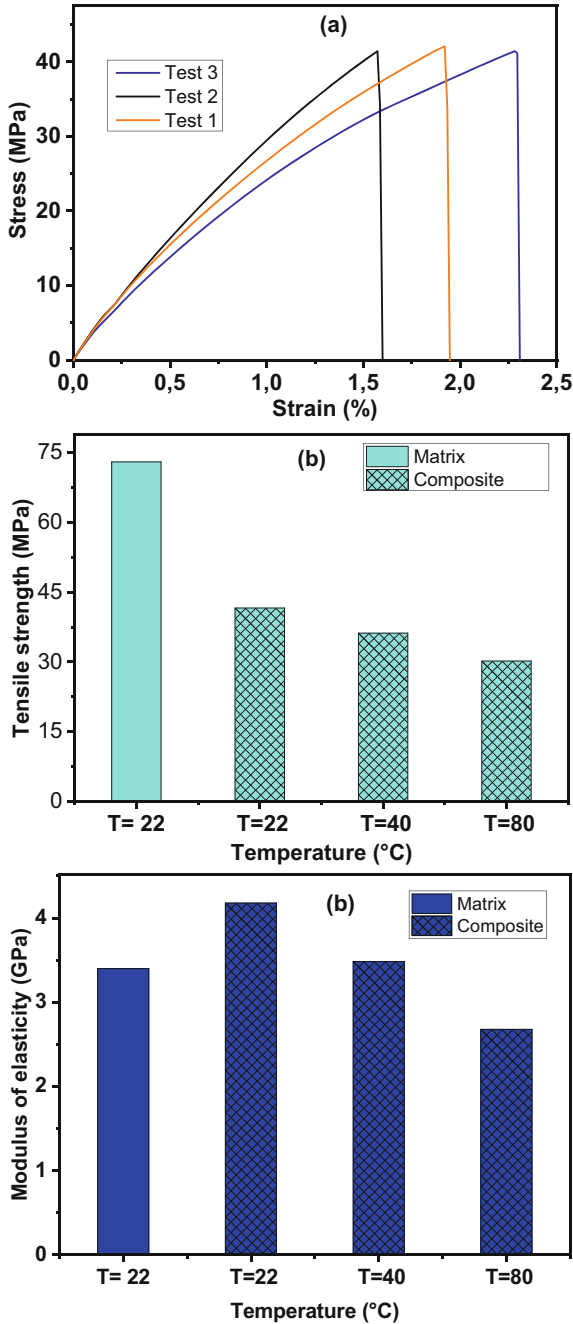


Fig. 6. (a) Stress-Strain curves of composite at temperature 22 °C; (b) tensile stress, (c) modulus of elasticity and (d) tensile strain of the composite as function of the temperature.

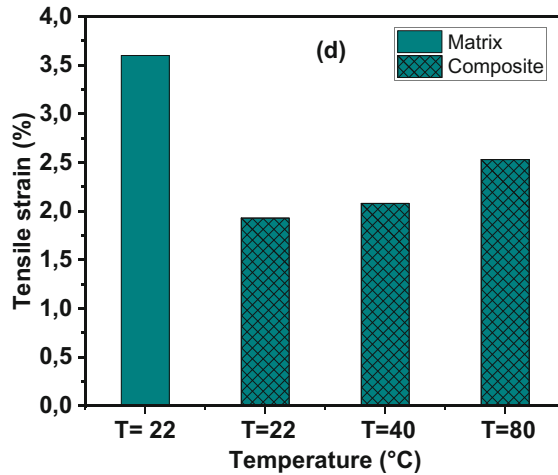


Fig. 6. (continued)

4 Conclusion

The effect of the heat treatment on the mechanical properties and thermal stability of matrix epoxy and jute fabric/epoxy composite were investigated and the conclusion drawn are the tensile strength and modulus of the elasticity reduce with the increase of the heated treatment temperature of the composite, whereas the tensile strain decreases with increase of the temperature. This explained by the softening of the matrix epoxy. Furthermore, to benefit of the mechanical properties of the composite the most possible their use must be at the low temperature.


References

1. Ben Smail, Y., El Moumen, A., Imad, F. Lmai, A., Elminor, H.: *Mater. Today Proc.* (Elsevier BV, 2020), pp. 3827–3833 (2020)
2. Franco-Urquiza, E.A., Escamilla, Y.R., Llanas, P.I.A.: *Polymers* (Basel). 13 (2021)
3. Komuriah, A., Kumar, N.S., Prasad, B.D.: *Mech. Compos. Mater.* **50**, 359 (2014)
4. Naveen Reddy, C., Rajeswari, C., Malyadri, T., Sai Hari, S.N.S.: *Mater. Today Proc.* **45**, 3307 (2021)
5. Mohanty, A.K., Khan, M.A., Hinrichsen, G.: *Compos. Sci. Technol.* **60**, 1115 (2000)
6. Ben Smail, Y., El Moumen, A., Imad, F. Lmai, A., Elminor, H.: *Mater. Today Proc.* **30**, 860 (2020)
7. Ben Smail, Y., El Moumen, A., Imad, F. Lmai, A., Ezahri, M.: *J. Compos. Mater.* 002199832199910 (2021)
8. Ozkur, S., Leskovšek, M., Golja, B., Demsar, A., Sezgin, H., Yalcin-Enis, I.: *Fibers Polym.* **22**, 3414 (2021)
9. Bhattacharyya, D., Baheti, V.: *Mater. Chem. Phys.* **296**, 127258 (2023)
10. Singh, S., Agarwal, C., Panwar, N.L., Upadhyay, V.: *J. Nat. Fibers* **20**, (2023)
11. Patnaik, P.K., Mishra, S.K., Swain, P.T.R., Sameer, Panda, D.: *J. Inst. Eng. Ser. E* **103**, 65 (2022)

12. Mennani, M., et al.: *Int. J. Biol. Macromol.* **221**, 149 (2022)
13. Selvaraj, M., Chapagain, P., Mylsamy, B.: *J. Nat. Fibers* **20** (2023)
14. Gupta, M.K.: *Proc. Inst. Mech. Eng. Part L J. Mater. Des. Appl.* **232**, 743 (2018)
15. Saaidia, A., Bezazi, A., Belbah, A., Bouchelaghem, H., Scarpa, F., Amirouche, S.: *Meas. J. Int. Meas. Confed.* **111**, 284 (2017)



Two and Three-Dimensional Computation of Dispersion Curves of Ultrasonic Guided Waves in Isotropic Plates by the Spectral Collocation Method

Moussa Mekkaoui¹✉, Salah Nissabouri² , and Hassan Rhimini¹

¹ Laboratory of Mechanics, Engineering and Innovation, National School of Electricity and Mechanics, Hassan II University, Casablanca, Morocco

{moussa.mekkaoui, h.rhimini}@ensem.ac.ma

² Laboratory M2S2I, ENSET, Mohammedia, Hassan II University, Casablanca, Morocco

salah.nissabouri@univh2c.ma.com

Abstract. The field of non-destructive evaluations (NDE) using ultrasonic waves is widely used in industry to guarantee the safety and proper functioning of materials. Thus, mastering the dispersion curves of propagation waves in a material is an essential first step. This paper presents a numerical approach used for plotting the dispersion curves of cross-section ultrasonic guided waves. The spectral collocation method (SCM) described here can turn the set of partial differential equations for sound waves into an eigenvalue problem. In order to evaluate the efficiency of this method for an isotropic aluminum plate, we have established algorithm executed with Matlab program. The results were compared with a classical bisection zero-finding method, the stiffness matrix method, and SAFE method. The results found confirm that the SCM remains conceptually simpler and depends on the differentiation matrices used. Finally, the method proves its accuracy, its calculation speed and its capacity to compute the phase velocity and wavenumber curves as well as the complete three-dimensional dispersion spectrum which includes both propagative (real wavenumber) and non-propagative modes (complex wave number).

Keywords: Dispersion curves · Spectral Collocation Method · Lamb waves · Guided waves

1 Introduction

Lamb waves propagating in solid materials were first described by Horace Lamb [1]. They are part of waves found in thin plates and shell structures without traction with the characteristic of being guided by the boundaries. This type of wave is widely used in industry for the non-destructive evaluation (NDE) of finite-dimensional solids. They make it possible to detect damage inside or on both surfaces of the plates.

According to Auld's classification [2], two types of Lamb modes solutions are distinguished: propagatif modes with a real wave number which transport energy inside

the structure and propagate without attenuation, for this they are often most useful for NDT engineering applications. The second type is that modes with a complex or purely imaginary wave number, these modes are non-propagating.

Dispersion curves are an indispensable tool in NDT with Lamb waves. They allow us to know the current phase and its propagation speeds (phase and group speed) depending on the frequency of the wave generated and the thickness of the plate that one wants to inspect. Several previous researches have worked on dispersion curves and their several applications in NDT. In this context, several techniques for plotting dispersion curves have been proposed. Among these methods we find: the bisection method [3], the Newton-Raphson method [4], the transfer matrix method [5], etc.

To properly study the behavior of Lamb waves, the FEM remains the most robust numerical tool available. But the major drawback of simulation with the FEM is that require a lot of computing time even with the current developed computing resources. These facts have prompted many researches to create and perfect other numerical methods. i.e. spectral element method [6], finite difference method [7], hybrid boundary element (HBE) method [8], wave finite element (WFE) method [9] and the semi-analytical finite element method (SAFE) [11]. The latter is also taken as a validation method in this paper. In the work of Barazanchy and Giurgiutiu, the performance and speed of the SAFE method have been demonstrated by comparison with Disperse software [12].

The first use of spectral methods was in fluid dynamics problem solving and was introduced by Kreiss and Olinger [13]. The spectral collocation method (SCM), [14], is used to solve elastic guided wave (GUW) problems. The principle of SCM consists in reducing the differential equations governing the GUWs to the ordinary differential equations on the thickness of the plate. Then, A discretization of the domain is carried out at a set of collocation points, thus, we obtain an approximation of the motion equations by an eigenvalue problem in matrix form. The method has the notable advantage of not missing any dispersion mode.

The purpose of this study is to evaluate the performance of the SCM in terms of accuracy and computational cost for plotting dispersion curves for an isotropic material. To verify the accuracy of the method, we compared the curves plotted with those plotted by the Dispersion Calculator software which uses the stiffness matrix method SMM [15] and with the SAFE method. We first present the theoretical formulation of the method for an arbitrary section waveguide, then, we discuss some parameters that need to be optimized to ensure accuracy.

2 SCM Formulation and Resolution of Motion's Equation for a Plate

2.1 Theoretical Model

The plate used in this paper is a homogeneous isotropic medium. The geometry of the plate and the system of axes are shown in Fig. 1. We consider a $2h$ thick plate with the z axis as a wave propagating direction.

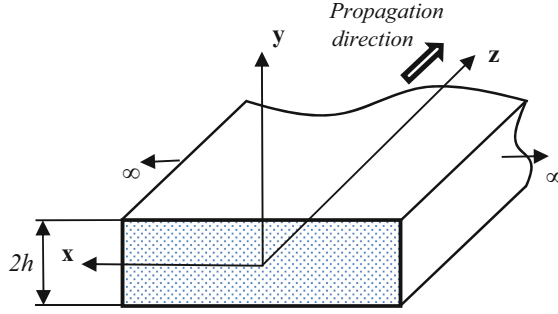


Fig. 1. Geometry of the plate. The free faces of the plate are placed at $y = +h$ and $y = -h$.

The Chebyshev interpolation using differentiation matrices described by Weideman and Reddy [16] is used here. The Chebyshev interpolation points are defined as:

$$y = \cos\left(\frac{(j-1)\pi}{N-1}\right), j = 1, \dots, N. \quad (1)$$

2.2 Equation of Motion

A detailed description of the SCM can be found in [17]. The motion's equations for a homogeneous anisotropic medium with linear elastic behavior are:

$$C_{ijkl}u_{k,jl} = -\rho\omega^2u_i \quad (2)$$

C_{ijkl} is the stiffness tensor of the plate [4], and u_i are the components of the vector of displacement.

$$u_j = U_j(y)e^{i(kz-\omega t)}, j = x, y, z, \quad (3)$$

With k is the wave number, ω is the angular frequency, and i is the imaginary unit ($i^2 = -1$).

As shown in Fig. 1, the faces of the plate are located at $y = \pm h$, and the plate is free in stress on both sides, the boundary conditions (BC) are expressed as:

$$\sigma_{yy}(\pm h) = \sigma_{yx}(\pm h) = \sigma_{yz}(\pm h) = 0. \quad (4)$$

The relationship between the stress tensor field and the strain tensor field is written as:

$$\sigma_{ij} = C_{ijkl} \varepsilon_{kl} \quad (5)$$

And the strain tensor field, ε_{ij} , is written as function of the displacement vector field, u_j , as:

$$\varepsilon_{ij} = \frac{1}{2} \left(\frac{\partial u_i}{\partial x_j} + \frac{\partial u_j}{\partial x_i} \right) \quad (6)$$

As a result, we end up with a system of three equations of motion and six equations for the boundary conditions. With this method we approximate the differential operators defined in y by Chebyshev differentiation matrices (DM).

$$\frac{\partial^n}{\partial y^n} \rightarrow D^n = [DM]_{N \times N}^n. \quad (7)$$

The order of derivation is noted n .

Each of Eq. (2) can be represented in matrix form and for the first component of displacement U_x , the motion' equation can be written as follow:

$$A_{N \times N} U_x + B_{N \times N} U_y + C_{N \times N} U_z = -\rho \omega^2 U_x. \quad (8)$$

The $N \times N$ matrices $A_{N \times N}$, $B_{N \times N}$ and $C_{N \times N}$ are defined as:

$$A_{N \times N} = C_{55} D^{(2)} - C_{11} k^2 I + 2C_{15} k i D^{(1)}$$

$$B_{N \times N} = C_{45} D^{(2)} - C_{16} k^2 I + C_{14} + C_{56} k i D^{(1)}$$

$$C_{N \times N} = C_{35} D^{(2)} - C_{15} k^2 I + C_{13} + C_{55} k i D^{(1)}$$

With I the identity matrix and C_{KL} the elastic stiffness constants.

The same approach is followed for a matrix representation of the other components of the vector field of displacement. Thus, the system of equations can be rewritten as an eigenvalue problem where the unknowns are the vectors U_j :

$$\begin{bmatrix} A & B & C \\ D & E & F \\ G & H & I \end{bmatrix}_{3N \times 3N} \begin{Bmatrix} U_x \\ U_y \\ U_z \end{Bmatrix}_{3N \times 1} = \omega^2 \begin{bmatrix} -\rho I & 0 & 0 \\ 0 & -\rho I & 0 \\ 0 & 0 & -\rho I \end{bmatrix} \begin{Bmatrix} U_x \\ U_y \\ U_z \end{Bmatrix}. \quad (9)$$

Or, in reduced form.

$$L(k)U = \omega^2 M U, \quad (10)$$

where U is the vector of displacement with three components: $[U_x, U_y, U_z]^T$.

Then, we proceed to a discretization of the six Eqs. (4) and a rearrangement of their terms, as in [17], so the boundary conditions can be represented in matrix notation:

$$S = \begin{bmatrix} S_1 & S_2 & S_3 \\ S_4 & S_5 & S_6 \\ S_7 & S_8 & S_9 \end{bmatrix} \begin{Bmatrix} U_x \\ U_y \\ U_z \end{Bmatrix}_{(\pm h)} = \begin{Bmatrix} 0 \\ 0 \\ 0 \end{Bmatrix}. \quad (11)$$

Before resolution, we introduce the boundary conditions to the system of Eq. (9), we replace the 1, N , $(N+1)$, $2N$, $(2N+1)$ and $3N$ rows of the matrix L with those of the matrix S of Eq. (11). These lines correspond, for each component of the field of displacement vectors U , to the points of the grid $y = \pm h$, i.e. lines 1 and N evaluate U_x on the top and bottom surfaces of the plate (at $y = h$ and $y = -h$), respectively, the rows $N+1$ and $2N$ go with U_y , and so on. The same rows modified in the matrix L are replaced in the matrix M with rows filled with zeros.

2.3 Eigenvalue Problem

A reorganization of the matrix Eq. (10) will lead to an eigenvalue problem in terms of the wavenumber k having the expression:

$$[P_2k^2 + P_1k + P_0\omega^2]U = 0 \quad (12)$$

The matrix on the left of Eq. (12) is not regular and admits infinite eigenvalues [18]. We use the Linear Companion Matrix Method [19] as a method of linearization, thus, the eigenvalue problem can be written as follow:

$$(A - kB)X = 0_{6N}. \quad (13)$$

where A ; B , and X are defined as:

$$A = \begin{bmatrix} P_1 & P_0 + M \\ I_{3N} & Z_{3N} \end{bmatrix}, B = \begin{bmatrix} -P_2 & Z_{3N} \\ Z_{3N} & I_{3N} \end{bmatrix}, X = \begin{Bmatrix} kU \\ U \end{Bmatrix}$$

The matrices $P_{(j)}$; ($j = 0, 1, 2,$) of size $3N \times 3N$ are formed from the DMs up to the second degree ($D^{(1)}, D^{(2)}$), the identity matrix I and the elastic stiffness constants C_{KL} .

To solve the noted problem of instability of the numerical results, we balanced the matrices A and B . The balancing is done by scaling the identity matrices located in the lower halves of A and B by a constant whose value is comparable to the entries in P_j and M .

Using this formulation, a complex wavenumbers $k = k_r + i k_i$ can be solved for by fixing real ω . So, we can study both propagative modes with real wavenumber and non-propagative modes with complex or purely imaginary wavenumber.

3 Results and Discussion

An example of isotropic plate is studied in this paper. The plate material is an aluminum with the characteristics cited in the Table 1 below:

Table 1. Characteristics of the studied plate.

Thickness	Young's modulus	Poisson's ratio	Mass density
1 mm	72.4 GPa	0.33	2770 kg/m ³

A Matlab programs are established based on SCM and SAFE methods to compute (k,f) dispersion curves. The separation between the symmetric modes (S) and the anti-symmetric modes (A) is performed by checking the displacement components obtained from the eigenvectors.

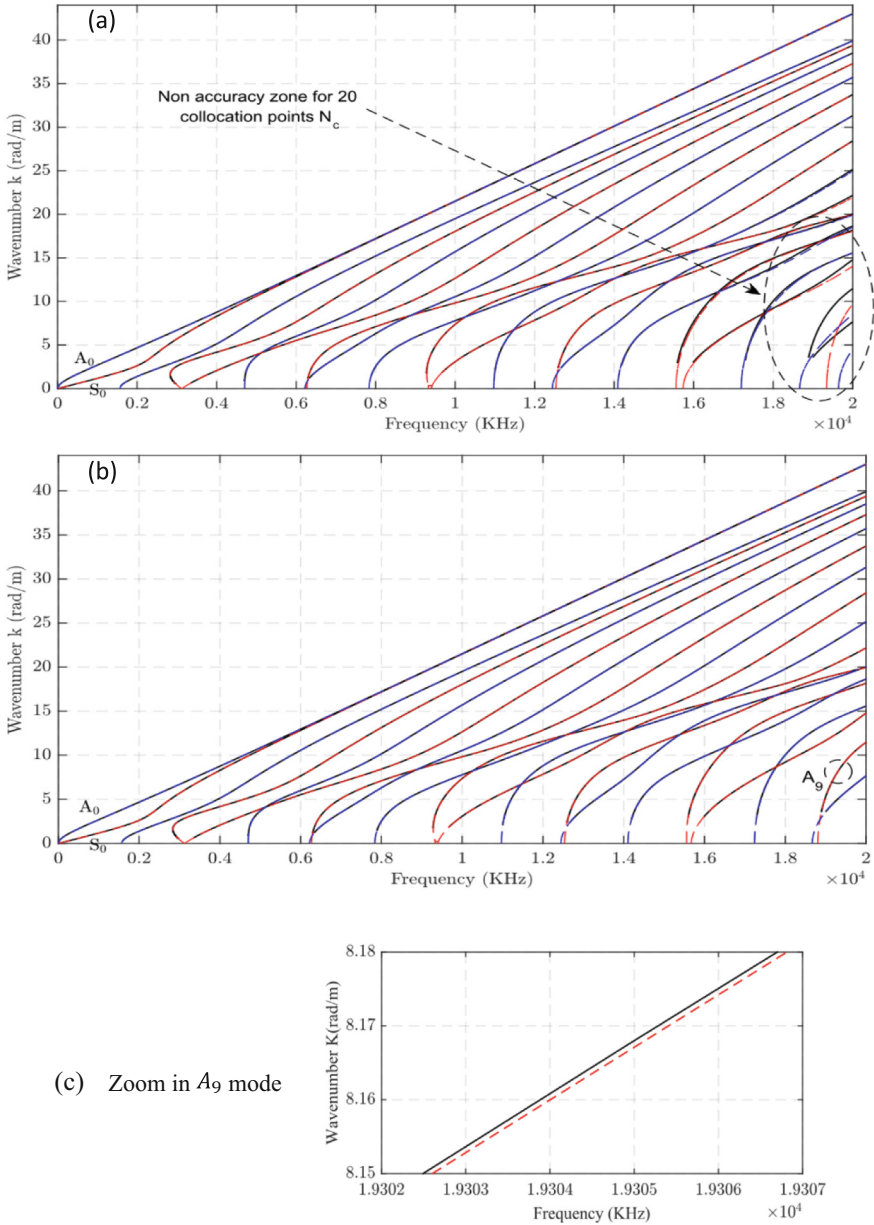


Fig. 2. Dispersion curves in the (f,k) plane plotted by SCM (dashed line) and by DC software (continuous line) according to the number of collocation points N_c : (a) $N_c = 20$; (b) $N_c = 30$; the symmetric modes (in red) and antisymmetric modes (in blue). (c) zoom in A_9 mode showing good accuracy after increasing N_c .

In works relating to the spectral method we define $N_c = 2m+10$ to obtain the necessary precision (see a detailed demonstration on convergence rates of Chebyshev series in Gottlieb and Orszag [20]), with m being the mode number. This condition is verified in the plotting of the wavenumber dispersion curve as a function of the frequency see Fig. 2. We note that the accuracy has improved from $N_c = 20$ to $N_c = 30$ for the first 10 modes, see Fig. 2(a) and Fig. 2(b), respectively.

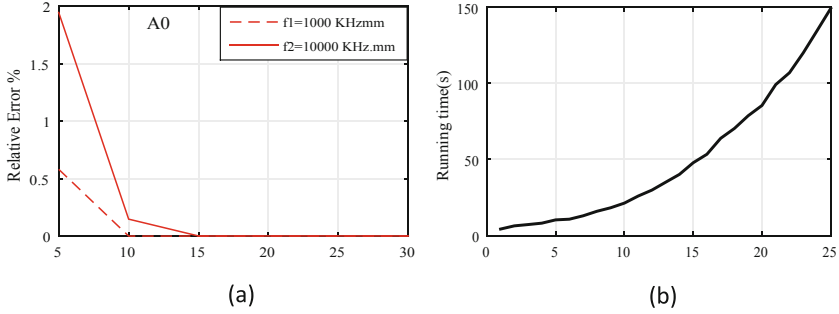


Fig. 3. (a) Evolution of relative error of A0 mode computed with SCM, with Bisection method as reference for a given two frequencies $f_1 < f_2$. (b) Running time using SCM in function of the number of collocation points (N_c).

Figure 3 (a) shows that is a positive correlation between the frequency and the relative error. For a given number of collocation points (N_c), when the frequency increases the error does as well.

Figure 3 (b) shows the variation in running time using a computer with a processor of 2 GHz and a memory (RAM) of 4 Go. The stepwise increment in the wavenumber k is set as 0.25. we note that the evolution of the computation time as function of N_c is of cubic form.

The dispersion curve representing the wavenumber-frequency dependence computed with the SCM are shown in Fig. 4 (a) and have been found to present very good concordance with those in Fig. 4 (b) computed with the SAFE method. On one hand, in Fig. 4 (a), junction points 1,2,3,4 show frequency-thickness products for which the modes change in nature and become propagative, non-propagative, or attenuated. On the other hand, in Fig. 4 (b), the SH modes are included and the purely imaginary modes too (non-propagating highly attenuated modes).

Very good accuracy observed at low frequencies for the non-propagative modes which remain confined in their excitation zone (Fig. 5).

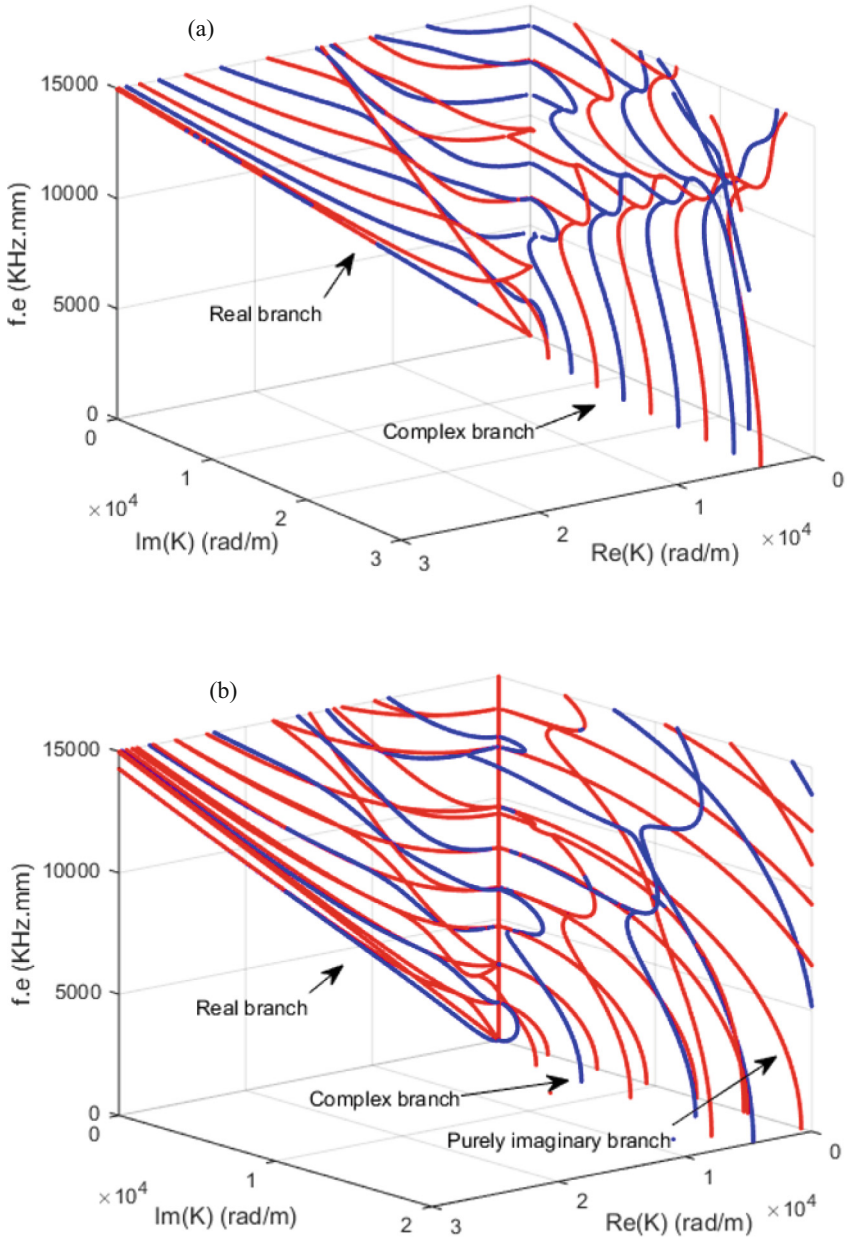


Fig. 4. 3D-dispersion curves in the complex domain: (a) Lamb modes plotted using the SCM. (b) Lamb and SH modes plotted using SAFE, corresponding to the symmetric (in red) and antisymmetric (in blue).

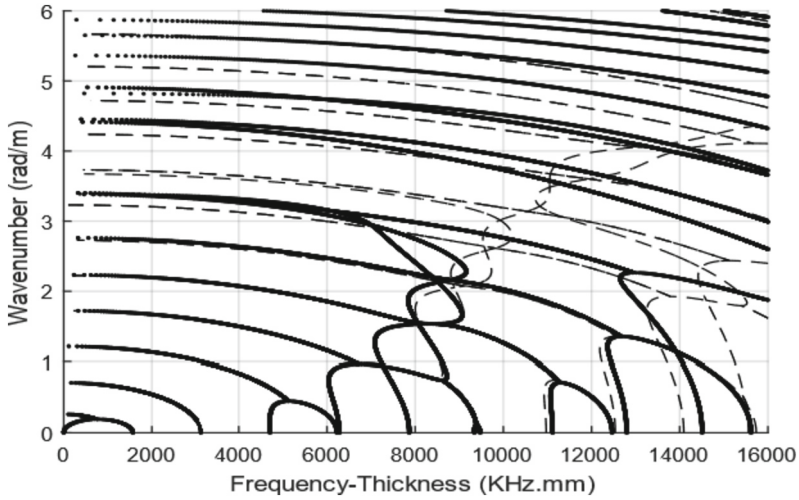


Fig. 5. Wavenumber curve of non-propagative Lamb modes: SCM (dashed lines) and SAFE (solid lines).

4 Conclusion

For the purpose of evaluating the performance of the SCM in plotting dispersion curves for an isotropic aluminum plate, an algorithm is established based on the theoretical formulation presented at the beginning of this paper. The results were compared with two numerical methods based on SMM and SAFE method.

The SCM remains conceptually simpler, no need to handle special functions such as interpolation functions, easy in programming and has a high convergence rate by increasing the number of collocation points.

The results found illustrate the significant capability of the method to compute all the modes without missing any and without parasitic modes, unlike zero-finding and SMM methods which require processing in the choice of the frequency-thickness step.

The ability of SCM to find complete real and complex solutions for dispersion curves has been confirmed here. The plots include real, complex, and purely imaginary wavenumbers.









References

1. Lamb, H.: On waves in an elastic plate. In: Proceedings of Royal Society, vol. 93, pp. 114–128. Ser A, London (1917)
2. Auld, B.A.: Acoustic Fields and Waves in Solids, 2nd edn. Krieger Publishing Company, Florida (1990)
3. Nissabouri, S., Mekkaoui, M., Rhimini, H., El Allami, M., Zamma, A.: Semi-analytical finite element method for calculating dispersion curves of a CFRP plate. In: MATEC Web of Conferences 2022, EDP Sciences, vol. 360, p. 00010. (2022)

4. Ndiaye, E.B., Duflo, H.: Non destructive testing of sandwich composites: adhesion defects evaluation; experimental and finite element method simulation comparison. *Acoustics 2012 Nantes, Nantes, France*, pp. 2659–2664 (2012)
5. Nayfeh, A.: The general problem of elastic wave propagation in multilayered anisotropic media. *J. Acoust. Soc. Am.* **89**(4), 1521–1531 (1991)
6. Mahapatra, D.R., Gopalakrishnan, S.: A spectral finite element model for analysis of axial flexural shear coupled wave propagation in laminated composite beams. *Compos. Struct.* **59**, 67–88 (2003)
7. Balasubramanyam, R., Quinney, D., Challis, R.E., Todd, C.P.D.: A finite difference simulation of ultrasonic lamb waves in metal sheets with experimental verification. *J. Phys. D Appl. Phys.* **29**, 147–155 (1996)
8. Cho, Y., Rose, J.L.: A boundary element solution for a mode conversion study on the edge reflection of lamb waves. *J. Acoust. Soc. Am.* **99**(4), 2097–2109 (1996)
9. Koreck, J.: Computational characterization of adhesive bond properties using guided waves in bonded plates. Master's thesis, Georgia Institute of Technology (2006)
10. Nissabouri, S., El Allami, M., Hassan Boutyour, E.: Quantitative evaluation of semi-analytical finite element method for modeling Lamb waves in orthotropic plates. *C. R.-Mec.* (5), 335–350 (2020)
11. Waas, G.: Analysis report for footing vibrations through layered media. PhD Thesis, University of California (1972)
12. Barazanchy, D., Giurgiutiu, V.: A comparative convergence and accuracy study of composite guided-ultrasonic wave solution methods: comparing the unified analytic method, safe method and disperse. *Proc. Inst. Mech. Eng., Part C. J. Mech. Eng. Sci.* **231**(16), 2961–2973 (2017)
13. Kreiss, H.O., Olinger, J.: Comparison of accurate methods for the integration of hyperbolic equations. *Tellus*, pp. 24–199 (1972)
14. Adamou, A.T.I., Craster, R.V.: Spectral methods for modelling guided waves in elastic media. *J. Acoust. Soc. Am.* **116**(3), 1524–1535 (2004)
15. Dispersion Calculator v.2.3.1, https://www.dlr.de/bt/en/desktopdefault.aspx/tabid-2478/11208_read-53373/. Accessed 11 Jan 2023
16. Weideman, J., Reddy, S.C., A. C.: A MATLAB differentiation matrix suite. *ACM Trans. Math. Softw.* **26**, 465–519 (2000)
17. Zitouni, I., Rhimini, H., Chouaf, A.: Modeling the propagation of ultrasonic guided waves in a composite plate by the spectral method. In: 2nd international conference on Mechanics, Materials, and Energy (MME), pp. 15–17, El Jadida, Morocco (2022)
18. Lancaster, P.: *Theory of Matrices*. Academic Press, New York (1969)
19. Quintanilla, F.H., Lowe, M.J.S., Craster, R.V.: Modeling guided elastic waves in generally anisotropic media using a spectral collocation method. *J. Acoust. Soc. Am.* **137**(3), 1180–1194 (2015)
20. Gottlieb, D., Orszag, S.A.: *Numerical Analysis of Spectral Methods: Theory and Applications*. Society for Industrial and Applied Mathematics, Philadelphia (1977)



Numerical Analysis of Mixed Convection Coupled with Thermal Radiation in a Ventilated Channel Containing Various Heat-Generating Blocks

Rachid Hidki , Lahcen El Moutaouakil , Mohammed Boukendil   ,
Zouhair Charqui , Zaki Zrikem , and Abdelhalim Abdelbaki 

LMFE, Department of Physics, Faculty of Sciences Semailia, Cadi Ayyad University, B.P. 2390,
Marrakesh, Morocco
m.boukendil@uca.ac.ma

Abstract. In this study, thermal radiation and mixed convection in a ventilated horizontal channel are analyzed. The channel contains five cylindrical blocks that produce different volumetric heat rates. The channel is ventilated by two openings; the inlet is located on the left wall, and the outflow is on the top one. All the channel walls are adiabatic, except for the upper wall, which is held at a constant low temperature of $T_C = 20^\circ\text{C}$. To numerically solve the differential equations governing the current problem, a numerical code based on the finite volume approach and the SIMPLE algorithm is utilized. The discrete ordinate method is used to discretize the radiative transfer equation. The impacts of the Reynolds number and the emissivity of the surfaces on the heat transfer and fluid flow are analyzed. The numerical simulations indicate that increasing the Reynolds number or the emissivity considerably decreases the maximum temperature in the cavity and improves the performance of the considered system.

Keywords: Mixed convection · Ventilated channel · Finite volume method · Numerical simulation · Heat sources

Nomenclature

d	cylinders diameter, m
D	cylinders diameter $D = d/H$
g	gravitational acceleration, ms^{-2}
h^*	openings size $h^* = h/H$
h	openings size, m
H	cavity's height, m
i	radiation intensity, Wm^{-2}
I	dimensionless intensity
k	thermal conductivity, $\text{Wm}^{-1}\text{K}^{-1}$
K	conductivity ratio $K = k_s/k_f$
L	cavity's length, m
Nu	Nusselt number

Pr	Prandtl number
Pl	Planck number
P	dimensionless pressure
Q	internal heat generation, Wm^{-3}
Ri	Richardson number
Re	Reynolds number
Ra	Rayleigh number
T_R	temperature ratio
T	dimensional temperature, $^{\circ}\text{C}$
t	time, s
U, V	velocity components
X, Y	Cartesian coordinates

Greek symbols

σ	Stefan-Boltzmann constant, $\text{Wm}^{-2}\text{K}^{-4}$
α	thermal diffusivity, m^2s^{-1}
β	thermal expansion coefficient, K^{-1}
ε	emissivity of radiative surface
ω	scattering albedo
ϕ	phase function
θ	dimensionless temperature
ν	kinematic viscosity, m^2s^{-1}
Ω	solid angle, sr
λ	heat generation parameter
ρ	density, kgm^{-3}
τ	dimensionless time
μ, η	direction cosines
τ^*	optical thickness
ψ	dimensionless stream function

Subscripts

C	convective term, cell, or cold wall
f	fluid
i	block index
in	inlet
LR	local radiative
LC	local convective
max	maximum
R	radiative
s	solid (blocks)
T	total

Abbreviations

B	block
---	-------

1 Introduction

The miniaturization of modern electronic devices has resulted in a reduction of physical space available for the components, leading to a rise in power density. Since electronic components are temperature-sensitive and can be damaged or perform poorly if their temperature falls outside the nominal operating range. Therefore, thermal dissipation has become a critical aspect of their operation. However, implementing cooling systems in compact electronic systems is often challenging, mainly when the components generate different amounts of heat or are not uniformly distributed in electronic packaging. To ensure effective cooling in these systems, it is necessary to employ convection in its three forms (forced, mixed, and natural) in conjunction with thermal radiation. Researchers are actively pursuing new cooling system designs (usually simulated using cavities containing heating bodies) that offer a balance of compactness, high performance, and cost-effectiveness [1–5].

Mixed convection (MC) occurs as a result of a combination of both free and forced convection, where the flow is impacted by both a non-uniform density distribution of the fluid and an external forcing system. Numerous numerical studies have investigated MC in cavities that contain isothermal blocks. One such study conducted by Chamkha et al. [6], analyzed two-dimensional MC surrounding an isothermal square body placed at the center of a vented air-filled cavity. The cavity's right wall is fixed at a low temperature, while the remaining walls are kept adiabatic. The study assessed the impact of various factors such as the Richardson number, Reynolds number, outlet position, position, and aspect ratio of the block on the thermal fields and flow patterns. The findings indicated that the heat transfer was optimal when the outflow was positioned at the top of the right wall. In their research, Javadzadegan et al. [7] investigated the MC heat transfer and fluid flow inside a ventilated cavity containing a hot elliptical obstacle maintained at a constant temperature. The study's main objective was to examine the impact of using a porous medium on the velocity and thermal fields.

In comparison to an isothermal block, a heat-generating block (HGB) offers a more accurate portrayal of an electrical component. A numerical investigation was carried out by Ahammad et al. [8] to examine the impact of various factors, such as the Richardson number, the solid/fluid thermal conductivity ratio, and the diameter of the HGB, on a magnetohydrodynamic MC problem in a vented cavity. The study found that a smaller block size and a lower thermal conductivity ratio improved heat transfer in the system. Ahammad et al. [9] revisited the same configuration to investigate the impact of the Reynolds, Hartmann, and Prandtl numbers on the flow and thermal fields. It was observed that these parameters have a considerable impact on both the thermal and flow fields. MC in cavities containing simple heat-conducting bodies (obstacles) has been studied in the references [10–12].

MC in channels is usually used as a methodology for designing and optimizing cooling systems for electronic equipment. Pirouz et al. [13] numerically examined the MC in a horizontal channel with upper and lower bodies mounted on the horizontal walls and receiving uniform heat flux through their base. Ghaneifar et al. [14] investigated numerically the MC of a nanofluid in an insulated horizontal channel containing two central HGBs. Hamouche and Bessaïh [15] considered a 2D channel with two identical heaters on the bottom wall. The same problem was considered by Boutina and Bessaïh [16] with

an inclined channel. Hssain et al. [17] studied numerically steady MC of a nanofluid in a horizontal channel with isothermal blocks to simulate extremely heat-conductive electronic components. All these studies are agreed with the effect of ventilation (Re effect) on the behavior of the considered system.

It is important to remember that thermal radiation (TR) is necessary for cooling electronic components [18]. Numerous studies have been conducted on the coupling of natural convection (NC) and TR in closed cavities containing heating blocks of various geometrical shapes, including rectangular [19], circular [20], and square [21, 22]. These investigations reveal that TR improves total heat exchange, enabling more effective cooling of the investigated heat sources. Mandal et al. [23] and Peiravi and Alinejad [24] examine the convective heat transfer and TR in a channel with blocks. Mandal et al. [23] investigated MC with TR in a channel containing discrete heat sources on the bottom wall. Their results show that the TR interaction between the surfaces decreases with an increase in the Reynolds number. Peiravi and Alinejad [24] evaluated the combined effects of TR and MC on heat transfer between a channel's working fluid and a square solid. The results reveal that when the radiation parameter rises, the heat transfer rate decreases.

The above literature review suggests that insufficient focus has been given to TR exchange, especially when heat-generating blocks are present in channels and cavities. This study aims to demonstrate the significance of MC and TR for cooling multiple HGBs located in a horizontal channel. This research is motivated by the search for cost-effective cooling systems for high-performance computers that are both compact and powerful. The findings are displayed in terms of isotherms, streamlines, maximum temperature profiles, and those of the Nusselt number.

2 Mathematical Model and Validation

2.1 Problem Description

Figure 1 presents a schematic representation of an open cavity, highlighting its various parameters. The air-filled rectangular cavity, with dimensions of $L = 3H = 15$ cm, contains five HGBs, representing different electronic components. The positions of the HGBs are at $X_i = 0.5i$ and $Y_i = 0.5$ with $1 \leq i \leq 5$. The blocks having the same thermal conductivity (k_S) and diameter (d), and generate heat at varying rates, with $Q_i = \lambda_i \times Q = 1720 \times \lambda_i$, where $\lambda_i = 2^{3-i}$ is the internal heat generation parameter. All the cavity walls are kept adiabatic except the upper one, which is kept at the same temperature as the air inlet $T_C = T_{in} = 20^\circ\text{C}$. The inlet and outlet are placed, respectively, on the left wall and the top wall, with equal sizes $h = h^* \times H$. The fluid enters the cavity with a velocity of u_{in} . Simulations were also carried out for $h^* = 0$, which represents a closed cavity, to show that combining TR and MC instead of NC may significantly enhance the total heat transfer.

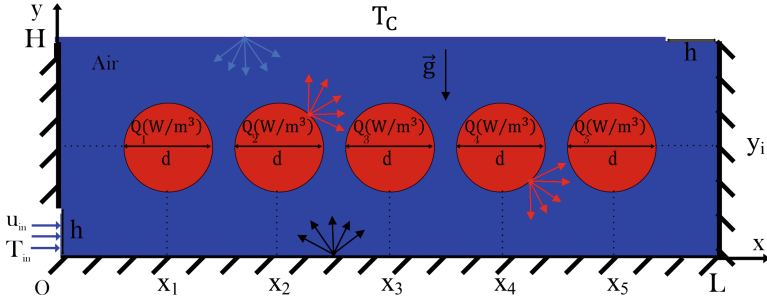


Fig. 1. Schematic configuration

2.2 Mathematical Model

The flow under examination is assumed to be two-dimensional, laminar, Newtonian, and incompressible. Except for the density in the buoyancy component, which is addressed using the Boussinesq approximation, the thermophysical characteristics of the air are maintained constant. These assumptions permit the formulation of governing equations, which are expressed in dimensionless form, including the conservation of mass, momentum, energy, and the radiative transfer equation (RTE).

$$\frac{\partial U}{\partial X} + \frac{\partial V}{\partial Y} = 0 \quad (1)$$

$$\frac{\partial U}{\partial \tau} + U \frac{\partial U}{\partial X} + V \frac{\partial U}{\partial Y} = -\frac{\partial P}{\partial X} + \text{Pr} \left(\frac{\partial^2 U}{\partial X^2} + \frac{\partial^2 U}{\partial Y^2} \right) \quad (2)$$

$$\frac{\partial V}{\partial \tau} + U \frac{\partial V}{\partial X} + V \frac{\partial V}{\partial Y} = -\frac{\partial P}{\partial Y} + \text{Pr} \left(\frac{\partial^2 V}{\partial X^2} + \frac{\partial^2 V}{\partial Y^2} \right) + \text{RaPr}\theta \quad (3)$$

$$\frac{\partial \theta}{\partial \tau} + U \frac{\partial \theta}{\partial X} + V \frac{\partial \theta}{\partial Y} = \left(\frac{\partial^2 \theta}{\partial X^2} + \frac{\partial^2 \theta}{\partial Y^2} \right) - \frac{\tau^*}{\text{Pl}} \left[4 \left(\frac{\theta}{T_R} + 1 \right)^4 - \int_0^{4\pi} I_R d\Omega \right] \quad (4)$$

$$\frac{\partial \theta}{\partial \tau} = K \left(\frac{\partial^2 \theta}{\partial X^2} + \frac{\partial^2 \theta}{\partial Y^2} \right) + \lambda_i \quad (5)$$

$$\mu \frac{\partial I_R}{\partial X} + \eta \frac{\partial I_R}{\partial Y} + \tau^* I_R = \frac{\tau^*}{4\pi} \left[\omega \int_0^{4\pi} I_R \phi d\Omega' + (1 - \epsilon) I_{Rb} \right] \quad (6)$$

Table 1 summarizes the boundary conditions utilized to solve these equations (Eqs. 1–6).

The non-dimensional parameters and variables that appear in Eqs. 1–6 are:

$$\tau = \frac{\alpha_f t}{H^2}, \quad (U, V) = \frac{(u, v)H}{\alpha_f}, \quad \Delta T = \frac{QH^2}{k_f}, \quad (X, Y) = \frac{(x, y)}{H}, \quad \theta = \frac{(T - T_C)}{\Delta T}, \quad I_R = \frac{i_R}{\sigma T_C^4} \quad (7)$$

$$\text{Pr} = \frac{\nu}{\alpha_f}, \quad \text{Re} = \frac{u_{in} L}{\nu}, \quad \text{Ra} = \frac{g\beta L^3 \Delta T}{\nu \alpha_f}, \quad \text{Pr} = \frac{\nu}{\alpha_f}, \quad K = \frac{k_s}{k_f}, \quad \text{Pl} = \frac{k_f \Delta T}{\sigma T_C^4 H}, \quad T_R = \frac{T_C}{\Delta T} \quad (8)$$

Table 1. Boundary conditions.

Inlet	Outlet	Solid walls
$\theta = 0$ $U = Re \times Pr$ $V = 0$	$\frac{\partial \theta}{\partial Y} = 0$ $\frac{\partial U}{\partial Y} = 0$ $\frac{\partial V}{\partial Y} = -\frac{\partial U}{\partial X}$	$\theta = 0$ at $Y = 1$ $U = V = 0$ $\frac{\partial \theta}{\partial n} = \pm \varepsilon \left(\frac{Q_{Rinc}}{PI} + I_{Rb} \right)$ at adiabatic walls $\frac{\partial \theta_f}{\partial n} = K \frac{\partial \theta_s}{\partial n} \pm \varepsilon \left(\frac{Q_{Rinc}}{PI} + I_{Rb} \right)$ and $\theta_f = \theta_s$ at the fluid-cylinder interface

$I_{Rb} = 4 \left(\frac{\theta}{T_R} + 1 \right)^4$ and ϕ correspond, respectively, to the non-dimensional emission and phase function of the blackbody. (μ, η) are the directional cosines and (ω, τ^*) denote, respectively, the scattering albedo and optical thickness. These latter are set to zero in this study.

The following equation gives the local and mean heat transfer by convection and radiation on the upper wall.

$$\begin{aligned}
 Nu_{LC}(X) &= - \left. \frac{\partial \theta}{\partial Y} \right|_{Y=1}, \quad Nu_{LR}(X) = \left. \frac{Q_R(X)}{PI} \right|_{Y=1}, \\
 Nu_{C \text{ or } R} &= \frac{1}{3 - h^*} \int_0^{3-h^*} Nu_{LC \text{ or } LR}(X) dX \quad \text{and} \quad Nu_T = Nu_R + Nu_{R'}
 \end{aligned} \tag{9}$$

2.3 Numerical Approach

The Finite Volume Method (FVM) is employed to discretize the previous equations and boundary conditions. The RTE is integrated using the Discrete Ordinate Method (DOM). A computer program written in FORTRAN is then used to solve the resulting system of equations. The solution is acceptable only if the following condition is satisfied on all variables: $\max \left| \left(\frac{\phi_{i,j}^{new} - \phi_{i,j}^{old}}{\phi_{i,j}^{old}} \right) \right| \leq 10^{-5}$, where ϕ represents a given dependence of the variables (ψ, θ) , and i, j are the coordinates of space. A mesh test was done on the accuracy of the results and the computation time, it was found that the mesh 250×80 gives good results.

To verify its accuracy, the numerical code underwent thorough testing using benchmark problems. The numerical results of Habchi and Acharya [25] in a horizontal channel that include a hot block fixed to the bottom wall were considered. The comparison of velocity obtained before and after the block (Fig. 2) shows a satisfactory matching. More validation of the numerical code with other previous studies can be found in the references [4, 5, 26, 27].

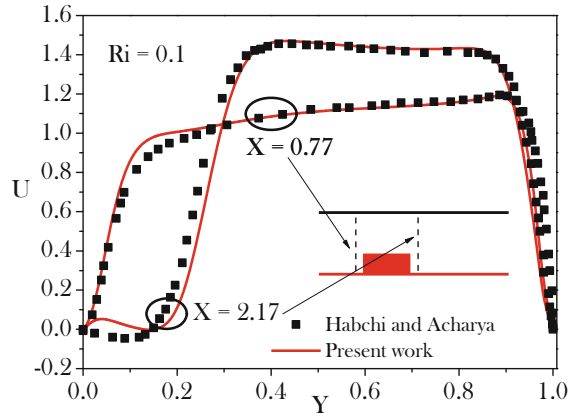


Fig. 2. Comparison of velocity profiles with Habchi and Acharya [25].

3 Results and Discussion

The effect of TR on MC cooling of electronic components simulated by HGBs in a ventilated rectangular channel is demonstrated in this section. The flow structure and thermal field are investigated for various Reynolds number and emissivity. The parameters Ra , D , K , and Pr are set to 2×10^6 , 0.4, 0.1, and 0.71, respectively.

The effect of the Reynolds number on the obtained results is analyzed for $\varepsilon = 0$, $h^* = 0.2$. The streamlines (a) and isotherms (b) obtained for various values of Re are shown in Fig. 3. For the case $h^* = 0$, the flow pattern exhibits a bicellular structure. The first cell, (C1), is concentrated around block B1 which generates over 50% of the total heat. The second cell, (C2), surrounds the remaining blocks, but with less intensity. These two cells (C1, C2) rotate in opposite directions, indicating that block B1 establishes the flow direction within the cavity. This behavior can be explained by considering that block B1 generates a considerable amount of heat, creating a thermal plume that induces fluid flow in the cavity. When the mode is changed to MC ($h^* \neq 0$), the cell (C2) is replaced by lines connecting the two openings via different paths. This change in the flow structure can be attributed to the presence of the cooling fluid, which alters the flow pattern and promotes more efficient heat transfer. Figure 3a also demonstrates that when the buoyancy force contribution reduces (Re rises), the number of lines flowing between the cylinders reduces.

According to Fig. 3b, the isotherms are tightly concentrated in the blocks that produce a significant amount of heat ($Q_i > Q$). Conversely, the last two blocks ($Q_i < Q$) appear to be nearly isothermal. The isotherms in the solids show a circular pattern, indicating that the temperature extremes ($\theta_{i,max}$) are located in the center of blocks B_i . This phenomenon can be explained by considering that the heat generated by the blocks is primarily conducted towards the center, where it accumulates, leading to the formation of a hot spot in the middle. At $h^* = 0$, a thermal plume appears over block B1, which generates a significant amount of heat. As the value of Re increases, the influence of buoyancy force decreases, resulting in a gradual reduction in the intensity of the thermal

plume. This reduction can be explained by the fact that as Re rises, the inertia of the fluid flow becomes dominant over the buoyancy force, leading to a more streamlined flow pattern.

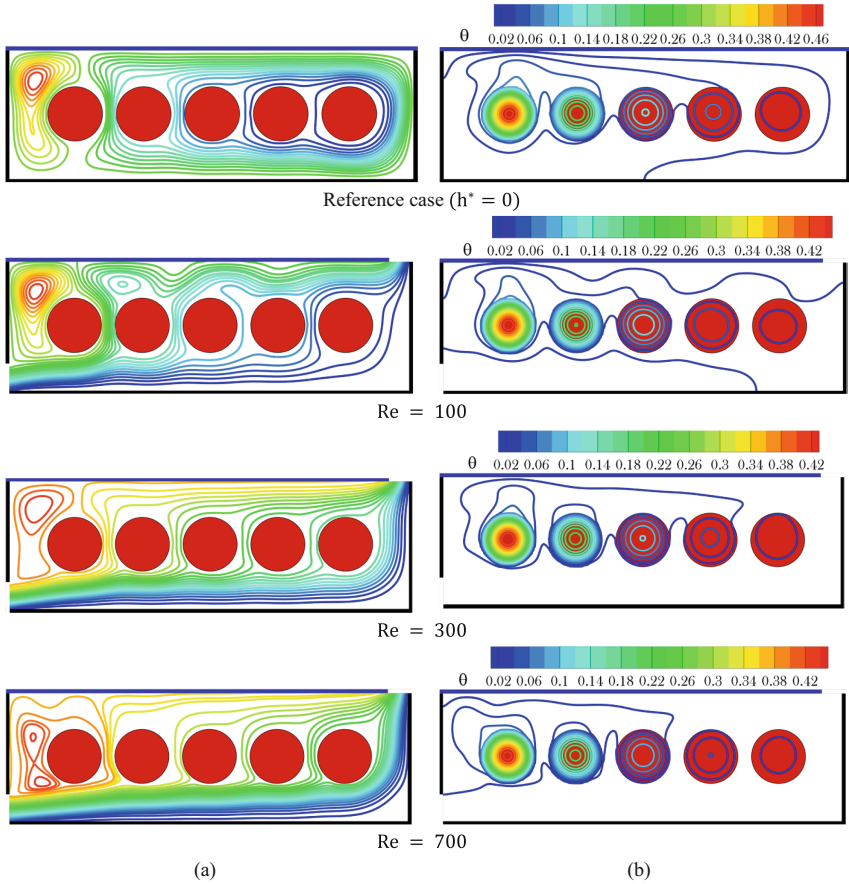


Fig. 3. Streamlines (a) and isotherms (b) obtained for different values of Re with $\epsilon = 0$.

The profiles of the average convective Nusselt number (Nu_C) and that of the maximum temperature (T_{max}) are plotted in Fig. 4. This figure shows that Nu_C decreases significantly with increasing Re number. For $Re = 700$, more than 40% of the overall heat generated ($Q_{tot} = 7.75Q$) is removed through the outlet, implying that the cooling method is effective in dissipating a considerable amount of heat from the system. In addition, a decrease of 4.4% is observed in the maximum temperature of block B1. This value reaches its lowest point at $Re \approx 300$ before experiencing a slight increase at higher values of Re . These findings suggest that the cooling method (MC) is effective in dissipating heat from multiple components (Bi) that generate varying levels of heat, as long as the Ri number is chosen appropriately (in this case, $Ri = Ra/Re^2Pr \approx 31$).

In other words, the cooling method can effectively dissipate heat in the presence of heat sources if the flow regime is appropriately selected.

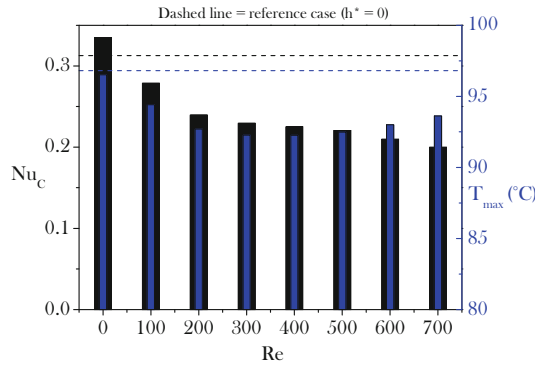


Fig. 4. Maximum temperature and mean convective Nusselt number for various values of Re with $\epsilon = 0$ and $h^* = 0.2$.

The impact of emissivity on the maximum temperature (T_{max}) and the total heat transfer (Nu_T) within the cavity was studied for $h^* = 0.2(0)$ and $Re = 300$ (Fig. 5). The results shown in Fig. 5a reveal that T_{max} decreases with ϵ for both MC ($h^* = 0.2$) and NC ($h^* = 0$) modes. The recorded temperature drop was 3.4% and 5.5% for $h^* = 0.2$ and $h^* = 0$, respectively, indicating the effectiveness of radiative cooling in both modes. This effect can be explained by considering that an increase in emissivity leads to a higher rate of radiation heat transfer, which can dissipate more heat from the system, reducing the maximum temperature. On the other hand, Fig. 5b demonstrates that Nu_T does not exhibit a significant change with an increase in emissivity. For NC mode, the total heat transfer is not dependent on emissivity as all the heat produced is removed by both radiation and convection via the active wall. However, in the MC mode, only a portion of the produced heat is removed through the cold wall, with $Nu_T(h^* = 0.2)/Nu_T(h^* = 0) = 71\%$ (78%) for $\epsilon = 0(1)$.

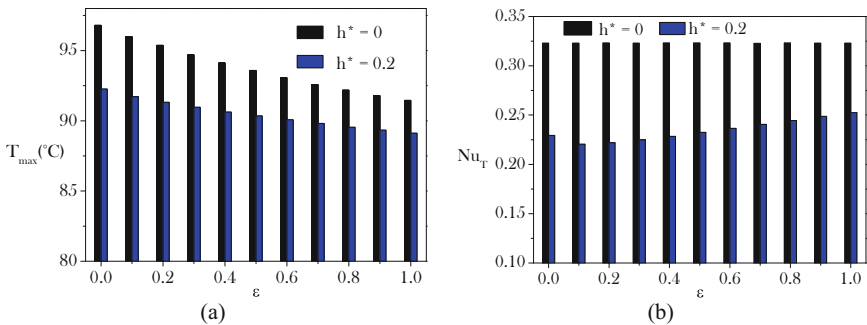


Fig. 5. Maximum temperature (a) and total Nusselt number (b) for $Re = 300$ and different values of ϵ .

Overall, these results provide insights into the impact of emissivity on the system's thermal behavior and can be useful for designing cooling systems that incorporate radiative cooling. The results suggest that the effectiveness of radiative cooling can vary depending on the cooling mode and the emissivity of the surfaces.

4 Conclusion

In this paper, coupled thermal radiation and mixed convection in an elongated horizontal ventilated cavity with five heat-generating blocks that generate varying levels of heat have been investigated. The outcomes of the mixed convection mode are contrasted to those found in the case of a closed unventilated cavity (natural convection). The key findings demonstrating the impact of surface emissivity and the Reynolds number are as follows:

- The cavity's maximum temperature decreases by 4.4% as the Re number increases and stabilizes around $Re \approx 300$.
- An increase in Re reduces lines flowing between the blocks, indicating a decrease in buoyancy contribution.
- The maximum temperature in the cavity reduces by 3.4% and 5.5% for $h^* = 0.2$ and $h^* = 0$, respectively, with an increase in emissivity from 0 to 1, demonstrating the effectiveness of radiative cooling in both mixed and natural convection.

References

1. Pandey, S., Park, Y.G., Ha, M.Y.: An exhaustive review of studies on natural convection in enclosures with and without internal bodies of various shapes. *Int. J. Heat Mass Transf.* **138**, 762–795 (2019). <https://doi.org/10.1016/j.ijheatmasstransfer.2019.04.097>
2. Rao, G.M., Narasimham, G.S.V.L.: Laminar conjugate mixed convection in a vertical channel with heat generating components. *Int. J. Heat Mass Transf.* **50**, 3561–3574 (2007). <https://doi.org/10.1016/j.ijheatmasstransfer.2006.12.030>
3. Hidki, R., El Moutaouakil, L., Boukendil, M., Charqui, Z., Zrikem, Z., Abdelbaki, A.: Impact of Cu, Al₂O₃-water hybrid nanofluid on natural convection inside a square cavity with two heat-generating bodies. *Mater. Today Proc.* **72**, 3749–3756 (2023). <https://doi.org/10.1016/j.matpr.2022.09.292>
4. Hidki, R., El Moutaouakil, L., Boukendil, M., Charqui, Z., Zrikem, Z., Abdelbaki, A.: Natural convection coupled to surface radiation in an air-filled square cavity containing two heat-generating bodies. *Heat Transf.* (2022). <https://doi.org/10.1002/HTJ.22778>
5. Hidki, R., El Moutaouakil, L., Boukendil, M., Charqui, Z., Zrikem, Z.: Mixed-convection coupled with thermal-radiation in a ventilated horizontal channel containing different electronic components. *J. Thermophys. Heat Transf.* **37**(3), 690–696 (2023). <https://doi.org/10.2514/1.T6659>
6. Chamkha, A.J., Hussain, S.H., Abd-Amer, Q.R.: Mixed convection heat transfer of air inside a square vented cavity with a heated horizontal square cylinder. *Numer. Heat Transf. Part A Appl.* **59**, 58–79 (2011). <https://doi.org/10.1080/10407782.2011.541216>
7. Javadzadegan, A., Joshaghani, M., Moshfegh, A., Akbari, O.A., Afrouzi, H.H., Toghraie, D.: Accurate meso-scale simulation of mixed convective heat transfer in a porous media for a vented square with hot elliptic obstacle: an LBM approach. *Phys. A Stat. Mech. its Appl.* **537**, 122439 (2020). <https://doi.org/10.1016/J.PHYSA.2019.122439>

8. Ahammad, M.U., Rahman, M.M., M. L. Rahman: Mixed convection flow and heat transfer behavior inside a vented enclosure in the presence of heat generating obstacle. *Int. J. Innov. Appl. Stud.* **3**, 967–978 (2013)
9. Ahammad, M.U., Rahman, M.M., Rahman, M.L.: A Study on the governing parameters of mhd mixed convection problem in a ventilated cavity containing a centered square block. *Int. J. Sci. Technol. Res.* **3**, 273–281 (2014)
10. Rahman, M., Alim, M.A., Saha, S., Chowdhury, M.K.: Mixed convection in a vented square cavity with a heat conducting horizontal solid circular cylinder. *J. Nav. Archit. Mar. Eng.* **5**, 37–46 (2009). <https://doi.org/10.3329/jname.v5i2.2504>
11. Rahman, M.M., Billah, M.M., Alim, M.A.: Effect of reynolds and prandtl numbers on mixed convection in an obstructed vented cavity. *J. Sci. Res.* **3**, 271–281 (2011). <https://doi.org/10.3329/jsr.v3i2.4344>
12. Gupta, S.K., Chatterjee, D., Mondal, B.: Investigation of mixed convection in a ventilated cavity in the presence of a heat conducting circular cylinder. *Numer. Heat Transf. Part A Appl.* **67**, 52–74 (2015). <https://doi.org/10.1080/10407782.2014.916113>
13. Pirouz, M.M., Farhadi, M., Sedighi, K., Nemati, H., Fattahi, E.: Lattice Boltzmann simulation of conjugate heat transfer in a rectangular channel with wall-mounted obstacles. *Sci. Iran.* **18**, 213–221 (2011). <https://doi.org/10.1016/j.scient.2011.03.016>
14. Ghaneifar, M., Raisi, A., Ali, H.M., Talebizadehsardari, P.: Mixed convection heat transfer of AL₂O₃ nanofluid in a horizontal channel subjected with two heat sources. *J. Therm. Anal. Calorim.* **143**, 2761–2774 (2021). <https://doi.org/10.1007/s10973-020-09887-2>
15. Hamouche, A., Bessaïh, R.: Mixed convection air cooling of protruding heat sources mounted in a horizontal channel. *Int. Commun. Heat Mass Transf.* **36**, 841–849 (2009). <https://doi.org/10.1016/j.icheatmasstransfer.2009.04.009>
16. Boutina, L., Bessaïh, R.: Numerical simulation of mixed convection air-cooling of electronic components mounted in an inclined channel. *Appl. Therm. Eng.* **31**, 2052–2062 (2011). <https://doi.org/10.1016/j.applthermaleng.2011.03.021>
17. Hssain, M.A., Mir, R., El Hammami, Y.: Numerical simulation of the cooling of heated electronic blocks in horizontal channel by mixed convection of nanofluids. *J. Nanomater.* **2020**, 1–11 (2020). <https://doi.org/10.1155/2020/4187074>
18. Sivaraj, C., Miroshnichenko, I.V., Sheremet, M.A.: Influence of thermal radiation on thermogravitational convection in a tilted chamber having heat-producing solid body. *Int. Commun. Heat Mass Transf.* **115**, 104611 (2020). <https://doi.org/10.1016/j.icheatmasstransfer.2020.104611>
19. Saravanan, S., Sivaraj, C.: Combined thermal radiation and natural convection in a cavity containing a discrete heater: effects of nature of heating and heater aspect ratio. *Int. J. Heat Fluid Flow* **66**, 1339–1351 (2017). <https://doi.org/10.1016/j.ijheatfluidflow.2017.05.004>
20. Ahmed Mezrhab, M.A., Moussaoui, H.N.: Lattice Boltzmann simulation of surface radiation and natural convection in a square cavity with an inner cylinder. *J. Phys. D Appl. Phys.* **41**(11), 115502 (2008). <https://doi.org/10.1088/0022-3727/41/11/115502>
21. Mezrhab, A., Bouali, H., Abid, C.: Modeling of combined radiative and convective heat transfer in an enclosure with a heat-generating conducting body. *Int. J. Comput. Methods* **02**, 431–450 (2005). <https://doi.org/10.1142/S0219876205000521>
22. Hidki, R., Moutaouakil, L.E., Boukendil, M., Charqui, Z., Abdelbaki, A.: Natural Convection and Surface Radiation in an Inclined Square Cavity with Two Heat-Generating Blocks. In: Vasant, P., Zelinka, I., Weber, G.-W. (eds.) *ICO 2021. LNNS*, vol. 371, pp. 948–957. Springer, Cham (2022). https://doi.org/10.1007/978-3-030-93247-3_90
23. Mandal, S.K., Deb, A., Sen, D.: A computational study on mixed convection with surface radiation in a channel in presence of discrete heat sources and vortex generator based on RSM. *J. Therm. Anal. Calorim.* **141**, 2239–2251 (2020). <https://doi.org/10.1007/s10973-020-09774-w>

24. Peiravi, M.M., Alinejad, J.: Hybrid conduction, convection and radiation heat transfer simulation in a channel with rectangular cylinder. *J. Therm. Anal. Calorim.* **140**, 2733–2747 (2020). <https://doi.org/10.1007/s10973-019-09010-0>
25. Habchi, S., Acharya, S.: Laminar mixed convection in a partially blocked, vertical channel. *Int. J. Heat Mass Transf.* **29**, 1711–1722 (1986). [https://doi.org/10.1016/0017-9310\(86\)90111-0](https://doi.org/10.1016/0017-9310(86)90111-0)
26. Hidki, R., El Moutaouakil, L., Boukendil, M., Charqui, Z., Zrikem, Z., Abdelbaki, A.: Mixed convection and surface radiation in a ventilated cavity containing two heat-generating solid bodies. *Mater. Today Proc.* **66**, 318–324 (2022). <https://doi.org/10.1016/j.matpr.2022.05.404>
27. El Moutaouakil, L., Boukendil, M., Zrikem, Z., Abdelbaki, A.: Natural convection and radiation in a cavity with a partially heated cylinder. *J. Thermophys. Heat Transf.* **35**, 312–322 (2021). <https://doi.org/10.2514/1.T6097>



Experimental and Numerical Analysis of the Vibration Behavior of a Bio-Based Sandwich with an Auxetic Core in a Humid Environment

Zeineb Kesentini^{1,2}(✉), Abderrahim El Mahi¹, Jean Luc Rebiere¹, Rachid El Guerjouma¹, Moez Beyaoui², and Mohamed Haddar²

¹ Acoustic Laboratory of Le Mans University (LAUM) UMR CNRS 6613, Acoustics Institute-Graduate School, CNRS, Avenue O. Messiaen, 72085 Le Mans Cedex 9, France
zeinebkesentini@gmail.com

² Laboratory of Mechanics Modeling and Production (LA2MP), National Engineering School of Sfax, University of Sfax, BP N° 1173, 3038 Sfax, Tunisia

Abstract. Water absorption and vibration issues are major concerns for manufacturers and researchers using bio-based composites. In light of this, this work examines how water aging affects the dynamic characteristics of a sandwich with a reentrant auxetic core. The material considered to manufacture the specimens is polylactic acid (PLA) reinforced with flax fibers. It is manufactured using 3D printing which proceeds by adding layers successively. For various immersion times, the impact of water absorption on the dynamic characteristics is examined. Water aging obviously affects equivalent stiffness and damping. We therefore observe a decrease in rigidity and an increase in damping. These results could be explained by the plasticizing effect of water on bio-based composites, stimulated by water absorption as well as by the architecture of the core of the sandwich. Finally, a numerical strategy based on the finite element technique is developed. It made it possible to evaluate the equivalent rigidity and the damping for different immersion times. The results of this approach are in close agreement with those obtained experimentally.

Keywords: auxetic core · bio-sourced composite · water aging · dynamic analysis · 3D-printing

1 Introduction

The advantage of natural fibers in several sectors compared to synthetic fibers is essentially due to the substantially equivalent mechanical properties. In addition, these new materials have ecological advantages. Several studies have shown the ability of plant fibers to replace glass fibers [1–3]. The fibers extracted from flax plants have properties equivalent to those of glass fibers, mainly in terms of rigidity and even better in terms of dissipation of vibrational energy. Apart from the environmental benefits, studies have

been done on how natural fiber composites behave when they vibrate. Duc et al. [4] have shown that the ability to dampen vibration is owing to the viscoelastic nature of the cellulose that this type of natural fiber contains, the friction between the different constituents of the fiber, the interaction between the fibers and the fiber/matrix interface. The effectiveness of the fiber/matrix contact was also discovered to be a significant factor affecting the damping qualities [5]. The comparison of the vibration behavior of epoxy composites reinforced with glass fibers and with flax fibers has been studied by Prabhakaran et al. [6] in free vibrations. The results obtained show that the damping behavior of composites reinforced with flax fibers exceeds that of fiberglass composites by 50%. The combination of natural fibers and biobased polymers can be interesting in several areas of use.

Essassi et al. [7] have explored the vibrational characteristics of a 3D-printed PLA/flax bio-composite in this context. The results obtained showed that this composite has, among other things, significant damping properties. 3D printing is an automated manufacturing technology that uses 3D model data to create structures [8]. It is used by Antony et al. [8] to study the mechanical characteristics of PLA/hemp composites with a honeycomb structure. Auxetic structures have shown their significant damping capacity [7]. This extensive study has demonstrated that a material with excellent mechanical and damping qualities may be created by combining sandwich composites, auxetic structures, and bio-based materials, particularly bio-composites reinforced with flax fibers.

However, all these works mentioned above are not exhaustive if one seeks to study the behavior of natural fiber auxetic sandwich materials in vibration combined with water absorption. Considering the water aging effect on the dynamic properties of the composite is essential to be able to use the sandwiches in all environments (dry and wet).

In this context, the influence of water absorption on the vibration behavior of a reentrant auxetic core sandwich with four auxetic cells along the width of the specimen (designated S4C in the figures) is studied in this article.

2 Experimental and Numerical Procedures

2.1 Experimental Setup

The sandwiches are made by a method of additive manufacturing that works by melt extrusion (3D printing). It makes it possible to develop parts with complex geometries at a lower cost and faster than conventional development methods.

The auxetic form studied in this work is that of a reentrant auxetic honeycomb. It was first presented by Gibson and Ashby in 1982 [9]. It is based on the hexagonal geometry of a conventional honeycomb structure. The design and geometry of the auxetic honeycomb core with a reentrant unit cell are shown in Fig. 1 and defined in Table 1.

The sandwich has a width of 25 mm, a length of 270 mm and a thickness of 7 mm. It consists of two skins and a soul with 4 elementary cells in PLA/flax. The limit value of the angle θ is set at -20° so as not to lose the auxetic character during the development of the structure. After making the sandwich with the 3D printing technique, several test pieces are immersed in tap water at room temperature. The specimens are removed from the water at various well-chosen times to study the effect of water aging.

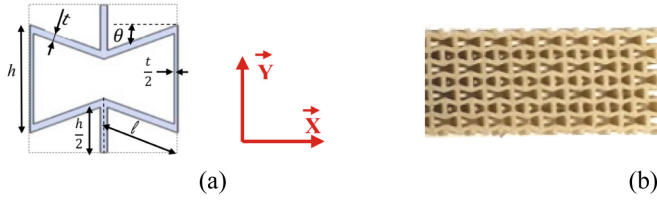


Fig. 1. a) Auxetic cell and b) Core with four cells.

Table 1. Design settings

Parameter	Definition
l	Length of the inclined walls
h	Length of the vertical walls
θ	Angle between the inclined walls and the X direction
t	Cell wall thickness
L	the lengths of the cell along the X axis
H	the lengths of the cell along the Y axis

The experimental method of excitation by impact is applied for different immersion time in order to determine the effect of water aging on the vibration characteristics of the sandwich.

Figure 2 presents the experimental device in clamped-free configuration. For embedding and clamping, a 40 mm block was printed at the end of all the specimens. Three lengths of specimens, 170 mm, 200 mm and 230 mm, were tested and this to vary the resonance frequencies. Using an impact hammer (PCB084A14), the specimen is excited near the clamping block. The response is recovered at the free end, the signals are detected using an OFV 303 Sensor Head laser vibrometer. Then, these signals are digitized with the acquisition card and processed with the NVGate software. These tests are carried out at least 3 times and this for each duration of immersion.

The frequency response function (FRF) was examined with an automated loop developed under MATLAB. Following this analysis, the damping factors and the frequencies of the resonance modes are determined. Subsequently, the equivalent moduli was deduced [10].

The -3 dB bandwidth method involves separating the resonance peaks from the FRF and processing them. This method makes it possible to determine the eigenfrequencies as well as the damping. For each isolated peak, the bandwidth at -3 dB is defined with respect to the maximum value of the amplitude.

2.2 Numerical Approach

The finite element analysis method is used to calculate frequencies and then determine the damping of the sandwich beams and the stiffness modulus. The CAD of the sandwich

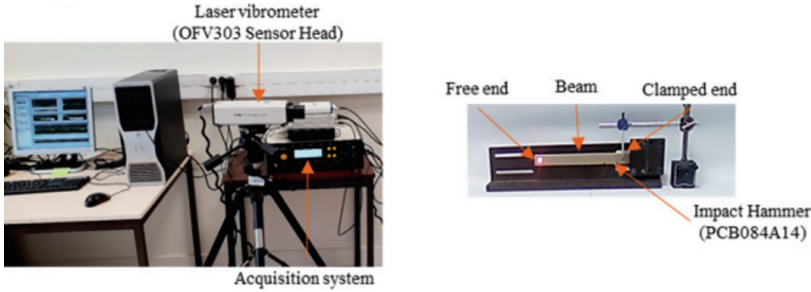


Fig. 2. Experimental equipment for clamped-free vibration tests

is carried out using the Solidworks software. Then, the geometric model is converted into instructions compatible with the finite element software ABAQUS, with which numerical simulations have been carried out. The model is studied in an embedded-free configuration. For the boundary conditions, the 6 degrees of freedom in translation and in rotation of the fixed end are blocked. For loading, a nodal force of 10 N is applied to a node close to the clamped end, to simulate the excitation of the vibration bench impact hammer. For the results, a node is chosen to visualize the behavior of the model on the other free end of the specimen. The results are proposed with curves plot for amplitude (dB) as a function of frequency (Hz). These responses were used to estimate the damping factor of the sandwich using the HPB method. The behavior of the sandwich is considered linear elastic. The behavior laws used for unaged and aged materials are determined from bending tests. The structure is meshed using tetrahedral linear elements (Fig. 3). The number of nodes used to mesh the sandwich structure depends on the core densities and the configuration used and it is equal to 29511.



Fig. 3. Example of meshed sandwich.

3 Results and Discussions

Figure 4 illustrates the results obtained following the experimental modal analysis for the unaged and aged sandwich. The equivalent stiffness is normalized to the initial value of the unaged sandwich. The same is done for the loss factor.

The results show that the equivalent stiffness decreases with increasing immersion time and this as a function of frequency. The damping increases according to the duration of immersion and the frequencies. These results can be explained by the dissipation of vibrational energy through the material on the one hand and by the penetration of water also. Indeed, the viscoelastic nature of flax fibers and the biobased resin PLA as well as the spaces created in this metamaterial by auxetic cells promote the dissipation of

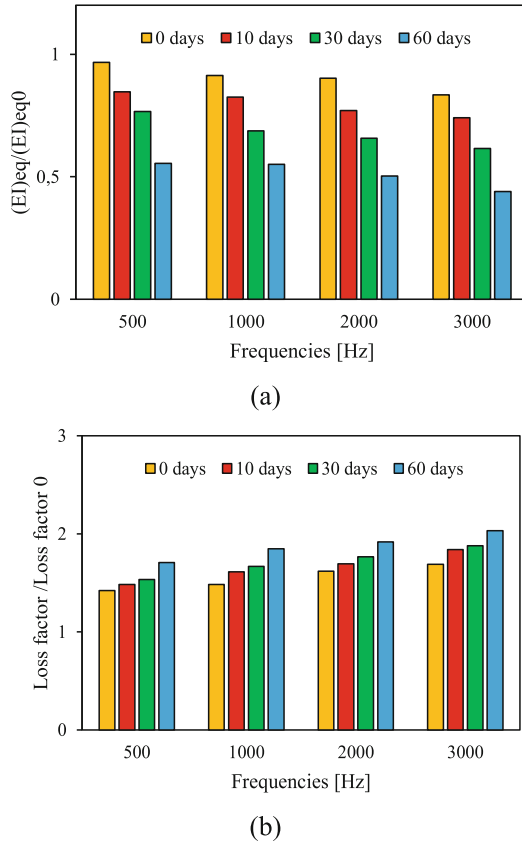


Fig. 4. Hydric aging effect on: a) equivalent stiffness and b) loss factor.

energy. It has been observed that an amount of energy is dissipated through the spaces of the auxetic cells.

The bio-based material's constituent macromolecular linkages become weaker due to the presence of water molecules inside. The modification of the mechanical properties of the composite by aging is potentially due to the phenomenon of decohesion or to the generation of microcracks in the matrix. Pantaloni et al. [11] showed that the two types of damage are related to the absorption of water by the bio-based composite. Water absorption plays an important role in the mobility of macromolecular chains, responsible for the evolution of dynamic properties. The water molecules cause the formation of hydrogen type bonds by replacing the bonds in the lattice of the composite. On the other hand, the energy is dissipated by friction between the different elementary layers of the fiber and also between the fibers and the matrix.

Figure 5 illustrates the comparison of the experimental results with the numerical simulation results for the unaged and aged sandwich. The curves present a superposition of the two results. However, a slight discrepancy is observed. The discrepancy can be attributed to the shape of the manufacturing process of the 3D printed structures,

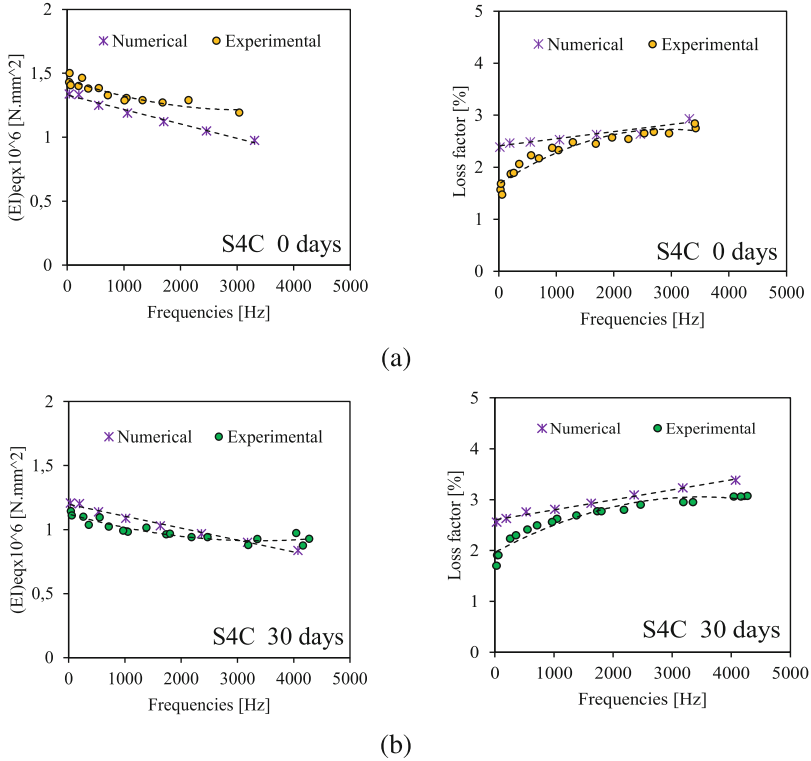


Fig. 5. Comparison of dynamic characteristics of experimental tests and numerical simulations: a) unaged and b) aged for 30 days.

the quality of the numerical calculations and the method used for the calculations. In addition, to have a repeatability of the test, the tightening of the specimen is carried out using a torque wrench. A slight dispersion in the tightening value can have an impact on the frequencies and damping coefficients of the sandwich. On the other hand, for the model, the material is considered as an isotropic and continuous homogeneous material in all the finite element analyses. These are the few factors that cause the numerical results and the results of the experimental tests not to overlap perfectly.

The results of the numerical simulations obtained present a good agreement with the results of the experimental tests.

4 Conclusion

The water absorption effect on a biobased sandwich’s vibrational behavior with a reentrant auxetic core fabricated using 3D printing technology is studied. Vibration tests in the embedded-free specimen configuration are carried out. The results show that with increasing immersion duration, damping has increased and equivalent stiffness has reduced. These results can be explained by the vibrational energy dissipation through the material on the one hand and by the penetration of water on the other hand. The

viscoelastic nature of PLA/flax (fibers and matrix) as well as the spaces created by the auxetic cells of this metamaterial favor the dissipation of energy. A finite element analysis is developed to evaluate the vibration behavior of the studied structures, using the material properties obtained during static bending tests. The outcomes of the experimental tests and the outcomes of the numerical simulations exhibit good agreement for the unaged and aged sandwich. An iterative method will be developed in future works to automate the frequency response for different configurations and different immersion times.

References

1. Monti, A., El Mahi, A., Jendli, Z., Guillaumat, L.: Quasi-static and fatigue properties of a balsa cored sandwich structure with thermoplastic skins reinforced by flax fibres. *J. Sandwich Struct. Mater.* **21**(7), 2358–2381 (2019)
2. Ameer, M.B., et al.: Investigation and identification of damage mechanisms of unidirectional carbon/flax hybrid composites using acoustic emission. *Eng. Fract. Mech.* **216**, 106511 (2019)
3. Allagui, S., El Mahi, A., Rebiere, J.L., Beyaoui, M., Bouguecha, A., Haddar, M.: Experimental studies of mechanical behavior and damage mechanisms of recycled flax/Elium thermoplastic composite. *Polym. Polym. Compos.* **30**, 09673911221090048 (2022)
4. Duc, F., Bourban, P.E., Plummer, C.J.G., Manson, J.A.: Damping of thermoset and thermoplastic flax fibre composites. *Compos. A Appl. Sci. Manuf.* **64**, 115–123 (2014)
5. Mounier, D., Poilâne, C., Khelfa, H., Picart, P.: Sub-gigahertz laser resonant ultrasound spectroscopy for the evaluation of elastic properties of micrometric fibers. *Ultrasonics* **54**(1), 259–267 (2014)
6. Prabhakaran, S., Krishnaraj, V., Zitoune, R.: Sound and vibration damping properties of flax fiber reinforced composites. *Procedia Eng.* **97**, 573–581 (2014)
7. Essassi, K., Rebiere, J.L., El Mahi, A., Souf, M.A.B., Bouguecha, A., Haddar, M.: Experimental and analytical investigation of the bending behaviour of 3D-printed bio-based sandwich structures composites with auxetic core under cyclic fatigue tests. *Compos. A Appl. Sci. Manuf.* **131**, 105775 (2020)
8. Antony, S., Cherouat, A., Montay, G.: Fabrication and characterization of hemp fibre based 3D printed honeycomb sandwich structure by FDM process. *Appl. Compos. Mater.* **27**(6), 935–953 (2020)
9. Gibson, I.J., Ashby, M.F.: The mechanics of three-dimensional cellular materials. *Proc. R. Soc. London A Math. Phys. Sci.* **382**(1782), 43–59 (1982)
10. Young, D., Felgar, R.P.: Tables of characteristic functions representing normal modes of vibration of a beam (1949)
11. Pantaloni, D., Melelli, A., Shah, D.U., Baley, C., Bourmaud, A.: Influence of water ageing on the mechanical properties of flax/PLA non-woven composites. *Polym. Degrad. Stab.* **200**, 109957 (2022)



A Microstructurally Motivated Hyperelastic Model for Elastomer Materials

Ayoub Ouardi^{1,2}(✉), Adnane Boukamel¹, and Nouredine Damil^{1,2}

¹ Centre de Recherche Systèmes Complexes et Interactions, Centrale Casablanca, Ville Verte, 27182 Bouskoura, Morocco

{ayoub.ouardi,adnane.boukamel,nouredine.damil}@centrale-casablanca.ma

² Hassan II University of Casablanca, Faculté des Sciences Ben M'Sik, Laboratoire d'Ingénierie et Matériaux, LIMAT, B.P 7955, Sidi Othman, Casablanca, Morocco

Abstract. In this work we propose a microstructurally motivated hyperelastic model to describe the behavior of elastomer materials. At the scale of the Representative Volume Element (RVE), composed of randomly oriented macromolecular chains, we assume that the segments of the chains are deformable and that there is a bending energy between two consecutive segments. We propose to model each macromolecular chain using micromechanical elements: linear elastic bars to represent the segments between the cross-linking points and non linear elastic spires to represent the flexibility of rotations around the cross-linking points. Numerical simulations, on different structured RVEs composed of 3, 4, and 8 chains in the case of three boundary conditions: uniaxial compressible tension, uniaxial incompressible tension, and shear, show that this modeling allows to find the classical response curves of hyperelastic elastomeric. In the proposed model, we have to identify only three parameters: a , M_0 and K . From numerical simulations, we show that the first parameter, a , control the first phase of activation of rotations between chain segments, the second parameter, M_0 , control the unfolding phase, and that the third parameter K control the stiffening phase at large deformations.

Keywords: Hyperelasticity · elastomer materials · polymer chains · micro-mechanical

1 Introduction

On a microscopic scale, an elastomer consists of long molecular chains with junctions. These macromolecules form a 3D network whose chain segments are randomly oriented. Rubber elasticity is the result of the weak interaction between the macro molecules.

Phenomenological or statistical models have been developed since years. Many works are interested in the modeling of the unfolding mechanisms of macromolecular chains to describe the microphysically motivated behavior of this type of network. In [1] the authors propose a form of hyperelastic strain energy

© The Author(s), under exclusive license to Springer Nature Switzerland AG 2024

Z. Azari et al. (Eds.): JET 2022, LNME, pp. 92–98, 2024.

https://doi.org/10.1007/978-3-031-49727-8_10

density of elastomers based on an 8-chain representation and a non-Gaussian behavior of the individual chain. In [5], the authors compare several statistical and phenomenological models with Treloar's experimental data under uniaxial, biaxial and shear loads [7]. In [2], the authors propose a statistical non-Gaussian macrochain model, coupled with tetrahedral finite elements to transfer the information from the micro scale to the macro scale. More recently the authors in [3] proposed a model that combines the mechanism of a crosslinked network of Langevin macrochains, and an entangled network with chains confined in a non-affine tube.

In this work, we propose a new microstructurally motivated hyperelastic model. We propose to model each macromolecular chain using micro-mechanical elements: elastic bars to represent the segments between crosslinking points and elastic spires, to translate the flexibility of rotations around the cross-linking [6]. The proposed model aims to reflect the three phases of the deformation mechanism of elastomers.

In Sect. 2, we present the proposed 2D modeling in the case of a Representative Volume Element (RVE) consisting of M chains. In Sect. 3, we present numerical simulations on some examples of RVE to assess the validity of the proposed model.

2 A Microstructurally Motivated Hyperelastic Model

The elastomers belong to the family of high polymers, microscopically, they are presented in the form of macromolecules constituted by long chains of polymers (see Fig. 1). In this section, we represent a 2D modeling of a proposed model that describes the hyperelastic behavior of this type of material, starting from the modeling of a macrochain thus the Representative Element Volume (RVE).

2.1 Model Description

In an elastomer material, we consider a Representative Volume Element (RVE) constituted by M random chains C_k made of n_k Kuhn segments [4] (see Fig. 1-a).

We limit ourselves to the 2D case and we will first consider the case of a single macromolecular chain (Fig. 1-b). In an orthonormal frame of reference of origin O and basis (\mathbf{i}, \mathbf{j}) , we designate by P_i the origin point of the i^{th} segment in the initial state and by p_i its transform in the deformed state. We note by (u_i, v_i) the components of the displacement vector of the initial point P_i .

For each chain, in the initial state the lengths of the segments will be noted L_i and the angle between the basis vector \mathbf{i} and the segments $\mathbf{P}_i\mathbf{P}_{i+1}$ will be noted $\Phi_i = (\mathbf{i}, \widehat{\mathbf{P}_i\mathbf{P}_{i+1}})$. In the deformed state, the lengths of the segments will be noted l_i and the angle between the basis vector \mathbf{i} and the segments $\mathbf{p}_i\mathbf{p}_{i+1}$ will be noted $\varphi_i = (\mathbf{i}, \widehat{\mathbf{p}_i\mathbf{p}_{i+1}})$.

We propose to model each macromolecular chain C_k in the RVE using micro-mechanical elements: n elastic bars to represent the effective segments between

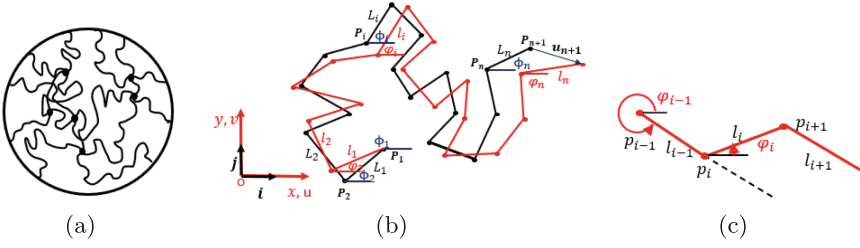


Fig. 1. (a) A Representative Volume Element (RVE) constituted by M chains C_k made of n_k Kuhn segments. (b) A single macromolecular chain: Initial and deformed states. (c) Variation of the angle φ_i between the basis vector i and the segment.

crosslinking points p_i (the Kuhn segments are assumed deformable) and n elastic spires, to translate the flexibility of rotations around the cross-linking points p_i . Each macromolecular chain will thus be represented by n elastic springs linked together by n elastic spiral springs.

We will assume that each effective segment of each molecular chain admits a tensile strain energy $w_{t_i}^k$ and we model the rotational flexibility between two consecutive effective segments by a bending strain energy $w_{b_i}^k$. The total strain energy $W(l_i^k, \varphi_i^k)$ of the RVE is then the sum of the strain energy of all chains C_k , each one is represented as a sum of tensile strain energy $w_{t_i}^k$ depending on the elongation of each segment $l_i^k - L_i^k$ and a bending strain energy $w_{b_i}^k$ depending on the variation of the angle between two consecutive segments $\theta_i^k = (\varphi_i^k - \varphi_{i-1}^k) - (\Phi_i^k - \Phi_{i-1}^k)$. The potential energy of the system is then written as:

$$E_p(l_i^k, \varphi_i^k) = W(l_i^k, \varphi_i^k) = \sum_{k=1}^M \left(\sum_{i=1}^{n_k} w_{t_i}^k (\Delta l_i^k) + w_{b_i}^k (\theta_i^k) \right) \quad (1)$$

We propose to model the tensile strain energy of the segments by an elastic tension spring's energy of stiffness K : $w_{t_i}^k (l_i^k - L_i^k) = \frac{1}{2} K (l_i^k - L_i^k)^2$ and, as in [7], we use a modeling of the strain energy for the spiral spring in the following form: $w_{b_i}^k (\theta_i^k) = a \cdot M_0 \cdot \ln \left(\cosh \left(\frac{\theta_i^k}{a} \right) \right)$, where a and M_0 are the characteristics of the material.

As boundary conditions, we will impose a gradient of the macroscopic deformation \mathbb{F} on the boundary ∂V . The displacement \mathbf{u} on the boundary ∂V of the RVE is then given by the following relation:

$$\begin{aligned} \mathbf{u} &= \mathbf{u}^d &= (\mathbb{F} - \mathbb{I})\mathbf{x} &\quad \text{on } \partial V \\ \mathbf{u}_j^k &= \mathbf{u}_j^{d,k} &= (\mathbb{F} - \mathbb{I})\mathbf{x}_j^k &\quad \text{for } k = 1 \text{ to } M \text{ and } j = 1 \text{ to } J \end{aligned} \quad (2)$$

where \mathbf{x}_j^k represents the coordinates of the points on the boundary ∂V of the RVE before deformation and J is the total number of the chains points on this boundary.

It is assumed that junctions can occur in the network of macromolecular chains, reflecting the cross-linking effect resulting from the vulcanization reaction of the material. This results in a network of cross-linked chains. We suppose that these junction points correspond to the smallest distance between two points r_1 and r_2 of the two chains C_{k_1} and C_{k_2} . The junction can be effective only if the distance between the two points is lower than a given characteristic distance. Thus, we must add $2R$ linking equations where R is the number of junctions between the chains:

$$\begin{cases} u_{r_1}^{k_1} - u_{r_2}^{k_2} = g_r(u) = 0 \\ v_{r_1}^{k_1} - v_{r_2}^{k_2} = g_r(v) = 0 \end{cases} \quad r = 1 \quad \text{to} \quad R \quad (3)$$

The optimum of the potential energy (1) under conditions (2) and (3), (boundary conditions (2) and linking conditions (3)), is the optimum of the following Lagrangian:

$$\begin{aligned} \mathcal{L}(l_i^k, \varphi_i^k, \eta_x^k, \eta_y^k, \xi_r, \mathbb{F}) = & E_p(l_i^k, \varphi_i^k) - \sum_{k=1}^M \sum_{j=1}^J \left(\eta_x^{j,k} (u_j^k - u_j^{d,k}) + \eta_y^{j,k} (v_j^k - v_j^{d,k}) \right) \\ & - \sum_{r=1}^{2R} \xi_r g_r \end{aligned} \quad (4)$$

The components of the displacements u_j^k and v_j^k in (4) can be expressed in terms of the main variables l_p^k and φ_p^k :

$$\begin{aligned} u_j^k &= \sum_{p=0}^{j-1} (l_p^k \cos \varphi_p^k - L_p^k \cos \Phi_p^k) \\ v_j^k &= \sum_{p=0}^{j-1} (l_p^k \sin \varphi_p^k - L_p^k \sin \Phi_p^k) \end{aligned} \quad (5)$$

In (4), $\eta_x^{j,k}$, $\eta_y^{j,k}$ and ξ_r , for $j = 1$ to $j = J$ and for $r = 1$ to $r = 2R$, are the Lagrange multipliers. The Lagrangian in (4) depends also on the imposed gradient of macroscopic deformation \mathbb{F} . Hence, the nonlinear equilibrium equations, $\delta \mathcal{L} = 0$, depend on the principal variables l_j^k, φ_j^k for $j = 1$ to $n_k; k = 1$ to M , on the Lagrange multipliers $\eta_x^{j,k}, \eta_y^{j,k}$ for $j = 1$ to $J; k = 1$ to M , ξ_r for $r = 1$ to $2R$ and on the imposed gradient of macroscopic deformation \mathbb{F} . We shall use an arc length Newton-Raphson method to solve this strongly nonlinear problem depending on the gradient of the macroscopic deformation \mathbb{F} .

In the numerical results we will present a component of the macroscopic first Piola-Kirchoff stress tensor $\bar{\Pi}_{ij}$ at the RVE scale as a function of a component of the imposed macroscopic strain gradient tensor \mathbb{F} . The macroscopic first global Piola-Kirshoff stress tensor $\bar{\Pi}_{ij}$ is obtained by [8]:

$$\bar{\Pi}_{ij} = \frac{1}{V} \int_{\partial V} \Pi_{ik} x_j n_k dl \quad (6)$$

where Π_{ik} , V and ∂V are respectively the microscopic first Piola-Kirchoff stress tensor, the volume and boundary of the RVE. We denote respectively by x_j , n_j and dl the components of the local coordinates, the normal vector external to the RVE and the element length of the boundary of the RVE. Using (6), the discretized form of the global first Piola-Kirshoff stress tensor on the boundary can be written as follow:

$$\bar{\Pi}_{ij} = \frac{1}{V} \sum_{p \in \partial V} (\Pi_{ik} n_k dl)^p x_j^p = \frac{1}{V} \sum_{p \in \partial V} \eta_i^p x_j^p \quad (7)$$

In formula (7) the summation is done on all the points x_j^p of the boundary ∂V of the RVE. The components of the forces applied on these nodes are given by $(\Pi_{ik} n_k dl)^p = \eta_i^p$, that have been calculated during the resolution of the nonlinear system.

3 Numerical Simulations, on Different RVEs

In this section, we evaluate the proposed model by presenting numerical simulations on three RVEs (see Fig. 2) composed of 3, 4, and 8 chains under three different boundary conditions: uniaxial compressible tension, uniaxial incompressible tension, and shear. Note that there is no junction for the first RVE formed by 3 chains and that for the two other RVEs (4-chains and 8-chains), we have assumed that there is only one junction at the intersection of the diagonals.

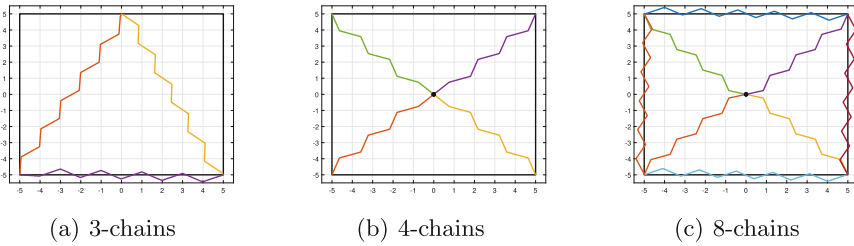


Fig. 2. Three specimens of RVE composed of 3, 4 and 8 chains.

Three boundary conditions will be considered in (9): an uniaxial compressible tension, an uniaxial incompressible tension, and a shear, which correspond respectively to a macroscopic gradient tensor \mathbb{F} , in 2D case, in the form: $\begin{bmatrix} \lambda & 0 \\ 0 & 1 \end{bmatrix}$,

$$\begin{bmatrix} \lambda & 0 \\ 0 & 1/\lambda \end{bmatrix} \text{ and } \begin{bmatrix} 1 & \gamma \\ 0 & 1 \end{bmatrix}.$$

In the numerical applications, we have considered that the number of segments of the 3-chains RVE are respectively $n_1 = 10, n_2 = n_3 = 11$ with an initial lengths of segments $L_i = 1.1$ nm; the number of segments of the 4-chains RVE are respectively $n_1 = n_2 = n_3 = n_4 = 7$ with an initial lengths of segments $L_i = 1.1$ nm; and the number of segments of the 8-chains RVE are respectively $n_1 = n_2 = n_3 = n_4 = 8, n_5 = n_6 = n_7 = n_8 = 11$ with an initial lengths of segments $L_i = 1$ nm. The orientation of the chains is as shown in Fig. 2.

The characteristics of the macrochains for each RVE were chosen equal to $a = 0.03$ nm, $M_0 = 0.01$ N.nm and $K = 10$ N/nm for 3-chains RVE; $a = 0.03$ nm, $M_0 = 0.02$ N.nm and $K = 10$ N/nm for 4-chains RVE; $a = 0.05$ nm, $M_0 = 0.01$ N.nm and $K = 10$ N/nm for 8-chains RVE.

We obtained the response curves shown in Fig. 3. In Fig. 3-a and 3-b, we plotted the $\bar{\Pi}_{11}$ component of the macroscopic first Piola Kirchhoff stress tensor

as a function of $F_{11} = \lambda$, where F_{11} is the first component of the macroscopic gradient tensor \mathbb{F} and in Fig. 3-c, we plotted the macroscopic first Piola Kirchhoff stress tensor $\bar{\Pi}_{12}$ component as a function of the component $F_{12} = \gamma$.

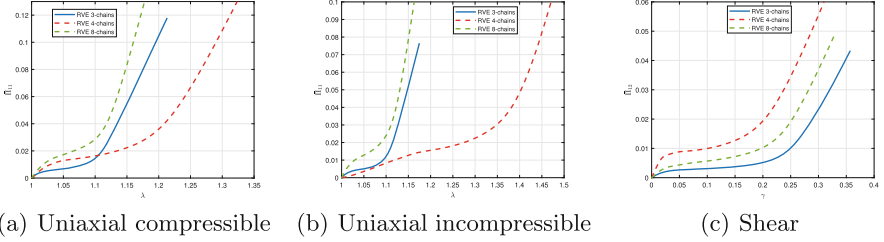
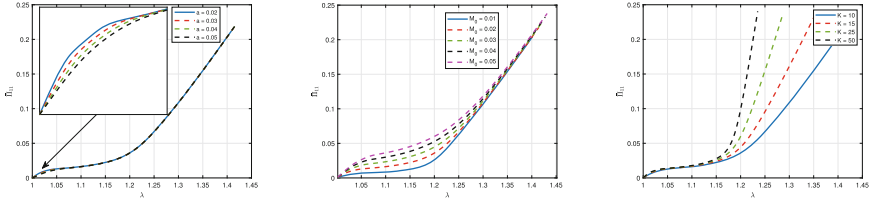


Fig. 3. Response curves for the three RVEs: 3-chain, 4-chain, and 8-chain representation (a) $\bar{\Pi}_{11}$ component of the 1st Piola-Kirchhoff stress tensor as a function of λ in uniaxial compressible case. (b) $\bar{\Pi}_{11}$ component of the 1st Piola-Kirchhoff stress tensor as a function of λ in uniaxial incompressible case. (c) $\bar{\Pi}_{12}$ component of the 1st Piola-Kirchhoff stress tensor as a function of γ in shear case.

The results, in Fig. 3, show that, for the three RVEs specimen and for the three boundary conditions, the model represents well the three phases of the behavior of an elastomer: an untangling phase, an unfolding phase and a stiffening phase due to the crystallization at large deformations. These results, using this microstructural modeling, agree with the hyperelastic models classically proposed and this using only three characteristic parameters a , M_0 and K , where the first is a bending angle, the second is the maximum moment, and the last one represents the stiffness of the longitudinal spring. It can be observed from these numerical simulations (Fig. 3) that this model, in large deformation, for the case of uniaxial tension, implies a greater stiffness for the RVE with 8 chains, followed by that with 3 chains and then that with 4 chains. In the shear case the most rigid RVE is the one with 4 chains followed by the one with 8 chains and finally the one with 3 chains in small and large deformation.

In Figs. 4-a, 4-b, and 4-c, we have presented, in the case of a 4-chain representation and in the case of compressible traction, respectively the effect of the three characteristics of the material a , M_0 and K . In each of these figures, we have fixed two parameters and varied the third. We can see that, the parameter a controls the first disentanglement zone (see Fig. 4-a), M_0 controls the second unfolding zone (see Fig. 4-b) and the third parameter K controls the third crystallization zone under large deformation (see Fig. 4-c). This effect of the three characteristics is valid whatever the RVE and whatever the boundary condition.



(a) Effect of a for $M_0 = 0.02N.nm$ and $K = 10N/nm$ (b) Effect of M_0 for $a = 0.03rad$ and $K = 10N/nm$ (c) Effect of K for $a = 0.03rad$ and $M_0 = 0.02N.nm$

Fig. 4. Effect of the 3 characteristics of the material a , M_0 and K on the behavior of the RVE in the case of 4-chain representation. Response in uniaxial compressible case. The \bar{I}_{11} component of the 1st Piola-Kirchhoff stress tensor as a function of $F_{11} = \lambda$.

4 Conclusion

These first numerical simulations show that the proposed model allows to find the classical response behavior of polymer materials with and without junctions. Only three parameters should be identified. We are working on integrating this model in the case of a micro macro modeling.

References

1. Arruda, E.M., Boyce, M.C.: A three-dimensional constitutive model for the large stretch behavior of rubber elastic materials. *J. Mech. Phys. Solids* **41**(2), 389–412 (1993)
2. Bol, M., Reese, S.: Finite element modelling of rubber like polymers based on chain statistics. *Int. J. Solids Struct.* **43**(1), 2–26 (2006)
3. Davidson, J.D., Goulbourne, N.C.: A nonaffine network model for elastomers undergoing finite deformations. *J. Mech. Phys. Solids* **61**(8), 1784–1797 (2013)
4. Kuhn, W., Grun, F., *Kolloid, Z.: CrossRef-CAS-Web of Science* Times Cited 972, vol. 101, pp. 248–271 (1942)
5. Ogden, R.W., Saccomandi, G., Sgura, I.: On wormlike chain models within the three-dimensional continuum mechanics framework. *Proc. R. Soc. A Math. Phys. Eng. Sci.* **462**(2067), 749–768 (2006)
6. Treloar, L.G.: *The Physics of Rubber Elasticity*, 3rd edn. Oxford University Press, Oxford (1975)
7. Ouardi, A., Boukamel, A., Damil, N.: Towards a macro-chain polymer model using a micromechanical approach, pp. 112–117. *Constitutive Models for Rubber XII, Chapitre* (2022)
8. Trinh, D.K.: *Méthodes d’homogénéisation d’ordre supérieur pour les matériaux architecturés* (Doctoral dissertation, École Nationale Supérieure des Mines de Paris) (2011)



Meshless Approach for the Simulation of Compressible Isothermal Fluid Flows

Rajaa Fadil¹(✉), Mohammed Rammane^{1,2}, Abdeljalil Tri^{3,4},
and Bouazza Braikat¹

¹ Laboratory of Engineering and Materials (LIMAT), Faculty of Sciences Ben M'sik, Hassan II University of Casablanca, B.P 7955, Sidi Othman, Casablanca, Morocco
rajaa.fadil3-etu@etu.univh2c.ma

² Laboratory of Materials, Signals, Systems and Physical Modeling, Faculty of Sciences of Agadir, University Ibn Zohr of Agadir, B.P 8106, 80000 Agadir, Morocco

³ Laboratory of Mechanics, Faculty of Sciences Ain Chock, Hassan II University of Casablanca, Casablanca, Morocco

⁴ Higher Institute of Maritime Studies (ISEM), Km 7 Route d'El Jadida, Casablanca, Morocco

Abstract. In this work, we propose an explicit meshless approach based on the coupling of the Weighted Least Squares (WLS) method and the explicit Runge-Kutta (RK) scheme. This last scheme is used to approximate time derivatives while WLS approximation is used for spatial discretization. The proposed meshless approach offers several advantages over traditional methods. This approach provides a powerful tool for simulating compressible fluid flows, offering improved accuracy and computational efficiency compared to traditional methods. This approach is dedicated to the study of the flows of compressible isothermal fluids whose mathematical formulation is governed by the Navier-Stokes equations written in a strong formulation to avoid any difficulty in integration calculating. This meshless approach is tested on the classic example of a square cavity with a discussion on effects of the Mach number and the monomial basis order. The results are compared to those obtained using a traditional finite difference method.

Keywords: WLS · Runge-Kutta · Navier-Stokes equations · Compressible fluid flow

1 Introduction

The simulation of physical problems described by systems of differential or partial differential equations is traditionally carried out using numerical resolution methods as Finite Element Method (FEM) [1] or Finite difference Method (FDM) [2].... In these methods, the spatial domain is discretized by meshes whose function is to define a topological link between the nodes. Meshless methods generally uses the same ingredients as traditional methods (approximation, resolution of the obtained algebraic system) but do not require a definition of the mesh then the considered domain is simply replaced by a cloud of nodes. Among

these methods, one can find the Smoothed Particle Hydrodynamics (SPH) [3,4], the Moving Least Squares (MLS) [5], the Radial Point Interpolation Method (RPIM) [6], the Weighted Least Squares (WLS) [7,8], etc. According to literature survey, these methods are widely used in various numerical algorithms to solve the Navier-Stokes equations for incompressible and compressible fluid flows [3–5,9].

For instationary problems, time scheme techniques are unavoidable and represent an active field of research. Many time discretization methods were used to solve the Navier-Stokes equations such as Euler Method [4,14], improved Euler [15] or Runge-Kutta [2,10,11], that uses either an explicit or an implicit time-stepping scheme. Explicit schemes are well known to be conditionally stable. Indeed, this requires a stability study of the numerical scheme leading to very small time steps and a large computation time.

In this work, a space-time procedure that combines the WLS approximation with the explicit Runge-Kutta scheme is proposed to study numerically the subsonic isothermal flows ($Ma < 0.4$) of a compressible viscous fluid, where Ma represents the Mach number. The performance of this approach will be tested on the standard benchmark lid-driven cavity problem, in order to display its advantage over the reference explicit scheme algorithms that uses FDM and MLS methods.

2 Governing Equations

Generally, the motion of a fluid is governed by three conservation laws that describe the conservation of mass, momentum and energy. For a subsonic isothermal viscous fluid flows ($Ma < 0.4$), the motion is described by the first two conservation laws, which are expressed as follows:

$$\begin{cases} \frac{\partial \rho}{\partial t} + \nabla \cdot (\rho \mathbf{V}) & = \mathbf{0} & \text{in } \Omega \\ \frac{\partial (\rho \mathbf{V})}{\partial t} + \nabla \cdot (\rho \mathbf{V} \cdot \mathbf{V}) = \nabla \cdot \boldsymbol{\sigma} & \text{in } \Omega \end{cases} \quad (1)$$

where ρ , ${}^T \mathbf{V} = \langle u, v \rangle$ and $\boldsymbol{\sigma}$ represent respectively the mass density, the bidimensional velocity vector and the stress tensor, this latter is defined for a Newtonian fluid by:

$$\begin{cases} \boldsymbol{\sigma} = -p\mathbf{I} + \boldsymbol{\tau} \\ \boldsymbol{\tau} = 2\mu\mathbf{D} - \frac{2}{3}\mu Tr(\mathbf{D})\mathbf{I} \\ \mathbf{D} = \frac{1}{2}({}^T \nabla \mathbf{V} + \nabla \mathbf{V}) \end{cases} \quad (2)$$

where p is the pressure term, \mathbf{I} denotes the identity tensor, $\boldsymbol{\tau}$ is the viscous stress tensor, μ denotes the dynamic viscosity and \mathbf{D} is the strain rate tensor.

The state equation relates the pressure term to the density of a compressible fluid. For isothermal subsonic flows ($Ma < 0.4$), this equation is defined by:

$$p = c^2 \rho \quad (3)$$

where c is the speed of sound propagation in the fluid [3,5,9].

By injecting Eqs. (2) and (3) into Eq. (1), the subsonic compressible isothermal Navier-Stokes equations are obtained as follows:

$$\begin{cases} \frac{\partial \rho}{\partial t} + \nabla \cdot (\rho \mathbf{V}) & = 0 & \text{in } \Omega \\ \frac{\partial (\rho \mathbf{V})}{\partial t} + \nabla (\rho \mathbf{V} \cdot \mathbf{V}) = \mu \Delta \mathbf{V} + \frac{\mu}{3} \nabla (\nabla \cdot \mathbf{V}) - c^2 \nabla \rho & \text{in } \Omega \end{cases} \quad (4)$$

The initial conditions for the velocity \mathbf{V} and for the mass density ρ are given as:

$$\begin{cases} \mathbf{V}(M, t_0) = \mathbf{V}_0 & \text{for } M \in \Omega \\ \rho(M, t_0) = \rho_0 & \text{for } M \in \Omega \end{cases} \quad (5)$$

where \mathbf{V}_0 and ρ_0 are respectively the initial state of fluid velocity and its mass density and M is a point of coordinates (x, y) .

For the boundary conditions, the non-slip condition of the velocity is used on $\partial\Omega_V$, while for the mass density they are derived from the momentum equation using the normal vector $n = {}^T \langle n_x, n_y \rangle$ on the boundary $\partial\Omega_\sigma$ as follows :

$$\begin{cases} c^2 \nabla \rho \cdot \mathbf{n} = (\mu \Delta \mathbf{V} + \mu/3 \nabla (\nabla \cdot \mathbf{V}) - \frac{\partial (\rho \mathbf{V})}{\partial t} - \nabla (\rho \mathbf{V} \cdot \mathbf{V})) \cdot \mathbf{n} & \text{for } M \in \partial\Omega_\sigma \\ \mathbf{V}(M, t) = \mathbf{V}_d & \text{for } M \in \partial\Omega_V \end{cases} \quad (6)$$

where \mathbf{V}_d is a given speed vector. In order to simply apply the proposed approach procedures, we choose to rewrite the system of Eqs. (4), (5) and (6) in the following compact quadratic form:

$$\mathbf{M} \dot{\mathbf{U}} + \mathbf{L}(\mathbf{U}) + \mathbf{Q}(\mathbf{U}, \mathbf{U}) = 0 \quad (7)$$

where \mathbf{M} is the mass operator, $\mathbf{U} = {}^T \langle u, v, \rho \rangle$ is a vector that collects the unknowns of the problem, \mathbf{L} is the linear operator and \mathbf{Q} represents the quadratic form.

3 Resolution Strategy

In the literature, the resolution of the instationary Navier-Stokes equations is accomplished by the use of space-time discretization methods. This combination represents a necessary tool to transform the continuous problem into a discrete problem in time and space. In this work, the explicit Runge-Kutta scheme and the WLS method are used to solve under the strong formulation the space-time problem of (7).

3.1 Approximation for Spatial Discretization

The Weighted Least Squares (WLS) approximation is an extensively used technique for data fitting and surface construction [6]. The WLS approximation is

one of the meshless methods that allows to avoid meshing generation techniques which requires considerable computation time. The approximation of a function $u(x, y)$ at a point of coordinates (x, y) is defined as follows:

$$u(x, y) = \sum_{i=0}^m p_i(x, y)a_i = \langle p(x, y) \rangle \{a\} \tag{8}$$

where $p_i(x, y)$ is a given monomial basis function in the space coordinates (x, y) , m is the number of monomials, and a_i is the coefficient for $p_i(x, y)$ which is yet to be determined. The $p_i(x, y)$ in Eq. (8) is built using Pascal's triangles, and a complete basis is usually (but not always) preferred. The most used vectors of monomial basis functions are defined as follows:

$$\begin{cases} m = 3 & : \langle p(x, y) \rangle = \langle 1, x, y \rangle \\ m = 6 & : \langle p(x, y) \rangle = \langle 1, x, y, xy, x^2, y^2 \rangle \\ m = 10 & : \langle p(x, y) \rangle = \langle 1, x, y, xy, x^2, y^2, x^2y, xy^2, x^3, y^3 \rangle \end{cases} \tag{9}$$

The determination of the unknown coefficients a_i is carried out by minimizing the following weighted discrete norm by using all the nodes selected inside the local support domain:

$$J = \sum_{i=1}^n W_i (u(x, y) - u_i)^2 \tag{10}$$

where n is the number of the selected nodes in the support domain, u_i is the nodal unknown of u and W_i is the Gaussian weighting function associated to node i defined by:

$$W_i = \frac{e^{-\left(\frac{r}{c_w}\right)^{2k}} - e^{-\left(\frac{1}{c_w}\right)^2}}{1 - e^{-\left(\frac{1}{c_w}\right)^2}} \tag{11}$$

with $r = \sqrt{(x - x_i)^2 + (y - y_i)^2}/rs$, (x, y) is the coordinate of the interest point, rs is the size of local support domain and c_w is a constant to be determined by the analyst before calculation. The stationary condition of Eq. (10) gives:

$$\frac{\partial J}{\partial \{a\}} = 0 \tag{12}$$

The Eq. (12) leads to the following linear relation between the vector $\{a\}$ and the nodal vector $\{U\}$:

$$[A]\{a\} = [B]\{U\} \tag{13}$$

where the matrices $[A]$ and $[B]$ the nodal vector $\{U\}$ are defined as follows:

$$\begin{cases} [A] & = \sum_{i=1}^n W_i \{p(x_i, y_i)\} \langle p(x_i, y_i) \rangle \\ [B] & = \sum_{i=1}^n W_i \{p(x_i, y_i)\} \\ \langle U \rangle & = \langle u_1, u_2, \dots, u_n \rangle \end{cases} \tag{14}$$

By injecting the expression of $\{a\}$ in Eq. (8), the WLS approximation of the field unknown $u(x, y)$ is obtained as follows:

$$u(x, y) = \langle \phi(x, y) \rangle \{U\} = \sum_{i=1}^n \phi_i(x, y) u_i \quad (15)$$

where $\langle \phi(x, y) \rangle$ is the vector of shape functions expressed by:

$$\langle \phi(x, y) \rangle = \langle p(x, y) \rangle [A]^{-1} [B] \quad (16)$$

Finally, the field unknowns of the problem (7) are approximated via WLS as follows:

$$\begin{cases} u = \sum_{i=1}^n \phi_i u_i \\ v = \sum_{i=1}^n \phi_i v_i \\ \rho = \sum_{i=1}^n \phi_i \rho_i \end{cases} \quad (17)$$

3.2 Explicit Runge-Kutta Scheme

Several numerical solvers, that use the explicit fourth-order Runge-Kutta scheme, have been used in literature to solve the Navier-Stokes equations for compressible and incompressible fluids [2, 9, 10]. The explicit time discretization aims at searching the temporal solution by using the time-stepping scheme at the current moment $t_n = n\Delta t$, with Δt is the time step, such as:

$$M\dot{U}^n = -L(U^n) - Q(U^n, U^n) \quad (18)$$

This latter allows to obtain a linear equation, by searching the unknowns at the moment t_{n+1} using a time-stepping integration of \dot{U}^n . In this study, the fourth-order Runge-Kutta time integration is used in order to obtain the unknowns at the moment $t_{n+1} = (n+1)\Delta t$ as follows:

$$\begin{cases} U^0 & : \text{Initial condition} \\ K_1 & = F(U^n) \\ K_2 & = F(U^n + \frac{\Delta t}{2} K_1) \\ K_3 & = F(U^n + \frac{\Delta t}{2} K_2) \\ K_4 & = F(U^n + \Delta t K_3) \\ \mathcal{F} & = \frac{\Delta t}{6} (K_1 + 2(K_2 + K_3) + K_4) \\ U^{n+1} & = U^n + M_n^{-1} \mathcal{F} \end{cases} \quad (19)$$

where $F(\bullet) = -L(\bullet) - Q(\bullet, \bullet)$. For this type of schemes, the study of the stability in time is limited to the choice of the time step Δt . It is usually calculated by the Courant-Friedrichs-Lewy condition (CFL-Condition) [2, 9, 12, 13]. The latter is a stability condition for unstable numerical schemes. For the Navier-Stokes equations of isothermal compressible Newtonian fluids, the time step Δt is defined by:

$$\Delta t < \min \left(\frac{h}{c + \sqrt{u^2 + v^2}}, \frac{\rho h^2}{4\mu} \right) \quad (20)$$

where h is the inter-point distance, c is the speed of sound, u and v are the components of the velocity of the fluid, ρ and μ are respectively the mass density and the dynamic viscosity of the fluid.

4 Numerical Application and Discussion

The classical flow in a cavity is used to test the validity of the proposed explicit meshless approach. The cavity is represented schematically in Fig. 1. The domain is assumed to be square with side $Lx = Ly = l_0 = 1m$ where the three sides AB , BC and AD are fixed, while the top wall DC moves with a constant horizontal velocity u_0 . The study of this problem is made in the system of origin M and of axes x and y .

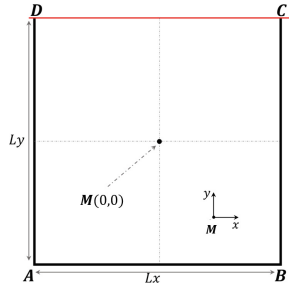
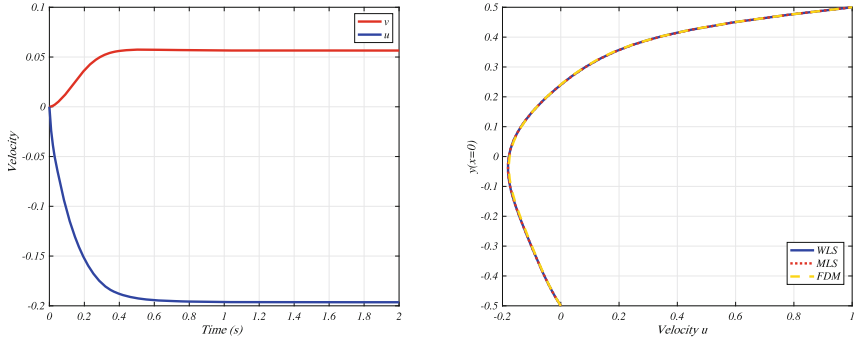


Fig. 1. Domain and boundary conditions

The properties of the fluid are chosen such as: the initial density of the fluid is taken equal to $\rho_0 = 1 \text{ kg/m}^3$, the dynamic viscosity $\mu = 0.1 \text{ kg/ms}$, the Mach number is chosen as $Ma = 0.1$, the Reynolds number is taken as $Re = 100$ and the speed of sound is given by $c = u_0/Ma$, where u_0 is the initial given velocity at the top wall DC , with $u_0 = \mu Re / (Lx \rho_0)$ (i.e. for $Re = 100$, $u_0 = 10 \text{ m/s}$).

To show the efficiency of our approach, we present in Fig. 2 the time evolution of the velocity components at the center of the cavity and a comparison of the stationary solutions obtained by WLS, MLS and FDM [2], using a number of nodes equal to 2601, a support domain radius $rs = 3.03h$, $h = \Delta x = \Delta y = 0.02$ and $c_\omega = 0.2$. The value of c_ω is selected after conducting a series of numerical

experiments. From this figure, we notice that the stationary state is reached after the time $t = 0.9$ s and that the stationary solutions obtained by the meshless methods coincide with the solution obtained using the FDM coupled with the explicit Runge-Kutta scheme.



(a) Temporal evolution of u and v at point $M(0,0)$ (b) Evolution of u along the line $y(x = 0)$

Fig. 2. Comparison of the solutions obtained by the three methods WLS, MLS and FDM

In Fig. 3, the steady state solutions of the streamlines are presented. The streamline results show a typical separation of one primary and two secondary vortices located at the lower corners of the cavity. The obtained solution represents a result similar to those in the literature [5].



Fig. 3. Streamlines of subsonic flow in a square cavity for $Re = 100$ and for $Ma = 0.1$

In the following, we will study the effects of the monomial basis order and the Mach number.

4.1 Effect of the Monomial Basis Order

In Table 1, we present the effect of the monomial basis order m used in the WLS and MLS approximations on the relative error of the stationary solutions obtained by the meshless methods with the FDM. The table shows that the WLS approximation has a good convergence whatever the order of the basis, while the MLS approximation converges only with order $m = 6$. These results show the stability of the WLS approximation compared to the MLS for the same radius of the domain support. Let note that to obtain good results via MLS, one must increase the support domain radius for each value of the monomial basis order $m > 6$.

Table 1. Effect of the monomial basis order m in the MLS and WLS approximations on the relative error with respect to the FDM

Approximation	number of basis m		
	6	10	15
MLS	10^{-6}	10^{-2}	10^{-1}
WLS	10^{-6}	10^{-6}	10^{-6}

4.2 Effect of Mach Number

The important parameter in the analysis of compressible fluid flow is the Mach number Ma . It is the ratio of the actual speed of the fluid to the speed of sound in the same fluid at the same state. For this, we propose to study the effect of this parameter on the fluid density behavior in square cavity. For that, we present in Fig. 4 the isovalues of mass density distribution at $Re = 100$ and for a Mach number equal to $Ma = 0.1, 0.2$ and 0.3 . The results show that the mass density reaches a maximum value where the flow speed is imposed and a minimum value at the primary fluid's recirculation. It is also noticed that the fluid density concentration increases when Mach number increases as well. Let note that these results are similar to those presented in the literature investigations [2, 5].

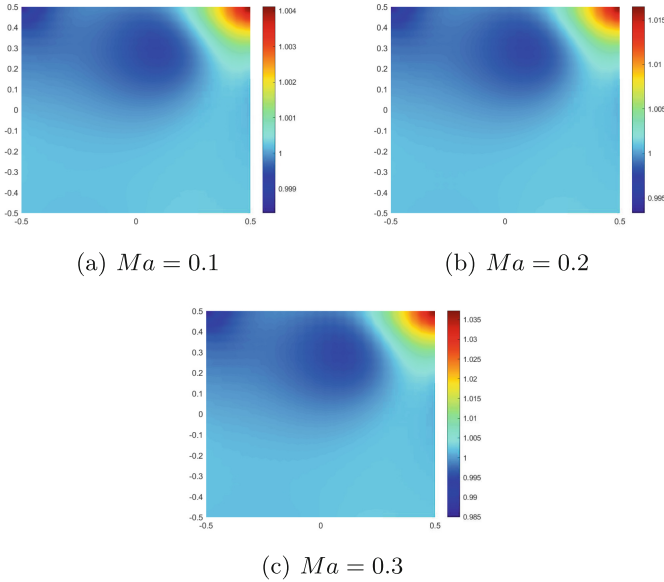


Fig. 4. Steady state density distribution of subsonic flow in a square cavity for $Ma = 0.1, 0.2, 0.3$

5 Conclusion

In this work, we proposed an algorithm combining the explicit Runge-Kutta scheme and the WLS approximation to solve the Navier-Stokes equations describing the isothermal subsonic flow of compressible fluids. The proposed approach is tested on the classical square cavity example. The results obtained from the presented tests have shown that our approach is able to simulate isothermal subsonic flows. Work is in progress to extend this technique to the study of supersonic flows.

References

1. Bathe, K.J.: Finite Element Method. Wiley Encyclopedia of Computer Science and Engineering (2007)
2. Bao, W., Jin, S.: High-order I-stable centered difference schemes for viscous compressible flows. *J. Comput. Math.* **21**, 101–112 (2003)
3. Xu, X., Deng, X.L.: An improved weakly compressible SPH method for simulating free surface flows of viscous and viscoelastic fluids. *Comput. Phys. Commun.* **201**, 43–62 (2016)
4. Hashemi, M.R., Manzari, M.T., Fatehi, R.: Evaluation of a pressure splitting formulation for Weakly Compressible SPH: fluid flow around periodic array of cylinders. *Comput. Math. Appl.* **71**(3), 758–778 (2016)

5. Rammane, M., Mesmoudi, S., Tri, A., Braikat, B., Damil, N.: A dimensionless numerical mesh-free model for the compressible fluid flows. *Comput. Fluids* **221**, 104845 (2021)
6. Liu, G.R., Gu, Y.T.: *An Introduction to Meshfree Methods and Their Programming*. Springer, Cham (2005). <https://doi.org/10.1007/1-4020-3468-7>
7. Elmhaia, O., Belaasilia, Y., Askour, O., Braikat, B., Damil, N.: An efficient mesh-free approach for the determination of stresses intensity factors. *Eng. Anal. Boundary Elem.* **133**, 49–60 (2021)
8. Elmhaia, O., Belaasilia, Y., Askour, O., Braikat, B., Damil, N.: Numerical analysis of frictional contact between crack lips in the framework of Linear Elastic Fracture Mechanics by a mesh-free approach. *Theor. Appl. Fract. Mech.* **2023**, 103749 (2023)
9. Felner, C.L., Walther, J.H., Henriksen, C.: Moving least squares simulation of free surface flows. *Comput. Fluids* **91**, 47–56 (2014)
10. Boretti, A.A.: An explicit Runge-Kutta method for turbulent reacting flows calculations. In: Dervieux, A., Larrouturou, B. (eds.) *Numerical Combustion: Proceedings of the Third International Conference on Numerical Combustion Held in Juan les Pins, Antibes, 23–26 May 1989*, vol. 351, pp. 199–210. Springer, Heidelberg (2005). <https://doi.org/10.1007/3-540-51968-8.84>
11. Bourantas, G.C., et al.: An explicit meshless point collocation solver for incompressible Navier-Stokes equations. *Fluids* **4**(3), 164 (2019)
12. Courant, R., Friedrichs, K., Lewy, H.: On the partial difference equations of mathematical physics. *IBM J. Res. Dev.* **11**(2), 215–234 (1967)
13. Anderson, J.D., Wendt, J.: *Computational Fluid Dynamics*, vol. 206, p. 332. McGraw-Hill, New York (1995)
14. Jamal, M., Braikat, B., Boutmir, S., Damil, N., Potier-Ferry, M.: A high order implicit algorithm for solving in stationary non-linear problems. *Comput. Mech.* **28**, 375–380 (2002)
15. Guevel, Y., Girault, G., Cadou, J.M.: Numerical comparisons of high-order non-linear solvers for the transient Navier-Stokes equations based on homotopy and perturbation techniques. *J. Comput. Appl. Math.* **289**, 356–370 (2015)



Effect of Thermal Parametric Excitation on the Destabilization of a Linearly Stable System

Mohamed Sakine¹, Mohamed Hayani Choujaa³, Mehdi Riahi^{2,3},
Abdelmajid Daya¹, and Saïd Aniss^{3(✉)}

¹ Laboratory of Mechanic Energy and Renewable Energy, FSTE, Moulay Ismail University, 509, Errachidia, Morocco

² Department of Mechanics, Royal Air School, Marrakech, Morocco
mehdi_riahi@hotmail.fr

³ Laboratory of Mechanics, Faculty of Sciences Aïn Chock, University Hassan II, B.P 5366, Mâarif, Casablanca, Morocco
said.aniss@etu.univh2c.ac.ma

Abstract. In this paper, we focus on analyzing the linear stability of a Newtonian fluid layer whose upper surface is subjected to parametric thermal excitation that is periodic in time with zero mean. The fluid layer is considered of infinite extension in the horizontal directions. The Floquet theory and the Chebyshev spectral collocation method are used to solve the linear stability problem in the case of rigid-rigid boundary conditions. Although the unmodulated version of this configuration, where the fluid layer is heated from above, is known to be linearly stable, it turns out that destabilization is possible in the presence of modulation on the top surface. Parametric resonances appear at the onset of the instability, and the convection threshold is harmonic or sub-harmonic depending on the range of oscillation frequencies. The dynamics of this instability is characterized by the existence of a bifurcation point in codimension two, giving rise to a discontinuity in the evolution of the critical wavenumber at a specific frequency number.

Keywords: stability · convection · temperature modulation · Floquet theory · spectral method

1 Introduction

The stability of time-dependent equilibrium states was the subject of several studies over the last century. This circumstance is encountered in several industrial and natural applications. Examples include the earth's atmosphere, which is periodically heated by the sun, and flows in internal combustion engines. A time-periodic heating/cooling, in addition to ventilation and air-conditioning, helps control the onset of instability, providing thermal comfort in a confined space. This control strategy could modify the energy performance of the building

by predicting the thermal responses and optimizing therefore the energy costs. Rayleigh-Bénard convection is considered one of the classic prototypes of natural convection, which appears in many building engineering applications, such as thermal comfort through floor heating or ceiling cooling. In this framework, classical textbooks on thermal convection and hydrodynamic instabilities in general (Chandrasekhar 1961 [1], Drazin & Reid 1982 [2]) were implemented in the case of steady temperatures in the boundaries. Recently, Nasser et al. [3] investigated the time-periodic cooling of Rayleigh-Bénard convection using the Lattice Boltzmann method with multiple relaxation time. It was shown that the flow structure shifts from a single-cell flow to a counter-rotating two-cell flow at very high Rayleigh numbers and low heating amplitudes. In this paper, we extend this flow configuration to a fluid layer with infinite extension in the horizontal directions, focusing on the critical onset of the transition between conductive and convective heat transfer regimes. We are interested in the case where the stationary component of the temperature gradient is zero, which means that the instability mechanism is governed by a parametric resonance. In other words, this is an example where a linearly stable equilibrium can be destabilized by parametric excitation.

Early work on modulating boundary conditions was initiated experimentally by Donnelly, who studied time-periodic flow between two concentric cylinders. He considered the case where the outer cylinder is stationary and the inner cylinder subject to a periodic angular velocity. He found that at low frequencies, instability is delayed compared to the stationary case. This configuration has been revisited by several authors in the literature in various forms of modulation of boundary conditions in the case of Newtonian and non-Newtonian fluids [5–11].

Donnelly's configuration was extended by Venezian to Rayleigh-Bénard convection. He asserted that an additional sinusoidal time-varying perturbation applied to the temperature of the lower surface can control the convection threshold. A linear stability analysis showed a stabilizing effect at low modulation amplitudes. For low-frequency modulation with arbitrary amplitude, Rosenblat and Herbert [13] gave an asymptotic solution. Yih and Li [14] also used the Galerkin method to study the case where the modulated temperature gradient is symmetrical with respect to the median plane. They showed that perturbations (or convective cells) oscillate either synchronously or sub-harmonically. Souhar et al. performed a linear stability analysis of an equilibrium state generated by in-phase time modulation without a stationary gradient component. In this case, the upper and lower plates were subjected to a time-periodic modulation of temperature with the same frequency and amplitude. The system proved potentially unstable at moderate frequencies, while stabilization occurs at low and high frequencies. The case of the Maxwellian liquid layer in the presence of temperature modulation was studied by Oukada et al. [16]. They emphasized the combined effects of fluid elasticity and time periodic boundary conditions on the onset of instability. Rayleigh-Bénard convection in a horizontal fluid layer subjected to time periodic heating with the presence

of two frequencies was analyzed numerically by Kaur et al. [17]. They showed that the frequency ratio and the mixing angle of the modulation amplitudes control instability. It was also concluded that, compared to single-frequency forcing, two-frequency modulation triggers more bicritical states between the well-known harmonic and subharmonic thresholds. Recently, Hazra et al. [18] studied the modulated magnetoconvection in Rayleigh-Benard configuration using Floquet theory. The system becomes dependent on a new magnetic parameter called the Chandrasekhar number Q , and it turned out that temperature modulation can either delay or accelerate the onset of magnetoconvection. They found a new type of bicritical state that occurs between two different sets of harmonically unstable tongues.

The aim of the present paper is to examine the effect of a time-periodic temperature modulation with zero mean on the stability of a Newtonian liquid layer, between two parallel horizontal walls. Here, we consider the case where the liquid layer is sinusoidally heated from above. Although the steady configuration corresponding to a fluid layer heated from above is well known to be linearly stable, we show that a temporal modulation can lead to a destabilization.

2 Linear Stability Analysis of the Basic State

Consider a Newtonian liquid layer, between two parallel horizontal walls, d apart and of infinite extension in the horizontal directions x^* and y^* , see Fig. 1. The two surfaces ($z^* = 0, z^* = d$) are respectively subject to the temperatures: $T(0, t^*) = T_m$ and $T(d, t^*) = T_m + T_s \cos(\omega^* t^*)$, where T_m is the ambient temperature, T_s is the modulation amplitude and ω^* is the modulation frequency. The system of equations governing the convective instability is that of classical conservation equations obeying to the Boussinesq approximation, written in the following dimensionless form:

$$\nabla \cdot \mathbf{V} = 0 \quad (1)$$

$$Pr^{-1} \left(\frac{\partial \mathbf{V}}{\partial t} + (\mathbf{V} \cdot \nabla) \mathbf{V} \right) = -\nabla P + \Delta \mathbf{V} + Ra T \mathbf{e}_z \quad (2)$$

$$\frac{\partial T}{\partial t} + \mathbf{V} \cdot \nabla T = \Delta T \quad (3)$$

This dimensionless form is obtained by using the characteristic distance between the two horizontal walls d as the space scale, κ/d for the velocity scale, d^2/κ for the time scale, T_s for the temperature and finally $\mu\kappa/d^2$ for the pressure, where μ and κ are the dynamic viscosity and thermal diffusivity respectively. The Prandtl number is given by $Pr = \frac{\nu}{\kappa}$ while the Rayleigh number is defined by $Ra = \frac{\beta g T_s d^3}{\nu \kappa}$, where κ is the coefficient of thermal dilatation and ν is the kinematic viscosity.

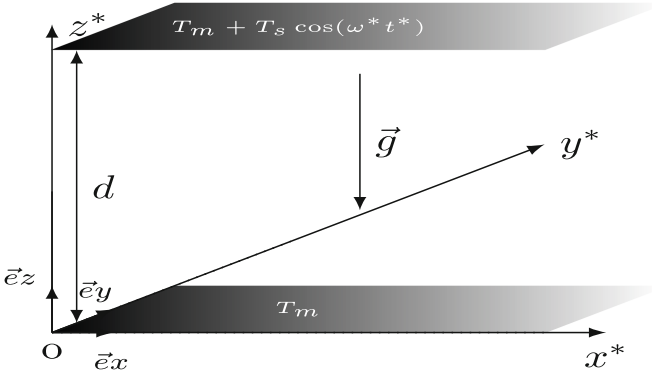


Fig. 1. Geometry of the problem

For very small Rayleigh number, the system is supposed in a purely conductive regime and the fluid is then considered at rest, $\mathbf{V} = \mathbf{0}$. The dimensionless energy Eq. (3) at equilibrium is expressed as follows

$$\frac{\partial T_b}{\partial t} = \frac{\partial^2 T_b}{\partial z^2}. \tag{4}$$

with the following boundary conditions:

$$T_b(z = 0, t) = 0 \quad \text{and} \quad T_b(z = 1, t) = \cos(\sigma t) \tag{5}$$

The Eq. (4) is solved for a very long time scale. The solution is therefore expressed as follows:

$$T(z, t) = T_1(z) \cos(\sigma t) + T_2(z) \sin(\sigma t) \tag{6}$$

where

$$T_1(z) = \frac{\cosh(\gamma z) \cos(\gamma(1 - z)) \cosh(\gamma) - \cosh(\gamma(1 - z)) \cos(\gamma z) \cosh(\gamma)}{\cosh^2(\gamma) - \cos^2(\gamma)} \tag{7}$$

$$T_2(z) = \frac{\sinh(\gamma z) \sin(\gamma(1 - z)) \cosh(\gamma) - \sinh(\gamma(1 - z)) \sin(\gamma z) \cosh(\gamma)}{\cosh^2(\gamma) - \cos^2(\gamma)} \tag{8}$$

The frequency parameter $\gamma = \sqrt{\sigma/2} = d/\delta_S$ is the ratio between two characteristic lengths: d and the thickness of the thermal boundary layer defined by: $\delta_S = (2\nu/\omega^*)^{1/2}$. The parameter $\sigma = \omega^* d^2/k$ is the ratio between the modulation period T and the thermal diffusive time d^2/k .

To study the stability of the basic solution, it is perturbed as follows:

$$\mathbf{V}^* = \mathbf{V}^*(x, y, z) = (u, v, w); \quad p^* = p_b + p; \quad T^* = T_b + T; \quad \rho^* = \rho_b + \rho \tag{9}$$

By substituting these variables (9) into the dimensionless governing Eqs. (1)–(3) and by subsequently neglecting all nonlinear terms, the following stability system is obtained:

$$\nabla \cdot \mathbf{V}^* = 0 \tag{10}$$

$$Pr^{-1} \frac{\partial \Delta w}{\partial t} = \Delta(\Delta w) + Ra \Delta_2 T \quad (11)$$

$$\frac{\partial T}{\partial t} + w \frac{\partial T_b}{\partial z} = \Delta T \quad (12)$$

The system (10)–(12) is associated to the rigid-rigid boundary conditions:

$$w = \frac{\partial w}{\partial z} = T = 0 \quad \text{at} \quad z = 0.1 \quad (13)$$

where $\Delta = \frac{\partial^2}{\partial x^2} + \frac{\partial^2}{\partial y^2} + \frac{\partial^2}{\partial z^2}$ and $\Delta_2 = \frac{\partial^2}{\partial x^2} + \frac{\partial^2}{\partial y^2}$. Taking into account spatial periodic conditions in the horizontal directions, solution of the system (10)–(12) is in the form:

$$(w(x, y, z, t), T(x, y, z, t)) = (\tilde{w}(z, t), \tilde{T}(z, t)) e^{i(q_x x + q_y y)}. \quad (14)$$

We denote by q_x and q_y the wavenumbers in the x and y directions respectively. Thus, the linear stability system (10)–(12) becomes:

$$\left(Pr^{-1} \frac{\partial}{\partial t} - M \right) M \tilde{w} + q^2 Ra \tilde{T} = 0 \quad (15)$$

$$\left(\frac{\partial}{\partial t} - M \right) \tilde{T} + \tilde{w} \frac{\partial T_b}{\partial t} = 0 \quad (16)$$

where $M = \frac{\partial^2}{\partial z^2} - q^2$ and $q^2 = q_x^2 + q_y^2$. The boundary conditions (17) are now written as follows:

$$\tilde{w} = \frac{d\tilde{w}}{dz} = \tilde{T} = 0 \quad \text{at} \quad z = 0.1 \quad (17)$$

3 Numerical Resolution

3.1 Spatial Discretization

The system of Eqs. (15)–(16) is solved numerically using a spatial discretization in the interval $[-1, 1]$ referring to Chebyshev's spectral collocation method. An example of this method is given in the references [10, 11]. This discretization leads to a matrix formulation written as follows:

$$\bar{\mathbf{B}} \frac{\partial}{\partial t} \hat{\mathbf{X}} = \bar{\mathbf{M}}(t) \hat{\mathbf{X}} \quad (18)$$

where $\bar{\mathbf{M}}(t) = \mathbf{M}_0 + \mathbf{M}_c \cos(\sigma t) + \mathbf{M}_s \sin(\sigma t)$ is a $\frac{2\pi}{\sigma}$ periodic matrix whereas $\bar{\mathbf{B}}$, M_0 , M_c and M_s are constant coefficient matrices.

3.2 Floquet Theory

The Floquet theory is used to solve the system (16) which is $2\pi/\sigma$ periodic in time. This theory stipulates that there exists a constant matrix \mathbf{R} such that;

$$\mathbf{S}(t + T) = \mathbf{R}\mathbf{S}(t) \quad (19)$$

Thus, we obtain

$$\bar{\mathbf{B}} \frac{\partial \mathbf{S}}{\partial t} = (\mathbf{M}_0 + \mathbf{M}_c \cos(\sigma t) + \mathbf{M}_o \sin(\sigma t)) \mathbf{S} \quad (20)$$

Moreover, if μ_j ($1; \dots; N+2$) denote the eigenvalues of the matrix \mathbf{R} , the solution of the system (20) is:

$$\phi_j = Z_j(t) \exp(\lambda_j t) \quad (21)$$

where $\mathbf{Z}(t)$ is a periodic function of period T and the Floquet exponents λ_j are given by the relation:

$$\lambda_j = \frac{1}{T} \ln(\mu_j) \quad (22)$$

Thus, \mathbf{R} is determined numerically via a fourth-order Runge-Kutta numerical scheme integrating the system (20) over one period with the initial condition $\mathbf{S}(0) = \mathbf{I}$, where \mathbf{I} is the identity matrix. The eigenvalues of the matrix \mathbf{R} , μ_j allow us to determine the Floquet exponents λ_j using Eq. (23). It should be noted here that the stability of the basic state is determined by the Floquet multipliers:

$$\mu = e^{(\lambda_r + i\lambda_i)T} \quad (23)$$

where the real part of its exponent, λ_r , represents the growth rate of the perturbation while the imaginary part, λ_i , designates the argument (angle) of the Floquet multiplier that represents the existence of a temporal quasi-periodicity in the system response. As there are no quasi-periodic solutions in the present study, this quantity is taken to be zero. Instability therefore depends only on λ_r in the sense that for $\lambda_r < 0$ perturbations decreases exponentially fast and the system is stable. Otherwise, the system is unstable, with perturbations increasing rather than decreasing. Equivalently, stability could be discussed on the basis of the Floquet multiplier, meaning that stability is conditioned by the moduli of the Floquet multipliers which are smaller than one. Moreover and as it is commonly known, systems subjected to time-periodic forcing (considered here as thermal) react synchronously or subharmonically according to the frequency response σ_F . Indeed, if $\sigma_F = \sigma$ the solution is harmonic, also called synchronous, whereas it is considered subharmonic if $\sigma_F = \sigma/2$. The distinction between these responses can be made by considering the growth rate λ_r . Harmonic solutions correspond to $\lambda_r = 1$ while $\lambda_r = -1$ corresponds to subharmonic ones.

4 Numerical Results

4.1 Instability in Sense of Floquet: Growth Rate and Floquet Multiplier

To illustrate the criterion of instability in the Floquet sense, we plot in Fig. 2(a) the evolution of the maximum growth rate of the perturbation as a function of the wavenumber q at frequency number $\gamma = 1.3$ and for different values assigned to the Rayleigh number. Considering water as the fluid confined between the horizontal walls, we assign Prandtl's number the value $Pr = 7$. For $Ra^{1/2} = 116$, we can clearly see that all calculated values of λ_r are negative, which means that the flow is stable. Instability arises at $Ra^{1/2} = 118.015$ for $q = 3.3$. These values of Rayleigh and wavenumbers are then said to be critical, as they correspond to a case where a value of the Floquet exponent crosses the 0 value. Note here that this evolution has two maxima, due to the existence of two types of solutions known as “harmonic” and “subharmonic”. These modes exist at $Ra^{1/2} = 118.051$, but the instability is initiated by the subharmonic mode, meaning that the harmonic mode is still stable. By increasing the Rayleigh number, in particular to $Ra^{1/2} = 121.8$, the harmonic mode becomes unstable and two solutions coexist for $Ra^{1/2} > 121.8$.

The same evolution is depicted in Fig. 2(b) for a constant value of the Rayleigh number, $Ra^{1/2} = 116$, and different values of the frequency number. The most interesting feature is the change in nature of the first instability as the frequency modulation is varied. Indeed, for $\gamma = 1.41$, the basic state is unstable with $q_c = 3.4$ and this instability corresponds to an harmonic solution. This instability is suppressed at a lower oscillation frequency $\gamma = 1.3$. Moreover, the system becomes unstable with subharmonic instability at $\gamma = 1.23$ with $q_c = 4.5$. We can therefore conclude that frequency modulation not only controls the onset of system instability, but also brings about a change in the nature of that instability.

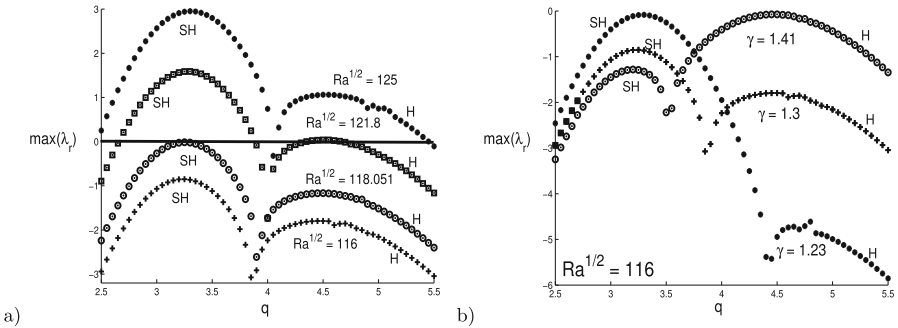


Fig. 2. Dominant growth rate of the perturbation versus the wavenumber for some representative values of the Rayleigh number at $\gamma = 1.3$.

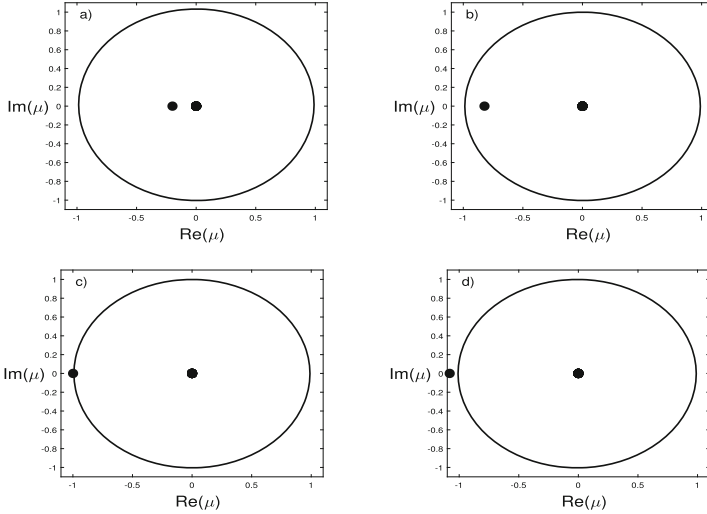


Fig. 3. Floquet multipliers at $\gamma = 1.3$ and $q = 3.2$ for: (a) $Ra^{1/2} = 116$, (b) $Ra^{1/2} = 117.8$, (c) $Ra^{1/2} = 118.051$ and (d) $Ra^{1/2} = 118.15$.

To determine the nature of the modes observed in Fig. 2(a) and 2(b), we recourse to the Floquet multiplier shown in Fig. 3 for $\gamma = 1.3$ in the complex plane. Let's start with the first branch in the low-wavenumber range and arbitrarily choose $q = 3.3$, since all points in this branch have the same characteristics. For $Ra^{1/2} = 116$, all Floquet multipliers (dots) lie inside the unit circle, which means the system is stable at this Rayleigh number with $|\mu| = 0.2$, see Fig. 3(a). As the Rayleigh number increases, particularly at $Ra^{1/2} = 117.8$, the multiplier approaches the unit circle, with $|\mu| = 0.82$. At the onset of instability where $Ra^{1/2} = 118.051$, this multiplier crosses the unit circle with $|\mu| = 1$. This latter becomes greater than one beyond $Ra^{1/2} = 118.051$ especially it takes $|\mu| = 1.08$ when $Ra^{1/2} = 118.15$ is reached. It should be noted here that the imaginary part of these multipliers vanishes since no quasi-periodic behavior is expected. Besides, the real part of this multiplier equals -1 since we are dealing with a subharmonic solution.

The same approach is adopted to determine the nature of the second branch of the Fig. 2, which corresponds to a harmonic mode. Here, a positive value of λ_r is expected, reaching 1 at the critical onset of instability.

4.2 Marginal Stability Curves and Instability Diagrams

For certain representative values of the frequency number, marginal stability curves are illustrated in Fig. 4. As one can see, these curves are composed of two parabolas with two minima and a bi-critical state is obtained. This latter corresponds to a state with two critical wavenumbers having the same critical Rayleigh number. Such behavior was observed in modulated Taylor-Couette

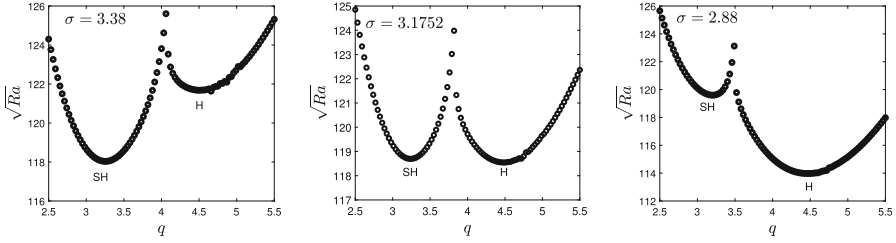


Fig. 4. Marginal stability curves near the co-dimension two bifurcation point.

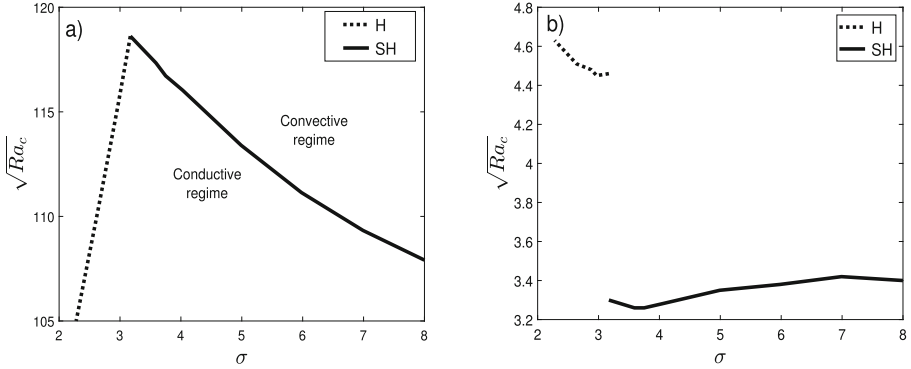


Fig. 5. Stability diagrams showing the evolution of the critical instability parameters. a) $\sqrt{Ra_c}$ versus σ and b) q_c versus σ .

flow [5–11] and Poiseuille flow [21] and dubbed the “mode competition” phenomenon and concerns the appearance of an inversion flow observed in similar configurations [22, 23]. Indeed, at $\sigma = 3.38$ two instability modes, harmonic and subharmonic, arise and the most unstable one is subharmonic. At $\sigma = 3.1752$ two incommensurate critical wavenumbers are obtained at the critical Rayleigh number $Ra_c = 14042.5$. However, the primary instability switch from subharmonic to harmonic mode by decreasing the frequency number.

In Fig. 5, we report the stability diagram of the system obtained from several computations of marginal stability curves at different frequencies showing the critical Rayleigh number versus the frequency modulation. At $\gamma = 8$ the onset of convection appears at $Ra_c = 11664$ and $q_c = 3.4$ and a decrease in the parameter σ leads to an increase in the critical Rayleigh number. In this situation, the system responds subharmonically (with half the frequency) to the thermal drive with a relatively constant critical wavenumber. This behavior also indicates a stabilizing effect of the modulation frequency. However, a jump in the evolution of the wavenumber from $q_c = 3.3$ to $q_c = 4.9$ is observed at $\sigma = 3.1752$ where the bicritical state occurs. This feature is accompanied by a discontinuity in the critical Rayleigh number evolution and a change in the primary bifurcation from subharmonic to harmonic solution. In this case, the system reacts harmonically

to the thermal drive (with the same frequency). Finally, a destabilizing effect of modulation frequency is observed when $\sigma > 3.1752$, where the critical Rayleigh number decreases.

5 Conclusion

We studied the effect of temperature modulation imposed on the upper boundary of a fluid layer of infinite extension on the convection threshold. This modulation is considered to have no stationary component in the temperature gradient. We determined the stability criterion by looking at the evolution of the critical Rayleigh number and the critical wavenumber versus the dimensionless frequency of the modulation. Using Floquet theory and spectral method, we showed that, depending on the frequency range, modulation generates a destabilizing or stabilizing effect. This work proposes the use of temporal periodic modulation of temperature boundary conditions as a means of controlling convective heat transfer in such a considered configuration.

References

1. Chandrasekhar, S.: Hydrodynamic and Hydromagnetic Stability. Oxford University Press, London (1961)
2. Drazin, P., Reid, W., Busse, F.H.: Hydrodynamic stability. *J. Appl. Mech.* **49**, 467–468 (1982). <https://doi.org/10.1115/1.3162197>
3. Nasser, I., Himrane, N., Ameziani, D.E., Bourada, A., Bennacer, R.: Time-periodic cooling of Rayleigh–Bénard convection. *Fluids* **6**, 87 (2021). <https://doi.org/10.3390/fluids6020087>
4. Donnelly, R.J.: Experiments on the stability of viscous flow between rotating cylinders. *Proc. R. Soc. A.* **281**(1384), 130 (1964)
5. Riahi, M., Aniss, S., Ouazzani, T.M., Skali, L.S.: Stability of a pulsed Taylor Couette flow in a viscoelastic fluid. *J. Soc. Rheol. Japan* **42**(5), 321–327 (2014)
6. Riahi, M., Aniss, S., Ouazzani, T.M., Skali, L.S.: Pulsed Taylor-Couette flow in a viscoelastic fluid under inner cylinder modulation. *Eur. Phys. J. Plus* **130**, 253 (2015)
7. Aouidef, A., Normand, C., Stegner, A., Wesfreid, J.E.: Centrifugal instability of pulsed flow. *Phys. Fluids* **6**(11), 3665–3676 (1994)
8. Riahi, M., Aniss, S., Ouazzani, T.M., Skali, L.S.: Centrifugal instability of pulsed Taylor-Couette flow in a Maxwell fluid. *Eur. Phys. J. E* **39**, 82 (2016)
9. Riahi, M., Aniss, S., Ouazzani, T.M.: Families of reversing and non-reversing Taylor vortex flows between two cooscillating cylinders with different amplitudes. *Phys. Fluids* **31**, 014101 (2019). <https://doi.org/10.1063/1.5064656>
10. Riahi, M., Ouazzani, T.M., Aniss, S.: Reversing and non-reversing Taylor vortex flows in modulated Taylor-Couette flow with counter-oscillating cylinders. *Eur. J. Mech./B Fluids* **95**, 148–159 (2022)
11. Hayani, C.M., Aniss, S., Ouazzani, T.M., Naciri, J.K., Riahi, M.: Stability of an oscillatory Taylor-Couette flow in an upper convected Maxwell fluid. *Phys. Fluids* **33**, 074105 (2021). <https://doi.org/10.1063/5.0057277>

12. Venezian, G.: Effect of modulation on the onset of thermal convection. Part 2 Convective instability. *J. Fluid Mech.* **35**(02), 243–254 (1969)
13. Rosenblat, S., Herbert, D.M.: Low frequency modulation of thermal instability. *J. Fluid Mech.* **43**(2), 385–398 (1970)
14. Yih, C.S., Li, C.H.: Instability of unsteady flows or configurations. *J. Fluid Mech.* **54**(01), 143152 (1972)
15. Souhar, K., Aniss, S.: Effect of phase thermal modulation without stationary temperature gradient on the threshold of convection. *J. Heat Transfer* **138**(10), 102502 (2016). <https://doi.org/10.1115/1.4033644>
16. Oukada, B., Ouazzani, M.T., Aniss, S.: Effects of a temperature modulation in phase at the frontier on the convective instability of a viscoelastic layer. *C. R. Mec.* **334**(3), 205–211 (2006)
17. Kaur, P., Singh, J., Bajaj, R.: Rayleigh-Bénard convection with two-frequency temperature modulation. *Phys. Rev. E* **93**, 043111 (2016). <https://doi.org/10.1103/PhysRevE.93.043111>
18. Hazra, S., Kumar, K., Mitra, S.: Rayleigh-Bénard magnetoconvection with temperature modulation. *Proc. Math. Phys. Eng. Sci.* **476**(2242), 20200289 (2020)
19. Weideman, J.A.C., Reddy, S.C.: A MATLAB differentiation matrix suite. *Math. Softw.* **26**, 465519 (2000)
20. Trefethen, L.N.: *Spectral Methods in Matlab* SIAM, Philadelphia (2000)
21. Lamine, M., Riahi, M., Hifdi, A.: Hydrodynamic stability of plane Poiseuille flow in Maxwell fluid with cross-flow. *Eur. Phys. J. Plus* **135**(2), 189 (2020). <https://doi.org/10.1140/epjp/s13360-020-00165-6>
22. Zaydan, M., Riahi, M., Mebarek-Oudina, F., Sehaqui, R.: Mixed convection in a two-sided lid-driven square cavity filled with different types of nanoparticles: a comparative study assuming nanoparticles with different shapes. *Fluid Dyn. Mater. Process.* **17**(4), 789 (2021). <https://doi.org/10.32604/fdmp.2021.015422>
23. Tiwari, R.K., Das, M.K.: Heat transfer augmentation in a two-sided lid-driven differentially heated square cavity utilizing nanofluids. *Int. J. Heat Mass Transf.* **50**(9–10), 2002–2018 (2007). <https://doi.org/10.1016/j.ijheatmasstransfer.2006.09.034>



A High-Order Implicit Algorithm Using an RBF-Type Meshless Method for the Simulation of Cardiac Electrical Activity

Sita Kaba^{1,2(✉)}, Loubna Salhi¹, Nouredine Damil^{1,2}, Nabyl El Moçayd³,
and Adnane Boukamel¹

¹ Centrale Casablanca, Centre de Recherche Systèmes Complexes et Interactions,
Ville Verte, Bouskoura 27182, Morocco

{sita.kaba,nouredine.damil,adnane.boukamel}@centrale-casablanca.ma

² Hassan II University of Casablanca, Faculté des Sciences Ben M'Sik, Laboratoire
d'Ingénierie et de Matériaux, LIMAT, B.P 7955 Sidi Othman, Casablanca, Morocco

³ University Mohammed VI Polytechnic, IWRI/AP, 46150 Benguerir, Morocco

Abstract. In this study, we present a new high-order implicit algorithm to simulate cardiac electrophysiological waves. Several cardiac pathologies are due to a malfunction in the propagation of the wave causing the contraction of the heart: the cardiac action potential. Its dynamics are described by a system of nonlinear and nonstationary partial differential equations (EDP). However, these equations retain major challenges for numerical simulation. These challenges are mainly reflected in the coexistence of a slow dynamic and a rapid dynamic inducing abrupt changes in time and space and having a wavefront type behavior. Faced with these challenges, we propose in this work an algorithm belonging to the family of asymptotic numerical methods (ANM), which combines representations in whole series, implicit time schemes, a mesh-less approach to spatial discretization using radial base functions (RBF) and a continuation method. This combination improves accuracy and significantly reduces computation time. To demonstrate its effectiveness, we first apply the algorithm to a one-dimensional equation (1D) of Fisher flame propagation, then to a two-dimensional equation (2D) modeling cardiac electrical activity, especially the well-known FitzHugh-Nagumo.

Keywords: Asymptotic Numerical Method · Implicite time scheme · RBF meshless method · cardiac action potential · Cardiac Electrical Activity

1 Introduction

Knowledge of the electrical activity of the myocardium is crucial for treating heart diseases and understanding heart rhythm disorders. Numerical modeling provides the tools to comprehend both normal and abnormal cardiac electrical activity. However, accurately simulating electrical waves in the human heart is

a challenging task. The simulation of cardiac electrophysiological waves is well-known to necessitate highly refined meshes, particularly when considering the transmembrane potential with its exceedingly thin depolarization and repolarization fronts. As a consequence, the current numerical models are constrained in their applicability, predominantly to simplified geometries and ionic models.

For instance, simulating the propagation of such waves across the entire myocardium using traditional discretization methods like the Finite Element Method, Finite Difference Method, or Finite Volume Methods necessitates an excessively fine mesh and extensive computation time. Despite the existence of mesh adaptation techniques in the literature, they remain computationally expensive. In reference [1], the authors estimate that a typical whole-core simulation may require approximately 10^7 grid points. Furthermore, the equations describing the electrical activity of the heart present significant challenges for numerical solutions. These challenges arise from the coexistence of slow and fast dynamics, resulting in abrupt changes in both time and space, reminiscent of wavefront behavior. From a numerical perspective, these wavefronts manifest as discontinuities in discrete solutions, leading to unstable calculations.

The equations used to describe the studied phenomenon of transmembrane potential propagation in the heart are a regular system of two non-linear differential equations, one for each of the intra- and extracellular potentials, coupled to a system of ordinary differential equations representing the ionic activity of the cell (the FitzHugh-Nagumo model is an example). The Asymptotic Numerical Method (ANM) is a highly efficient computational tool for numerically solving nonlinear equations. The first step in the ANM is the representation of the solution in integer series, which in this case poses no difficulty since the solution to the problem under study is analytic. In the case of non-regular equations, we have proposed various regularization methods in order to use integer series representations, such as contact or plasticity problems, see, for example, [6].

The aim of this study is to introduce a novel, efficient, and cost-effective algorithm that effectively addresses these challenges and mitigates mesh-related issues. The proposed algorithm's robustness and efficiency are initially demonstrated in a 1D scenario using the Fisher flame propagation equation, with a comparison of the results to those obtained in reference [3]. Subsequently, the algorithm's performance is evaluated in a 2D setting, specifically on the FitzHugh-Nagumo equation that models the electrical activity of the human heart in a 2D geometry. These results are then contrasted with those obtained in the 3D case, as described in reference [1].

Section 2 outlines the proposed implicit high-order algorithm's application in a general context, encompassing unsteady nonlinear PDEs. In Sect. 3, we present the numerical results and engage in discussions, focusing on both the 1D and 2D scenarios.

2 An Implicit High-Order Algorithm: Coupling ANM and RBF

In this section, we present our algorithm, which is a coupling of the global RBF meshless method with the techniques of the Asymptotic Numerical Method

(ANM): homotopic transformation, high-order truncated Taylor series representation of the solution and continuation method [3,4]. The interest of this coupling is to treat well the nonlinearity and to reduce considerably the computation time. The ANM allows us to transform our non-linear problem into a succession of linear problems with the same tangent matrix and the use of RBFs allows us to reduce the degree of freedom.

Consider a problem with initial values, verified by the unknown of the problem $u(t)$, where t denotes time, which can be written as :

$$\begin{cases} \frac{\partial u}{\partial t} + F(u) = \frac{\partial u}{\partial t} + L(u) + F^{nl}(u) = f \\ u(t_0) = u_0 \end{cases} \quad (1)$$

where $f(t)$ is a given external excitation, u_0 is the initial condition, $F(.)$ denotes a spatial non-linear operator, which has been separated into a linear part $L(.)$ and a non-linear part $F^{nl}(.)$. In order to facilitate the calculations in the Asymptotic Numerical Method (ANM) [4], it is possible, by adding additional variables, to reduce the nonlinear part $F^{nl}(.)$ in (1) to a quadratic form $Q(.,.)$. We then write the problem (1) in the following form:

$$\begin{cases} \frac{\partial u}{\partial t} + L(u) + Q(u, u) = f \\ u(t_0) = u_0 \end{cases} \quad (2)$$

To solve problem (2), we propose a new implicit high-order algorithm based on the following steps: (a) variable change, (b) time discretization, (c) homotopy technique, (d) Taylor series representation, (e) meshless RBF method and (f) continuation. In order to have zero initial conditions, the following change of variable is introduced: $u = u_0 + v$. The new unknown v thus verifies the following equation:

$$\begin{cases} \frac{\partial v}{\partial t} + L_t(v) + Q(v, v) = g \\ v(t_0) = 0 \end{cases} \quad (3)$$

The operator $L_t(.)$ and the second member $g(t)$ in (3) are defined by $L_t(.) = L(.) + Q(u_0, .) + Q(., u_0)$ and $g = f - L(u_0) - Q(u_0, u_0)$. The time interval considered $[0, T]$ is subdivided into N time intervals $[n\Delta t, (n+1)\Delta t]$ where $\Delta t = \frac{T}{N}$ is the time step. The method of the finite differences off-centre on the right makes it possible to approach $\frac{\partial v}{\partial t}$ at time $t = (n+1)\Delta t$ by the expression :

$$\frac{\partial v}{\partial t}(n+1)\Delta t \simeq \frac{v^{n+1} - v^n}{\Delta t} \quad (4)$$

where v^k is the solution at time $k\Delta t$. Substituting relation (4) into problem (3), written at time $(n+1)\Delta t$, we obtain the nonlinear problem verified by the solution v^{n+1} :

$$\begin{cases} \mathcal{L}_t v^{n+1} + \Delta t Q(v^{n+1}, v^{n+1}) = v^n + \Delta t g^{n+1} \\ v^0 = 0 \end{cases} \quad (5)$$

\mathcal{L}_t is the tangent operator given by : $\mathcal{L}_t(.) = I(.) + .\Delta t L_t(.)$ and where $I(.)$ est l'opérateur identité.

To solve the nonlinear problem (5), we define a homotopy transformation. We then introduce a parameter ε in front of the nonlinear term in (5), which leads to the following problem:

$$\begin{cases} \mathcal{L}_t w^{n+1} + \varepsilon \Delta t Q(w^{n+1}, w^{n+1}) = v^n + \Delta t g^{n+1} \\ w^0(\varepsilon) = 0 \end{cases} \quad (6)$$

In this way, the solution $w^{n+1}(\varepsilon)$ of (6) continuously changes from the solution of a linear problem from (6) (make $\varepsilon = 0$ in (6)) to the solution v^{n+1} of the starting problem (5) when $\varepsilon = 1$.

The solution of the non-linear problem (6) is sought in the form of an integer series representation truncated to order p with respect to the parameter ε :

$$w^{n+1}(\varepsilon) = w_0^{n+1} + \varepsilon w_1^{n+1} + \dots + \varepsilon^p w_p^{n+1} \quad (7)$$

The terms $w_k^{n+1} (k = 0, 1, 2, \dots, p)$ in the series (7) are then the new unknowns of the problem. The use of the expansion (7) transforms the problem (6) into a succession of $p + 1$ linear problems with the same tangent operator $\mathcal{L}_t(\cdot)$:

$$(k = 0) \begin{cases} \mathcal{L}_t w_0^{n+1} = v^n + \Delta t g^{n+1} \\ w_0^0 = 0 \end{cases} \quad (8)$$

$$(1 \leq k \leq p) \begin{cases} \mathcal{L}_t w_k^{n+1} = -\Delta t \sum_{r=0}^{k-1} Q(w_r^{n+1}, w_{k-r-1}^{n+1}) \\ w_k^0 = 0 \end{cases} \quad (9)$$

Note that all problems (9), verified by the terms of the vector series (7), are linear and admit the same tangent operator. We have thus replaced the resolution of the non-linear problem (5) by the succession of linear problems (9).

The solution of these linear problems will be done using a meshless method based on the introduction of radial basis functions (RBF) [2]. Let then be N points x_1, x_2, \dots, x_N arbitrarily distributed in the study domain. We approach the solution $w_k^{n+1} (1 \leq k \leq p)$ at any evaluation point x as :

$$w_k^{n+1}(x) = \sum_{j=1}^N \alpha_{k,j}^{n+1} \varphi_j(x) \quad (10)$$

where the functions in (9) are given by : $\varphi_j(x) = \varphi(\|x - x_j\|_2)$, φ being a radial basis function [2], $\|\cdot\|_2$ denotes the norm used. The introduction of (10) into the linear problems (9), leads to the following matrix linear problems :

$$(k = 0) \begin{cases} K_t W_0^{n+1} = V^n + \Delta t G^{n+1} \\ W_0^0 = 0 \end{cases} \quad (11)$$

$$(1 \leq k \leq p) \begin{cases} K_t W_k^{n+1} = -\Delta t \sum_{r=0}^{k-1} q(W_r^{n+1}, W_{k-1-r}^{n+1}) \\ W_k^{n+1} = 0 \end{cases} \quad (12)$$

where W_k^{n+1}, V^n, q are the spatial discretizations of w_k^{n+1}, v^n, Q . The tangent matrix K_t is the discretized form of the tangent operator \mathcal{L}_t . Once the W_k^{n+1} are calculated numerically, the solution of problem (2) at time t^{n+1} is obtained by equating ε to the unit :

$$U^{n+1} = U_0 + V^{n+1} = U_0 + w^{n+1} (\varepsilon = 1) = U_0 + W_0^{n+1} + W_1^{n+1} + \dots + W_p^{n+1} \quad (13)$$

The development in series (7), truncated at a given order p , is only valid on its domain of convergence. To be able to attribute to ε the unit value it is necessary that the unit is lower than this radius of convergence. An approximation of the radius of convergence is obtained by comparing two series solutions at consecutive orders. This led to an estimate of the domain of convergence which depends on the truncation order p , the tolerance δ and the time t given by the criterion [3,4]:

$$\varepsilon_{\text{validity}}(t) = \left(\delta \frac{\|W_1^n\|}{\|W_p^n\|} \right)^{\frac{1}{p-1}} \quad (14)$$

The acceptable solutions then correspond to $\varepsilon_{\text{validity}}(t)$ greater than unity. The solution-series given by (7) are therefore valid up to a maximum time $t_{\text{max}} = n_{\text{max}} \Delta t$ which is the largest t such that :

$$\varepsilon_{\text{validity}}(t) \geq 1, \quad t \in [0, t_{\text{max}}], \quad \varepsilon_{\text{validity}}(t + \Delta t) < 1 \quad (15)$$

3 Numerical Application and Discussion

3.1 Simulation of the Flame Propagation Equation

In order to validate the proposed algorithm, we will take the same Fisher flame propagation equation which is modelled by a PDE of the type (2) :

$$\begin{cases} \frac{\partial u}{\partial t} - \frac{\partial^2 u}{\partial x^2} + u(u-1) = 0 \\ u(x, t=0) = \left(1 + \exp\left(\frac{\mu x}{\sqrt{6}}\right) \right)^{-2} \\ u(x = -\infty, t) = 0, u(x = +\infty, t) = 1 \end{cases} \quad (16)$$

This nonlinear diffusion equation was solved in reference [3] using the same implicit high-order algorithm but the discretisation in space was done by finite differences. The analytical solution is known:

$$u(x, t) = \left(1 + \exp\left(\frac{\mu(x - \mu ct)}{\sqrt{6}}\right) \right)^{-2} \quad (17)$$

We will look for the numerical solution of (15) on the time interval $[0,20]$ and on the spatial interval $[-150,150]$. We will take $\mu = -1$ and $c = \frac{5}{\sqrt{6}}$, we discretise the temporal domain in 200 time steps $\Delta t = 0.1$ and the spatial domain using 301 nodes with a space step of $\Delta x = 1$. The RBF used is the Hardy multiquadric defined by [2] : $\varphi(r) = \sqrt{r^2 + c^2}$ with $r = \|x_i - x_j\|_2$, where c is the shape parameter (Fig. 2 and Fig. 3).

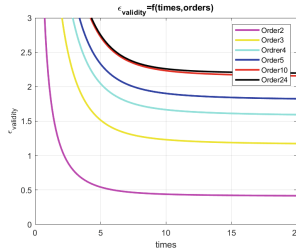


Fig. 1. Proposed algorithm. First large computational step. Evolution of the convergence criterion $\varepsilon_{\text{validity}}(t)$ as a function of time for various orders, $\delta = 10^{-4}$, $c = 10$ (shape).

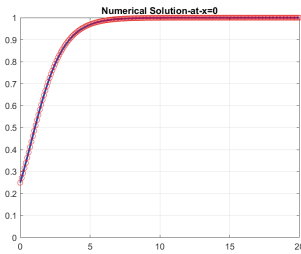


Fig. 2. Curve $u(0, t)$ as a function of time. In blue, the numerical solution and in red the exact solution. $\delta = 10^{-4}$, $c = 10$ (shape parameter).

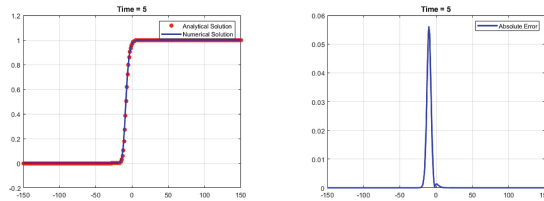


Fig. 3. Solution at time $t = 5$. Left: Curves of the numerical and exact solutions. Right: Absolute error curve. $\delta = 10^{-4}$, $c = 10$ (shape parameter).

In Fig. 1 , we notice that beyond order 2, $\varepsilon_{\text{validity}}(t)$ remains significantly greater than 1 over the entire interval studied. This means that the proposed algorithm can obtain the whole response $u(t)$, $0 \leq t \leq 20$ with a single matrix inversion.

3.2 Simulation of the Propagation Equation of the Cardiac Transmembrane Potential (FitzHugh-Nagumo Model)

It is proposed to use this algorithm to simulate cardiac electrophysiological waves. Several mathematical models have been established to study the phenomenon of the electrical activity of the heart [8–10].

In this work we consider the most commonly used monodomain model in the literature and the simple FitzHugh-Nagumo (FHN) ionic kinetics [1]. This model is given by the following PDEs :

$$\begin{cases} \frac{\partial U}{\partial t} = \nabla \cdot (D\nabla U) + I_{\text{ion}}(U, V) + I_S \\ \frac{\partial V}{\partial t} = G(U, V) \end{cases} \quad (18)$$

The FHN ionic model is given by: $I_{\text{ion}} = kU(U - a)(1 - U) - V$ and $G(U, V) = \varepsilon(\gamma U - \beta V)$, where U denotes the transmembrane potential of the heart, V is the recovery variable. The variable V and the associated ordinary differential equation mimic the slow ionic behaviour of myocardial cell membranes, “slow” compared to the fast dynamics of the transmembrane potential U . All parameters including time are dimensionless.

The numerical solution of this model was done in the paper [1], in 3D cubic geometry, using a second-order implicit scheme in time and discretising the study domain by quadratic finite elements in space. The resulting non-linear problem is solved using a 3D Newton-Raphson type correction prediction method.

In this work, we first restrict ourselves to the 2D case: we consider only a 2D square cut of the initial 3D domain used in [1]. In this case, in the initial solution used in [1] we imposed $z = 0$:

$$\begin{cases} 1 & \text{if } \sqrt{(x - 100)^2 + (y - 100)^2} < 30, \\ 0 & \text{if } \sqrt{(x - 100)^2 + (y - 100)^2} \geq 30 \end{cases} \quad (19)$$

The values of the parameters used are: $k = 1$; $a = 0.25$; $\varepsilon = 0.01$; $\beta = 1$; $\gamma = 0.16875$; $D = 1$. The homogeneous Neumann conditions are applied on all the edges of the domain.

By introducing additional variables, one can write the nonlinear PDE (17) in the form (2) and use the proposed implicit high-order algorithm.

We used a uniform regular distribution of, (see Fig. 4). We use the meshless method, the multiquadric function (MQ-RBF), which was used in the previous problem (flame propagation), and the inverse quadratic function (IQ-RBF): $\varphi(r) = \frac{1}{1 + \varepsilon^2 r^2}$, with $r = \|x_i - x_j\|_2$, where c is the shape parameter.

The convergence criterion of the proposed algorithm for choosing the time step and spatial step is difficult to establish because, with RBF-meshless methods, the stability of the solutions depends on the number of used points and the

spacing between these points. Therefore, the RBF method depends on a parameter called the shape parameter, which has a significant influence on the stability of the solution. This parameter has been the subject of several research studies, and one of the most commonly used and reliable criteria for its optimal selection is as follows: $shape = \alpha ds$, $ds = \frac{1}{N_p} \sum_i^{N_p} d_i$ [7], where α is a coefficient to be determined and d_i is the distance from the i th center to its nearest neighbor. It has been proven that with MQ-RBF, the value $\alpha = 0.815$ is the most reliable.

In Fig. 5, we plot $\varepsilon_{validity}(t)$ as a function of time for various orders. The convergence curve shows that the algorithm allows obtaining all the solutions $U(t)$ and $V(t)$, $0 \leq t \leq 700$ with a single matrix inversion starting from order 20 using the MQ-RBF and IQ-RBF methods.

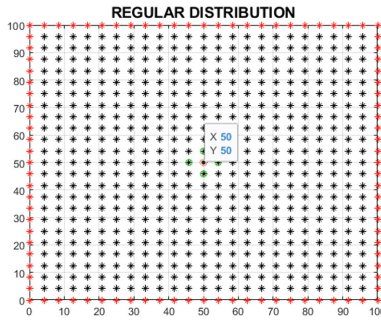


Fig. 4. Regular Uniform distribution of 625 points. Interpolation point (50,50)

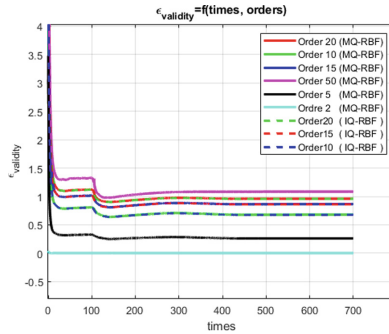


Fig. 5. Proposed algorithm. First large computational step. Evolution of the convergence criterion $\varepsilon_{validity}(t)$ as a function of time for various orders, $\delta = 10^{-3}$ (shape). In solid line, we used MQ-RBF with $c = 7$. In dashed line, we used IQ-RBF with $c = 0.1$.

Because of the lack of an exact solution, we compared the results obtained by the proposed 2D algorithm with the time response curves of the transmembrane

potential $U(t)$ and the recovery variable $V(t)$ found in the 3D [1]. We found the same trend with the depolarization time: $t \simeq 117$. see Fig. 6.

Time responses of the transmembrane potential and the recovery variable in the interval $[0, 700]$ at the central point of the domain $X1 = (50, 50)$, at order $p = 20$, with $\Delta t = 0.1$, $\delta = 10^{-3}$ using MQ-RBF method ($c=7$) and IQ-RBF method ($c=0.1$):

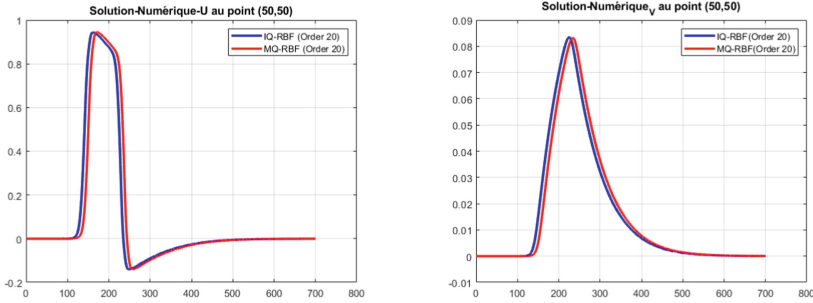


Fig. 6. Temporal Solution at order $p = 20$ for MQ-RBF and IQ-RBF methods. Left: Curve of transmembrane potential. Right: Recovery variable curve. $\delta = 10^{-3}$

The MQ-RBF and IQ-RBF method can achieve better accuracy and efficiency due to its superior performance in global interpolation with few points. Therefore, the algorithm is much more computationally efficient in terms of CPU time. The major disadvantage is that we do not precisely control the criterion for choosing the numerical parameters for solution stability [4].

4 Conclusion and Perspectives

In this study, we have demonstrated the effectiveness of combining meshless methods with high-order implicit algorithms. Our algorithm utilizes 625 evenly distributed points, resulting in 625 degrees of freedom. Remarkably, a single inversion of the tangent matrix proved sufficient to achieve accurate solutions up to time 700, with a remarkable computation time of only 180s. The numerical results have clearly shown the efficiency of this algorithm in simulating the equations that describe the electrical activity of the heart.

The next step of our work will be the simulation of cardiac electro-mechanical activity, which involves coupling the electrical model presented in this study with the non-linear stress equilibrium equations that govern large deformation hyperelasticity, in order to investigate the mechanisms of cardiac arrhythmias in electrophysiology [11]. Finally, we will utilize deep learning techniques for inverse modeling, which involves using the results of previous studies to infer the characteristics of the heart [12–14].

References

1. Belhamadia, Y., Fortin, A., Bourgault, Y.: Towards accurate numerical method for monodomain models using a realistic heart geometry. *Math. Biosci.* **220**(2), 89–101 (2009)
2. Defontaine, A.: Modélisation multirésolution et multiformalisme de l'activité électrique cardiaque (Doctoral dissertation, Université Rennes 1) (2006)
3. Halassi, A., Jounady, Y., Salhi, L., Taik, A.: A meshfree method for heat explosion problems with natural convection in inclined porous media. In: *MATEC Web of Conferences* (Vol. 241, p. 01019). EDP Sciences (2018)
4. Sarra, S.A., Kansa, E.J.: Multiquadric radial basis function approximation methods for the numerical solution of partial differential equations. *Adv. Comput. Mech.* **2**(2), 220 (2009)
5. Braikat, B., Jamal, M., Damil, N., Potier-Ferry, M.: Algorithmes d'intégration temporelle implicites couplés avec des résolveurs d'ordre élevé. *Revue Européenne des Eléments* **11**(6), 749–772 (2002)
6. Cochelin, B., Damil, N., Potier-Ferry, M.: Méthode asymptotique numérique (p. 297). Hermes Lavoisier (2007)
7. Hardy, R.L.: Multiquadric equations of topography and other irregular surfaces. *J. Geophys. Res.* **76**(8), 1905–1915 (1971)
8. Bourgault, Y., Ethier, M., LeBlanc, V.G.: Simulation of electrophysiological waves with an unstructured finite element method. *ESAIM: Math. Modell. Num. Anal.* **37**(4), 649–661 (2003)
9. Franzone, P.C., Pavarino, L.F., Taccardi, B.: Simulating patterns of excitation, repolarization and action potential duration with cardiac bidomain and monodomain models. *Math. Biosci.* **197**(1), 35–66 (2005)
10. Roth, B.J.: Approximate analytical solutions to the bidomain equations with unequal anisotropy ratios. *Phys. Rev. E* **55**(2), 1819 (1997)
11. Nash, M.P., Panfilov, A.V.: Electromechanical model of excitable tissue to study reentrant cardiac arrhythmias. *Prog. Biophys. Mol. Biol.* **85**(2–3), 501–522 (2004)
12. Rudi, J., Bessac, J., Lenzi, A.: Parameter estimation with dense and convolutional neural networks applied to the FitzHugh-Nagumo ODE. In: *Mathematical and Scientific Machine Learning*, pp. 781–808. PMLR (2022)
13. Doruk, R.O., Abosharb, L.: Estimating the parameters of FitzHugh-Nagumo neurons from neural spiking data. *Brain Sci.* **9**(12), 364 (2019)
14. Liang, H., Wu, H.: Parameter estimation for differential equation models using a framework of measurement error in regression models. *J. Am. Stat. Assoc.* **103**(484), 1570–1583 (2008)



Effect of Vertical Periodic Oscillation with Two Commensurate Frequencies on the Rayleigh-Taylor Instability

Chaimaa Taouzer, Mouh Assoul, and Saïd Aniss^(✉)

Faculty of Sciences Ain -Chock, Laboratory of Mechanics, University of Hassan II,
Maarif, B.P. 5366 Casablanca, Morocco
said.aniss@etu.univh2c.ac.ma

Abstract. The aim of this work is to examine the effect of a periodic vertical oscillation with two frequencies on the instability of a thin horizontal fluid layer in a Rayleigh Taylor configuration. The linear stability analysis leads to the periodic Mathieu equation, which describes the evolution of the interface amplitude. To solve the linear problem numerically, a combination of Floquet's theory and the Runge-Kutta method is used. Numerical results show, as indicated in previous works for a single frequency, that the Rayleigh Taylor instability is not affected by the oscillation, while the resonances are. Moreover, the incorporation of two frequencies produces a richer dynamic, in terms of parametric resonances, than in the case of a single-frequency oscillation. The most unstable parametric resonances depend on the frequency ratio and can occur over a wide range of wavenumbers (large or small). Thus, the wavelength of the waves can be selected according to this ratio. It should also be noted that this ratio can have a stabilizing or destabilizing effect. The effect of fluid layer thickness on the threshold of parametric resonances is also discussed in this study.

Keywords: Rayleigh-Taylor instability · interfacial instability · periodic oscillation · commensurate frequencies · Floquet's theory

1 Introduction

The Rayleigh-Taylor instability (RTI) [1] represents one of the classical and paradigmatic types of hydrodynamic instabilities, including the well-known Kelvin-Helmholtz, Rayleigh-Bénard, and Benard-Marangoni instabilities, which have captivated significant attention for several decades. It appears when a lighter fluid layer provides support to a heavier layer from below within the gravitational field. In its general context, Rayleigh-Taylor instability (RTI) manifests when a denser fluid accelerates into a less dense one. This phenomenon is observed in various fields such as astrophysics, ballistics, coatings on solid substrates, technological applications like the flow of liquid polymer films, environmental aspects involving raindrop dynamics and their impact on the biosphere, microfluidics, and others.

Recent study [2] focused on the flow dynamics of a thin liquid film placed on the underside of a solid planar substrate, subjected to two commensurate frequencies asymmetric forcing in the tangential direction to the substrate. The effect of the amplitude ratio was examined with a linear stability analysis.

In this study, our primary focus is on investigating the impact vertical periodic oscillation with two frequencies on the stability of the interface between two layers of immiscible and incompressible fluids with varying densities. The Fourier differentiation matrix method (Fourdif) [4] and Floquet's theory combined with the Runge-Kutta method are used to solve numerically the linear problem. After validating the results in the case of oscillation with one frequency [3], We examine the impact of the frequencies ratio ω , the thickness d and the angular vibration frequency ω_x on the threshold of the interfacial instability.

2 Formulation

Let's consider a rigid substrate supporting an isothermal, incompressible, Newtonian liquid film of thickness d and infinite extension in the horizontal directions. In contrast to the previous works [2,3] that has focused on single frequency oscillation, in the present work we consider the situation where the substrate is subjected to a periodic oscillation having two commensurate frequencies. The system is therefore considered to be subject to the field of gravity g and to an oscillating motion in the vertical direction with an acceleration as follows: $\tilde{a}(\tilde{t}) = g a(\tilde{t}) = \tilde{A} (\tilde{\omega}_1^2 \cos(\tilde{\omega}_1 \tilde{t}) + \alpha \tilde{\omega}_2^2 \cos(\tilde{\omega}_2 \tilde{t}))$ where $\tilde{\omega}_1$ and $\tilde{\omega}_2$ are two commensurate frequencies, α is the amplitudes ratio and \tilde{t} is the time. The system is analyzed within the $\tilde{x} - \tilde{z}$ plane, with the \tilde{x} axis aligned parallel to the substrate, while the \tilde{z} axis is perpendicular to the substrate, (see Fig. 1).

The equations describing the flow are the continuity equation and the momentum equations written in the relative frame linked to the substrate:

$$\frac{\partial \tilde{u}}{\partial \tilde{x}} + \frac{\partial \tilde{w}}{\partial \tilde{z}} = 0 \quad (1)$$

$$\frac{\partial \tilde{u}}{\partial \tilde{t}} + \tilde{u} \frac{\partial \tilde{u}}{\partial \tilde{x}} + \tilde{w} \frac{\partial \tilde{u}}{\partial \tilde{z}} = -\frac{1}{\rho} \frac{\partial \tilde{p}}{\partial \tilde{x}} + \nu \Delta \tilde{u} \quad (2)$$

$$\frac{\partial \tilde{w}}{\partial \tilde{t}} + \tilde{u} \frac{\partial \tilde{w}}{\partial \tilde{x}} + \tilde{w} \frac{\partial \tilde{w}}{\partial \tilde{z}} = -\frac{1}{\rho} \frac{\partial \tilde{p}}{\partial \tilde{z}} + \nu \Delta \tilde{w} - g(1 + a(\tilde{t})) \quad (3)$$

where the quantities \tilde{u} , \tilde{v} , \tilde{p} , g , ρ and $\nu = \mu/\rho$ designate respectively the axial and longitudinal components of the velocity field, the pressure, the acceleration of gravity, the density and the kinematic viscosity.

The boundary conditions at the solid substrate, $\tilde{z} = 0$, are the no slip and no penetration conditions:

$$\tilde{u} = 0 \quad , \tilde{w} = 0 \quad \text{en} \quad \tilde{z} = 0 \quad (4)$$

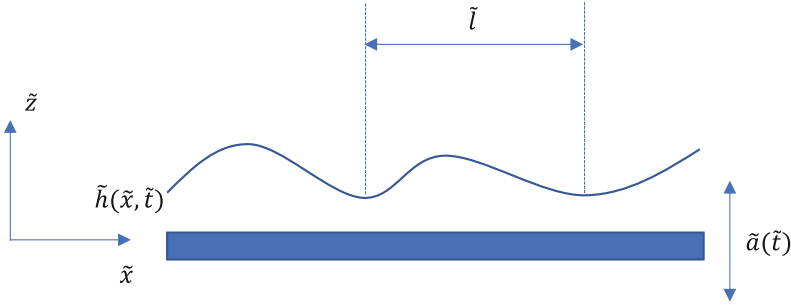


Fig. 1. Schematic illustration of the studied configuration. In the Rayleigh-Taylor configuration, the force of gravity acts in the upward direction of the \tilde{z} axis and $g > 0$.

At the free surface, the kinematic and the dynamic condition, are given respectively by:

$$\frac{\partial \tilde{h}}{\partial \tilde{t}} + \frac{\partial}{\partial \tilde{x}} \int_0^{\tilde{h}(\tilde{x}, \tilde{t})} \tilde{u} \, d\tilde{z} = 0 \tag{5}$$

$$(\tilde{p}_a - \tilde{p}) \mathbf{n} + \mathbf{D} \mathbf{n} = \kappa \gamma \mathbf{n} \tag{6}$$

where $\mathbf{D} = \begin{pmatrix} 2\mu \frac{\partial \tilde{u}}{\partial \tilde{x}} & \mu (\frac{\partial \tilde{w}}{\partial \tilde{x}} + \frac{\partial \tilde{u}}{\partial \tilde{z}}) \\ \mu (\frac{\partial \tilde{w}}{\partial \tilde{x}} + \frac{\partial \tilde{u}}{\partial \tilde{z}}) & 2\mu \frac{\partial \tilde{w}}{\partial \tilde{z}} \end{pmatrix}$ is the viscous stress tensor in the liquid phase, γ is the surface tension coefficient, $\mathbf{n} = \frac{(-\frac{\partial}{\partial \tilde{x}} \tilde{h}, 1)}{\sqrt{1 + \frac{\partial \tilde{h}^2}{\partial \tilde{x}^2}}}$ is the unit vector normal to the

interface, $\kappa = \frac{\frac{\partial^2 \tilde{h}}{\partial \tilde{x}^2}}{(1 + \frac{\partial \tilde{h}^2}{\partial \tilde{x}^2})^{\frac{3}{2}}}$ is the interface curvature.

The dimensionless form of Eqs. (1)–(3) and boundary conditions (2)–(6) are rewritten in a dimensionless form using the following scales : d (liquid film thickness) and \tilde{l} (wavelength) for the vertical and horizontal coordinates, respectively, w_0 for velocities, and d/w_0 for time. By introducing a small film parameter :

$$\delta = \frac{d}{\tilde{l}} \ll 1,$$

and using the approximation of lubrication, the dimensionless equations governing the problem in the relative frame correspond to those in references [2,3]:

$$\frac{\partial h}{\partial t} + \frac{\partial q}{\partial x} = 0 \tag{7}$$

$$\frac{6}{5} \text{Re} \left(\frac{\partial q}{\partial t} + \frac{17}{7} \frac{q}{h} \frac{\partial q}{\partial x} - \frac{9}{7} \frac{q^2}{h^2} \frac{\partial h}{\partial x} \right) = -\frac{3q}{h^2} + h \left(\Gamma \frac{\partial^3 h}{\partial x^3} - G(1 + a(t)) \frac{\partial h}{\partial x} \right) \tag{8}$$

where $q = \int_0^h u dz$. The dimensionless quantities $Re = \frac{w_0 d}{\nu}$, $G = \frac{\delta^2 g d^2}{\nu w_0}$, $\Gamma = \frac{\delta^4 \gamma}{\rho \nu w_0}$ are respectively, the Reynolds, Galileo and the inverse capillary numbers. The dimensionless vertical acceleration, denoted $a(t)$, is given by:

$$a(t) = A (\omega_1^2 \cos(\omega_1 t) + \alpha \omega_2^2 \cos(\omega_2 t)) \quad (9)$$

where $A = \frac{\bar{A} w_0^2}{g d^2}$, $\omega_1 = \tilde{\omega}_1 \frac{d}{w_0}$, $\omega_2 = \tilde{\omega}_2 \frac{d}{w_0}$. Hereafter, we denote by $\omega = \frac{\omega_1}{\omega_2}$ the ratio of frequencies. The parameter α , in Eq. (9), remains the ratio of the amplitudes of the oscillatory motion related to each cosine function.

3 Linear Stability Analysis

Equations (7)–(8) are linearized in the vicinity of the basic solution, $q = 0$ and $h = 1$. The solutions of the linear problem are sought in the normal modes : $q = q_k(t) e^{i k x}$ and $h = 1 + \eta_k(t) e^{i k x}$. Equations (7)–(8) and dimensionless form of boundary conditions (2)–(6) are reduced to the Mathieu equation with damping [2, 3] :

$$Re \epsilon \ddot{\eta}_k + \frac{5}{2} \dot{\eta}_k + \frac{5}{6} k^2 [G[1 + a(t)] + \Gamma k^2] \eta_k = 0 \quad (10)$$

This differential Eq. (10) corresponds to the amplitude equation of the elevation of the interface governing the Rayleigh-Taylor instability problem in the presence of vertical periodic oscillation. It is solved numerically using Fourier differentiation matrix method [4]. The numerical results are also obtained using the Floquet's theory combined with the four order Runge-Kutta method.

4 Discussion

The marginal stability curves are presented in Figs. 2, 3 and 4. These curves can be used to determine the value of the amplitude, \tilde{A} , at which the liquid layer interface becomes unstable to standing waves of wavenumber \tilde{k} .

In Fig. 2, for $\omega_x = 125$ rad/s and $\alpha = 0$, we validate the work in which a single frequency is considered [3]. Figure 2 agrees with the results of reference [3] and illustrates the presence of two distinct types of marginal stability curves. The first is the Rayleigh-Taylor instability that occurs at long wavelengths (small wavenumbers), here for $\tilde{k} < 0.37$ mm. The second appears for $\tilde{k} > 0.37$ mm and corresponds to several parametric tongue-shaped resonance zones whose origin is the presence of oscillation. Note that the zone corresponding to the second resonance is the most unstable compared with the other three resonance zones.

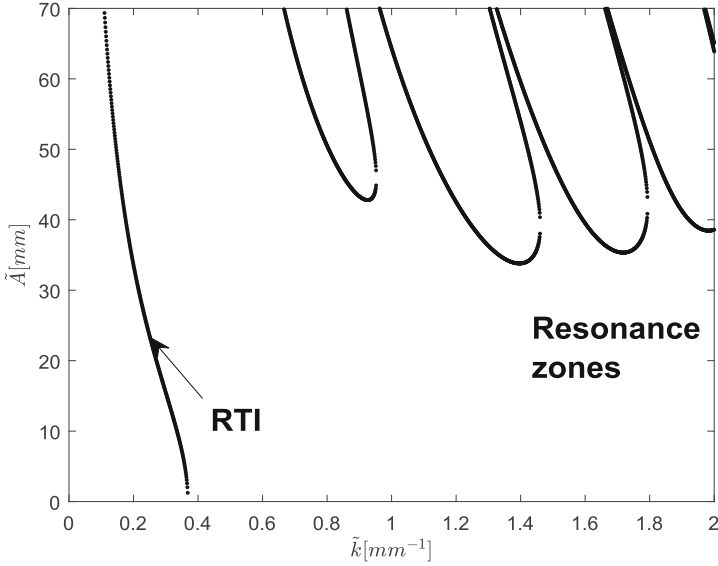


Fig. 2. Validation of the numerical procedure with results in reference [3] : Marginal stability curves showing the amplitude, \tilde{A} , versus the wavenumber, \tilde{k} , for the film thickness $d = 0.1$ mm, the angular oscillation frequency $\omega_x = 125$ rad/s and $\alpha = 0$.

4.1 Effect of the Thickness

In Fig. 3 (a), (b), (c), numerical results are obtained with the angular frequency $\omega_x = 125$ rad/s and for the frequencies ratios $\omega = \frac{5}{4}$, $\omega = \frac{2}{3}$ and $\omega = \frac{1}{2}$. Here we restrict our study to the situation where α satisfies the relation: $\alpha\omega^2 = 1$. As expected, the Rayleigh-Taylor instability is not affected by oscillation, whereas parametric reso-

Table 1. Effect of the depth and frequency ratio on the threshold of resonances.

(a) : $\omega = \frac{5}{4}$	$k_{min} [mm^{-1}]$	$A_{min} [mm]$	The most unstable resonance
$d = 0.1$ mm	1.36	29.16	second resonance
$d = 0.14$ mm	0.9	11.57	second resonance
(b) : $\omega = \frac{2}{3}$	$k_{min} [mm^{-1}]$	$A_{min} [mm]$	The most unstable resonance
$d = 0.1$ mm	1.91	30.75	ninth resonance
$d = 0.14$ mm	1.016	11.9	first resonance
(c) : $\omega = \frac{1}{2}$	$k_{min} [mm^{-1}]$	$A_{min} [mm]$	The most unstable resonance
$d = 0.1$ mm	1.11	22.38	second resonance
$d = 0.14$ mm	0.75	7.619	first resonance

nances are. Note that the layer with thickness $d = 0.14$ mm is more unstable and has a smaller wavenumber than the layer with $d = 0.1$ mm.

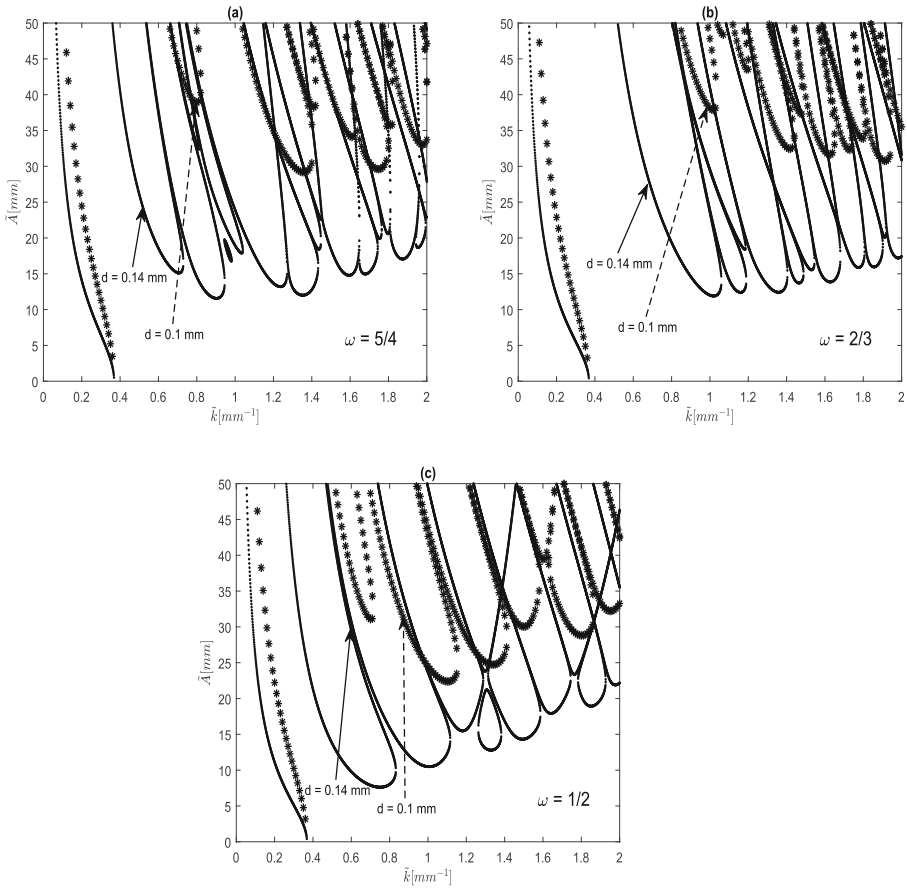


Fig. 3. Marginal stability curves showing the amplitude \tilde{A} versus the wavenumber \tilde{k} for the angular oscillation frequency $\omega_1 = 125$ rad/s, $\alpha\omega^2 = 1$ and for the frequencies ratios $\omega = \frac{5}{4}$, $\omega = \frac{2}{3}$, $\omega = \frac{1}{2}$. The star and solid lines correspond to film thicknesses of $d = 0.1$ mm and $d = 0.14$ mm respectively.

For the ratio of frequencies $\omega = \frac{5}{4}$ (Fig. 3(a), Table 1), the most unstable resonance zones are the second for $d = 0.1$ mm and $d = 0.14$ mm. However, For $\omega = \frac{2}{3}$ (Fig. 3(b), Table 1), the most unstable resonance zones become the ninth for $d = 0.1$ mm and the first for $d = 0.14$ mm. For $\omega = \frac{1}{2}$ (Fig. 3(c), Table 1), the most unstable resonance zones are the second for $d = 0.1$ mm and the first one for $d = 0.14$ mm.

From $\omega = \frac{5}{4}$ to $\omega = \frac{2}{3}$, and for both film thicknesses $d = 0.1$ mm and $d = 0.14$ mm a stabilizing effect is observed with a slight increase in the wavenumber. However from $\omega = \frac{2}{3}$ to $\omega = \frac{1}{2}$ a destabilizing effect is noticed with a decrease in the wavenumber.

4.2 Effect of the Angular Frequency

Figure 4 (a), (b), (c) shows the marginal stability curves, again as in Fig. 3, including Rayleigh-Taylor instability and parametric resonances for two angular frequencies $\omega_1 = 125$ rad/s and $\omega_1 = 200$ rad/s, for $d = 0.1$ mm and for the same frequency ratios as in Fig. 3. Table 2 contains the critical parameters of the instability thresholds for the same parameters. As can be observed, for each frequency ratio, when decreasing the angular frequency of oscillation, the resonance curves undergo upward translations, which means we're in the presence of a stabilizing effect.

For each angular frequency ω_1 , the transition from $\omega = \frac{5}{4}$ to $\omega = \frac{2}{3}$ is accompanied by a very slight stabilizing effect with a constant wavenumber. Whereas the transition from $\omega = \frac{2}{3}$ to $\omega = \frac{1}{2}$ is accompanied by a significant destabilizing effect, with an equally significant decrease in the wavenumber.

Table 2. Effect of the angular frequency ω_1 , for different frequency ratios ω , on the threshold of resonances.

(a) : $\omega = \frac{5}{4}$	$k_{min}[mm^{-1}]$	$A_{min}[mm]$	The most unstable resonance
$\omega_1 = 125$ rad/s	1.36	29.16	second resonance
$\omega_1 = 200$ rad/s	1.858	11.15	fifth resonance
(b) : $\omega = \frac{2}{3}$	$k_{min}[mm^{-1}]$	$A_{min}[mm]$	The most unstable resonance
$\omega_1 = 125$ rad/s	1.91	30.75	ninth resonance
$\omega_1 = 200$ rad/s	1.85	11.23	third resonance
(c) : $\omega = \frac{1}{2}$	$k_{min}[mm^{-1}]$	$A_{min}[mm]$	The most unstable resonance
$\omega_1 = 125$ rad/s	1.11	22.38	second resonance
$\omega_1 = 200$ rad/s	1.004	7.861	first resonance

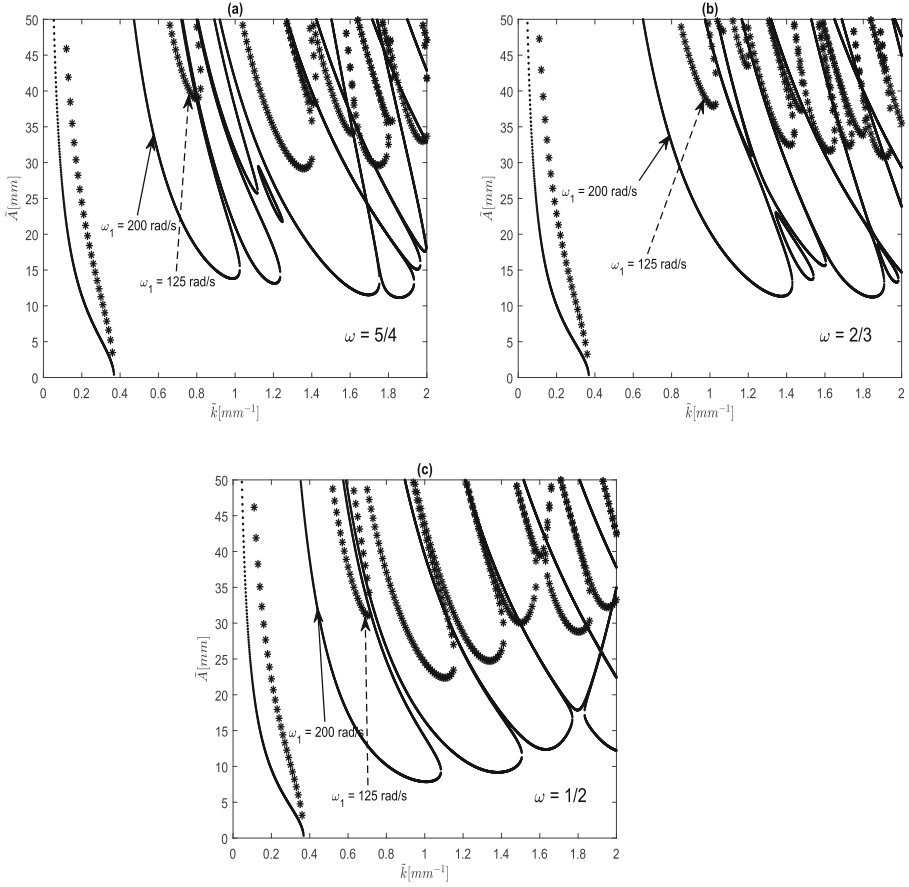


Fig. 4. Marginal stability curves showing the amplitude \tilde{A} versus the wavenumber \tilde{k} for $d = 0.1$ mm, and the frequencies ratios $\omega = \frac{5}{4}$, $\omega = \frac{2}{3}$, $\omega = \frac{1}{2}$. The star and solid curves correspond to the angular oscillation frequencies of $\omega_1 = 125$ rad/s and $\omega_1 = 200$ rad/s, respectively.

5 Conclusion

We studied the Rayleigh-Taylor instability under periodic vertical oscillation with two commensurate frequencies by performing a linear stability analysis on the behavior of the liquid-air interface. The governing equations are reduced, as in the references [2,3], to a periodic Mathieu equation describing the evolution of the interface amplitude. This initial study enabled us to identify stable and unstable regions and modes by considering the various physical parameters associated with the problem. The effect of thickness and that of angular frequency of vibration ω_1 were studied for different frequency ratios ω . Finally, the introduction of two frequencies into the oscillation generates richer dynamics than single-frequency oscillation in terms of resonance zones and wavenumber selection.

References

1. Rayleigh, L.: Investigation of the character of the equilibrium of an incompressible heavy fluid of variable density. Proc. London Math. Soc. **s1-14**, 170 (1882)
2. Cohen, E.S., Bestehorn, M., Oron, A.: Ratchet flow of thin liquid films induced by a two-frequency tangential forcing. Phys. Fluids **30**, 022101 (2018)
3. Cohen, E.S., Bestehorn, M., Oron, A.: Rayleigh-Taylor instability in thin liquid films subjected to harmonic vibration. Phys. Fluids **29**, 052105 (2017)
4. Weideman, A.C., Reddy, S.C.: A MATLAB differentiation matrix suite. ACM Trans. Math. Softw **26**, 465–519 (2000)



On a Novel Micromechanical Modeling of the Elastic Behavior of Nanocomposites

El Hassane Barhdadi^(✉)

Engineering Sciences and Applications Laboratory, National School of Applied Sciences
Al-Hoceima, Al-Hoceima, Morocco
ebarhdadi@uea.ac.ma

Abstract. This work aims to the introduction of a new micromechanical modeling of the elastic behavior of nanocomposite materials with coated nanoparticles. The model is developed taking into account the interphase and particle clustering effects. The model is used to explain the relationship between mechanical properties of nanocomposites and their complex microstructure. Here we consider that the micromechanical modeling of the complex microstructure of nanocomposites requires the combination of the four-phase model and the three-phase model and we assume that all phases are elastic, isotropic and perfectly bonded. In this way, the effective elastic properties are derived using the integral equation and interfacial operators. In the micromechanical study, it was observed that the elastic modulus increases with the increasing in the volume fraction of nanoparticles. The effect of interphase zone is studied and the performance of the present model is showing by comparing with numerical and experiment results and show a good agreement.

Keywords: Nanocomposite · Micromechanics · Coated nanoparticles · Cluster · Three-phase model · Four-phase model

1 Introduction

Real microstructure of nanocomposites is very complex and can be decomposed to a several representative volume elements RVE. Therefore, many micromechanical modeling have been applied to evaluate the mechanical properties of nanocomposites (see e.g. [1–6]). These nanomaterials are very important due to their mechanical, thermo/mechanical, optical and electrical properties.

When the radius of nanoparticles is about one nanometer, the interphase zone linking the nanoparticle and matrix in nanocomposite play a decisive role in the manufacturing and performance of nanomaterial. The interphase can be taken as the third phase in the nanocomposite with different properties and form with special atomistic, soft interfacial coatings, diffusion and chemical interaction phases at the interface between nanoparticles and matrix. Peng et al. [1] developed a numerical/analytical model of nanocomposites, which allows to characterize the interphase and clustering effects. Amraei et al. [2] developed a interphase model based on finite/size representative volume element to

obtain the mechanical properties of nanocomposites. Mortazavi et al. [6] evaluate the effect of the interphase on the conductivity and the elastic behavior of nanocomposite.

Here we consider that the present micromechanical modeling requires the combination of two patterns [7] consisting of the four-phase model [8] and of the three-phase model. Analytical equations for the effective elastic properties of the nanocomposite are given and use the integral equation [9] and interfacial operators [10]. We suppose that all constituents are isotropic, homogeneous and the interfaces (bonds) are perfect.

2 General Framework and Micromechanical Model

Figure 1 shows a typical nanocomposite material. In this figure, we can distinguish two different patterns [7] consisting of coated nanoparticles and clusters formed by the same coated nanoparticles.

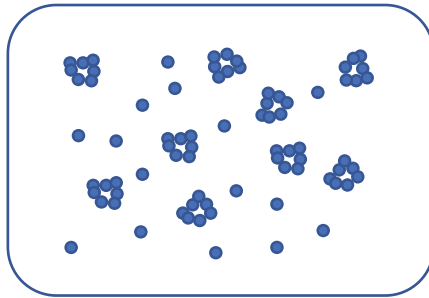


Fig. 1. Microstructure of nanocomposite

Here and following the generalized self-consistent scheme [11], the nanocomposite is modeled as shown in Fig. 2; except for one coated nanoparticle surrounding by a shell matrix and except for one cluster surrounding by matrix layer, all other constituents are replaced by the effective medium.

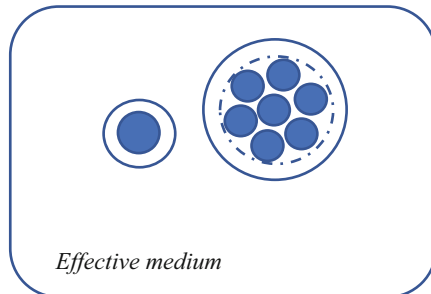


Fig. 2. Schematization of nanocomposites using the generalized self-consistent scheme

In the next, we consider that the cluster can be considered as an assemblage of coated spherical nanoparticles [12]. To determine the cluster properties, we use the generalized

self-consistent scheme [11] and then the final topology of the present model is shown in Fig. 3.

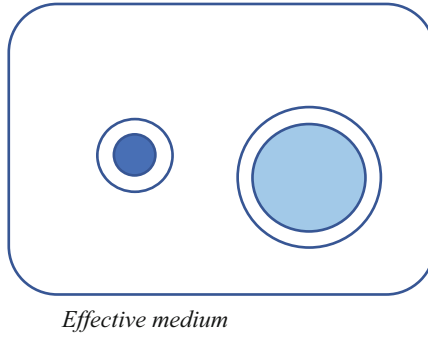


Fig. 3. Four-phase and three-phase models

In the Fig. 3, the four-phase model is made with nanoparticle, interphase, matrix coating and effective medium while the three-phase model is made with homogenized cluster, matrix coating and effective medium. The inclusion, the interphase, the homogenized cluster, the matrix and the effective medium are characterized by the elastic moduli c^i , c^z , c^c , c^m and C^{eff} , respectively.

The mean global stress and strain in the nanocomposite are given, respectively, by:

$$\Sigma = f_i \sigma^i + f_z \sigma^z + f_c \sigma^c + f_m \sigma^m \quad (1)$$

$$E = f_i \varepsilon^i + f_z \varepsilon^z + f_c \varepsilon^c + f_m \varepsilon^m \quad (2)$$

f , σ and ε indicate the volume fraction, the mean stress and the mean strain in inclusion (i), in interphase (z), in cluster (c) and in matrix (m).

The elastic stiffness C^{eff} of nanocomposite are given as follow:

$$C^{eff} = c^m + f_i (c^i - c^m) : A^{(i4)} + f_z (c^z - c^m) : A^{(z4)} + f_c (c^c - c^m) : A^{(c)} \quad (3)$$

The determination of C^{eff} implies the determination of the strain localization tensors $A^{(i4)}$, $A^{(z4)}$ and $A^{(c)}$.

$A^{(i4)}$ and $A^{(z4)}$ are the localization tensors of global strain in nanoparticle and in interphase, respectively. These tensors are given in [8].

$A^{(c)}$ is the localization tensor of global strain in the homogenized cluster, such that:

$$A^{(c)} = A^{(i3)} + A^{(z3)} \quad (4)$$

$A^{(i3)}$ and $A^{(z3)}$ are the localization tensors of global strain in nanoparticle and in interphase in the three-phase model. These tensors are deduced from [8].

c^c are the elastic properties of homogenized cluster and are determined by considering each cluster as an assemblage of composite spheres [12] and using the generalized self-consistent scheme [11] such that:

$$c^c = c^z + f_i (c^i - c^z) : A^{(i3)} \quad (5)$$

2.1 Four-Phase Model

$A^{(i4)}$ And $A^{(z4)}$ are determined by the four-phase model shown in Fig. 4.

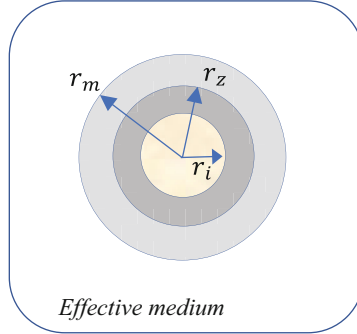


Fig. 4. Four-phase model

According to Barhdadi et al. [8], The tensors $A^{(i4)}$, $A^{(z4)}$ are given by:

$$A^{(i4)} = \left[f_i (I + T^J (C^{eff}) : (c^i - C^{eff})) + f_z (I + T^J (C^{eff}) : (c^z - C^{eff})) : \omega^{(z/i)} + f_m (I + T^J (C^{eff}) : (c^m - C^{eff})) : \left(\frac{f_i}{f_i + f_z} \omega^{(m/i)} + \frac{f_z}{f_i + f_z} \omega^{(m/z)} : \omega^{(z/i)} \right) \right]^{-1} \quad (6)$$

$$A^{(z4)} = \omega^{(z/i)} : A^{(i4)} \quad (7)$$

The tensors $T^J (C^{eff})$, $\omega^{(z/i)}$, $\omega^{(m/i)}$ and $\omega^{(m/z)}$ are obtained from the Eshelby's tensor [13] and can be decomposed into spherical and deviatoric parts;

$$T^J (C^{eff}) = \frac{1}{(3k^{eff} + 4\mu^{eff})} \mathbf{J} + \frac{3(k^{eff} + 2\mu^{eff})}{5\mu^{eff} (3k^{eff} + 4\mu^{eff})} \mathbf{K} \quad (8)$$

$$\omega^{(z/i)} = \frac{4\mu_z + 3k_i}{(3k_z + 4\mu_z)} \mathbf{J} + \frac{3k_z(2\mu_i + 3\mu_z) + 4\mu_z(3\mu_i + 2\mu_z)}{5\mu_z(3k_z + 4\mu_z)} \mathbf{K} \quad (9)$$

$$\omega^{(m/i)} = \frac{4\mu_m + 3k_i}{(3k_m + 4\mu_m)} \mathbf{J} + \frac{3k_m(2\mu_i + 3\mu_m) + 4\mu_m(3\mu_i + 2\mu_m)}{5\mu_m(3k_m + 4\mu_m)} \mathbf{K} \quad (10)$$

$$\omega^{(m/z)} = \frac{4\mu_m + 3k_z}{(3k_m + 4\mu_m)} \mathbf{J} + \frac{3k_m(2\mu_z + 3\mu_m) + 4\mu_m(3\mu_z + 2\mu_m)}{5\mu_m(3k_m + 4\mu_m)} \mathbf{K} \quad (11)$$

k and μ are the bulk and shear moduli, respectively, while \mathbf{J} and \mathbf{K} result from the decomposition of the unit tensor \mathbf{I} .

2.2 Three-Phase Model

$A^{(c)}$ Is determined by the three-phase model shown in Fig. 5.

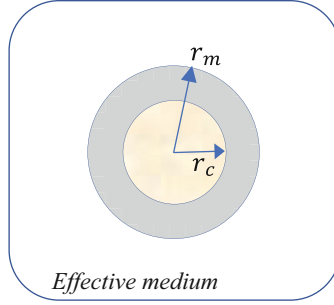


Fig. 5. Three-phase model.

According to Barhdadi [8], the tensor $A^{(c)}$ is given by:

$$A^{(c)} = \left[f_c (I + T^J (C^{eff}) : (c^c - C^{eff})) + f_m (I + T^J (C^{eff}) : (c^m - C^{eff})) : (I - T^H (c^m) : (c^m - c^c)) \right]^{-1} \quad (12)$$

$(I - T^H (c^m) : (c^m - c^c))$ is the localization tensor expressing the jump of mean strain between the matrix coating and the homogenized cluster and is obtained from the Eshelby's tensor [13] as follow:

$$\left[I - T^H (c^m) : (c^m - c^c) \right] = \frac{4\mu_m + 3k_c}{(3k_2 + 4\mu_2)} J + \frac{3k_m(2\mu_c + 3\mu_m) + 4\mu_m(3\mu_c + 2\mu_m)}{5\mu_m(3k_m + 4\mu_m)} K \quad (13)$$

According to the Eq. (5) the properties of cluster are given by:

$$k_c = k_z + f_i(k_i - k_z) : M^{(i3)} \quad (14)$$

$$\mu_c = \mu_z + f_i(\mu_i - \mu_z) : D^{(i3)} \quad (15)$$

$M^{(i3)}$ and $D^{(i3)}$ express the isotropic and deviatoric parts, respectively, of $A^{(i3)}$.

According to the Eq. (3), The effective properties of nanocomposite are given by:

$$K^{eff} = k_m + f_i(k_i - k_m) : M^{(i4)} + f_z(k_z - k_m) : M^{(z4)} + f_c(k_c - k_m) : M^{(c)} \quad (16)$$

$$\mu^{eff} = \mu_m + f_i(\mu_i - \mu_m) : D^{(i4)} + f_z(\mu_z - \mu_m) : D^{(z4)} + f_c(\mu_c - \mu_m) : D^{(c)} \quad (17)$$

$M^{(i4)}$, $D^{(i4)}$, $M^{(z4)}$, $D^{(z4)}$, $M^{(c)}$ and $D^{(c)}$ Are the Isotropic and Deviatoric Parts, Respectively, of $A^{(i4)}$, $A^{(z4)}$ and $A^{(c)}$, Such that:

$$M^{(c)} = M^{(i3)} + M^{(z3)} \quad (18)$$

$$D^{(c)} = D^{(i3)} + D^{(z3)} \tag{19}$$

$$A^{(c)} = A^{(i3)} + A^{(z3)} \tag{20}$$

$M^{(z3)}$ and $D^{(z3)}$ Are the Isotropic and Deviatoric Parts, Respectively, of $A^{(z3)}$.
 The Tensors $M^{(i4)}, D^{(i4)}, M^{(z4)}, D^{(z4)}, M^{(i3)}, M^{(z3)}, D^{(i3)}$ and $D^{(z3)}$ Are Given in [8].

3 Results and Discussions

In Figs. 6 and 7, the Poisson’s ratio of nanoparticles, interphase and matrix are equal to 0.3 and the Young’s moduli of silica nanoparticles is $E_i = 70GPa = 20E_m$, where E_m is the Young’s modulus of polymer matrix. In the Fig. 6, the interphase thickness is taken as 0.5 nm and the nanoparticles radius is assumed as 1 nm. This figure shows the effect of IMC (properties contrast of interphase to matrix) on the effective elastic modulus. For IMC equal to 0.5, we observe that the reinforcement with nanoparticles is stabilized due to the low interphase properties and when the IMC increase, we observe a higher reinforcement effects. The Fig. 7 shows the effect of interphase thickness at IMC = 2. The higher effect of reinforcement is also due to the increasing of interphase thickness. Figures 6 and 7 clearly show the importance of interphase for the case of nanocomposite structures filled with nanoparticles.

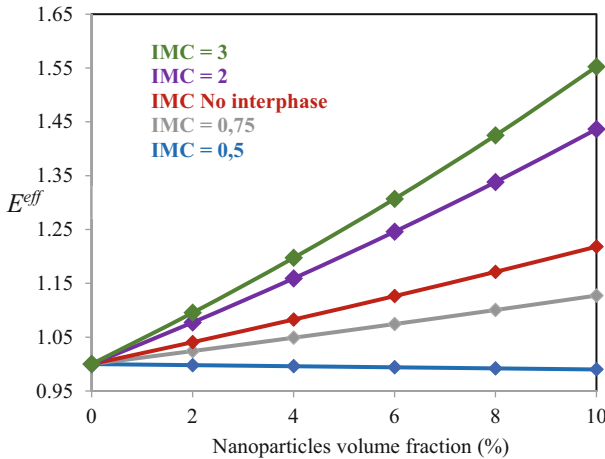


Fig. 6. Young’s modulus (GPa) as a function of IMC and nanoparticles content. The reinforcement to matrix properties contrast is equal to 20.

Figure 8 shows the overall elastic modulus of nanocomposite at various volume fractions of nanoparticles. In this application the radius of the nanoparticle was taken to be 1 nm. The thickness of interphase is 0.6 nm. The Young’s moduli for each phase is assumed as: nanoparticles, 88.7GPa; interphase, 3.5GPa; and matrix, 4.2GPa. The

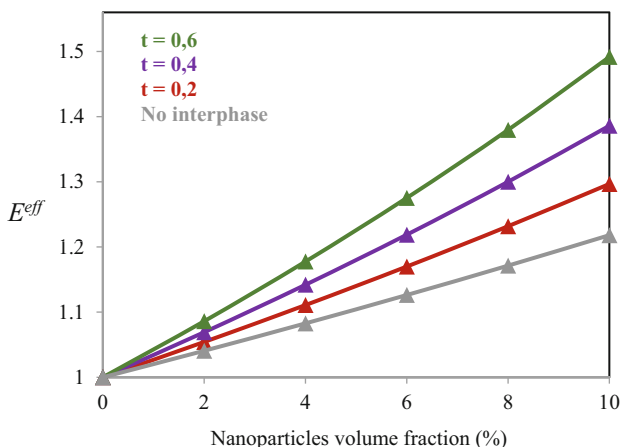


Fig. 7. Young’s modulus (*GPa*) as a function of interphase thickness and nanoparticles content. The reinforcement to matrix properties contrast is equal to 20.

Poisson’s ratio is taken as: 0.26, 0.4, and 0.4 for nanoparticles, interphase and matrix, respectively. As shown in Fig. 8, the effective elastic modulus decreases with increasing the thickness of interphase. This figure shows also that the present model is in a good agreement with numerical results [1].

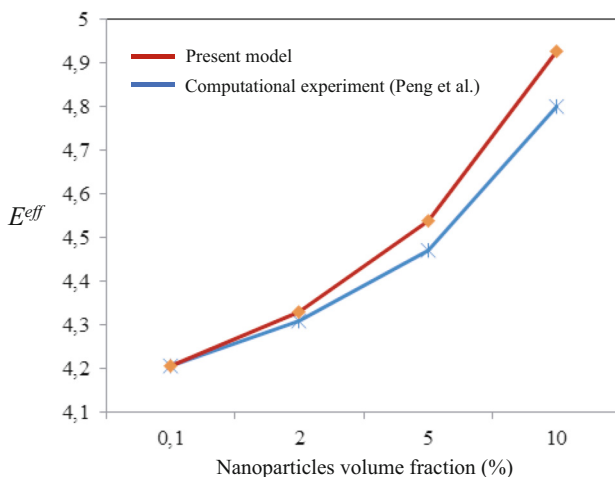


Fig. 8. Young’s modulus (*GPa*) as a function of nanoparticle content (Interphase thickness = 0.6 nm)

Figure 9 shows the effect of nanoparticle content on the effective elastic modulus of nanocomposites. The elastic modulus of nanocomposites estimated by the new model is compared with experimental data [14] and with the predictions of Halpin-Tsai model [15]. Here the radius of the nanoparticle is taken equal to 3 nm and the thickness of

interphase is 0.5 nm . The Young's moduli of nanoparticles and matrix are 69 GPa and 3 GPa , respectively. The Poisson's ration of nanoparticles and matrix are 0.15 and 0.35 , respectively.

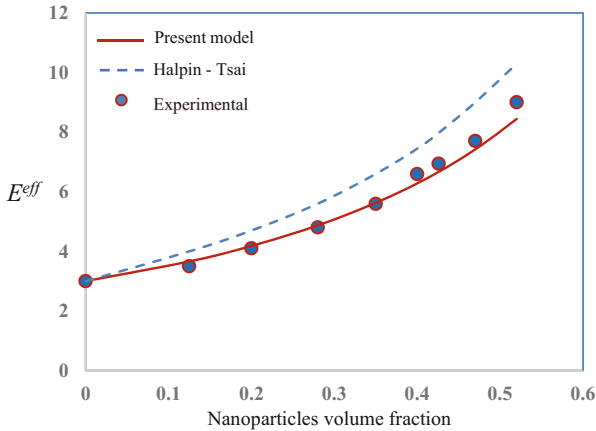


Fig. 9. Young's modulus (GPa) as a function of nanoparticle content (Interphase thickness = 0.5 nm)

The interphases properties are evaluated by Saber-Samandari et al. [16]. Young's moduli and Poisson's ratio of interphase are 3.48 GPa and 0.4 , respectively.

As shown in Fig. 9, a very good accuracy between experimental data [14] and the present model while the Halpin–Tsai [15] model overestimate the experimental data.

4 Conclusion

A micromechanical model for evaluating the elastic properties of nanocomposite materials has been developed. The model takes into account the interphase and clustering effects and use the Green function and interfacial operators. The methodology requires the combination of the four-phase model and the three-phase model. In the obtained results, it was observed that the Young's modulus increases with increasing the interphase thickness and with increasing the interphase to matrix properties contrast (IMC). It was shown also that the present model is compared successfully with computational and experiment results. This suggests that the proposed model is suitable for determining the effective elastic modulus of nanocomposites.

References

1. Peng, R. D., Zhou, H. W., Wang, H. D., Leon Mishnaevsky, Jr.: Modeling of nano-reinforced polymer composites: microstructure effect on Young's modulus. *Compos. Mater. Sci.* **60**, 19–31 (2012)

2. Amraei, J.E., Jam, J., Arab, B., Firouz-Abadi, R.D.: Effect of interphase zone on the overall elastic properties of nanoparticle reinforced polymer nanocomposites. *J. Compos. Mater.* **9**(53), 1–14 (2018)
3. Abu Taqa, A. G., Abu Al-Rub, R. k., Senouci, A., Al-Nuaimi, N., Bani-Hani, K. A.: The effect of interfacial transition zone properties on the elastic properties of cementitious nanocomposite materials. *J. Nanomater.* **1**(16), 1–13 (2015)
4. Wernik, J.M., Meguid, S.A.: Multiscale modeling of the nonlinear response of nano-reinforced polymers. *Acta Mech.* **82**(217), 1–16 (2010)
5. Paliwal, B., Cherkaoui, M.: Estimation of anisotropic elastic properties of nanocomposites using atomistic-continuum interphase model. *Int. J. Solids Struct.* **18**(49), 2424–2438 (2012)
6. Mortazavi, B., Bardon, J., Ahzi, S.: Interphase effect on the elastic and thermal conductivity response of polymer nanocomposite materials: 3D finite element study. *Compos. Mater. Sci.* **69**, 100–106 (2013)
7. Bornert, M., Stolz, C., Zaoui, A.: Morphologically representative pattern-based bounding in elasticity. *J. Mech. Phys. Solid.* **3**(44), 307–331 (1996)
8. Barhdadi, E.H., Lipinski, P., Cherkaoui, M.: Four phase model: a new formulation to predict the effective elastic moduli of composites. *J. Eng. Mater. Technol.* **129**(2), 313–320 (2007)
9. Dederichs, P.H., Zeller, R.: Variational Treatment of the Elastic Constants of Disordered Materials. *Zeitschrift für Physik A Hadrons and nuclei* **259**, 103–113 (1973)
10. Hill, R.: Interfacial operators in the mechanics of composite media. *J. Mech. Phys. Solid.* **29**, 347–357 (1983)
11. Christensen, R.M., Lo, K.H.: Solutions for effective shear properties in three phase sphere and cylinder models. *J. Mech. Phys. Solid.* **27**, 315–330 (1983)
12. Hashin, Z.: The elastic moduli of heterogeneous materials. *J. Appl. Mech.* **17**, 143–150 (1962)
13. Eshelby, J.D.: The determination of the elastic field of an ellipsoidal inclusion and related problems. *Proc. Royal Soc. London A* **241**, 376–396 (1957)
14. Rousseau, C.E., Tippur, H.V.: Compositionally graded materials with cracks normal to the elastic gradient. *Acta Mater.* **48**, 4021–4033 (2000)
15. Halpin, J.C., Tsai, S.W. : Effects of Environmental Factors on Composite Materials, AFML-TR, 67–243 (1969)
16. Saber-Samandari, S., Afaghi-Khatib, A.: Evaluation of elastic modulus of polymer matrix nanocomposites. *Polym. Compos.* **28**, 405–411 (2007)



Effect of Number of Engines and Payload Weight on Static Stability of an Unmanned Aerial Vehicle

Amina Kottat^(✉) and Mohamed ElAmine Ait Ali

Université Mohammed V de Rabat, Ecole Mohammadia d'Ingénieurs, ERG2(ME),
Av. Ibn Sina, Rabat, Morocco

amina.kottat@research.emi.ac.ma, aitali@emi.ac.ma

Abstract. The goal of this work is to study the effect of number of engines and payload weight on the static stability of an unmanned aerial vehicle (uav) after the pre-sizing phase of its design. The aim is to answer the designer's question, at this early stage, what will happen to the uav's static stability if we increase these two parameters? After pre-sizing an uav that satisfies our requirements, we start by using the semi-empirical method known as Data Compendium to calculate and quantify their effect on static stability derivatives coefficients. In the next step, we develop a model using the vortex lattice method of the XFLR5 software to characterize these effects. Both methods give similar qualitative results. Using these results, we show that increasing the number of engines of this uav induces a non-monotonic change in its static stability with respect to the three axes. We also show that increasing the payload weight increases its static stability. However, this increase is non-monotonic with the increase of the number of engines. These conclusions show uav designers, focused on increasing static stability with respect to specific axis, how to choose the right number of engines and to manage payload's weight during operations.

Keywords: Unmanned Aerial Vehicle · Static stability · uav design · VLM · XFLR5 · engines number effect · payload weight effect

1 Introduction

Stability of an unmanned aerial vehicle (uav) is its ability to return to its original equilibrium state after a disturbance that could induce a sudden change in its angle of attack or sideslip. It is said to have static stability if the forces generated by this disturbance tend to bring it to the original equilibrium. And it is said to have dynamic stability if it has a dynamic motion, with or without oscillation, after the same disturbance during its movement towards this equilibrium. Both types of stability are important characteristics of handling and control of uavs. A lack of stability leads to losing control, to possible serious accidents and to loss of equipment. Which explain why stability analysis is an integrated part of uav design process. It is first considered in the conceptual design phase with formulas to have an initial geometry and ensure equilibrium [12], then in preliminary design phase [1] where we calculate aerodynamic forces and moments for different flying conditions to deduce stability coefficients.

Before fabrication of a prototype, calculating these stability coefficients is done by mainly three approaches. i. either by high fidelity computational fluid dynamic (cfD) which is time consuming and limits its use to a limited number of simulations of flying conditions; ii. or by low fidelity numerical analysis such as panel methods described by [15], lifting line theory [16] and vortex lattice methods [17]. These methods are considered as an effective numerical method in aircraft stability analysis [8]; iii. or by semi-empirical systematic methods such as DATCOM method, described thoroughly in [7]. The latter two approaches give good and fast results making them a good compromise between computational cost and accuracy [3] to study the effect of various parameters on stability. Sun et al. [18] used cfd simulation to evaluate the stability of Diamond Joined-Wing uav. Sugandi et al. [6] used the same approach on a tandem wing uav. Moelyadi et al. [4] used a similar simulation and compared the results to those of panel methods in evaluating the stability of a twin tail boom. Septiyana et al. [2] used the three approaches to validate the static stability of the same type of uav. Kuitche et al. [19] used these approaches to study the stability of similar type of uav for multiple altitudes. Kim et al. [3] used a less time consuming cfd method, called actuator method, to study the effect of engines location in the uav on the static stability of two fixed wings uavs with four engines. Pobikrowska et al. [5] used a panel method to analyze the stability of an airplane and rectify its geometry to better its stability. In these mentioned works, studies are carried out on frozen configuration and sensibility studies to design parameters are limited. In this study, we pre-size an uav that satisfies our requirement, and we quantify the effect of number of engines on the static stability of this fixed wing uav. For this, we consider three uavs where we increase their number from one to three, all other parameters are the same. Then we consider two more payload weights and quantify their effect on static stability of each of the three uavs. This change represents the increase of payload weight during effective use of the uav. We carry out these studies using first DATCOM approach then using a vortex lattice method (VLM) included in XFRL5 and we compare the results. We have a good agreement between the two methods. These results help the designer to answer the question, in early stages of the design process: what will happen to the uav's static stability if we increase the number of engines and if we increase its payload weight?

2 Study of the Effect of Engines Number and Payload Weight on Static Stability Using DATCOM Method

2.1 Preliminary Sizing and Calculating Stability Coefficients of the Uav

Before proceeding to the static stability study, we start by pre-sizing the uav based on a design methodology described by Raymer [12], Sadraey [13] and Gundlach [14]. A detailed description of the method, parameters and formulas used are given in [20]. We set the following requirements: payload weight 8.5 kg, takeoff and landing distances 12 m, rate of climb 3 m/s, range 20 km, maximum cruise speed 22 m/s, stall speed 7 m/s, ceiling 200 m, 4h endurance and a flight mission with a single cruise. After the preliminary design, we obtain all the initial parameters of the uav's geometry as shown in (Fig. 1). For this study, we chose NACA 4418 as profile for the wing and NACA 64012-A for the horizontal and vertical tail.

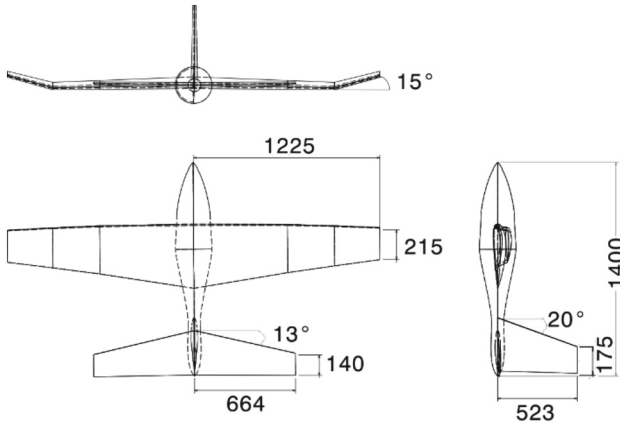


Fig. 1. Views of the uav model developed with preliminary method (all distance measures are in mm)

To determine its static stability characteristics, we calculate three stability coefficients [9] in the body axis system: i. derivative of the pitching moment coefficient, $C_{m\alpha}$ to evaluate static longitudinal stability; ii. Derivative of the yawing moment coefficient $C_{n\beta}$ to evaluate static directional stability; iii. And derivative of the rolling moment coefficient, $C_{l\beta}$ to evaluate static lateral stability.

In this section, we use DATCOM method for estimating these coefficients. A complete description of the method and the equations are described in [7]. We followed the implementation of Nelson [10] and Roskam [11] of DATCOM procedures to calculate them. To have a statically stable uav in longitudinal, lateral and directional modes $C_{m\alpha}$ and $C_{l\beta}$ must be negative and $C_{n\beta}$ must be positive. In addition to pitching moment coefficient C_{m0} for an angle of attack of zero, must be positive. If these conditions are satisfied, any increase of the modulus value of the stability coefficients means an increase of the uav's static stability relative to that direction (longitudinal, directional or lateral).

2.2 Effect of the Number of Engines on the Static Stability of the Uav

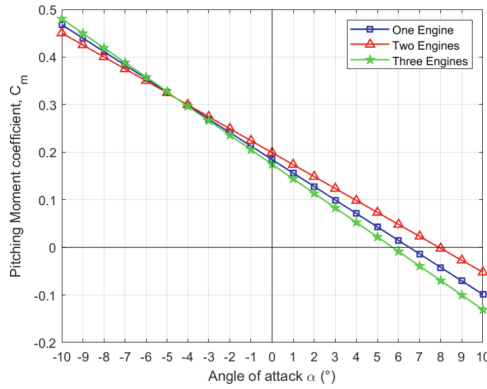
To study the effect of the number of engines on the static stability of the uav, we keep the same geometry, and we change the number of engines from one to three. For the uav with one engine, we put it on its nose; for the one with two engines, we put them on its wings; for the one with three engines, we put one on its nose and two on its wings. Then we use DATCOM method to calculate pitching moments for angle of attack, α , varying from -10° to 10° and yawing and rolling moments for angle of sideslip, β , varying from -10° to 10° .

Figure 2 and Fig. 3 show the results for the three cases considered. Then we calculate the coefficients: $C_{m\alpha}$, $C_{n\beta}$, $C_{l\beta}$, C_{m0} and the trim point (angle).

of attack), α_s , where the pitching moment is zero. Table 1 summarizes the values of these parameters for each case. From this table we find that: i. according to the conditions mentioned in Sect. 2.1 all three uavs are statically stable ii. The static longitudinal and directional stability of the uav with three engines is greater than the one with one engine

Table 1. Static stability parameters for uav with a payload of 8.5kg with one, two and three engines calculated using DATCOM method

Uav characteristics	Uav (1 engine)	Uav (2 engines)	Uav (3 engines)
C_{m0}	0.1846	0.1991	0.1747
$C_{m\alpha}$ (rad^{-1}) (increase relative to uav with 1 engine in %)	-1.6242	-1.4405 (-11.3%)	-1.7507 (7.8%)
$C_{n\beta}$ (rad^{-1}) (increase relative to uav with 1 engine in %)	0.1402	0.1363 (-2.8%)	0.1440 (2.7%)
$C_{l\beta}$ (rad^{-1}) (increase relative to uav with 1 engine in %)	-0.0454	-0.0421 (-7.3%)	-0.0440 (-7%)
Trim point α_s ($^\circ$)	6.5	7.9	5.7

**Fig. 2.** Pitching moment versus angle of attack in the case of uav with one, two and three engines calculated using DATCOM method

and both are more static stable than the one with two engines; iii. The static lateral stability of the uav with one engine is greater than the one with three engines and both are more static stable than the one with two engines; vi. Each uav has a different value for the trim point α_s .

2.3 Effect of Payload Weight on the Static Stability of the Uav

To study the effect of payload weight on the static stability of the uav, we consider the three uavs of the previous section and we increase the payload weight to 20 kg and 30 kg for each uav. In total, we have nine cases to study their static stability. For each case, similarly to the previous section we use DATCOM method to calculate the necessary moments by varying α and β from -10° to 10° by a step of 1° . Table 2 shows the calculated parameters. The cases with a payload weight of 8.5kg are already presented in Table 1. From Table 1 and 2 we find that: i. according to the conditions mentioned in Sect. 2.1 all the cases studied in this section are statically stable. ii. Increasing the payload

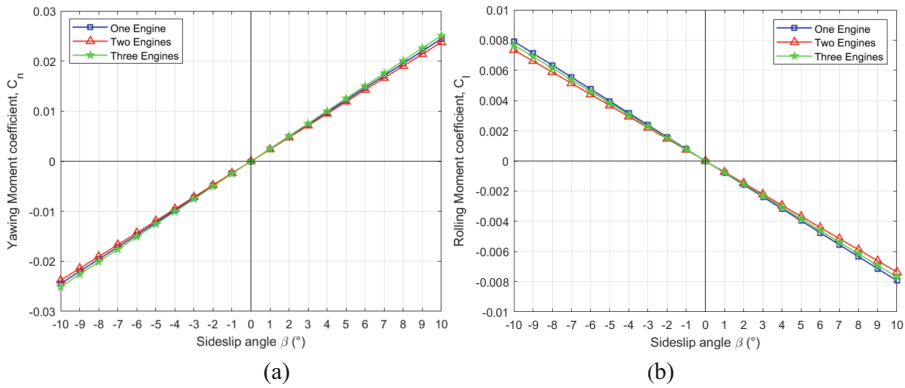


Fig. 3. (a) Yawing moment versus sideslip angle, and (b) Rolling moment versus sideslip angle in the case of uav one, two and three engines calculated using DATCOM method

weight increases the static stability in the three directions: longitudinal, directional and lateral; iii. The increase is more important in the case of uav with two engines followed by the one with one engine then by the one with three engines for static longitudinal and directional stability; iv. For static lateral stability increase is more important in the case of two engines followed by the one with three engines then by the one with one engine; v. therefore, the trim point α_s changes for every case. This quantification of changes is valuable information in controlling the uav during flying.

Table 2. Static stability parameters of uavs with a payload weight of 20 kg and 30 kg compared to the uav with same number of engines and a payload weight of 8.5 kg calculated using DATCOM method

Uav characteristics	Uav (1 engine)		Uav (2 engine)		Uav (3 engine)	
	20 kg	30 kg	20 kg	30 kg	20 kg	30 kg
C_{m0}	0.1658	0.1602	0.1736	0.1658	0.1613	0.1569
$C_{m\alpha}$ (rad^{-1})	-1.8641	-1.9351	-1.7648	-1.8641	-1.9209	-1.9776
Increase relative to 8.5 kg in %	-14.8%	-19.1%	-22.5%	-29.4%	-9.7%	-12.9%
$C_{n\beta}$ (rad^{-1})	0.1430	0.1436	0.1421	0.1428	0.1449	0.1457
Increase relative to 8.5 kg in %	1.2%	2.4%	4.3%	4.8%	0.6%	1.2%
$C_{l\beta}$ (rad^{-1})	-0.0457	-0.0465	-0.0452	-0.0460	-0.0461	-0.0466
Increase relative to 8.5 kg in %	-3.4%	-1.7%	-7.4%	-9.3%	-4.8%	-5.9%
Trim point α_s (°)	5.1	4.7	5.6	5	4.8	4.5

3 Numerical Study and Comparison to DATCOM Method of the Effect of Engines Number and Payload Weight on Static Stability

3.1 Description of the Numerical Model Developed Using XFLR5

To compare the DATCOM results to those of numerical approach for the nine cases studied in the previous section, we used the open-source program XFLR5 [21]. This software employs various methods such as lifting line theory and vlm method to determine aerodynamic properties of small aircrafts and to calculate their static stability coefficients. We inserted same geometrical details and data specified (profiles, air density, altitude...) in Sect. 2.1 without including the fuselage as its participation in the static stability coefficients is negligible. For the study of the effect of engines number, we positioned for each case the engines as described in Sect. 2.2. For the study of the effect of payload weight, we kept it in the same position, and we changed only its weight. To solve the problem, we used the vlm method and we segmented the geometry into 3655 panels. Then we obtain the static stability coefficients of every case in addition to C_{m0} and trim point α_s .

3.2 Numerical Study of the Effect of the Number of Engines on the Static Stability of the Uav

We used the model described in the previous section in the case of the three uavs with one, two and three engines and a payload of 8.5 kg. Table 3 shows the stability parameters calculated with XFLR5 and its comparison to the values calculated using DATCOM method. On one hand, we find that results given by XFLR5 confirm all the findings (i. to vi.) by DATCOM method in Sect. 2.2. On the other hand, the numerical results are close to those of DATCOM method for the static longitudinal stability coefficient (1.6% as mean difference in the three cases); less so for static directional stability coefficient (-9.3% as mean difference in the three cases); and quite different for the static lateral stability coefficient (-27.9% as mean difference in the three cases).

3.3 Numerical Study of Payload Weight Effect on the Static Stability of the Uav

To study the payload weight effect, in addition to the three uavs with a payload of 8.5 kg we modeled using XFLR5 in the previous section, we modeled six additional uavs where we increase the payload weight to 20 kg and 30 kg. Table 4 shows the stability parameters calculated using XFLR5 and its comparison to the values calculated using DATCOM method. On one hand, we find that results given by XFLR5 confirm all the findings (i. to v.) by DATCOM method in Sect. 2.3. On the other hand, the numerical results are close to those of DATCOM method for the static longitudinal stability coefficient (0.8% as mean difference in the nine cases); less so for static directional stability coefficient (-9.1% as mean difference in the nine cases); and quite far for the static lateral stability coefficient (-26.3% as mean difference in the nine cases).

Table 3. Static stability parameters for uav with a payload of 8.5 kg with one, two and three engines calculated using XFLR5 and compared to those calculated using DATCOM method

Uav characteristics	Uav (1 engine)	Uav (2 engines)	Uav (3 engines)
C_{m0}	0.2047	0.2126	0.1996
$C_{m\alpha}$ (rad^{-1}) (increase relative to uav with 1 engine in %)	-1.6044	-1.3809 (-13.9%)	-1.7519 (9.2%)
$C_{m\alpha}$ increase relative to DATCOM result %	-1%	-4%	0.07%
$C_{n\beta}$ (rad^{-1}) (increase relative to uav with 1 engine in %)	0.1275	0.1246 (-2.3%)	0.1294 (1.5%)
$C_{n\beta}$ increase relative to DATCOM result %	-9.1%	-8.6%	-10.1%
$C_{l\beta}$ (rad^{-1}) (increase relative to uav with 1 engine in %)	-0.0329	-0.0296 (-10%)	-0.0324 (-1.5%)
$C_{l\beta}$ increase relative to DATCOM result %	-27.5%	-29.7%	-26.4%
Trim point α_s ($^\circ$)	7.3	8.8	6.5

Table 4. Static stability parameters for uav with a payload of 20 kg and 30 kg compared to the uav with same number of engines and a payload weight of 8.5 kg calculated using XFLR5 and compared to those calculated using DATCOM method

Uav characteristics	Uav (1 engine)		Uav (2 engine)		Uav (3 engine)	
	20 kg	30 kg	20 kg	30 kg	20 kg	30 kg
C_{m0}	0.1940	0.1908	0.1982	0.1938	0.1918	0.1894
$C_{m\alpha}$ (rad^{-1})	-1.9006	-1.9878	-1.7792	-1.9017	-1.9625	-2.0288
Increase relative to 8.5 kg in %	18.5%	23.9%	28.8%	37.7%	12%	15.8%
Increase relative to DATCOM result %	1.9%	2.7%	0.8%	2%	2.2%	2.6%
$C_{n\beta}$ (rad^{-1})	0.1313	0.1325	0.1297	0.1313	0.1321	0.1330
Increase relative to 8.5 kg in %	3%	3.9%	4.1%	5.3%	2.1%	2.8%
Increase relative to DATCOM result %	-8.9%	-8.3%	-9.6%	-8.2%	-9.8%	-9.5%
$C_{l\beta}$ (rad^{-1})	-0.0340	-0.0347	-0.0335	-0.0343	-0.0344	-0.0349

(continued)

Table 4. (continued)

Uav characteristics	Uav (1 engine)		Uav (2 engine)		Uav (3 engine)	
	20 kg	30 kg	20 kg	30 kg	20 kg	30 kg
Increase relative to 8.5 kg in %	3.2%	5.2%	11.6%	13.7%	5.8%	7.2%
Increase relative to DATCOM result %	-25.6%	-25.4%	-25.9%	-25.4%	-25.4%	-25.1%
Trim point α_s (°)	5.1	4.7	5.6	5	4.8	4.5

4 Conclusion and perspectives

In this work we studied the effect of the number of engines and payload weight on the static stability of a fixed wing uav, to help the designer, in the pre-sizing phase, understand the relations of these parameters to static stability of an uav. We started by pre-sizing an uav that satisfies our requirements, and we obtained all the initial parameters of the uav's geometry that we took as a reference for our study.

In the first part, we used DATCOM method to calculate the static stability parameters. To study the effect of the number of engines, we varied the number of engines from one to three and we kept the other parameters unchanged. For the uav with one engine, we put it on its nose; for the one with two engines, we put them on its wings; for the one with three engines, we put one on its nose and two on its wings. This effect is different depending on the direction. We showed that the static longitudinal and directional stability of the uav with three engines is greater than the one with one engine and both are more static stable than the one with two engines. On the other hand, we showed that the static lateral stability of the uav with one engine is greater than the one with three engines and both are more static stable than the one with two engines.

In the next step, we increased the payload weight from 8.5 kg to 20 kg and 30 kg in each uav with a different number of engines and we kept it in the same position in the uav. We showed an increase of static stability in the three directions. However, this increase is more important in the case of uav with two engines followed by the one with one engine then by the one with three engines for static longitudinal and directional stability. For static lateral stability the increase is more important in the case of two engines followed by the one with three engines then by the one with one engine. This quantification of static stability increase would help in better controlling the uav.

In the second part, to compare the obtained results to those of numerical approach based on vlm method. We used XFRL5 to calculate the static stability parameters. All the findings are confirmed qualitatively. Quantitatively the numerical results are close for the static longitudinal stability coefficient (0.8% as mean difference in the nine cases); less so for static directional stability coefficient (-9.1% as mean difference in the nine cases); and quite far for the static lateral stability coefficient (-26.3% as mean difference in the nine cases). Which makes this tool a viable option for future studies that would

interest the designer at pre-sizing phase such as studying the relationship between these, or other, parameters to better the uav's dynamic stability.

References

1. Gudmundsson, S.: *General Aviation Aircraft Design: Applied Methods and Procedures*, 2nd edn. Butterworth-Heinemann, United States (2022)
2. Septiyana, A., et al.: Static stability analysis on twin tail boom UAV using numerical method. In: *AIP Conference Proceedings. The 8th International Seminar on Aerospace Science and Technology – ISAST 2020*, vol. 2366, pp. 1–9. AIP Publishing, Bogor (2021)
3. Kim, D., Lee, Y., Oh, S., Park, Y., Choi, J., Park, D.: Aerodynamic analysis and static stability analysis of Manned/unmanned distributed propulsion aircrafts using actuator methods. *J. Wind Eng. Ind. Aerodyn.* **214**, 104648 (2021). <https://doi.org/10.1016/j.jweia.2021.104648>
4. Moelyadi, M.A., Rohmahwati, Y.A.T., Nugraha, A.P.: CFD based determination of longitudinal static and dynamic stability derivatives of twin boom UAV. *J. Appl. Sci. Eng.* **22**, 259–266 (2019). [https://doi.org/10.6180/jase.201906_22\(2\).0007](https://doi.org/10.6180/jase.201906_22(2).0007)
5. Pobikrowska, K., Goetzendorf-Grabowski, T.: Stability analysis of the experimental airplane powered by a pulsejet engine. *Aircr. Eng. Aerosp. Technol.* **91**, 843–850 (2019). <https://doi.org/10.1108/AEAT-07-2018-0184>
6. Sugandi, T.S., Nathan, Subrata, S.K., Arifianto, O., Moelyadi, M.A.: Prediction of static stability in tandem wing unmanned aerial vehicle. In: *Journal of Physics: Conference Series, 6th International Seminar of Aerospace Science and Technology*, vol. 1130, pp. 12–28, Jakarta (2018). <https://doi.org/10.1088/1742-6596/1130/1/012028>
7. Hoak, D.E.: *USAF stability and control - DATCOM. 1, Sections 1–3*. Air Force Flight Dynamics Laboratory Wright - Patterson Air Force Base, Ohio (1978)
8. Voß, A.: An Implementation of the Vortex Lattice and the Doublet Lattice Method. *DLR-Interner Bericht. DLR-IB-AE-GO-2020-137. 52 S* (2020)
9. Delecroix, T.: *Étude de stabilité statique et dynamique d'un avion Blended-Wing-Body de 100 passagers* (2017)
10. Nelson, R.C.: *Flight stability and automatic control - Chapter 2*. 2nd ed. WCB/McGraw Hill, Boston, Mass. (1998)
11. Roskam, J.: *Methods for estimating stability and control derivatives of conventional subsonic airplanes* (1971)
12. Raymer, D.P.: *Aircraft Design: A Conceptual Approach*. American Institute of Aeronautics and Astronautics, Reston (2021)
13. Sadraey, M.H.: *Aircraft Design: A Systems Engineering Approach*. Wiley, Chichester (2013)
14. Gundlach, J.: *Designing unmanned aircraft systems: a comprehensive approach*. American Institute of Aeronautics and Astronautics, Reston, VA (2014)
15. Erickson, L.: *Panel Methods: An Introduction*. NASA, California (1990)
16. Prandtl, L.: *Applications of Modern Hydrodynamics to Aeronautics Part 1: Fundamental Concepts and the Most Important Theorems. Part 2: Applications*. <https://ntrs.nasa.gov/citations/19930091180>
17. Deyoung, J.: Historical evolution of vortex-lattice methods. A workshop held at Langley research center, pp.1–11. NASA, Virginia (1976)
18. Sun, J., Wang, H., Zhou, Z., Lei, S.: Aerodynamic numerical analysis of the low reynolds number diamond joined-wing configuration unmanned aerial vehicle. *Int. J. Aeronaut. Space Sci.* **19**, 544–562 (2018). <https://doi.org/10.1007/s42405-018-0072-9>

19. Kuitche, M., Botez, R.M.: Methodology of Estimation of Aerodynamic Coefficients of the UAS-E4 Ehécatl using Datcom and VLM Procedure. In: AIAA Modeling and Simulation Technologies Conference. American Institute of Aeronautics and Astronautics, pp. 1–14. AIAA, Denver (2016). <https://doi.org/10.2514/6.2017-3152>
20. Kottat, A., Ait Ali, M.E.: Quantifying the Number of Engines and Endurance Effect on the Initial Geometry of an Unmanned Aerial Vehicle Using an Adapted Pre-sizing Method. In: advances in Integrated Design and Production II. CIP 2022. Lecture Notes in Mechanical Engineering. Springer, Cham (2022). https://doi.org/10.1007/978-3-031-23615-0_41
21. Deperrois, A.: Analysis of Foils and Wings Operating at Low Reynolds Number. Guidelines for XFLR5 v6.03 (2011)

Author Index

A

Abdelbaki, Abdelhalim 73
Abdelhalim, Abdelbaki 34
Abdelilah, Ghammaz 43
Ait Ali, Mohamed ElAmine 148
Aniss, Saïd 109, 130
Assoul, Mouh 130
Aze-eddine, Naamane 43

B

Barhdadi, El Hassane 139
Ben smail, Youssef 54
Beyaoui, Moez 85
Bouchaib, Jamal 34
Boukamel, Adnane 92, 120
Boukendil, Mohammed 34, 73
Braikat, Bouazza 99

C

Charqui, Zouhair 73
Chouaf, Abdelkerim 25
Choukri, Saad 16

D

Damil, Noureddine 92, 120
Daya, Abdelmajid 109

E

El Guerjouma, Rachid 85
El Mahi, Abderrahim 85
El Moçayd, Nabyl 120
El moumen, Ahmed 54
El Moutaouakil, Lahcen 34, 73

F

Fadil, Rajaa 99

H

Haddar, Mohamed 85
Hakim, Mohamed 16
Hassan, Belahrach 43
Hayani Choujaa, Mohamed 109
Hidki, Rachid 73

I

Imad, Abdellatif 54

K

Kaba, Sita 120
Kesentini, Zeineb 85
Kottat, Amina 148
Kouassi, A. Y. E. 1

L

Lmai, Fatima 54

M

Matadi Boumbimba, R. 1
Mekkaoui, Moussa 63

N

Nissabouri, Salah 63

O

Ouardi, Ayoub 92
Oubrek, Mohamed 16

R

Radouani, Mohammed 43
Rammane, Mohammed 99

Rebiere, Jean Luc 85
Rhimini, Hassan 25, 63
Riahi, Mehdi 109

S

Sakine, Mohamed 109
Salhi, Loubna 120
Sangaré, M. K. 1

T

Taouzer, Chaimaa 130
Tri, Abdeljalil 99

Y

Youssef, Nadir 43

Z

Zitouni, Ismaïne 25
Zrikem, Zaki 34, 73